Algoritme-ontwikkeling en protocoloptimalisatie
voor farmacokinetische modellering
van dynamische contrast-versterkte magnetische resonantiebeeldvorming

Algorithm Development and Protocol Optimization
for Pharmacokinetic Modeling
of Dynamic Contrast-Enhanced Magnetic Resonance Imaging

Dieter De Naeyer

Promotoren: prof. dr. ir. P. Verdonck, prof. dr. W. Ceelen
Proefschrift ingediend tot het behalen van de graad van
Doctor in de Ingenieurswetenschappen: Biomedische Ingenieurstechnieken

Vakgroep Civiele Techniek
Voorzitter: prof. dr. ir. J. De Rouck
Faculteit Ingenieurswetenschappen en Architectuur
Academiejaar 2011 - 2012

UNIVERSITEIT
GENT

ISBN 978-90-8578-473-9
NUR 954, 919
Wettelijk depot: D/2011/10.500/76

# Voorwoord

In de afgelopen weken werd me meermaals gevraagd of ik, met wat ik nu weet, nog aan een doctoraat zou beginnen. Het antwoord mag misschien evident lijken vanuit het beeld van de ingenieur wiens boek netjes afgedrukt voor u openligt en die breedglimlachend en zichtbaar opgelucht zijn werk staat te presenteren op een openbare verdediging. Mijn IBiTech collega's zullen echter bevestigen dat je dat beeld toch enigszins moet relativeren. En toch ís het antwoord evident, maar dan wel om een aantal bijkomende redenen. Eerst en vooral hebben de vier voorbije jaren me als geen andere ervaring geholpen om mezelf te leren kennen, niet in het minst mijn beperkingen. Daarenboven heb ik elke dag de kans gekregen om die beperkingen te overwinnen. Of dat laatste gelukt is, laat ik in het midden, maar het staat vast dat mijn promotor, prof. Verdonck, me een aantal niet louter wetenschappelijke kwaliteiten heeft bijgebracht waarvan ik de voordelen in mijn huidige job al ondervind. Ten tweede heb ik steeds mijn eigen weg kunnen kiezen, zowel op inhoudelijk vlak als voor de dagdagelijkse invulling van mijn onderzoek. Dergelijke vrijheid, die voor mij persoonlijk echt wel belangrijk en bevorderlijk is geweest, was enkel mogelijk dankzij een grenzeloos vertrouwen vanwege mijn promotoren. Ik kan prof. Verdonck en prof. Ceelen daarvoor dan ook niet genoeg bedanken. Tenslotte heeft mijn doctoraatsonderzoek me uiteraard een grote wetenschappelijk voldoening gegeven, ondanks of misschien dankzij, de vele onoverkomelijke knelpunten waarmee ik in die vier jaar geconfronteerd werd. Gelukkig was er op dergelijke momenten het ongebreidelde positivisme van prof. Segers, wiens luisterbereidheid stilaan legendarische vormen begint aan te nemen. Ik zou nog een heel aantal andere redenen kunnen bedenken, maar U heeft al begrepen dat het antwoord op de openingsvraag volmondig 'ja' is.

Ik wil hier uiteraard een aantal mensen vermelden die me met raad en daad bijgestaan hebben. In de eerste plaats wil ik Prof. Ceelen bedanken, die de bezieler van deze doctoraatsthesis was en me op experimenteel vlak vaak heeft geholpen. Ook Dr. Debergh, Dr. Verhulst, Dr. Smeets en prof. De Deene ben ik zeer erkentelijk, alsook al mijn IBiTech collega's en alle leden van de jury. Ik wil ook mijn ex-ex-collega Marloes uitgebreid bedanken, wiens Latexkennis en gedrevenheid op zich misschien al een doctoraat verdienen. Tenslotte hoop

ik voor Koen dat Cercle Brugge ooit kampioen mag worden, uiteraard het liefst na een intensieve en spannende strijd met AA Gent, en als het dan nog even kan, in tweede klasse.

De afgelopen vier jaar hebben me evenwel ook veel voldoening geschonken op andere vlakken. Mijn ouders hebben steeds een resem van 'service flat diensten' verstrokken die het uitvoeren van doctoraatsonderzoek zoveel gemakkelijker en aangenamer maakten. Niet zozeer de gemakken die hiermee gepaard gingen, maar veeleer het besef van hun tomeloze inzet en bereidwilligheid om me op alle, voor hen mogelijke, manieren vooruit te proberen helpen, zijn de echte bron van geluk. Ook mijn broers en zussen, en in het bijzonder de ondertussen negen nichtjes en neefjes zijn die term meer dan waardig. Verder hoop ik dat Ken en Bart evenveel plezier beleefd hebben aan de (te?) vele fifa- en voetbaluren en dat Rudy zijn secretarispensioen nog niet te gauw aanvraagt.

Rest me tenslotte nog mijn vriendin Inge te bedanken, omdat ze het al zo lang uithoudt met mij en een onmisbare bron van geluk is. Zonder het allicht zelf te beseffen heeft ze een belangrijke inhoudelijke invloed gehad op dit proefschrift, door op om het even welk uur van dag of nacht naar mijn problemen te willen luisteren.

# Contents

# Abbreviations and symbols

## Abbreviations

| | |
|---|---|
| CA | contrast agent |
| MRI | magnetic resonance imaging |
| CT | computed tomography |
| PET | positron emission tomography |
| DCE-MRI | dynamic contrast-enhanced magnetic resonance imaging |
| TK-model | Tofts & Kermode model |
| ETK-model | extended Tofts & Kermode model |
| TH-model | tissue homogeneity model |
| AATH-model | adiabatic approximation of the tissue homogeneity model |
| AIF | arterial input function |
| SPGRE | spoiled gradient echo |
| IR-SGPRE | inversion recovery spoiled gradient echo |
| FOV | field of view |
| SNR | signal-to-noise ratio |
| LSQ | least-square |
| MLM | maximum likelihood |
| ssq | sum of squared differences |
| SAR | specific absorption rate |

## Symbols

| | |
|---|---|
| $\Delta t$ | sampling time |
| $T_{scan}$ | total scan time |
| $\alpha$ | flip angle |
| $T_R$ | repetition time |
| $T_E$ | echo time |

| | |
|---|---|
| $T_1$ | longitudinal relaxation time |
| $T_2$ | transverse relaxation time |
| $T_2^*$ | effective transverse relaxation time |
| $R_1$ | longitudinal relaxation rate |
| $R_2$ | transverse relaxation rate |
| $R_2^*$ | effective transverse relaxation rate |
| $r_1$ | longitudinal relaxivity coefficient |
| $r_2$ | transverse relaxivity coefficient |
| $T_{10}$ | native longitudinal relaxation time |
| $\boldsymbol{B_0}$ | static magnetic field |
| $\boldsymbol{B_1}$ | varying magnetic field |
| $\Delta x$ | spatial resolution of MR-image in x-direction |
| $\Delta y$ | spatial resolution of MR-image in y-direction |
| $\Delta z$ | slice thickness |
| $N_x$ | number of voxels in MR-image in x-direction |
| $N_y$ | number of voxels in MR-image in y-direction |
| $FOV_x$ | field of view of MR-image in x-direction |
| $FOV_y$ | field of view of MR-image in y-direction |
| $NEX$ | number of averages |
| $BW$ | receiver bandwidth |
| $F_p$ | plasma flow per unit mass of tissue |
| $PS$ | permeability-surface area product |
| $K^{trans}$ | endothelial transfer constant |
| $\sigma_K$ | standard deviation on the parameter $\theta$ |
| $c_\theta$ | coefficient of variation of the parameter $\theta$ |
| $\nu_e$ | EES volume fraction |
| $\nu_p$ | blood plasma volume fraction |
| $\theta$ | Generalized model parameter |
| $\hat{\theta}$ | Estimate for the parameter $\theta$ |
| $\boldsymbol{C}$ | measured concentration vector |
| $C_T(t, \boldsymbol{\theta})$ | General pharmacokinetic model |
| $\boldsymbol{\theta}$ | Parameter vector |
| $L(\boldsymbol{\theta} \mid (C))$ | Likelihood function |
| $\sigma_S$ | Signal intensity standard deviation |
| $\sigma_C$ | Concentration standard deviation |
| $\boldsymbol{\Sigma}$ | covariance matrix |
| $F_{ij}$ | Fisher matrix elements |
| $B_0$ | static magnetic field |
| $B_1$ | varying magnetic field |

# Samenvatting

Dynamische contrastversterkte magnetische resonantiebeeldvorming (DCE-MRI) is een functionele beeldvormingstechniek die, na de injectie van een contraststofbolus, de signaalintensiteit in een specifiek weefsel opvolgt. De techniek kent een groot succes in tumoren, waarin de signaalintensiteit typisch sterk stijgt na contraststofinjectie, een fenomeen dat aankleuring wordt genoemd. De fysiologische achtergrond van deze aankleuring is zogenaamde angiogenese, i.e. de vorming van nieuwe bloedvaten in een tumor uit het vertakken van de bestaande omliggende bloedvaten. Zolang zijn afmetingen klein zijn (1-2mm) kan diffusie de tumor voorzien in zijn zuurstof- en energiebehoeften. Een groeiende tumor heeft echter nood aan een eigen vasculair netwerk om aan zijn toenemende zuurstof- en energiebehoeften te voldoen. Dit gebeurt doordat de tumorcellen zogenaamde angiogenese-stimulerende factoren gaan uitscheiden, wanneer zij in een hypoxische toestand komen. Zoals de naam het zegt, veroorzaken zulke moleculen de vorming van nieuwe tumorbloedvaten door angiogenese. In normaal weefsel gebeurt angiogenese gestaag, door een imbalans tussen angiogenese-stimulerende en angiogenese-inhibiterende factoren, die lichtjes overhelt in de richting van stimulatie. In tumorweefsel echter, is deze imbalans zodanig sterk, dat de groei van het vasculaire netwerk zeer snel en ongecontroleerd optreedt. Als gevolg hebben tumorbloedvaten een aantal morfologische kenmerken die hen onderscheidt van normale bloedvaten. Zo worden zij gekenmerkt door een chaotische structuur, met een grote heterogeniteit in dichtheid en bloedstroom. Ook vertonen zij grote discontinuïteiten die hen extreem permeabel maken in vergelijking met normale bloedvaten. Een geïnjecteerde contraststof, die in een normale vasculatuur grotendeels intravasculair blijft, extravaseert uit de poreuze tumorbloedvaten en hoopt op in de interstitiële ruimte tussen de cellen. Deze toename in contraststofconcentratie wordt in DCE-MRI waargenomen als een aankleuring.

Farmacokinetische modellering is een recente ($\pm$ 20 jaar) en zeer krachtige techniek om deze aankleuring te kwantificeren. Het vereist de omzetting van de opgemeten signaalintensiteitscurve naar een contraststofconcentratiecurve, die op haar beurt wordt gefit aan een farmacokinetisch model. Het resultaat is een aantal farmacokinetische parameters, die een maat zijn voor de toestand

van het vaatnetwerk van de tumor en dus voor diens angiogene activiteit. Dergelijke parameters zou men onmogelijk uit conventionele beeldvorming kunnen afleiden, gezien daar enkel anatomische informatie in vervat zit. Men kan zich nu afvragen wat het nut is om de angiogene activiteit van de tumor te kwantificeren. Vooreerst is aangetoond dat de toestand van het tumorvaatnetwerk als maat kan gebruikt worden om de agressiviteit van de tumor en de prognose van de patiënt te evalueren. Traag groeiende goedaardige tumoren hebben vaak een meer normaal vaatbed in vergelijking met snelgroeiende kwaadaardige gezwellen. Ook de capaciteit van de kanker om uit te zaaien naar andere lichaamsdelen is sterk afhankelijk van de toestand van het vaatbed. Dit maakt duidelijk dat farmacokinetische modellering een belangrijke rol kan spelen in het stellen van een kankerdiagnose en het beoordelen van de prognose voor de patiënt. Farmacokinetische modellering is ook een niet-invasieve methode om de respons van een tumor op een behandeling te evalueren en te voorspellen. Zo bijvoorbeeld zijn een aantal farmacokinetische parameters een maat voor de bloedstroom in de tumor. Regio's waar die bloedstroom ontoereikend is worden hypoxisch en vertonen typisch een hoge resistentie ten aanzien van radiotherapie. Farmacokinetische modellering kan deze hypoxische regio's opsporen en daarbij het succes van een radiotherapiebehandeling voorspellen. Tenslotte wordt deze modelleringstechniek tegenwoordig standaard gebruikt in studies die nieuwe anti-angiogene behandelingen testen. Conventionele cytotoxische therapieën hebben als doel het doden van de tumorcellen. Anti-angiogene behandelingen daarentegen beïnvloeden de toestand van de vaatnetwerk en zorgen voor een zogenaamde renormalisatie, waarbij de morfologische kenmerken verdwijnen, die het tumorvaatbed onderscheiden van een normaal vaatbed. Het is aangetoond dat deze renormalisatie de efficiëntie van chemo-en radiotherapie verhoogt, deze laatste bijvoorbeeld door het verdwijnen van de hypoxische regio's. Nieuwe anti-angiogene therapieën dienen aldus beoordeeld te worden met een niet-invasieve beeldvormingstechniek die de toestand van het vaatnetwerk in kaart brengt, een rol die farmacokinetische modellering kan vervullen.

Ondanks het enorme potentieel en niet-invasieve karakter van farmacokinetische modellering blijft het gebruik van de techniek beperkt tot klinische studies. Om een doorstroming naar de dagelijkse klinische praktijk te realiseren zijn het merendeel van de prominente onderzoekers in het domein het erover eens dat drie belangrijke facetten van farmacokinetische modellering nog aangepakt dienen te worden. Ten eerste is er geen consensus over gestandardiseerde DCE-MRI protocols voor het opmeten van de concentratiecurve. Het DCE-MRI protocol, bestaat uit een MR-pulssequentie, met belangrijke parameters zoals de repetitietijd en de fliphoek, die elke $\Delta t$ seconden herhaald wordt gedurende een volledige scantijd $T_{scan}$. Het hoeft geen betoog dat dit DCE-MRI protocol een grote invloed heeft op zowel de nauwkeurigheid als de precisie van de farmacokinetische schattingen. Zo bijvoorbeeld kan verwacht worden dat een verhoogde temporele resolutie aanleiding geeft tot betere schattingen. In

DCE-MRI echter kan het verkorten van $\Delta t$ niet gerealiseerd worden zonder een opoffering te doen in de signaal-ruis verhouding (SNR) van de MR-metingen, of zonder aan de spatiale resolutie te raken. Ook zijn er een aantal MR-gerelateerde foutenbronnen, die de nauwkeurigheid van de farmacokinetische parameters aantasten, en afhankelijk zijn van de DCE-MRI instellingen. Tenslotte is er geen consensus over de beste methode om de arteriële inputfunctie (AIF) op te meten. De AIF is de contraststofconcentratie in het bloedplasma van een voedende arterie van de tumor. De kennis van de AIF is onontbeerlijk om de farmacokinetisch modellen aan de opgemeten weefselconcentratiecurve te fitten. Er bestaan een aantal manieren om deze AIF te bepalen, gaande van het veronderstellen van een populatiegemiddelde AIF, tot het patiënt-specifiek en gelijktijdig opmeten van de AIF met de weefselconcentraties. Elke manier heeft een aantal voor-en nadelen en in het bijzonder de patiënt-specifieke manier introduceert een aantal extra protocolvereisten die voor de andere methoden niet noodzakelijk zijn. Dit alles maakt duidelijk dat er nood is aan gestandaardiseerde DCE-MRI protocols voor farmacokinetische modellering en aan een mathematisch kader dat de invloed van alle protocolparameterss op de precisie van de kinetische parameters kan beschrijven, rekening houdend met de trade-off tussen temporele resolutie, spatiale resolutie en SNR.

Een tweede facet dat de klinische aanvaarding van farmacokinetische modellering hypothekeert is het niet-voorhanden zijn van gestandardiseerde post-processing technieken. De post-processing van de DCE-MRI data bestaat uit de conversie van signaalintensiteit naar contraststofconcentratie, het fitten van de aldus verkregen curves aan een farmacokinetisch model en het construeren van betrouwbaarheidsintervallen voor de geschatte parameters. Voor geen van deze drie onderdelen bestaat overeenstemming in de literatuur en de betrouwhaarheidsintervalconstructie is zelfs nauwelijks of niet onderzocht. Nochtans is het nauwkeurig schatten van een betrouwbaarheidsinterval voor toepassingen, zoals anti-angiogene behandelingen, van cruciaal belang gezien het de statistische significantie van verschillen in pre- en post-behandeling opgemeten parameters evalueert. Zonder gestandardiseerde post-processingstechnieken is het onmogelijk om farmacokinetische modelleringsresultaten uit verschillende onderzoekscentra te vergelijken.

Tenslotte bestaat er geen gouden standaard voor het valideren van de modelleringstechniek. De vraag of de farmacokinetische parameters daadwerkelijk de fysiologische grootheden opmeten die ze beweren te reflecteren, blijft tot op vandaag onbeantwoord. Een aantal studies heeft correlaties aangetoond tussen de farmacokinetische parameters en ondermeer de histologische dichtheid aan microbloedvaten, of de expressie van angiogenese-stimulerende factoren, terwijl anderen geen correlaties konden vinden. Verder blijken de farmacokinetische parameters ook te verschillen wanneer ze opgemeten worden via DCE-MRI of DCE-CT. Validatie van de modellen blijft dus tot op heden een ingewikkeld probleem. Elke modellering houdt een aantal veronderstellingen

in, die in realtiteit niet vervuld kunnen zijn. Wanneer data gefit worden aan een bepaald model kan in het algemeen gesteld worden dat een hoger-order model, i.e. een model dat meer parameters bevat, de opgemeten curve beter zal beschrijven. Echter, het hoger aantal parameter brengt ook een hogere onzekerheid op de fitparameters met zich mee, tot zelf intercorrelaties tussen de parameter die voor instabiliteit in de fitprocedures kunnen zorgen. Dit is niet anders voor farmacokinetische modellering, waarvoor 2- 3- en 4-parameter modellen bestaan. Een befaamde studie heeft aangetoond dat de parameters in het 4-parameter model het best overeenkomen met de fysiologische grootheden die ze willen meten, waar voor het 2- en 3-parameter model duidelijke fouten optreden ten gevolge van te vereenvoudigde veronderstellingen. Het 4-parameter model ondervindt echter grote instabiliteit bij het fitten aan DCE-MRI data, ondermeer ten gevolge van intercorrelaties tussen de parameters. Ook zijn de onzekerheden op de overeenkomstige parameters groter. Aanbevelingen voor modelselectie zijn niet beschikbaar in de literatuur.

In dit proefschrift wordt een aantal studies voorgesteld, die als doel hebben (een deel van) bovenvermelde limitaties te verhelpen. De eerste drie hoofdstukken bevatten respectievelijk een overzicht van het kader van het onderzoek, de principes en trade-off van DCE-MRI en de modellen en toepassingen van de farmacokinetische modelleringstechniek. In het vierde hoofdstuk worden de conversiemethodes voor het omzetten van signaalintensiteit naar constraststofconcentratie voor 'spoiled gradient echo' (SPGRE) pulssequenties besproken. SPGRE-pulssequenties worden zeer vaak aangewend in DCE-MRI voor het opmeten van concentratiecurves omdat ze MR-beelden met goede spatiale resolutie en aanvaardbare SNR kunnen opmeten met een temporele resolutie die geschikt is voor farmacokinetische modellering. Er wordt in dit hoofdstuk een nieuwe conversiemethode voor SPGRE-pulssequenties voorgesteld, die nauwkeuriger is dan de huidig gebruikte conversiemethodes en deel kan uitmaken van een gestandardiseerd verwerkingprotocol. Ook wordt in dit hoofdstuk aangetoond, dat omwille van de niet-lineaire relatie tussen signaalintensiteit en contraststofconcentratie, de variantie van ruis op de concentratiecurves sterk afhangt van de pulssequentieparameters, maar ook van de contraststofconcentratie zelf. In het vijfde hoofdstuk wordt de relatie tussen concentratieruis en pulssequentieparameters verder uitgespit. Er wordt een procedure voorgesteld voor het bepalen van een optimale SPGRE-fliphoek om een gegeven concentratie-interval zo precies mogelijk op te meten. Dergelijke optimale fliphoek blijkt de precisie van kinetische parameter ten goede te komen, en moet in acht genomen worden bij het opstellen van gestandardiseerde DCE-MRI protocols. In hoofdstuk 6 wordt een nieuwe schatter voorgesteld voor farmacokinetische modellering. Gezien de variantie van de concentratieruis afhankelijk is van de concentratie zelf, zijn de opgemeten concentratiecurves heteroskedastisch. In dergelijke omstandigheden is de traditionele schatter die de residuele kwadratensom minimaliseert (LSQ-schatter), niet langer optimaal. In plaats daarvan wordt een zogenaamde maximum likelihood schatter (MLM-schatter)

geïntroduceerd, die zowel de precisie als de nauwkeurigheid van de farmacokinetische parameters verbetert. In het bijzonder zijn de betrouwbaarheidsintervallen, geconstrueerd met de MLM-schatter, veel nauwkeuriger dan die van de LSQ-schatter. Gezien betrouwbaarheidsintervallen op de farmacokinetische parameters van cruciaal belang zijn voor bepaalde toepassingen, zoals het testen van anti-angiogene behandelingen, kan deze MLM-schatter een belangrijk onderdeel vormen van een gestandardiseerd verwerkingsprotocol. In hoofdstuk 7 wordt een nieuwe stabiele en snelle fitprocedure voorgesteld voor het 4-parameter model, die in vergelijking met de conventionele fitprocedures zowel de precisie als de nauwkeurigheid van de farmacokinetische parameters sterk verhoogt. Gezien de parameters van dit model de grootste fysiologische relevantie vertonen, maar het tot nu toe weinig onderzocht werd omwille van de instabiliteiten in de fitprocedure, kan deze nieuwe schattingsmethode een belangrijke stap zijn voor de validatie van farmacokinetische parameters. In hoofdstuk 8, wordt een statistisch kader voorgesteld, gebaseerd op de zogenaamde Cramer-Rao ondergrenzen, dat de precisie van een fitparameter voorspelt, gegeven pulssequentieparameters, de temporele resolutie en totale scanduur. Het wordt aangetoond dat deze methode kan gebruikt worden voor protocoloptimalisatie: de invloed van de totale scantijd wordt verduidelijkt en een aantal methodes om de temporele resolutie van de DCE-MRI scans te verhogen wordt onderzocht. Deze Cramer-Rao ondergrenzen kunnen gebruikt worden bij het ontwerp van gestandardiseerde protocols. Tenslotte worden in hoofdstuk 9 de voornaamste conclusies, vernieuwingen en limitaties van dit proefschrift samengevat.

# Summary

Dynamic contrast-enhanced magnetic resonance imaging (DCE-MRI) is a functional imaging technique, that monitors the signal intensity in a tissue of interest after the injection of a contrast agent. The technique is increasingly used in cancer research. In tumors, the measured signal intensity typically increases after contrast agent injection, a phenomenon that is denoted signal enhancement. The physiogical basis of this contrast enhancement is angiogenesis, i.e. the formation of new blood vessels in the tumor by the branching of the blood vessels in the surrounding tissue. In small tumors (1-2 mm in diameter) diffusion supplies the tumor in oxygen and nutrients. A growing tumor however requires an own vascular network to maintain its increasing oxygen and nutrient demands. The formation of such a vascular structure is governed by angiogenesis, stimulated by the production of angiogenesis promoting substances in hypoxic tumor cells. In normal tissue, angiogenesis is a slow and controlled process, maintained by a slight imbalance between angiogenesis-promoting and angiogenesis-inhibiting factors. In tumors however, the extent of this imbalance is so high, that the vessel growth occurs fast and uncontrolled. As a result, the tumor vasculature has a number of morphologic features that distinguish it from normal vasculature. The vascular network is highly chaotic and exhibits a large degree of heterogeneity in microvessel density and blood flow. In addition, the blood vessels are permeable and discontinuous, allowing the injected contrast agent to extravasate into the interstitial space between the cells. As in normal vasculature the contrast agent remains largely intravascular, this explains the typically observed contrast enhancement in tumor tissue.

Pharmacokinetic modeling is a recent and powerful technique to quantify the contrast enhancement. It requires the conversion of the measured signal intensity curves to contrast agent concentration curves, which on their turn are fit to a pharmacokinetic model. The result is a number of pharmacokinetic parameters, that characterize the state of the tumor vasculature and its angiogenic activity. Such a quantitative characterization of the angiogenic activity of a tumor is physiologically highly sigficant. Firstly, it is shown that the state of the tumor blood vessels can serve as a measure for the aggresiveness

of the tumor and the prognosis of the corresponding patient. Slowly growing benign tumors often exhibit a more normalized vasculature when compared to more swiftly growing malignant lesions. In addition, the capacity of a tumor to metastasize to distant site of the body is strongly dependent on the state of its vasculature. Pharmacokinetic modeling has therefore an important role in tumor diagnosis, lesion characterization and patient prognosis. Secondly, pharmacokinetic modeling is a non-invasive method to monitor and evaluate tumor response to treatment. Pharmacokinetic parameters can for instance be a measure for tumor blood flow. Regions with insufficient blood flow become hypoxic and are typically more resistant to radiotherapy. Pharmacokinetic models can identify those hypoxic regions, thereby predicting the outcome of the patient after radiotherapy. Finally, pharmacokinetic modeling is increasingly used for the testing of novel anti-angiogenic treatments. Conventional cytotoxic therapies principally attack and kill the tumor cells. Anti-angiogenic treatment target the tumor blood vessels and may result in a renormalisation of the tumor vasculature, i.e. the disappearance of the morphologic features that are not apparent in normal vasculature. It is shown that this renormalisation enhances the efficiency of chemo- and radiotherapy, the latter for instance by the removal of hypoxic regions. New anti-angiogenic therapies require a non-invasive imaging technique, as pharmacokinetic modeling & DCE-MRI, that can serve as a biomarker for the state of the tumor vasculature.

Despite it huge potential and its non-invasive character, pharmacokinetic modeling remains restricted to clinical studies. To increase its general clincal acceptance, the major authors in the field agree that 3 important limitations of pharmacokinetic modeling have to be assessed. Firstly, no consensus exists in literature about standardized DCE-MRI protocols. The DCE-MRI protocol, consists of a MR pulse sequence, with important settings as repetition time and flip angle, that is repeated every $\Delta t$ seconds to monitor the CA concentration for a total scan time $T_{scan}$. The influence of the DCE-MRI protocol on both the accuracy and the precision of the pharmacokinetic estimates is of course high. It may for instance be expected that an increased temporal resolution allows improved quality of the pharmacokinetic estimates. However, in DCE-MRI the reduction of $\Delta t$ is impossible without making sacrifices in the signal-to-noise ratio (SNR), the spatial resolution or the spatial coverage. In addition, a number of MR-related error sources occur, that affect the accuracy of the pharmacokinetic parameters, and whose extent is dependent upon the DCE-MRI settings. Furthermore, a number of determination strategies exists for the arterial input function (AIF). The AIF is the CA concentration in the blood plasma of a feeding artery of the tumor and its knowledge is indispensable for fitting the tumor concentration curves to a pharmacokinetic model. Often a population-averaged AIF is used, while other studies measure the AIF individually, by monitoring the signal intensity in a feeding artery, together with the signal intensity in the tumor tisse. Every method has a number of advantages, but no agreement about the best determination strategy

is attained. In particular the individual monitoring technique, imposes a number of extra protocol requirements, as increased temporal resolution, when compared to other AIF strategies. These considerations show the need for standardized DCE-MRI protocols which can be investigated for their accuracy and precision and for a mathematical framework that can assess the trade-off between temporal resolution, spatial resolution, spatial coverage and SNR.

A second limitation that prevents the clinical acceptance of pharmacokinetic modeling, is the lack of standardized post-processing techniques and the absence of clear recommendations for developping post-processing software. The post-processing of DCE-MRI data consists of the conversion of the signal intensity to contrast agent concentration, the fitting of the resulting concentration curves to a pharmacokinetic model, and the construction of confidence intervals for the estimated parameters. In literature the different parts of the post-processing are done in multiple ways, and the accuracy of confidence interval construction has not been investigated up to now. Nevertheless is the robust and accurate estimation of the confidence intervals on the kinetic parameters of crucial importance for several applications. When testing the effect of an anti-angiogenic therapy by comparing pre- and post-treatment kinetic parameters, these confidence intervals determine the statistical significance of the observed change. Without standardized post-processing techniques, it is impossible to compare pharmacokinetic modeling results from different research centra.

The third limitation is the absence of a golden standard for the validation of pharmacokinetic modeling. It is unclear whether the pharmacokinetic parameters truly reflect the physiological quantities they aim to measure. A number of studies has found correlations between the pharmacokinetic parameters and microvessel density or the expression level of angiogenesis stimulating factors, while other studies could not establish a significant correlation. Pharmacokinetic parameters also appear to differ when measured with DCE-MRI or DCE-CT. Validation of the pharmacokinetic models is therefore a difficult task. Every model comprises a number of assumptions, that in reality may not be valid. In general, higher order model, i.e. models with a higher number of parameters, comprise less assumptions and their parameters more truly reflect their physiological counterparts. However, the higher number of parameters also induces higher parameter uncertainties, or even intercorrelations between the model parameters that cause instabilities in the fitting procedure. These generalities were shown for pharmacokinetic modeling as well, for which 2-, 3- and 4-parameter models exist. A often-cited study proved that the parameters of the 4-parameter model exhibit the best correlation with the physiological quantities they aim to measure. In the 2- and 3- parameter models, significant errors occur, caused by invalid and oversimplified model assumptions. The 4-parameter model however suffers from sever instabilities in the fitting procedures caused by intercorrelations

between its parameters. In addition the uncertainties on the corresponding parameters are higher. No guidelines are available in literature for model selection.

In this work, a number of studies is proposed to assess (a part of) the limitations mentioned above. The first three chapters contain a description of the scope of the research, the basic principles and trade-offs in DCE-MRI, and an overview of the pharmacokinetic models and their applications, respectively. In the fourth chapter, the methods are reviewed, to convert the DCE-MRI signal intensity to contrast agent concentrations for spoiled gradient echo (SPGRE) pulse sequences. SGPRE pulse sequences are very often employed in DCE-MRI for the monitoring of contrast agent concentration, due to their ability to combine high spatial resolution with acceptable SNR and a temporal resolution that is suitable for pharmacokinetic modeling. In this chapter a new conversion method is proposed, that has higher accuracy than the currently used conversion methods and can be part of standardized post-processing protocol. In addition, it is shown in chapter 4, that due to the non-linear relationship between signal intensity and contrast agent concentration, the variance of the concentation noise is highly dependent on the pulse sequence parameters and on the contrast agent concentration itself. In chapter 5, this relationship between concentration noise and pulse sequence parameters is more thoroughly investigated. A procedure is proposed to determine an optimal SPGRE flip angle, for the most precise measurement of contrast agent concentrations within a premised range. The precision of the pharmacokinetic parameters benefits from the use of this optimal flip angle, which should be considered as an important part of a standardized protocol design. In chapter 6, a new estimator is proposed and tested for pharmacokinetic modeling. As the variance of the concentration noise is dependent upon the contrast agent concentration itself, the measured concentration data are heteroskedastic. In this case, the commonly used least square estimator (LSQ) is not optimal and instead a maximum likelihood estimator is proposed. Both the precision and the accuracy of the pharmacokinetic estimates is shown to benefit from the use of the MLM estimator. More importantly however, the MLM-based constructed confidence intervals appear to be much more accurate than their LSQ-counterparts. As accurate confidence intervals for the kinetic parameters are of crucial importance for several applications, as the testing of novel anti-angiogenic therapies, the MLM estimator should be part of a standardized post-processing protocol. In chapter 7, a new and stable fitting procedure for the 4-parameter model is proposed, that increases both the precision and the accuracy of the pharmacokinetic parameter estimates. The 4-parameter model has the highest physiological significance, i.e. its parameter show the highest correlation with the physiological quantities they aim to measure. However, due to the instabilities in the fitting procedure, it is used in a minority of the studies. Therefore, the introduction of this new accurate and fast estimation procedure may be an important step in the validation of the

pharmacokinetic parameters. In chapter 8, a statistical framework is proposed, based on the so-called Cramer-Rao lower bounds, that predicts the precision of the pharmacokinetic estimates and takes into account the influence of the pulse sequence parameters on the concentration noise, the temporal resolution and the total scan time. It is shown that this framework may be used for protocol optimzation: the influence of the total scan time is elucidated and a number of methods to increase the temporal resolution of the DCE-MRI scans are investigated, considering the trade-off between temporal resolution and SNR. This Cramer-Rao lower bound framework may be used for the design and evaluation of standardized DCE-MRI protocols. Finally, in chapter 9, the most important conclusions, innovations and limitations of this work are summarized.

# Chapter 1

# Introduction

## 1.1 Cancer & functional imaging

Cancer is a pathology characterized by an uncontrolled proliferation of cells, that tend to invade the surrounding tissue and metastasize to other parts of the human body. A tumor is a general indication for a cell mass or an abnormal growth in a tissue, but can be benign or malignant. While malignant or cancerous tumors have the tendency to metastasize, benign or not-cancerous tumors do not and may be less harmfull. Apart from cardiovascular diseases, cancer is the second most common cause of death in the Western world. According to the US national center for health statistics, in 2007 it accounted for 23.2 % of all US deaths. Fig. 1.1 and fig. 1.2 show the incidence and mortality rates for different cancer types. In women, breast cancer is the most common diagnosed cancer type, while prostate cancer has the highest incidence in men. For both sexes however, lung cancer has the highest mortality rate. In the last two decades, cancer mortality rates have been steadily decreasing as shown in fig. 1.3. This decrease may be attributed to the continuously expanding research in this field: it has provided insight into the cellullar and epi-genetic background and the corresponding risk factors of cancer growth. The latter has for instance lead to the development of screening programs to enable early diagnosis. In addition, significant progress in cancer treatment has been made throughout the last years. Technological improvements have enabled more effective radiotherapy and a number of new techniques such as robot-assisted surgery. A wide range of chemotherapeutic agents has been developped and introduced by the pharmaceutical companies, to effectively cure the cancer patient or at least prolonge its life expectation. Furthermore, the imaging modalities used for the visualization of cancer, such as computed tomography (CT), positron emission tomography (PET), or magnetic resonance imaging (MRI), have gained in quality, quantity and availability. Apart from technological developments that have enabled better

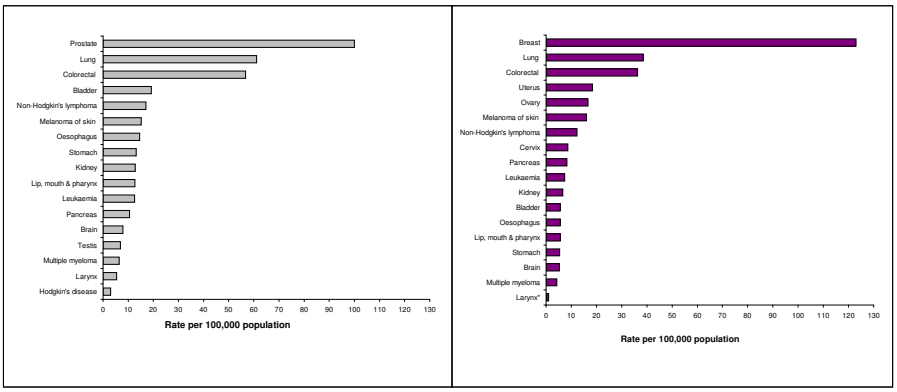


**Figure 1.1:** Major cancers in the U.K. : incidence by sex for 2006-2008 (source:www.statistics.gov.uk)

image quality, a number of new techniques has been developped that can be described as functional imaging. Conventional medical imaging techniques rely on the acquisition of a limited number of images that contain solely anatomical information. Functional imaging, on the other hand, is based on the acquisition of a time course of images after the intra-venous injection of a contrast agent (CA). Apart from anatomical information, these images contain additional functional information about the behaviour of the tissue over time. Dynamic contrast-enhanced MRI (DCE-MRI), which is the main application field of this work, is the generic name for all techniques that monitor the $T_1$-weighted MR signal intensity in a tissue of interest over time after the injection of a CA. Other functional imaging techniques are dynamic susceptibility contrast MRI (DSC-MRI), denoting all the $T_2$-weighted[1] techniques, or dynamic contrast-enhanced CT (DCE-CT), the corresponding tomography application.

Fig. 1.4 shows typical DCE-MRI signal intensity variations measured in different regions of interest (ROI) in a patient with a breast tumor after the injection of a CA. Within the tumor a strong increase is seen in the signal intensity, that is denoted as contrast enhancement. This contrast enhancement is not visible in fat, and appears to a far lesser extent in normal breast tissue. In the next section the patophysiological basis of this contrast enhancement, angiogenesis, is described and it is explained which information about the tumor is comprised within the enhancement curve.

[1]The difference between $T_1$ and $T_2$-weighted techniques is explained in chapter 2

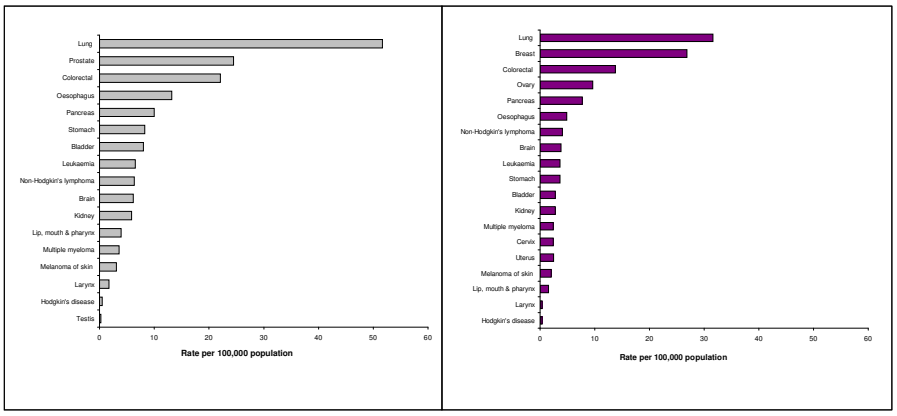


**Figure 1.2:** Major cancers in the U.K.: mortality by sex for 2006-2008 (source:www.statistics.gov.uk)

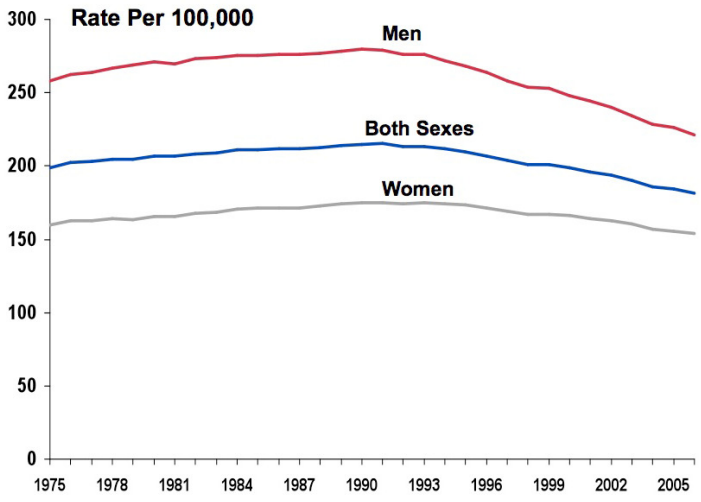


**Figure 1.3:** Cancer mortality rate in the U.S. over the period 1975-2006 (source:www.cancer.org)

## 1.2 Tumor angiogenesis & contrast enhancement

Angiogenesis denotes the sprouting of new capillaries from the existing blood vessels. It is a natural component of a number of normal physiological

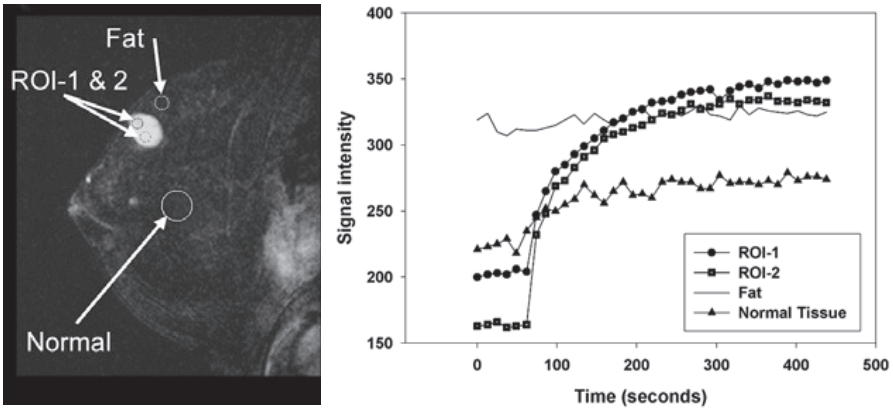


**Figure 1.4:** Left: anatomical breast MR image in a patient with a breast tumor (white region) with indication of the regions of interest. Right: signal intensity variations in the regions of interest shown in the figure on the left after the injection of a contrast agent. Contrast enhancement is seen in the tumor but (almost) not in normal tissue or fat. Figure adopted from [1].

processes, as wound healing or organ regeneration, but it forms a crucial step in the progression and metastasis of cancer cells [2, 3]. In the most early stages of a tumor, its growth and survival is based on diffusion of oxygen and nutrients from the vessels in the surrounding tissue. The diameter of these so-called avascular tumors, is limited by the maximum diffusion distance of oxygen and can reach up to 1-2 mm [4]. Tumor growth beyond these boundaries can only occur by the development of a vascular network within the tumor, to maintain its nutrients and oxygen supply. When the avascular tumor cells become hypoxic, i.e. the partial oxygen pressure is too low, they secrete angiogenesis promoting factors of which the most important is VEGF, vascular endothelial growth factor. These substances stimulate the endothelial cells of the neighbouring blood vessels to form endothelial sprouts that can grow towards the tumor cells [3, 4]. This process is shown in fig. 1.5. It has been shown that angiogensis is a key process in the progression of an avascular tumor to an invasive cancer [2]. In addition, the vascular access is indispensable for malignant tumor cells to metastasize to other sites in the body [2, 5]. In normal tissues, angiogenesis is regulated by a balance between angiogenic inhibiting and angiogenic stimulating factors. In tumors however, an imbalance between these factors exists and the resulting fast development of the vascular network causes a number of specific morphologic properties, distinguishing the network from normal vasculature. Tumor vasculature is highly chaotic and heterogeneous, i.e. areas of high and low vascular density succeed one another.

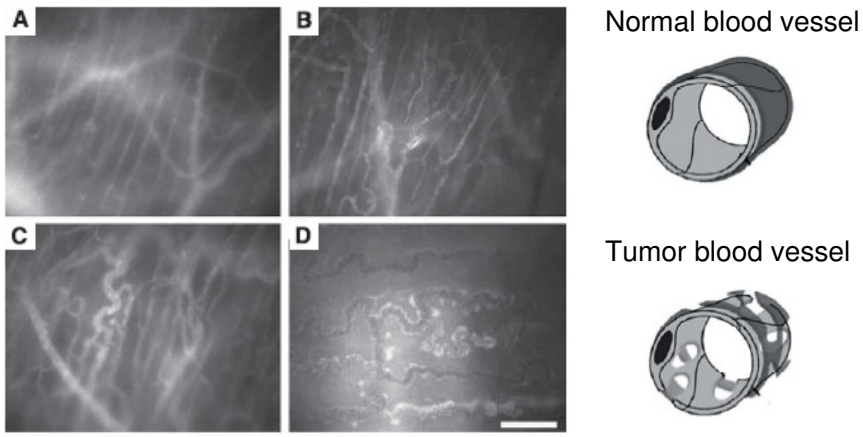


**Figure 1.5:** Left: in vivo fluorescence microscopy images of angiogenesis and tumor growth in hamsters with a dorsal skinfold window chamber. Images on day 0 (A), 3 (B), 6 (C) and 9 (D) after tumor implantation. Adopted from [8] Right: permeability discrepancy between normal and tumor vasculature.

It exhibits arteriovenous shunting and blindly ending vessels [2, 3]. These features can be noticed in fig. 1.5 as well. In addition, the blood flow in these vessels is highly unstable and blood vessels may collapse acutely. Lymphatic vessels are absent or disfunctional [6]. However, the most important feature in the framework of DCE-MRI is the hyperpermeability of the tumor vasculature when compared to a normal vascular network [2–4, 7]. This is illustrated in fig. 1.5 as well. In normal tissue, an intravenously injected CA remains largely intravascular. On the contrary, the leaky tumor vessels allow extravasation of the CA that initially accumulates in the space between the tumor cells and after a while washes out again. These CA kinetics are comprised in the time course of DCE-MRI images. An enhancement curve, measured in a region of interest within the tumor, as depicted in fig. 1.4, is therefore determined by the local microvessel density, the cell density in the ROI, the local blood flow in the tumor capillaries, and the local permeability and surface area of the vessel wall. In summary, the signal intensity curves measured in a DCE-MRI or DCE-CT investigation are reflections of the angiogenic activity of the tumor.

What is the clinical significance of gaining insight in the state of the tumors' vascular network? Firstly many studies have shown that patient prognosis is related to the state of the tumor angiogenesis. The level of increased VEGF-expression or microvessel density measurements have been associated with worse prognosis or metastastic ability of the cancer [2, 7]. The degree

of abnormality observed in the tumor vascular network is, among others, dependent on the growth rate of the tumor. Slowly growing benign tumor types may therefore show a relatively normal vasculature, while the vascular network of fastly growing malignant tumors tends to be highly disordered [4]. Secondly, due to arteriovenous shunting, low vessel density and unstable blood flow, hypoxic[2] regions originate within the tumor. It has long been acknowledged that hypoxia renders cells more resistant to a number of cytotoxic[3] therapies and in particular to radiotherapy [9], but may also induce genetic changes that increase the metastatic potential of the cells [6]. Furthermore, the metastatic potential of a malignant tumor is dependent on the state of it vascular network [6]. Finally, the high permeability of the tumor vessels, the absence or disfunctionality of a lymphatic system and the proliferating tumor cells cause an elevated interstitial fluid pressure (IFP), i.e. a higher hydrostatic pressure outside the blood vessels than in normal tissue. This increased IFP raises a severe obstruction for the delivery of chemotherapeutics to tumor cells. In area's with high IFP, the convective transport of the chemotherapeutic molecules from the blood vessels to the interstitial space is blocked and they cannot adequately reach the tumor cells, reducing the efficacy of the treatment. All these features (VEGF-expression, microvessel density, partial oxygen pressure, IFP, ...) can be assessed by mainly invasive measurement methods. Their derivation from the information available in the non-invasive functional imaging modalities, in particular by DCE-MRI, has therefore a high clinical relevance.

Apart from the assessment of the above cited features describing the state of the tumor vasculature, the enhancement curves in DCE-MRI can be used for evaluating the response of a tumor to treatment as well. In particular for so-called anti-angiogenic treatments that target the tumor vasculature instead of the tumor cells, DCE-MRI has been acknowledged as an important imaging tool [2, 10–12]. As angiogenesis is indispensable for the growth and metastasis of a tumor, a wide range of anti-angiogenic therapies has been developped in the last years, that prevent the formation of new blood vessels or destroy the existing vasculature in the tumor [6, 13]. The corresponding strategy is to deprive the tumor cells from oxygen and nutrients and thereby instigating the indirect killing of tumor cells. When administered as a single agent, such anti-angiogenic agents have not shown significant tumor response or improved long-term survival [6, 14, 15]. However, when administered in combination with cytotoxic therapies, an increase in survival has been demonstrated [6]. The success of this combined treatment is attributed to a normalisation of the tumor vascular network: anti-angiogenic therapies relie on reducing the imbalance between angiogenic inhibiting and angiogenic stimulating factors thereby causing vasculature normalization. This normalization means that the

[2] regions with insufficient oxygen supply
[3] Chemo- or radiotherapy

morphologic features, distinghuising the tumor vessels from normal vasculature largely disappear. The corresponding effects, as hypoxia, increased IFP or blood flow heterogeneity are highly diminished, and the resistance to radio-or chemotherapy is reduced. This combined treatment is highly promising, but requires an objective and non-invasive method, such as DCE-MRI, to characterize the effect of the anti-angiogenic treatment on the tumor microvasculature.

## 1.3 Pharmacokinetic modeling

In the previous sections, it was explained which information is comprised in an enhancement curve measured with DCE-MRI. The question still remains, how this information is quantitatively assessed and which parameters can be derived from these curves that characterize the angiogenic activity of the tumor. Generally, there are two main strategies to process the enhancement curves: heuristic and semi-quantitative measures on the one hand, and pharmacokinetic modeling on the other hand. The heuristic and semi-quantitative approaches are not investigated in this work, but a short summary of the most common methods is given in chapter 2. Pharmacokinetic modeling requires the conversion of the signal intensity curve to a CA concentration curve, that on its turn is fitted to a pharmacokinetic model describing the kinetics of the CA in the tumor tissue. This fitting results in a number of estimated pharmacokinetic parameters that characterize the state of the tumor microvasculature. A broad overview of the currently used pharmacokinetic models is given in chapter 3. The most familiar is the compartmental model of Tofts & Kermode, that desribes the measured concentration curve $C_t(t)$ by means of two kinetic parameters [16]:

$$C_t(t) = K^{trans} \int_0^t C_p(t') e^{-\frac{K^{trans}}{\nu_e}(t-t')} dt' \tag{1.1}$$

$K^{trans}$ $(min^{-1})$ is the transendothelial transfer constant, $\nu_e$ is the interstitial space fraction. In theory, $K^{trans}$ is a measure for the plasma flow through the vessel and the permeability and surface area of the vessel wall [17]. In practice, the value of $K^{trans}$ is also affected by the microvessel density [18]. $C_p(t)$ is the variation of the CA concentration in the blood plasma of a feeding artery of the tumor, the so-called arterial input function (AIF). In pharmacokinetic modeling, it is assumed that the AIF is known, as it is indispensable to estimate the pharmacokinetic parameter from the measured CA tissue concentration curve. Several other models exists, with a higher number of parameters: in the 3-parameter model the plasma volume fraction is estimated as well, which physiologically may be expected to correlate with the microvessel density. The 4-parameter model allows separate estimation of permeability and blood flow.

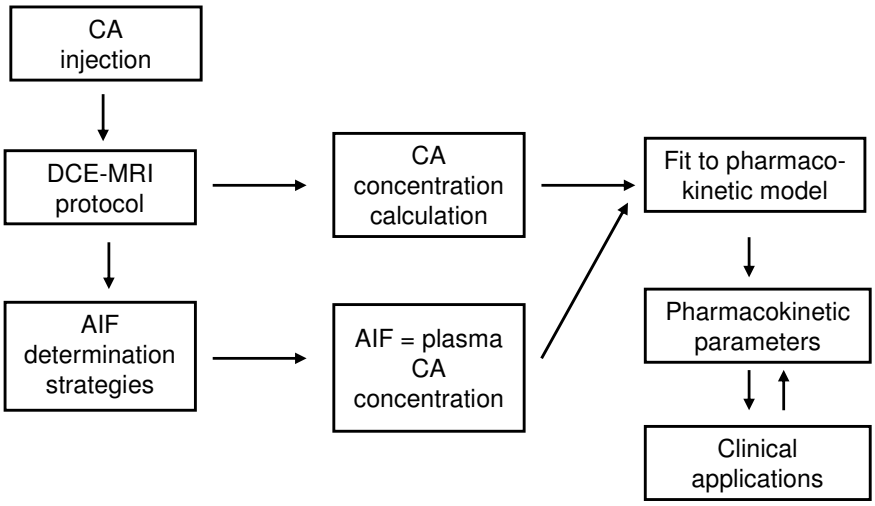


**Figure 1.6:** Chart flow of a DCE-MRI investigation combined with pharmacokinetic modeling.

## 1.4 DCE-MRI & pharmacokinetic modeling chart flow

The chart flow of a DCE-MRI investigation combined with pharmacokinetic modeling is shown in fig. 1.6. It can be subdivided into 3 major parts: the DCE-MRI protocol, the determination of the AIF, the post-processing of the DCE-MRI enhancement curves.

### 1.4.1 DCE-MRI protocol

The DCE-MRI protocol comprises all MRI measurements performed both before and after the injection of a CA. The signal intensity in a DCE-MRI pulse sequence is mainly dependent on the $T_1$-relaxation time[4] in the tissue of interest. This relaxation time, whose physical meaning is explained in chapter 2, depends in a quantifiable manner on the CA concentration. Monitoring the MR signal intensity over time therefore allows calculation of the CA concentration curve. Absolute quantification of the CA concentration however requires a number of quantities, as the relaxation time $T_{10}$ in the absence of CA and the pre-contrast signal $S_0$, that have to be determined before the CA is injected. A typical DCE-MRI investigation starts with a number of pre-contrast scans, from which $S_0$ and $T_{10}$ can be estimated.

[4]As mentioned in the introduction, DCE-MRI pulse sequences are mainly $T_1$-weighted

After the injection of a CA, a dynamic series of MR-images is started: every $\Delta t$ seconds an MR image is acquired, for a total time $T_{scan}$. $\Delta t$ is the sampling time, the inverse of the temporal resolution and is in practice the time necessary to acquire one MR-image with the employed pulse sequence. It seems obvious that an increased temporal resolution is beneficial for the quality of the estimated parameters. However, in DCE-MRI, reducing $\Delta t$ is impossible without sacrifices: a trade-off exists between temporal resolution, spatial resolution, spatial coverage and signal-to-noise ratio. This trade-off is elucidated in chapter 2, and makes DCE-MRI protocol design a difficult task.

### 1.4.2 Arterial input function

As mentioned in the previous section, the knowledge of the AIF is indispensable for the estimation of the pharmacokinetic parameters. A wide range of methods exists to determine the AIF, going from co-measurement of the CA concentration in a feeding artery of the tissue of interest during the dynamic DCE-MRI series (patient-specific), to the use of a population averaged AIF (non-patient specific). An overview of the AIF determination methods is given in chapter 3, together with their respective advantages and drawbacks. Typically, the CA concentration in the blood varies much more swiftly than the concentrations in tumor tissue. Therefore, if the AIF is to be measured together with the tissue concentration curves, its accurate determination will require a higher temporal resolution, than when a population averaged AIF is used.

### 1.4.3 Post-processing

The post-processing of DCE-MRI images begins with the CA concentration calculation from the measured signal intensities in the dynamic series and the quantities determined in the pre-contrast measurements. The relationship between the CA concentration and the MR signal intensity is reviewed in chapter 2. In contradiction to for instance DCE-CT, the measured signal intensity is not linearly related to the CA concentration and specific conversion methods are necessary. These conversion methods are discussed in chapter 4. In the second step of the post-processing protocol, this concentration curve is fitted to a pharmacokinetic model, given the AIF. This results in a number of pharmacokinetic parameter estimates and their respective confidence intervals, that can be used for a wide range of applications. A number of these applications is discussed in chapter 3.

## 1.5 Limitations

Despite its high physiological relevance and its huge clinical potential, DCE-MRI and pharmacokinetic modeling have not been introduced in daily clinical practice. In chapter 3, a wide range of specific error sources and their influence on the precision and the accuracy of the pharmacokinetic estimates are described. However the three main issues that limit the clinical acceptance of pharmacokinetic modeling & DCE-MRI have been acknowlegded by many of the leading authors in the field [2, 10, 19–22]:

1. Lack of standardized measurement protocols: both the precision and the accuracy of the estimated pharmacokinetic parameters are highly influenced by the design of the DCE-MRI protocol and the choice of the AIF determination method. The influence of the temporal resolution of the DCE-MRI measurement for instance, has been the subject of investigation in many studies. These resulted in a number of general recommendations regarding the sampling strategy. Unfortunately, no consensus is found in literature regarding this issue and the reported maximal sampling times vary between 1.5s and 15s [22–28]. The reason for this high variation is threefold. Firstly, the required temporal resolution is model-dependent: a model that estimates a higher number of parameters from the measured concentration curve requires high data quality [24]. Secondly, as explained above, a trade-off exists in DCE-MRI between signal-to-noise ratio, spatial coverage, spatial resolution and temporal resolution. Therefore, the temporal resolution is not only model dependent, but depends on the necessary spatial coverage and resolution for the pathology as well. Finally, the required temporal resolution depends on the AIF determination strategy as well. When the AIF is co-measured with the tissue concentrations in a feeding artery, the fastly varying concentration curve has to be sampled with high temporal resolution. On the other hand, when a population averaged AIF is used, the more slowly varying tissue concentration curves do not require similar small sampling times [27, 29]. Also, total scan time is a protocol parameter whose influence remains uninvestigated and for which no clear recommendations exist [22]. Finally, the pulse sequence type and its design in DCE-MRI, is of crucial importance for pharmacokinetic modeling. Most pulse sequence parameters are determined by the trade-off mentioned above, but a degree of freedom exists in the choice of the flip angle[5]. A number of studies has investigated the influence of the flip angle on the accuracy and the precision of pharmacokinetic estimates, but no agreement regarding an optimal flip angle exists [22,30–32].

2. Lack of robust post-processing methods and the unavailability of post-

[5] in chapter 2, the flip angle concept is elucidated

processing software: a large discrepancy exists in the post-processing of the DCE-MRI signal intensity curves, employed in different pharmacokinetic modeling studies and no general recommendations are available to develop robust post-processing software. The signal intensity conversion to CA concentration for instance, is performed in a variety of ways [30, 33, 34]. General approaches for the fitting of DCE-MRI concentration data to a pharmacokinetic model have been developped [35], and the accuracy of the pharmacokinetic estimates in the presence of a number of MR-related error sources has been assessed in case studies [30, 36]. This accuracy seems to be highly dependent on the DCE-MRI protocol, implying that without standardized measurement protocols, intercomparison of pharmacokinetic modeling studies from different center is hazardous. In addition, the precision of the pharmacokinetic estimates has hardly been investigated. Statistical significance of pharmacokinetic parameter differences pre- and post anti-angiogenic therapies is highly dependent on the existence of a robust framework to construct accurate confidence intervals for the pharmacokinetic estimates. Up to now, no such framework is available. These considerations all contribute to the statement that intercomparison of results from different scanning sites is difficult and pose a severe drawback on the multi-centre application of pharmacokinetic modeling. Several authors have therefore postulated that a general statistical framework should be developped to evaluate the precision and measurement variability of pharmacokinetic parameters between and within centers [2, 21, 37].

3. Lack of a gold standard for validation: it is very difficult to show that pharmacokinetic parameters truly reflect the angiogenic activity of the tumors. Several authors have tried to compare invasive histologic measurement methods for angiogenic activity, such as microvascular density or angiogenic factor expression, but found only broad correlations [10, 32, 38]. This may be attributed to the difficulty in co-localizing the histologic section with the MR sections [10] and to the fact that pharmacokinetic parameters as $K^{trans}$ represent a mixed effect of blood flow and permeability. Other researchers have compared pharmacokinetic estimates from DCE-MRI with similar parameters from other imaging modalities such as ultrasound [39], CT [40] or PET [41]. It was for instance demonstrated that $K^{trans}$ obtained from DCE-CT or DCE-MRI are comparable. No correlation could however be found between the interstitial space or plasma volume fraction [40]. These findings demonstrate that no golden standard exists to validate the pharmacokinetic models. In a famous paper, Buckley investigated the physiological relevance of 2-, 3-, and 4 parameter models [18]. He found that the parameters from the higher order models more truly reflect the physiological quantities they aim to measure. However, if

more parameters have to be fit from a concentration curve, increased data quality is required for acceptable accuracy and precision. The formulation of guidelines facilitating model selection for a fixed protocol design, or vice versa, concerning the required data quality for a given pharmacokinetic model, would therefore be highly relevant. In addition, the 4-parameter model, whose parameters shows the highest degree of correlation with their true physiological counterparts, experiences severe fitting stability problems, preventing its clinical acceptance.

## 1.6 Accuracy & precision

When evaluating the quality of an estimated parameter $\hat{\theta}$, a discrepancy has to be made between its accuracy and its precision. Just as an ordinary measured quantity, an estimated parameter has a probability distribution as shown in fig 1.7A and B. The difference between the average of this distribution and the true value $\theta$ of the parameter is called the bias and is a measure for the accuracy of the parameter. In other words, if the experiment would be repeated a considerable number of times, the accuracy describes the difference between the true value of the parameter and the average of its estimated values over the experiments. The width of the distribution on the other hand, is a measure for the uncertainty or the precision on the estimated parameter. The precision describes the probability that when the experiment is repeated under similar conditions, the estimated parameter remains unchanged. Precision is closely related to the reproducibility or repeatability of the pharmacokinetic modeling technique. If the precision of the estimate is very low, as in fig. 1.7B , the experiment is irreproducible and therefore useless, even if the bias is small. On the other hand, if both the bias and the precision are high as in fig. 1.7A, reproducible but inaccurate estimates may be extracted. This shows that before assessing the accuracy of an estimated parameter acceptable precision has to be ensured.

Bias in an estimated parameter is caused by systematic errors. In DCE-MRI such errors include insufficient temporal resolution (Nyquist), error in the AIF determination or a number of MR-related artifacts that cause inaccuracies in the concentration calculation (see chapter 2 & 3). Uncertainty on the pharmacokinetic estimates is caused by the limited signal to noise ratio (SNR) in the DCE-MRI measurement. The noise on the MR signal intensities is converted to noise on the concentration curves. As a result, parameters estimated from these curves have limited precision. The extent to which the SNR of the DCE-MRI measurement is converted to uncertainty on the kinetic estimates depends on the temporal resolution, the total scan time, but also on the settings of the MRI pulse sequence. For a number of applications of pharmacokinetic modeling the precision of the pharmacokinetic estimates is far

more important than their accuracy. For instance, consider an anti-angiogenic therapy that truly has an effect on the morphology of the tumor vasculature and has to be evaluated by a paired DCE-MRI investigation. Suppose the true value of a pharmacokinetic parameter $\theta$ before therapy is $\theta_1$, while after therapy it increases to $\theta_2$. As shown in fig. 1.7C, a DCE-MRI protocol with a high precision evaluates the effect correctly, even in the presence of a large bias, provided that this bias is comparable in both measurements. On the contrary, a low precision, may lead to the erroneous conclusion that the therapy decreases the kinetic parameter, even in the absence of measurement bias, as illustrated in fig. 1.7D. This simple example shows that statistical significance testing of an observed change in a kinetic parameter, requires the knowledge of the width of the distribution, i.e. a framework is necessary that describes the precision of the pharmacokinetic estimates.

The precision of the pharmacokinetic estimate imposes a lower bound on the reproducibility. Additional variations in the estimated parameter may occur by for instance improper patient repositioning or if the extent of the systematic errors in both investigations is not comparable. Therefore, the accuracy of the parameter has to be assessed as well.

## 1.7 Aim & Overview

In this work, the three limitations as described in section 1.5 are adressed. The emphasis is on improvements and characterization of the precision of the pharmacokinetic estimates, that is of crucial importance for several applications of pharmacokinetic modeling, as illustrated in the previous section. Concerning the DCE-MRI protocol, we have proposed an optimization strategy for the flip angle in spoiled gradient echo pulse (SPGRE) sequences, the most commonly used pulse sequence family in DCE-MRI. This flip angle selection effectively enhances the precision of the pharmacokinetic estimates. Secondly, a framework has been developped to assess the influence of the protocol design on the precision of the estimated parameters. Although many studies already investigated the influence of for instance the temporal resolution, our framework accounts for the trade-offs between spatial resolution, temporal resolution and SNR, characteristic for DCE-MRI, and allows protocol optimization. Concerning the post-processing protocol, this work investigates the influence of the estimator for pharmacokinetic modeling of DCE-MRI data and proposes a robust and accurate method for confidence interval construction. This may be used as a part of the statistical framework to describe the precision and measurement variability of the pharmacokinetic parameters. In addition, a new accurate conversion method is developped for calculating the CA concentration from the SPGRE signal intensity. Finally a new fast and stable fitting procedure is introduced for the 4-parameter model, that leaves

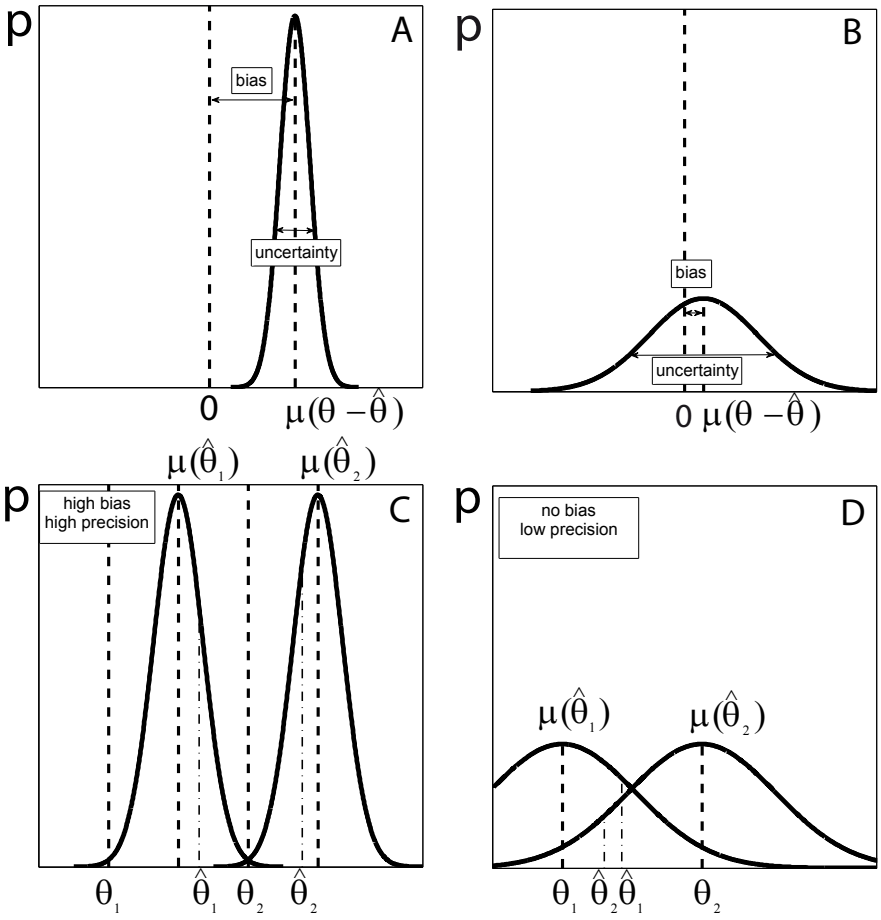


**Figure 1.7:** A: probability distribution of the difference between an estimated parameter $\hat{\theta}$ and its true value $\theta$. The width of the distribution is a measure for the uncertainty. The difference between the mean of the distribution, $\mu(\theta - \hat{\theta})$, is the bias. B: similar as A, but for the case of a low bias and high uncertainty. C. probability distributions of the estimates $\hat{\theta}_1$ and $\hat{\theta}_2$ for a pharmacokinetic parameter whose true value has been increased by an anti-angiogenic therapy from $\theta_1$ to $\theta_2$. In the case of a low uncertainty but high bias, the effect of an anti-angiogenic therapy is correctly assessed by the pharmacokinetic parameter change. D: in the case of a low bias but high uncertainty, the observed pharmacokinetic parameter change may not reflect the true effect of the therapy.

behind the instability problems and has a profound effect on the accuracy and the precision of its parameters. The latter study may also increase the clinical acceptance of the physiologically relevant 4-parameter model and enable better validation of the pharmacokinetic modeling techniques.

In chapter 2, on overview is given of the principles of MRI and the trade-offs in DCE-MRI, as cited above, are discussed. Chapter 3 describes the current status of the pharmacokinetic modeling techniques, reviews the different models and summarizes a number of important clinical applications. Chapter 4 discusses the conversion methods, among which a newly proposed one, and their effect on the accuracy and the precision of DCE-MRI measured CA concentration. The flip angle optimization strategy is derived and explained in chapter 5. Chapter 6 compares the quality of estimators for pharmacokinetic modeling and evaluates the accuracy of confidence interval construction for pharmacokinetic estimates. In chapter 7, the fast and stable fitting procedure for the AATH model is explained. The framework for protocol optimization is discussed in chapter 8. Finally, chapter 9 reviews the different results of the previous chapter and discusses their potential in addressing the limitations of DCE-MRI and pharmacokinetic modeling.

# Chapter 2

# Dynamic contrast-enhanced magnetic resonance imaging: Basic principles, pulse sequences, contrast agents & artefacts

## 2.1 Introduction

As explained in the introductory chapter, DCE-MRI monitors the signal intensity in a tissue of interest is over time, after the injection of a CA. Its goal is to obtain functional information about the tissue or the pathology, that can aid the clinician for diagnostical or therapeutical decisions. It is one of the numerous applications of MR-imaging. MR imaging itself relies on the behaviour of the protons in the tissue water of the human body, when subjected to a large static magnetic field. In comparison with other medical imaging modalities, MRI achieves improved soft tissue contrast and it has the advantage that the patient is not exposed to ionizing radiation. Being intrinsically impossible to describe without quantummechanics, MRI is a product of the second part of the $20^{th}$ century, with the first clinical scanner introduced around 1980. Many physical, technological and signal processing challenges have been met in clinical scanners: e.g. the high magnetic field strength (1.5T-3T[1]) is obtained by superconducting magnets, cooled to below 4K by liquid helium; a wide range of MRI coils and pulse sequences have been introduced to achieve optimal imaging of all parts of the human body;

[1]For comparison, the earth magnetic field strength is in the order of 30-60 $\mu$T

spatial localisation in MRI requires magnetic field gradients and fast fourier transform algorithms for image reconstruction; etc. By the introduction of contrast agents, a number of chemical and toxicological considerations have to be considered as well. Henceforth, MRI is probably one of the most multidisciplinary imaging modalities in medicine, and a complete overview of this continuously expanding technique is far beyond the scope of this work. However, the aim of this chapter is threefold. Firstly it is tried to provide the reader with both a qualitative and quantitative understanding of several MR concepts, such as flip angle, pulse sequence, signal-to-noise ratio, repetition time, ... All these terms are indispensable for a thorough understanding of the next chapters. Secondly, extensive attention is paid to the spoiled gradient echo pulse (SPGRE) sequence. This pulse sequence is used in the majority of DCE-MRI studies and the relationship between signal intensity and CA concentration has important consequences for pharmacokinetic modeling. Therefore, this relationship is derived analytically and artifacts are explained. Finally, the trade-offs in DCE-MRI are illustrated. For a regular MR investigation, the choice of imaging parameters comprises a trade-off between field of view, spatial resolution and signal-to-noise ratio (SNR). For a DCE-MRI measurement, to be combined with pharmacokinetic modeling, acceptable temporal resolution has to be taken into account as well. As in the next chapters, a number of these trade-off's are investigated and discussed, it is important to understand what sacrifices are necessary to achieve acceptable temporal resolution in a DCE-MRI study.

The chapter start with an overview of the basic MR principles, both quantum-mechanical and classical (section 2.2). Afterwards the spatial encoding in MRI is shortly discussed and the concepts of k-space and k-space sampling and SNR are introduced to derive the trade-offs mentioned above (section 2.3). In section 2.4, the SPGRE pulse sequence is explained, while section 2.5 discusses the properties of MR contrast agents and their effect on the MR signal intensity. Section 2.6 reviews two techniques to measure native relaxation times. Finally a short overview is given of the artefacts that occur in DCE-MRI in section 2.7 and some qualitative and heuristic measures to obtain functional information from DCE-MRI signal curves are mentioned in section 2.8. It is stressed again that this chapter is only a simplified and brief overview of MR-imaging. For a more rigorous and profound description of MRI, the reader is referred to standard works as [42] and [43], which served as basic literature for this chapter.

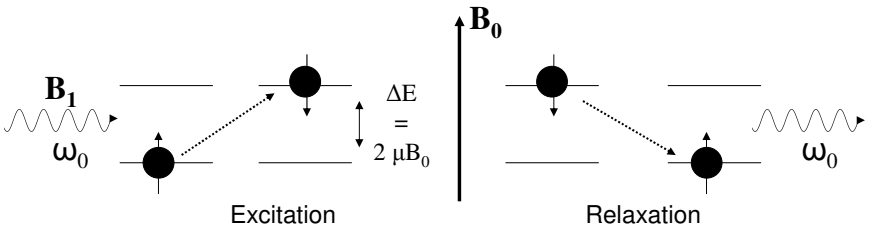


**Figure 2.1:** Schematic overview of Zeeman energy levels and of the processes of excitation and relaxation. Protons in the spin-up state are excitated by the time varying $B_1$-field, with the larmor frequence $\omega_0$ and jump to the spin-down state. When the $B_1$-field is switched off, relaxation occurs: spin-down protons flip by sending out photons with the larmor frequency.

## 2.2 Basic principles of MRI

### 2.2.1 Zeeman-effect

Magnetic resonance imaging (MRI) is an imaging technique that exploits the intrinsic magnetic properties of the hydrogen nuclei, abundant in the water of the human body, to obtain anatomical information for a wide range of applications. A proton is a so-called fermion, a particle with an intrinsic spin moment $\mathbf{I}$ with magnitude $\frac{1}{2}\hbar$ [2]. With this intrinsic nuclear spin, an intrinsic magnetic moment $\boldsymbol{\mu}$ is coupled by the gyromagnetic ratio $\gamma$, which amounts 42.58 MHz/T for $^1H$:

$$\boldsymbol{\mu} = \gamma \boldsymbol{I} \tag{2.1}$$

When a external magnetic field $\boldsymbol{B_0}$ is applied, the proton acts as a magnetic dipole, with potential energy given by:

$$E = -\boldsymbol{\mu} \cdot \boldsymbol{B_0} \tag{2.2}$$

According to the quantummechanical exclusion rules, 2 possible energy states can occur for a fermion: parallel to the external field (spin-up) or anti-parallel to $\boldsymbol{B_0}$ (spin-down). As a result two distinctive energy levels arise, with an energy gap that can be derived from eq. 2.2:

$$\Delta E = \hbar \gamma B_0 \tag{2.3}$$

with $B_0$ the magnitude of the external field. This energy level division is called the Zeeman-effect (fig. 2.1). In thermodynamic equilibrium, the protons in the body water are more likely to adopt the spin-up state, as it is lower in energy

[2] $\hbar$ is the reduced Planck constant

than the spin-down state. The ratio of the population in the Zeeman energy levels is then given by the Boltzmann statistic:

$$\frac{N\uparrow}{N\downarrow} = e^{\frac{\Delta E}{kT}} \tag{2.4}$$

in which k is the Boltzmann constant. MR-imaging relies on the perturbation of this equilibrium by applying an oscillating external field $\boldsymbol{B_1}$, perpendicular to $\boldsymbol{B_0}$. The frequency of this $B_1$-field is called the larmor frequency $\omega_0$, and the energy of its photons equals the energy gap between the Zeeman levels:

$$\Delta E = \hbar\omega_0 \tag{2.5}$$

$$\omega_0 = \gamma B_0 \tag{2.6}$$

For the duration of $\boldsymbol{B_1}$, protons in the spin-up state gather the necessary energy and jump to the spin-down state. In this way population inversion is obtained. When the $B_1$-field is switched off, the system returns to its ground state by sending out photons itself. These electromagnetic signals are detected by the scanner hardware and form the base of the MR images. These processes of excitation and relaxation are shown in fig. 2.1.

### 2.2.2 Classical description

In practice, the spatial resolution of an MR image is in the order of 0.1-1 mm. Therefore, the number of hydrogen nuclei in a voxel of $10^{-3} - 1\ mm^3$ is of that order, to allow the description of MR imaging in terms of the macroscopic magnetization vector **M**, the resultant of the individual dipoles. In thermodynamic equilibrium, **M** is parallel to the external magnetic field, as the spin-up state is more populated than the spin down state[3] (eq. 2.4). The equation describing the motion of the magnetization vector **M** in the presence of external magnetic fields $\mathbf{B_0}$ and $\mathbf{B_1}$ is given by:

$$\frac{1}{\gamma}\frac{d\boldsymbol{M}}{dt} = -\boldsymbol{B} \times \boldsymbol{M} \tag{2.7}$$

$$= -(\boldsymbol{B_1} + \boldsymbol{B_0}) \times \boldsymbol{M} \tag{2.8}$$

in which '$\times$' denotes the vector cross product. From this equation it can easily be seen that **M** describes a superposition of two circular motions[4]. The first part of this superposition is a precession around $\boldsymbol{B_0}$ with the larmor frequency. To facilitate the interpretation, the second part of the motion is described in a reference frame that rotates with the larmor frequency. In such a rotating frame, the second motion, caused by the $B_1$-field is a circular motion in the

[3] It can be shown that in thermodynamic equilibrium the magnitude of **M** equals $\frac{N\gamma^2\hbar^2 B_0}{4kT}$, N being the proton density [43]

[4] The general equation of a particle describing a circular motion around a rotation axis $\boldsymbol{\Omega}$, with a angular frequency $\mid \boldsymbol{\Omega} \mid$ is given by $\frac{d\mathbf{r}}{dt} = \boldsymbol{\Omega} \times \mathbf{r}$

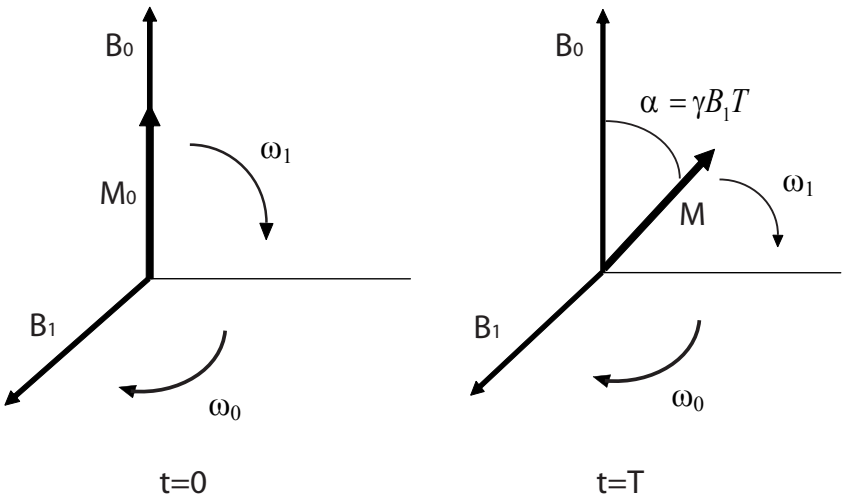


**Figure 2.2:** Motion of the magnetization vector **M** when a external $B_1$-field is applied. The reference frame rotates around $\mathbf{B_0}$ with the larmor frequency. In such a rotating reference frame, **M** describes a circular motion with angular frequency $\gamma B_1$ from its equilibrium position $M_0$ to a position after a time T, in which an angle $\alpha$ with $\mathbf{B_0}$ is achieved. $\alpha$ is the so-called flip angle.

plane perpendicular to $\boldsymbol{B_1}$, with a frequency $\omega_1 = \gamma B_1$. Fig. 2.2 shows this rotational motion in the rotating reference frame. The angle between $\boldsymbol{B_0}$ and **M** after applying the $B_1$-field for a time $T$ is given by:

$$\alpha = \gamma B_1 T \tag{2.9}$$

$\alpha$ is called the flip angle, a basic concept in MRI. When the $B_1$-field is switched off, the magnetization is rotated over a flip angle $\alpha$ with respect to $\boldsymbol{B_0}$. To describe how the magnetization vector returns to its equilibrium state, the Bloch[5] equations are employed. These equations describe the relaxation of the longitudinal magnetization $M_z$ (2.11) and the transverse magnetization vector $M_{xy}$ (2.10).

$$\frac{d\boldsymbol{M_{xy}}}{dt} = -\gamma \boldsymbol{B_0} \times \boldsymbol{M_{xy}} - \frac{\boldsymbol{M_{xy}}}{T_2} \tag{2.10}$$

[5]In 1952, Felix Bloch and Edward Purcell received the nobel prize for physics for their discoveries regarding nuclear magnetic resonance

$$\frac{dM_z}{dt} = \frac{M_0 - M_z}{T_1} \tag{2.11}$$

$T_1$ and $T_2$ are the longitudinal and transverse relaxation times respectively and will be discussed in the next section. Eq. 2.11 can be solved on sight. Regarding $\boldsymbol{M_{xy}}$, taking the vector cross product of both sides of eq. 2.10, shows that the transverse magnetization vector also describes a circular motion around $\boldsymbol{B_0}$ with the larmor frequency. Taking the dot product of both sides of eq. 2.10 with $\boldsymbol{M_{xy}}$ yields:

$$\frac{dM_{xy}^2}{dt} = -2\frac{M_{xy}^2}{T_2} \tag{2.12}$$

The analytical solutions of eq. 2.11 and eq. 2.12 form the basis of pulse sequence signal intensity derivations (see section 2.4), and are given by:

$$M_{xy}(t) = M_{1xy}e^{-\frac{t}{T_2}} \tag{2.13}$$

$$M_z(t) = M_0 + (M_{1z} - M_0)e^{-\frac{t}{T_1}} \tag{2.14}$$

$M_0$ is the equilibrium magnetization, $M_{1z}$ and $M_{1xy}$ are the longitudinal and tranverse magnetizations just after the excitation pulse respectively.

### 2.2.3 Relaxation times

Relaxation is the phenomenom that causes the magnetization vector to return to its equilibrium state. The Bloch equations presume that relaxation is a first order process, with time constants $T_1$ and $T_2$ for longitudinal and transverse magnetization respectively. The two distinctive time constants indicate that these relaxation phenomena are caused by different physical processes. In short two main dipole-dipole interactions underly magnetization relaxation[6]. Relaxation of $M_z$ requires the flipping of dipoles and is therefore a process that attends with energy exchange. The local motion of the tissue water molecules causes a varying magnetic field with a wide range of frequencies. Just as it is the case for the $B_1$-field, when this frequency equals the larmor frequency, a resonance process occurs that can flip a spin-down proton to the spin-up state. The waste energy is absorbed by the tissue and results in a restored longitudinal magnetization. This process is called the spin-lattice interaction and affects mainly $T_1$- relaxation times. $M_{xy}$-relaxation on the other hand is caused by the dephasing of dipoles. This is shown in fig. 2.3. In the absence of a $B_1$-field, the individual dipoles precess around the static magnetic field. As their mutual phase is arbitrary, the net $M_{xy}$ is zero. The applied $B_1$-field makes the individual dipoles rotate in phase and a net transverse magnetization arises. When the $B_1$-field is switched

[6] In theory 5 interactions of magnetic dipoles determine the relaxation phenomenons. See [43]

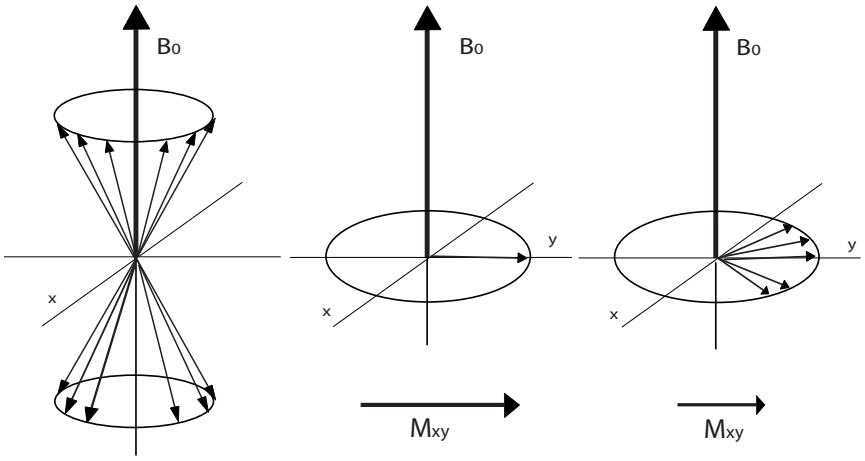


**Figure 2.3:** Graphical representation of 'dephasing'. Left: in the absence of a $B_1$-field, the individual dipoles precess around $B_0$ and no net transverse magnetization is apparent. Middle: a time varying $B_1$-field brings the precession of the dipoles in phase and induces a net $M_{xy}$. Right: after switching off $B_1$, local variations in larmor frequency cause the dipoles to dephase and results in a loss of transverse magnetization.

off, $M_{xy}$ would remain unchanged if the dipoles continu to rotate in phase. However, variations in their angular frequency induces dephasing, with a loss of transverse magnetization. These variations in the larmor frequency are caused by so-called spin-spin interactions: the hydrogen atoms in tissue water experience a small magnetic field variation caused by the magnetic field of the other hydrogen atom. These spin-spin interactions mainly affect $T_2$. Relaxation times are therefore highly dependent on the mobility of the water molecules in tissue and differ according to the tissue composition. Table 2.1 contains the relaxation times found in several tissues in a number of studies. Relaxation times also depend on $B_0$-field strength and temperature.

These $T_1$- and $T_2$-relaxation times lay the foundation of the contrast observed in MRI images. By chosing an intelligent sequence of $B_1$-pulses, the MR signal intensity can be made mainly $T_1$- or $T_2$-dependent. Such sequences are called $T_1$- and $T_2$-weighted respectively. These pulse sequences are described in section 2.4. In DCE-MRI, the presence of the contrast agents induces a quantifiable shortening of both relaxation times which underlie the quantitative concentration measurement with MRI (see section 2.5).

A third relaxation time has to be discussed. When one would measure the

**Table 2.1:** Typical $T_1$- and $T_2$-relaxation times in several tissues or pathologies at 1.5T. Values from [18, 43–45]. $T_2^*$-values in breast and prostate tumors were not measured in these studies.

| | $T_1$ [ms] | $T_2$ [ms] |
|---|---|---|
| blood plasma | 1580 | 417 |
| blood | 1250 | 227 |
| skeletal muscle | 870 | 50 |
| brain white matter | 790 | 90 |
| brain gray matter | 920 | 100 |
| breast tumor | 675 | - |
| prostate tumor | 916 | - |

magnetization variation after a 90°-pulse (i.e. a $B_1$-pulse that causes a flip angle of 90°) in a given tissue, eq. 2.13 predicts an exponential decay with time constant $T_2$ ($M_{1xy} = M_0$ for a 90°-pulse). However the measured time constant is shorter than $T_2$ and is denoted $T_2^*$, the effective transverse relaxation time. This faster relaxation is caused by inhomogeneities in the $B_0$-field that are not induced by the local field of neigbouring spins, but by an inhomogenous magnetic susceptibility distribution. When a patient is brought into the magnet bore of a MRI scanner, the $B_0$-field will be redistributed according to the local susceptibility. Microscopic variations in susceptibility, will cause microscopic variations in the magnetic field, that contribute to the dephasing of dipoles and the $M_{xy}$-relaxation. The effective relaxation time $T_2^*$ is given by:

$$\frac{1}{T_2^*} = \frac{1}{T_2} + \frac{1}{T_2'} \tag{2.15}$$

in which $T_2'$ is the relaxation time related to magnetic field inhomogeneities.

## 2.3 Trade-offs in MRI and DCE-MRI

### 2.3.1 Definitions

A typical DCE-MRI investigation consists of the capturing of a 2D MR image, every $\Delta t$ seconds. The MR image contains of $N_x \times N_y$ voxels (the matrix size) with dimensions $\Delta x \times \Delta y \times \Delta z$. The total field of view in the x- and y-direction is $FOV_x$ and $FOV_y$ respectively. In fig. 2.4, a simplified MR image (matrix size $= 8 \times 8$) is shown (in practice $N_x$ and $N_y$ are typically 128-256-512).

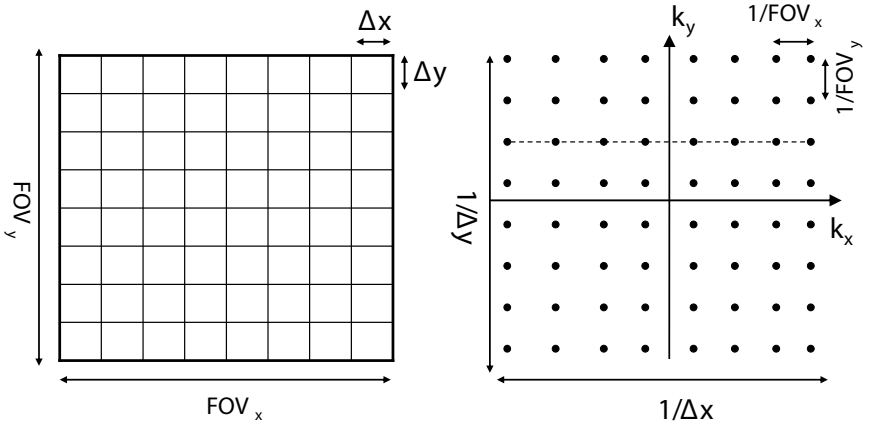


**Figure 2.4:** Left: example of an $N_x \times N_y$ MR-imaging matrix (8×8), containing voxels with dimensions $\Delta x$ and $\Delta_y$ in x- and y-direction respectively. The field of views in x- and y-direction are $FOV_x = N_x\Delta_x$ and $FOV_y = N_y\Delta_y$ respectively. Right: k-space corresponding to the MR-image on the left. The distances between subsequent k-space points are denoted in the figure. For the reconstruction of the magnetizations in all voxels of the imaging matrix on the left, the signal intensities in every point of k-space have to be acquired. The dotted line is a phase-encoding line.

### 2.3.2 Spatial encoding and k-space formalism

Spatial encoding in MRI is obtained by using magnetic field gradients. 3 different gradients are used to obtain spatially encoded MR signal intensities:

- Slice selection: by applying a gradient along the $B_0$-field the larmor-frequency varies in the z-direction. When this is combined with a selective RF pulse, i.e. a pulse with a restricted band width [7], only the slice with larmor frequencies in that bandwidth is excitated. The width of this slice, $\Delta z$, is called the slice thickness.
- Phase encoding: after the excitation and before the signal is received, a gradient is applied in the y-direction. This causes the spins to precess with a distinctive frequency according to their position in the y-direction. When this gradient is switched off, the phase of the spins will contain the necessary spatial information.
- Frequency encoding: during signal reception, a gradient is applied in the x-direction. Therefore the frequency of the received signal will contain spatial information about the x-position of the spins.

[7] in practice sinc pulses can be used to achieve selective RF excitation.

The mathematical description of spatial encoding needs the introduction of k-space, the fourier conjugate of the spatial domain. According to standard MR theory the final signal measured in the MRI hardware is complex, i.e. it has a real and an imaginary part, and is proportional to:

$$S(t) \propto \int M_T(x,y) exp(-i\phi(x,y,t)) dxdydz \tag{2.16}$$

in which the volume integral is taken over the complete excitation slice. $M_T(x,y)$ is proportional to the transverse magnetization at the time of the read-out. It also contains a factor determined by the MRI receiver circuit gain. This $M_T$ is the final goal of the MR-image, as it contains the information regarding the proton density and $T_1$ and $T_2$-relaxation times. $\phi(x,y,t)$ is the phase[8] that a spin at position [x,y] has accumulated at a time t, due to the application of the gradients. This phase is given by:

$$\begin{aligned} \phi(x,y,t) &= \gamma \int_0^t (xG_x(t') + yG_y(t'))\, dt' && (2.17) \\ &= 2\pi \boldsymbol{r} \cdot \boldsymbol{k}(t) && (2.18) \\ \boldsymbol{k}(t) &= \frac{\gamma}{2\pi} \int_0^t \boldsymbol{G}(t') dt' && (2.19) \end{aligned}$$

$\boldsymbol{r}$ is the spatial vector [x,y], while $\boldsymbol{k}(t)$ is a vector in k-space. Eq. 2.16 can now be rewritten as:

$$S(t) = S(k_x(t), k_y(t)) = \int M_T(x,y) exp(-2\pi i \boldsymbol{r} \cdot \boldsymbol{k}(t)) dxdydz \tag{2.20}$$

In other words, the measured signal in the MR hardware is the 2-D fourier transform of the magnetization $M_T(x,y)$ with respect to the spatial coordinates x and y. Therefore, to obtain the final $M_T(x,y)$, the inverse fourier transform of the signal has to be performed, based on the measurement of $S(k_x,k_y)$ in k-space. An MR acquisition therefore consists of a variation of $G_x$ and $G_y$ gradients to obtain a sufficient number of points in k-space and a fast fourier transform (FFT) of this set of $S(k_x,k_y)$ to calculate the final $M_T$. The path described by the vector $\boldsymbol{k}$ over time is called the k-space trajectory. This path determines the acquisition strategy, the types of artefacts that can occur and the choice of reconstruction algorithm [42]. Fig. 2.4 shows the k-space corresponding to the MR-image defined above. First of all, the number of points that has to be acquired in the k-space is identical to the number of voxels. The distance between two subsequent points in k-space is $1/FOV_x$ in $k_x$-direction and $1/FOV_y$ in $k_y$-direction. The extent of the k-space is the inverse of the spatial resolution: $1/\Delta x$ in $k_x$-direction and $1/\Delta y$ in $k_y$-direction.

[8] This phase is defined relative to the phase the spin would have accumulated if precessing at the larmor frequency $\gamma B_0$

There are numerous strategies for the sampling of k-space. This discussion will be restricted to the most straightforward one, cartesian k-space sampling. The dotted line in fig. 2.4 is a so-called phase-encoding line, i.e. a line in k-space that corresponds to a single value of the phase-encoding gradient $G_y$. In a cartesian k-space sampling strategy, these phase encoding lines are acquired one by one: After the first excitation pulse, a value for the phase encoding gradient is applied, corresponding to the top phase encoding line in fig. 2.4. A frequency encoding gradient $G_x$ is applied for read-out in the $k_x$-direction. After the second excitation pulse, a different $G_y$-value is applied, corresponding to the second phase encoding line, and signal is again read-out in $k_x$-direction. This is applied untill all $N_y$ phase encoding lines are acquired. The final temporal resolution of a DCE-MRI investigation using cartesian k-space sampling is therefore:

$$\Delta t = T_R N_y NEX \tag{2.21}$$

$T_R$ is the repetition time, the time between two excitation pulses. NEX is the number of times that the full k-space is sampled, the so-called number of averages. For every point in k-space, signal is collected during a time $T_s$, the inverse of the receiver bandwidth $BW$. The total time needed for the collection of 1 phase encoding line is therefore given by $N_x/BW$.

### 2.3.3 Signal-to-noise ratio

The signal-to-noise ratio (SNR) in MR imaging is dependent on the pulse sequence used. However, a general scaling relationship can be obtained:

$$SNR = B_0 \Delta x \Delta y \Delta z \sqrt{T_{acq,total}} \tag{2.22}$$

The SNR is proportional to the static magnetic field strenght. $T_{acq,total}$ is the total amount of time during which k-space data is collected. As collection time for the sampling of 1 k-space line is $N_x/BW$, the SNR can be rewritten as:

$$SNR = B_0 \frac{\Delta x \Delta y \Delta z \sqrt{N_x N_y NEX}}{\sqrt{BW}} \tag{2.23}$$

### 2.3.4 Trade-offs between temporal and spatial resolution, field of view and SNR

Given the relations above (eq. 2.21 & eq. 2.23) and the number of points that have to be acquired in k-space ($N_x = FOV_x/\Delta x$, $N_y = FOV_y/\Delta y$), a number of trade-offs in DCE-MRI have to be discussed. In an ordinary MR investigation (where temporal resolution is of little interest), FOV is mostly fixed and dictated by the tissue of interest. Therefore a trade-off has to be made between spatial resolution and SNR. Images with increased spatial resolution will have lower SNR. In other words, the anatomical information

that is gained by increasing the spatial resolution may be distorted by increasing noise levels. However, this can be compensated by taking a number of averages (NEX $> 1$), thereby increasing SNR without changing the spatial resolution, at the cost of prolonged acquisition time for the final image. In DCE-MRI, temporal resolution is of crucial importance if pharmacokinetic modeling is to be applied on the measured concentration curves. Again FOV tends to be imposed by the physiology. Increasing the spatial resolution ($N_x, N_y \uparrow$) reduces both SNR and temporal resolution. This poses for instance a significant problem in DCE-MRI of breast tumours. Breast DCE-MRI requires a large FOV ($\sim$ 20cm $\times$ 20 cm) with high spatial resolution ($\sim$ 1mm $\times$ 1mm $\times$ 3mm) for the discrimination of tumor tissue from normal tissue [7]. Acceptable SNR in this kind of images can only be achieved with limited temporal resolution ($\sim$ 90-120s). For other pathologies, the FOV and necessary spatial resolution do not prohibit the MR-images to be taken with sufficient temporal resolution. The trade-off between temporal resolution and spatial resolution depends upon the pathology, and the identification of the most important factor of both, should be investigated by case studies.

Several strategies exist to increase the temporal resolution. Firstly, the use of 3T scanners enables higher SNR at fixed temporal resolution or identical SNR at higher temporal resolution. However, at higher field strenghts, a number of errors has to be taken into account (see section 2.7) that reduces the accuracy of DCE-MRI concentration measurement. For breast imaging at 3T, it has been shown that these errors (see section 2.7) impose severe accuracy considerations to pharmacokinetic modeling [36]. This susceptibility to MR-related errors applies to other k-space sampling strategies as well. Echo-planar imaging for instance, which only requires 1 excitation pulse for complete k-space coverage, is more prone to a variety of artifacts [42]. A third strategy is to decrease the repetition time as small as possible. The minimal value of $T_R$ is however determined by time needed to play all necessary pulses and gradients for the read-out of 1 phase encoding line. Reduction of $T_R$ may therefore be technically unfeasible. Moreover, it will be shown in chapter 8, that pharmacokinetic modeling does not benefit from thoughtless reduction of the repetition time. Finally, a freedom exists in the choice of the NEX-parameter. When the k-space is sampled twice and the average image is constructed, the SNR increases with a factor $\sqrt{2}$ at the cost of a halved temporal resolution. A number of acquisition strategies have been developped, so called partial fourier methods, for which NEX is smaller than 1. In partial fourier acquisition, data are not collected throughout the entire k-space, but e.g. only the upper part (i.e. above $k_x$-axis) of the k-space is collected [9]. This acquisition strategy enhances temporal resolution at the cost of reduced SNR and can be described by a NEX-value smaller than 1, depending on the fraction of the full k-space that is acquired.

[9] Reconstruction of $M_T$ remains possible, as the the fourier transform of a real object is Hermitian, i.e. its real part is symmetric and its imaginary part is anti-symmetry around the center of k-space

This is a very interesting trade-off for pharmacokinetic modeling: is it better to have more noisy high temporal resolution data, or do more precise data with lower temporal resolution yield better model fits?

## 2.4 Pulse sequences

In this section it is explained how an intelligent sequence of $B_1$-pulses can result in a final fourier reconstructed signal ($M_T$ from the previous paragraph) that is weighted according to the relaxation times of the tissue of interest.

### 2.4.1 Spin-echo sequence and the principle of echo creation

In this paragraph a qualitative description is given of the spin echo sequence to enlight the principle of echo-creation. The spin-echo sequence was developped to annihilate the effect of the spatial inhomogeneities that cause the signal to decrease with a $T_2^*$-time constant instead of the $T_2$-constant. The sequence, shown in fig. 2.5 and explained in fig. 2.6, starts with a 90°-pulse which brings the magnetization in the $xy$-plane (fig. 2.6a). The signal decreases with a time constant $T_2^*$ as both spin-spin interactions and spatial inhomogeneities in $B_0$ cause the dephasing of the individual spins (fig. 2.6b). After a time $T_E/2$, a 180°-pulse is applied, which flips all of the dipoles. The spatial inhomogeneities, however, still cause dephasing in the same way as before the inversion pulse (fig. 2.6c), and now rephase the individual spins (fig. 2.6d). As a result a time $T_E$ after the 90°-pulse, a maximum in the signal is observed, which is denoted an echo (fig. 2.5). $T_E$ is called the echo-time. The amplitude of this echo signal is reduced only by spin-spin effects, and therefore only dependent on the true $T_2$-value (fig. 2.5).

### 2.4.2 Spoiled gradient echo sequence

The spoiled gradient echo pulse sequence (SPGRE) is used in the majority of DCE-MRI studies, as it combines relatively high spatial and temporal resolution with acceptable SNR. Fig. 2.7 shows a schematical overview of the rf-pulses and the gradients applied during an SPGRE sequence. Every $T_R$ seconds, an $\alpha$-pulse is applied which flips the longitudinal magnetization. The high acquisition speed is partially due to the SPGRE's ability to operate at low flip angles (eq. 2.9). Secondly, SPGRE-pulses use a variation in the sign of the spatial encoding gradient ($G_x$) to create echo as described above, which is much faster than the 180°-pulse in the spin-echo sequence. Applying a gradient causes neighbouring dipoles to dephase due to the spatial variation of their larmor frequencies. When the sign of this gradient is flipped, the opposite spatial variation in larmor frequency compensates the dephasing and a similar echo pulse is created. However, the amplitude

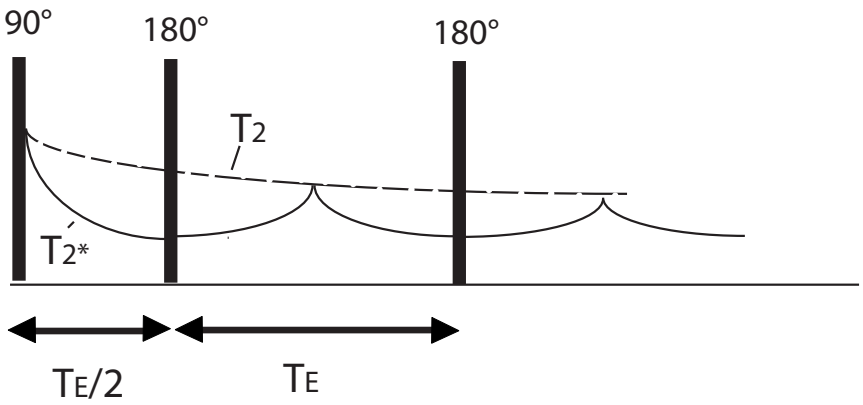


**Figure 2.5:** RF pulses and signal decay in the spin-echo sequence. A time $T_E$ after the 90°-pulse an echo is observed in the signal. The amplitude of this echo is only influenced by $T_2$-effects.

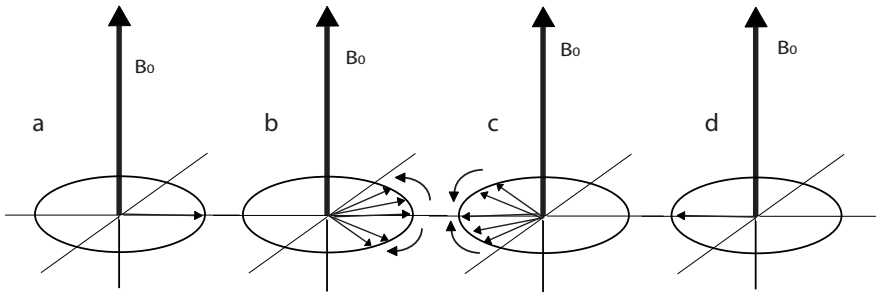


**Figure 2.6:** Graphical explanation of the principle of echo creation. a: after a RF pulse a net transverse magnetization exists. b: the transverse magnetization decays due to the dephasing of the dipoles, by both spin-spin interactions and magnetic field inhomogeneities. c: after a 180°-pulse, all dipoles are flipped. The magnetic field inhomogeneities now cause rephasing of the spins. d: an echo-pulse is created.

of this pulse is subject to $T_2^*$ effects instead of $T_2$-effects, as no correction for the magnetic field inhomogeneities is applied. The term 'spoiled' denotes that before every FA-pulse, the remaining transverse magnetization is destroyed. This can be accomplished in several ways (see section 2.7), but in this section the use of a spoiler gradient in slice selective direction is assumed. This gradient enforces the local magnetic field inhomogeneities

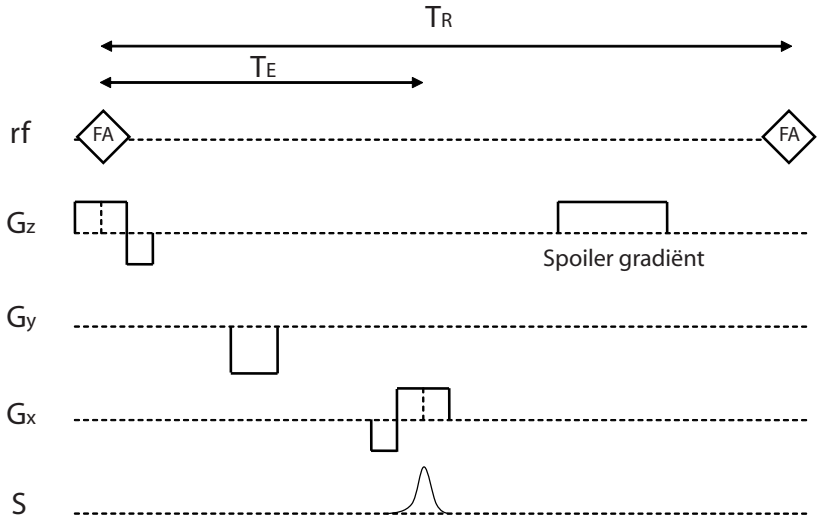


**Figure 2.7:** RF-pulses and gradients in the spoiled gradient echo pulse sequence. Echo signal is created by the flipping the sign of the read-out gradient. A spoiler gradient is used to destruct the remaining transverse magnetization just before each $\alpha$-pulse.

and thereby decreases $T_2^*$ (eq. 2.15), to ensure that at the end of every repetition period a complete relaxation of the transverse magnetization is obtained.

To determine an analytical expression for the signal intensity measured during the echo pulse, the notations $M_n^{pre}$ and $M_n^{post}$ are introduced, the longitudinal magnetizations just before and just after the $n^{th}$ FA-pulse respectively. According to eq. 2.14:

$$M_n^{post} = M_n^{pre} cos(\alpha) \tag{2.24}$$
$$M_{n+1}^{pre} = M_n^{post} + (M_0 - M_n^{post})(1 - e^{-T_R/T_1}) \tag{2.25}$$

After a number of excitations, a periodic answer is established, i.e. $M_n^{pre} = M_{n+1}^{pre}$. Combining this equation with eq. 2.24 and eq. 2.25 it can be easily be shown that:

$$M_n^{pre}(1 - cos(\alpha)e^{-T_R/T_1}) = M_0(1 - e^{-T_R/T_1}) \tag{2.26}$$

The transverse magnetization before every $\alpha$-pulse is assumed to be zero. Therefore its magnitude just after the $\alpha$-pulse is given by $M_n^{pre} sin(\alpha)$. Taking into account the $T_2^*$-relaxation of the transverse relaxation at the time of readout (i.e. during the echo-signal), the final signal intensity can be obtained by using eq. 2.27 :

$$S(T_1, T_2^*) = kM_0 sin(\alpha) \frac{1 - e^{-T_R/T_1}}{1 - cos(\alpha)e^{-T_R/T_1}} e^{-T_E/T_2^*} \tag{2.27}$$

$kM_0$ is a proportionality factor depending on equilibrium magnetization and receiver gain (in the rest of this work, the influence of the receiver gain is comprised within $M_0$ and the proportionality factor $kM_0$ is denoted as $M_0$).

### 2.4.3 Inversion-recovery spoiled gradient echo sequence

The inversion-recovery spoiled gradient echo sequence (IR-SPGRE) is part of an in-house (Ghent University hospital) protocol for DCE-MRI on the 1.5 T clinical scanner (Siemens Symphony). It is therefore used throughout this work. The pulse sequence is almost identical to the SPGRE-sequence, with the exception of an 180°-pulse, which is played a time $T_I$ (the inversion time) before the $\alpha$-pulse. The pulse sequence signal intensity is given by [46]:

$$S(T_1, T_2^*) = kM_0 sin(\alpha) \frac{1 - 2e^{-T_I/T_1} + e^{-T_R/T_1}}{1 + cos(\alpha)e^{-T_R/T_1}} e^{-T_E/T_2^*} \tag{2.28}$$

## 2.5 Contrast agents for $T_1$-weighted DCE-MRI

Contrast agents for $T_1$-weighted DCE-MRI are non-toxic and biocompatible substances that cause a reduction in local $T_1$- and $T_2$-relaxation times. These

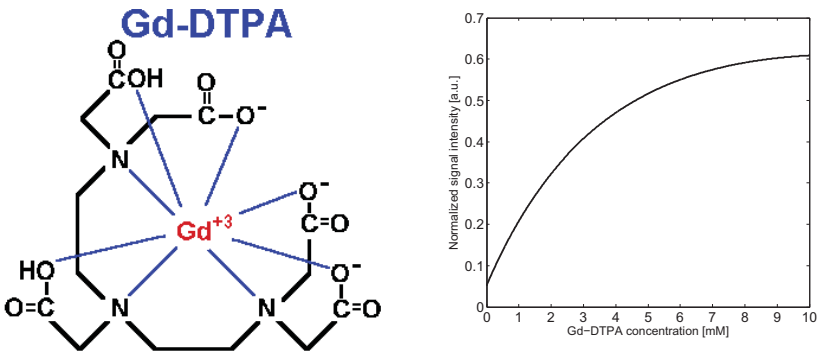


**Figure 2.8:** Left: structure formula of Gd-DTPA. Right: normalized SPGRE signal intensity ($S/M_0$) versus Gd-DTPA concentration ($T_R/T_E = 35/5ms$, $\alpha = 70°$, $T_{10}/T_{20} = 916/200ms$)

CA's are chelates of paramagnetic ions such as $Gd^{3+}$ or $Mn^{2+}$, whose unbound electrons induce a magnetic moment up to 1000 times larger than the intrinsic magnetic moment of the proton. The oldest approved CA for in vivo application is Gd-DTPA (gadiolinium diethylenetriamine penta-acetic acid), trade name Magnevist (Schering, Berlin, Germany), shown in fig 2.8. The Gd-ion is tightly bound to the DTPA-arms, protecting the body against the toxicity of free Gd. A number of CA's frequently used in clinical DCE-MRI and pharmacokinetic modeling studies, are mentioned in table 2.2. For physiological concentrations of these CA's, it is assumed that the relaxation rates change linearly with the CA concentration [CA] [47]:

$$\frac{1}{T_1} = \frac{1}{T_{10}} + r_1[CA] \tag{2.29}$$

$$\frac{1}{T_2} = \frac{1}{T_{20}} + r_2[CA] \tag{2.30}$$

$T_{10}$ and $T_{20}$ are the relaxation times of the tissue in the absence of a CA, the so-called native relaxation times. Their measurement is discussed in the next section. The proportionality coefficients $r_1$ and $r_2$ are the longitudinal and transverse relaxivity coefficients respectively. Their values depend on the paramagnetic ion, the protective coating (the type of contrast agent), the temperature and the magnetic field strength. These relationships have been confirmed in vitro [30, 44] and for $T_1$ in vivo [48]. In table 2.2, the relaxivity coefficients are mentioned for a number of clinically approved CA's at 1.5T and 37°C in water and in plasma respectively. It is clear that $r_1$ and $r_2$-values

**Table 2.2:** Short name, trade name and relaxivity coefficients for a number of contrast agents approved for clinical use at 1.5T and 37° in blood and in plasma. Values for $r_1$ and $r_2$ are in $[mM^{-1}s^{-1}]$ and were adopted from [44]

| Short name | Trade name | in water | | in plasma | |
|---|---|---|---|---|---|
| | | $r_1$ | $r_2$ | $r_1$ | $r_2$ |
| Gd-DTPA | Magnevist | 3.3 | 3.9 | 4.1 | 4.9 |
| Gd-DOTA | Dotarem | 2.9 | 3.3 | 3.6 | 4.3 |
| Gd-DO3A-butrol | Gadovist | 3.3 | 3.9 | 5.2 | 6.1 |
| Gd-DTPA-BMA | Omniscan | 3.3 | 3.6 | 4.3 | 5.2 |

depend upon the physicochemical nature of the tissue or solvent. This poses a severe problem for in vivo quantification. If the physiological conditions in vivo do not resemble the conditions for which the relaxivity coefficients were measured[10], protein binding may affect the values significantly and errors in concentration quantification can occur.

The physical mechanism causing $T_1$ and $T_2$ shortening are short-range phenomena (order of nm scale). In contradiction to nuclear medicine or CT tracer methodologies, DCE-MRI does not measure the signal change arising from the CA itself, but rather the effect of the CA presence on the local proton relaxation times. As a results, the relationship between signal intensity and CA concentration is non-linear. This is shown in fig. 2.8B, plotting the variation of the SPGRE pulse sequence intensity with the Gd-DTPA concentration. Typical tissue concentrations of the CA's from table 2.2 are in the order of 1-2 mM, while typical blood concentration reach up to 10 mM. The extent of this non-linearity depends on the concentration range to be measured and on the pulse sequence settings (see chapter 4). The inclusion of this non-linearity in the pre- and post-processing of DCE-MRI experiments for pharmacokinetic modeling is one of the innovations introduced throughout this work.

## 2.6 Measurement of native relaxation times

A DCE-MRI investigation monitors the $T_1$-relaxation time, to determine the concentration of the CA in the tissue of interest. However, absolute

[10]This is typically done in an in vitro dilution series experiment. For every vial in the dilution series, the $T_1$ and $T_2$ are measured and the slope of the relaxation times versus concentration curve is estimated for the corresponding relaxivity coefficient.

quantification of the CA concentration from these $T_1$-relaxation time requires the knowledge of the native longitudinal relaxation time (eq. 2.29). The 2- or 3-dimensional pixelwise mapping of these $T_{10}$-values is called $T_1$-relaxometry. Although from eq. 2.30 it may seem necessary to know $T_{20}$ as well, in chapter 4 it will be shown that its knowledge is abundant when signal intensity is converted to concentration values based on relative signal enhancement. A wide range of methods for relaxometry has been described [43, 49]. A very precise and accurate method is based on acquiring a number of inversion recovery based pulse sequence images with different inversion times. However, these methods are very time consuming, in the order of 5-30 minutes, which is unfeasible in clinical practice. The most frequently used method in clinical studies is the multiple flip angle approach. For this method, multiple SPGRE images are acquired with different flip angles. In the two-point method, the $T_1$-value can be determined analytically while the multiple flip angle case requires non linear regression to determine $T_1$. These methods have the advantage that the imaging matrix for which the $T_{10}$-values are determined pixelwize, is automatically identical to the imaging matrix of the dynamic series. Secondly the necessary acquisition time is acceptable (in the order of minutes). Although the absolute precision of the $T_{10}$-values is lower, they have superior precision efficiency (precision/time). The method is susceptible to errors, s.a. flip angle inhomogeneity (see below), but in conjunction with flip angle mapping, their accuracy is comparable to other relaxometry techniques [49,50].

In the two-point method, signal intensities from a SPGRE pulse sequence with repetition time $T_R$ and echo time $T_E$ are acquired at 2 different flip angles $\alpha_1$ and $\alpha_2$. Their ratio R is used for calculation of the $T_{10}$-value [51]:

$$R = \frac{S(\alpha_1)}{S(\alpha_2)} \tag{2.31}$$

$$T_1 = T_R \left[ log \left( \frac{Rsin(\alpha_1)cos(\alpha_2) - cos(\alpha_1)sin(\alpha_2)}{Rsin(\alpha_1) - sin(\alpha_2)} \right) \right] \tag{2.32}$$

Eq. 2.32 can easily be checked based on eq. 2.27. The precision of the resulting $T_1$ is highly dependent on the chosen flip angles. Schabel & Morell have derived analytical expression for the flip angles delivering optimal $T_{10}$-precision [49].

The multiple flip angle method [50] requires 3 or more SPGRE signal intensities $S(\alpha_i)$ at different flip angle $\alpha_i$. It relies on the following transformation of the SPGRE signal intensity equation:

$$\frac{S_i}{sin(\alpha_i)} = E_1 \frac{S_i}{tan(\alpha_i)} + M_0(1 - E_1) \tag{2.33}$$

$E_1$ is given by $e^{-T_R/T_1}$. By plotting $S_i/sin(\alpha_i)$ as a function of $S_i/tan(\alpha_i)$ and estimating the slope $m = E_1$ of the resulting straight line, $T_1$ can be obtained as:

$$T_1 = -\frac{T_R}{ln(m)} \tag{2.34}$$

## 2.7 Artefacts

In this section a number of MR artefacts is described and their consequences for SPGRE pulse sequences are illustrated.

### 2.7.1 $B_1$-field inhomogeneity

The $B_1$-field is created by the RF transmit coils of the MRI hardware. As a result of technical imperfection of these transmitter coils [52,53] and due to the dielectric properties of the human body, inhomogeneities occur in the $B_1$-field. The resulting spatially dependent $B_1$-field, $\boldsymbol{B_1}(\boldsymbol{r})$, induces spatially dependent flip angle values (eq. 2.9):

$$\alpha(\boldsymbol{r}) = \gamma B_1(\boldsymbol{r})T \tag{2.35}$$

When the nominal flip angle, i.e. the flip angle requested by the MRI control panel, is used to calculate tissue concentration or native relaxation times, the resulting values are subject to spatially dependent inaccuracies. The extent of the $B_1$-inhomogeneities is assumed to be small at 1.5T, but increases significantly at higher field strengths ($\geq$ 3T) [36,54] and in particular for a large field of view. Breast DCE-MRI is highly sensitive, as it frequently operates at 3T for reasons described above and requires a large FOV. In a DCE-MRI breast imaging study with a 2D- gradient echo pulse sequence, Kuhl et al. found large variation in $B_1$-field across the FOV. While the nominal flip angle was set to 20°, the true flip angle varied between spatially between 12.5 and 22° [55]. Recently Azlan et al. found that median $B_1$-field in a 3D GRE sequence, in the right breast of 25 volunteers was reduced to 40% of its expected value, leading to error of 55% in the true flip angle [54]. Other studies found variation in the order of 20-63% in cardial and head images [53]. $B_1$-field inhomogeneity is of particular importance in $T_{10}$-measurement as these values are highly sensitive to errors in the flip angles of the two- or multiple-point techniques. Several authors have proposed methods for $B_1$-calibration and for flip angle inhomogeneity correction [50, 51, 53, 56–58]. Parker et al. achieved to reduce mean errors in SPGRE $T_1$-measurement to 1.4% by deriving the spatial flip angle distribution from a phantom experiment [56]. To account for this important error source, several DCE-MRI studies employ $B_1$-calibration prior to DCE-MRI pre- and post contrast scans.

### 2.7.2 Slice profile inaccuracies

The slice profile denotes the distribution of the flip angle across the direction of the $B_0$-field (z-direction). While $B_1$-inhomogeneities cause flip angle variation

in a plane perpendicular to $\boldsymbol{B_0}$, the flip angle variation across the slice selective direction is determined by the shape of the excitation pulse[11]. The ideal slice profile consists of a uniform flip angle distribution within the desired slice, while outside the slice the transverse magnetization is zero ($\alpha$=0). This profile however, requires an infinitely long excitation pulse and is unfeasible in practice. For small flip angle ($\leq 30°$), it can be approximated by using sinc-pulses [12]. For larger flip angle, the slice profile can significantly deviate from the ideal case and the flip angle may vary considerably through the slice [42,43,56]. As a result, the accuracy of the SPGRE signal intensity equation is reduced. Parker et al. used a correction method for $T_1$-measurements, based on numerical calculation of the SPGRE pulse sequence intensity [56].

### 2.7.3 Incomplete spoiling

In the derivation of the SPGRE-pulse sequence intensity it was assumed that before each $\alpha$-pulse the remaining transverse magnetization is zero. This $M_{xy}$-destruction after each echo-acquisition is named spoiling. The simplest way to accomplish spoiling is to select $T_R$, at least four or five times larger than $T_2^*$, so that the remaining transverse magnetization is negligible at the start of a new $\alpha$-pulse (eq. 2.13). From a temporal resolutions aspect, this is obviously unfeasible. Other spoiling techniques include the use of a spoiler gradient before the $\alpha$-pulse (fig. 2.7) or RF spoiling [42,59]. Nevertheless, no spoiling technique is perfect and the remaining transverse magnetization effectively reduces the accuracy of the SPGRE signal equation. Errors have been demonstrated in SPGRE concentration determination and dual flip angle $T_{10}$-measurement [59, 60]. Several studies have investigated optimized spoiling techniques [59, 61]. Recently Yarnykh et al. proposed an optimized RF-spoiling strategy at the cost of a high repetition time ($T_R > 20ms$) and reduced temporal resolution [61].

### 2.7.4 Inflow effects

Inflow effects can be observed when measuring the signal intensity in flowing blood. Consider a SPGRE-pulse sequence on a slice, intersected by an artery of a vein containing flowing blood. After the first $\alpha$-pulse, the spins in the blood of the selected slice are excited. By the time that the next $\alpha$-pulse is played however, the blood flow has caused a fraction of these excited spins to leave the slice, while a number of unexcited spins has entered the slice. The longitudinal magnetization of these unexcited spins has not been reduced by a previous $\alpha$-pulse and is therefore larger than the longitudinal magnetization from the remaining excited spins. As a result, the total longitudinal magnetization just before the second $\alpha$-pulse is higher than predicted by eq. 2.25. The transverse

[11] When an excitation pulse is played together with a concurrent slice-selective gradient, the slice profile for small flip angle is given by the inverse fourier transform of the $B_1$-amplitude time profile

[12] The inverse fourier transform of a sinc pulse is a bloc function

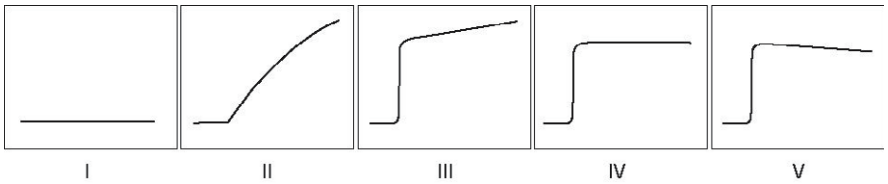


**Figure 2.9:** Classification system for visual evaluation of enhancement curves, adopted from [63]. I: No enhancement. II: slow sustained enhancement. III: rapid initial enhancement and sustained late enhancement. IV: rapid initial and stable late enhancement. V: rapid initial and decreasing late enhancement. The higher numbered curves are assumed to represent more aggresive tumor types.

magnetization after the second $\alpha$-pulse is higher as well, and an increase in the signal can be observed. This is the so-called flow related enhancement. While this effect is exploited in MR-angiography[13], it is highly undesirable in DCE-MRI, causing an overestimation of the CA concentration in flowing blood (the arterial input function). The extent of this effect is dependent on the velocity of the blood perpendicular to the imaging slice, and the repetition time and flip angle of the SPGRE-sequence. Peeters et al. a correction method based on an analytical model for the SPGRE signal intensity equation under inflow [62].

## 2.8 Qualitative analysis

In the next chapter pharmacokinetic modeling of DCE-MRI measured concentration curves is described. However, a number of qualitative or semi-quantitative methods exists to obtain functional information about the tissue of interest, by analysing the signal intensity versus times curves. In this section a short overview is given of these very popular methods and their advantages and shortcomings are discussed.

### 2.8.1 Visual inspection of enhancement curves

Visual inspection of the signal intensity or enhancement curve by a radiologist is the most subjective method for analysing a DCE-MRI examination. Several classification systems have been proposed based on the sharpness of the slope and the evidence of contrast washout after the initial upslope. Daniel et al. distinguished 5 different types of enhancement curves (fig. 2.9) and achieved

[13] so-called time-of-flight angiography

very good diagnostic performance for discriminating malignant from benign breast lesions [63]. Kuhl et al. found excellent sensitivity and specificity values (91% and 83%) with a 4 type-classification system [55].

### 2.8.2 semi-quantitative analysis

A wide range of semi-quantitative parameters has been used to describe the DCE-MRI signal intensity curves. A number of them is mentioned in table 2.3 and explained in fig. 2.10. These heuristic measures have several important advantages, that may explain why up to today they are widely used in DCE-MRI studies. First of all, no signal intensity conversion to CA concentation is required, avoiding the need to know CA or tissue characteristics ($r_1$, $r_2$, $T_{10}$). In addition, the heuristic parameters are easy to calculate, and embedded in most post-processing software packages. No model fitting has to be performed and AIF measurement is abundant. Finally, they seem to have wide clinical acceptance and good clinical significance, as was shown by numerous studies [1, 47, 64–66].

These semi-quantitative measures, however, also have a number of important disadvantages. First of all, these heuristic parameters are highly dependent on scanner and pulse sequence parameters, as well as on the native $T_1$-values of the tissue of interest. Therefore it may be impossible to reproduce the results of a study in another clinical setting. For longitudinal and multi-centre studies, more reproducible and scanner-independent measures are necessary. Especially in clinical trials of new therapeutic agents, it should be ensured that the parameter used for hypothesis testing truly reflects properties of tumor microvasculature and is as independent as possible of scanner and acquisition strategy. This is related to the second disadvantage of semi-quantitative analysis, the inability to distinguish between different physiological changes. A difference in enhancement may be due to a change in permeability, blood volume, interstitial volume or blood flow, but these effects cannot be separated or from an individual enhancement parameter. Finally, the heuristic parameters are determined by the arterial input function as well. A difference in contrast delivery to the tumor, caused by varied injection protocol, anatomical or physiological abnormalities such as poor cardiovascular function, will induce changes in the enhancement curves, not attributed to true physiological changes.

## 2.9 Conclusion

DCE-MRI is a technique to measure the CA concentration in a tissue of interest over time, by monitoring its effects on the $T_1$-relaxation time of the tissue. SPGRE-pulse sequences are commonly used in DCE-MRI studies

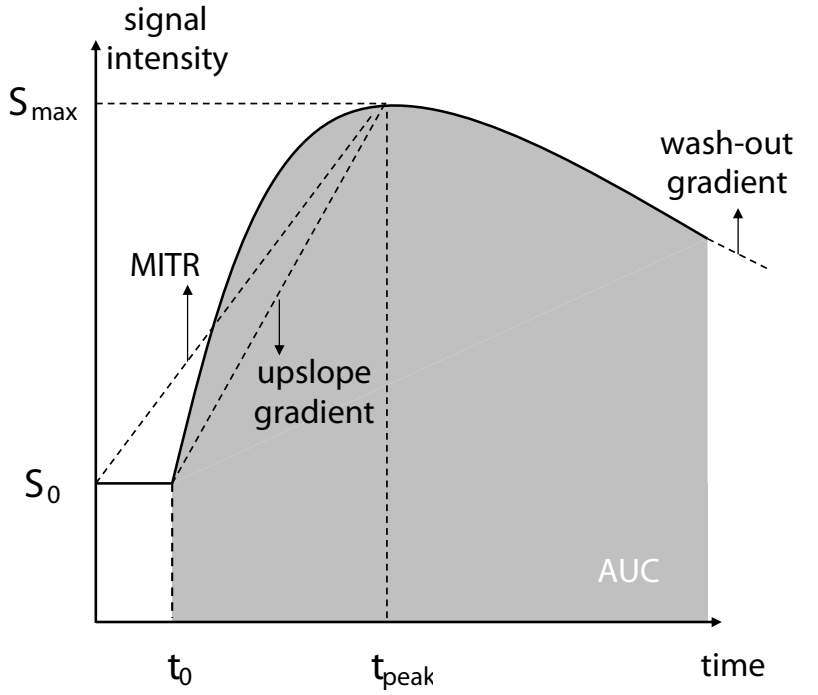


**Figure 2.10:** Illustration of a number of semi-quantitative parameters used to obtain functional/diagnostical information from DCE-MRI signal intensity curves. Symbols are explained in table 2.3

and comprise a non-linear relationship between CA concentration and MR signal intensity. The temporal resolution of the DCE-MRI measurement is an important protocol parameter when the concentration curve is to be fit to a pharmacokinetic model. Increasing temporal resolution is feasible, at the cost of a reduced spatial resolution, less spatial coverage, a reduced SNR, increased error-sensitivity (fast k-space sampling strategies), or by technological improvements (decreased $T_R$). The effect of these trade-offs on the precision and accuracy of pharmacokinetic estimates have to be investigated. In particular for breast DCE-MRI, these trade-offs oblige the use of high-field strenght for acceptable SNR at acceptable temporal resolution. In addition, a number of MR-related errors occur, whose extent is dependent on the protocol design: $B_1$-field inhomogeneities for instance, impose a severe drawback to breast DCE-MRI at high field strength. Incomplete spoiling may occur at small repetition times, while at high flip angle in 2D-sequences slice profile considerations have to be taken into account. Inflow effects pose a technological

**Table 2.3:** Semi-quantitative parameters for DCE-MRI curve analysis. Several quantities are described in figure 2.10

| Parameter | Description/comment |
|---|---|
| $t_{peak}$ | time between CA administration and maximal signal intensity |
| $t_0$ | onset time or bolus arrival time<br>time between CA administration and bolus arrival |
| $t_{90}$ | time to reach 90% of maximal signal intensity |
| Maximal absolute enhancement | $S_{max} - S_0$ |
| Maximal relative enhancement | $(S_{max} - S_0)/S_0$ |
| Enhancement change | defined over a fixed time period<br>both relative or absolute |
| Gradient of the upslope | figure 2.10 shows the mean gradient of the upslope<br>initial gradient is also used. Both relative or absolute. |
| Washout gradient | both relative or absolute |
| MITR | maximum intensity time ratio<br>$=(S_{max} - S_0)/t_{peak}$ |
| nMITR | normalized MITR<br>$=(S_{max} - S_0)/(S_0 t_{peak})$ |
| $AUC_t$ | area under the (relative of absolute) enhancement of signal intensity curve. Defined for a time point t |

difficulty for the individual AIF-determination strategy. DCE-MRI protocol design for pharmacokinetic modeling is therefore a complicated task.

# Chapter 3

# Current status of pharmacokinetic modeling of DCE-MRI data

## 3.1 Introduction

In this chapter an overview is given of the pharmacokinetic models that are used throughout the rest of this work. A discrepancy is made between 2- 3- and 4-parameter models. Instead of deriving the model equations separately for every model, we start from a number of general assumptions, that all models have in common. Based on these generalities the 4-parameter tissue homogeneity (TH) model is proposed. This TH-model comprises the most correct description of the processes, describing CA exchange. It is however not suitable for pharmacokinetic modeling as no time-domain solution is available. By making a number of additional assumptions we subsequently derive the model equations for the 4-parameter adiabatic approximation of the tissue homogeneity (AATH) model, the 3-parameter extended Tofts & Kermode (ETK) model and the 2-parameter Tofts & Kermode (TK) model, which have all been investigated in a wide range of clinical studies. Afterwards, an overview is given of the clinical applications of pharmacokinetic modeling, both for tumors as for non-tumor pathologies. As explained in the previous chapter, the arterial input function (AIF) is indispensable for the fitting of pharmacokinetic models to DCE-MRI data. The strategies for AIF determination are summarized and their main advantages and drawbacks are discussed. Finally, the limitations of pharmacokinetic modeling are illustrated by mentioning the results of a number of studies in the field. The three main limitations, as reviewed in chapter 1, return: the absence of standardized measurement protocols, the absence of post-processing techniques and the

absence of guidelines for model selection. The importance of model selection is illustrated by means of a straightforward example.

## 3.2 Pharmacokinetic models

### 3.2.1 Historical overview

Pharmacokinetic modeling of DCE-MRI data was initiated around 1990's, mainly by the work of Tofts & Kermode [67], Brix [68] and Larsson [69]. Initially, the purpose of their compartmental models was the investigation of the blood-brain barrier in the brain of patients with multiple sclerosis or brain tumors. Later on, the field expanded and applications of pharmacokinetic modeling in several tumor types were demonstrated. Pilot studies were succesively performed in breast tumors [70, 71], cervical and prostate cancers [38], up untill very recently in hepatic metastases [72]. The pharmacokinetic models themselves, were adopted from other area's of physiological modeling and therefore developped much earlier. In 1951, Kety was the first researcher to employ 2 well-mixed compartments for the description of inert gas exchange between plasma and tissue in the lungs [73]. Its model was used in later studies for the measurement of cerebral blood flow as well. Kety poses however, that the venous blood in a tissue is in diffusion equilibrium with the tissue itself, implicitly assuming an infinite permeability of the vessel wall with respect to the tracer of interest. The kinetics of such 'freely diffusable' tracer are flow-limited and vessel wall permeability is not taken into account in the model equations. Ohno, Pettigrew and Rapoport, described a similar compartmental model for permeability-limited cases, for the measurement of cerebrovascular permeability to nonelectrolytes [74]. For DCE-MRI studies however, the many MR contrast agents approved for clinical or experimental use, have very different molecular size, osmolarity or hydrophylicity , etc. which greatly affect their permeability [75]. In addition, the wide range of pathologies with considerable inter- and intra-individual differences in plasma flow or vessel porosity, indicate that this classification in flow- or permeability limited cases is insufficient. Therefore, both approaches were combined for DCE-MRI by the extraction fraction concept, introduced by Renkin [76] and Crone [77]. The extraction fraction is the relative difference in plasma concentration at the arterial and venous side of the tissue respectively, and combines the permeability and plasma flow in a single parameter describing the exchange of the tracer between tissue and plasma. In combination with the studies of Kety and Ohno, Pettigrew and Rapoport, this concept forms the base of the 2- and 3-parameter compartmental pharmacokinetic models currently used in DCE-MRI studies.

The first semi-compartmental model for capillary exchange was proposed by

Johnson & Wilson in 1968 [78]. In this work the authors aim to explain the transport of nonelectrolytes in the perfused heart. This so called tissue homogeneity model, has been used in many fields of quantitative medicine. However, the model has no closed-form time-domain solution and is therefore inefficient to use for fitting pharmacokinetic parameters from DCE-MRI data. In 1998, St. Lawrence & Lee developped an adiabatic approximation of the tissue homogeneity model, based on the presumption that the tracer concentration in the tissue changes slowly relative to the concentration in the capillaries [79,80]. They derived a closed-form time domain solution, which can be used for DCE-MRI purposes. In recent years, increasing interest is shown in this model as in contradiction to the standard compartmental models it enables separate estimation of both permeability and plasma flow.

### 3.2.2 Model generalities

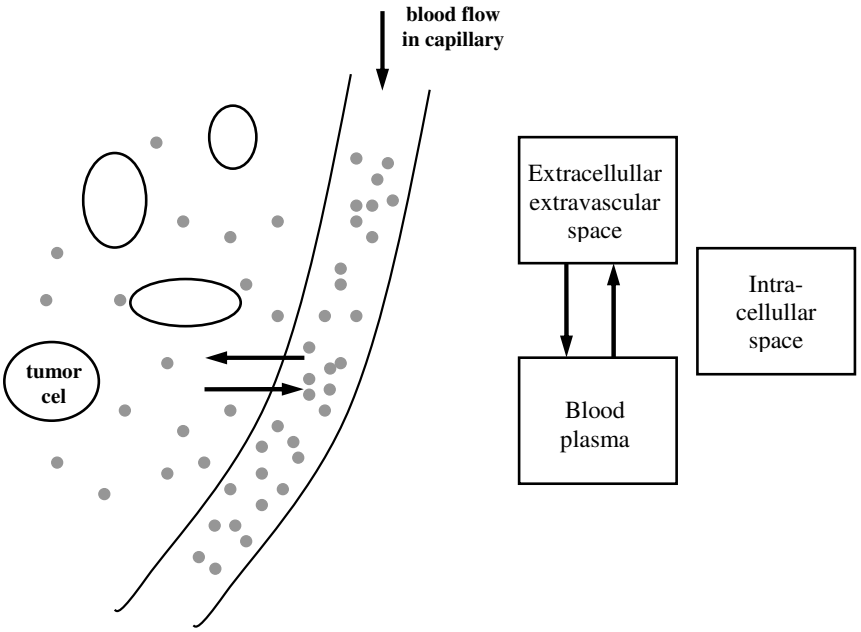


**Figure 3.1:** Tumor physiology and its compartmental depiction. Tracer is exchanged between the blood plasma and the extracellullar extravascular space.

The different models, describing the tracer kinetics, have a number of underlying presumptions in common:

- Compartmental representation of tumor physiology: all models assume that the tumor physiology can be depicted by 3 compartments (fig. 3.1): an extracellullar extravascular space (EES) compartment representing the interstitial space between the cells, a blood plasma compartment and an intracellullar compartment. CA arrives by the blood flow and is exchanged between the plasma and the EES, as the hydrophilic character of the clinically used Gd-chelates prevent the agent from penetrating cellullar membranes [75]. The intracellullar compartment contains therefore both the tumor cells and the blood cells.

- Well-mixed condition : each model assumes that at least one of the compartments is well-mixed, i.e. that the concentration can be considered uniform throughout the compartment. In a well-mixed compartment no spatial variation in CA concentration has to be accounted for. In the lumped-parameter models, all compartments are assumed to be well-mixed. In the distributed parameter models only the EES compartment is considered well-mixed.

- Linear intercompartment flux : the flux between the EES and the plasma compartment is proportional to the difference between the respective compartment concentrations.

- Standardization of quantities and parameters: in a famous paper from 1999, jointly published by the majority of the leading authors in the field [17], a set of standardized pharmacokinetic parameters and working quantities was established for pharmacokinetic modeling of $T_1$-weighted DCE-MRI data. The paper only considers the 2- and 3-parameter models, as the tissue homogeneity model and its adiabatic approximation were not yet in use at the time of publication. The standardized kinetic parameters are adopted in table 3.1, extended with the kinetic parameters from adiabatic approximation of the tissue homogeneity model. In table 3.2, the working quantities are mentioned, used throughout the derivation of the model equations, as well as several important mutual relationships. Generally a tissue density of 1 g/ml is assumed and the true estimated pharmacokinetic parameters are those from table 3.1 multiplicated with the tissue density.

- Time invariance: the parameters describing the CA kinetics are constant during the period of the data-acquisition.

- Arterial input function is known: the AIF is the CA concentration in the arterial plasma. Any kinetic model assumes that this concentration versus time curve is known.

**Table 3.1:** Standard kinetic parameters

| Parameter | Description | Unit |
|---|---|---|
| $F_p$ | plasma flow per unit mass of tissue | $ml\ g^{-1}\ min^{-1}$ |
| $PS$ | permeability-surface area product | $ml\ g^{-1}\ min^{-1}$ |
| $K^{trans}$ | endothelial transfer constant | $min^{-1}$ |
| $\nu_e$ | EES volume fraction | - |
| $\nu_p$ | blood plasma volume fraction | - |

**Table 3.2:** Standard working quantities

| Symbol | Description | Unit | Relationships |
|---|---|---|---|
| $\rho$ | tissue density | $g\ ml^{-1}$ | asummed to be 1 |
| $\tau$ | mean transit time | $min$ | $\tau = \nu_p/F_p$ |
| $E$ | extraction fraction | - | $E = 1 - e^{-\frac{PS}{F_p}}$ |
| | | | $K^{trans} = \rho E F_p$ |
| $k_{ep}$ | rate constant between EES and plasma | $min^{-1}$ | $k_{ep} = K^{trans}/\nu_e$ |
| P | permeability of the capillary wall | $cm\ min^{-1}$ | |
| S | capillary surface area per unit mass of tissue | $cm^2\ g$ | |
| $V_t$ | total tissue volume | ml | |
| $V_b$ | total blood volume | ml | |
| $V_p$ | total plasma volume | ml | $\nu_p = V_p/V_t$ |
| $V_e$ | total EES volume | ml | $\nu_e = V_e/V_t$ |
| Hct | haematocrit | - | Hct$= 1 - V_p/V_b$ |
| $\nu_i$ | intracellullar space volume fraction | - | $\nu_e + \nu_p + \nu_i = 1$ |
| $C_a$ | tracer concentration in arterial blood | mM | |
| $C_v$ | tracer concentration in venous blood | mM | |
| $C_b$ | tracer concentration in blood | mM | |
| $C_p$ | tracer concentraction in blood plasma | mM | $C_p = C_b/(1 - Hct)$ |
| $C_e$ | tracer concentration in EES | mM | |
| $C_t$ | tracer concentration in tissue | mM | $C_t = \nu_e C_e + \nu_p C_p$ |

### 3.2.3 Tissue homogeneity model

The tissue homogeneity model is a distributed parameter model, that describes the extravasation of CA from the capillaries into the interstitial space by means of 4 physiological parameters (table 3.3): $F_p$, $PS$, $\nu_p$ and $\nu_e$. The TH-model assumes a 2-compartmental representation of the tumor physiology as in fig. 3.1. The EES-compartment is considered to be well-mixed and the EES-concentration $C_e(t)$ is consequently only time-dependent. The plasma concen-

**Table 3.3:** Overview of standard pharmacokinetic models and the estimated kinetic parameters

| Model | Parameters |
|---|---|
| Tissue homogeneity model | $F_p$, $PS$, $\nu_e$, $\nu_p$ |
| Adiabatic approximation of TH model | $F_p$,$PS$, $\nu_e$, $\nu_p$ |
| Tofts & Kermode model | $K^{trans}$, $\nu_e$ |
| Extended Tofts & Kermode model | $K^{trans}$, $\nu_e$, $\nu_p$ |

tration $C_p(x,t)$ however, is assumed to be both spatially and time-dependent. The equations governing the exchange of CA in TH model can be easily derived from mass conservation in both compartments:

$$\nu_p \frac{\partial C_p(x,t)}{\partial t} = -LF_p \frac{\partial C_p(x,t)}{\partial x} - PS\left[C_p(x,t) - C_e(t)\right] \tag{3.1}$$

$$\nu_e \frac{\partial C_e(t)}{\partial t} = \frac{PS}{L}\int_0^L \left[C_p(x,t) - C_e(t)\right] dx \tag{3.2}$$

$$C_p(0,t) = C_a(t)/\nu_p = AIF(t) \tag{3.3}$$

$$C_e(0) = 0 \tag{3.4}$$

The right hand of eq. 3.1 contains both a convection term caused by the plasma flow and linear diffusion term due to the permeability (in accordance with the linear intercompartimental flux presumption). Diffusion within the capillary (so-called curve dispersion) is neglected. The right hand of eq. 3.2 consists of a diffusion term only, as no spatial concentration gradient is taken into account for the EES compartment. L is the length of the capillary. This system of coupled partial differential equations has no closed-form solution in the time-domain. In the laplace domain, however, a closed-form solution can be obtained by laplace transforming the system of equations with respect to time. The result is an ordinary differential equation in the spatial parameter x, which can be solved to yield the following expression:

$$C_t(s,\boldsymbol{\theta}) = H(s,\boldsymbol{\theta})AIF(s) \tag{3.5}$$

$$H(s,\boldsymbol{\theta}) = \frac{(e^{-\alpha+\beta s}-1)(\alpha+\beta s)(\alpha\nu_e + \nu_p(s\chi\beta+\alpha))}{\alpha^2(e^{-(\alpha+\beta s)}-1) - (\alpha+\beta s)s\beta(\chi(\alpha+\beta s)+\alpha)} \tag{3.6}$$

s is the parameter associated with the laplace transform, $\alpha = PS/F_p$, $\beta = \nu_p/Fp$ and $\chi = \nu_e/\nu_p$. The simulation of the TH-model concentrations throughout this work, is done based on a method described in [24].

### 3.2.4 Adiabatic approximation of the tissue homogeneity model

The adiabatic approximation of the tissue homogeneity (AATH) model was derived by St. Lawrence & Lee in 1999 [79, 80] to describe water exchange in the brain. It yields a closed-form time domain solution to the equations governing CA exchange based on the presumption that tracer concentration in the EES changes slowly relative to the plasma compartment. St-Lawrence & Lee justified this so-called adiabatic approximation since in the brain the ratio of water distribution volume in the extravascular and intravascular space is approximately 20 to 1. In tumors the ratio $\nu_e/\nu_p$ is typically smaller, but it remains high enough for the approximation to be valid. The derivation of the closed-form solution for the impulse answer of the AATH model can be found in [79]. The impulse answer $H(t)$ is given by:

$$H(t) = \begin{cases} 0 & t < 0 \\ F_p & 0 < t \leq \tau \\ EF_p exp(-\frac{EF_p}{\nu_e}(t-\tau)) & t > \tau \end{cases} \tag{3.7}$$

$\tau$ is the mean transit time of the tracer in the tissue, E is the extraction fraction. Both are related to the physiological parameters that can be estimated from the AATH model:

$$\tau = \frac{\nu_p}{F_p} \tag{3.8}$$

$$E = 1 - exp(-\frac{PS}{F_p}) \tag{3.9}$$

The product $EF_p$ is often reffered to as $K^{trans}$ for conformity with the lumped-parameter models. The tissue concentration $C_t(t)$ can be obtained by taking the convolution of the impulse answer with the AIF:

$$C_t(t) = H(t) \otimes C_p(0,t) \tag{3.10}$$

For the simplicity of notation, the x-dependence of the AIF is not explicitly mentioned in the following equations:

$$C_t(t) = \begin{cases} F_p \int_0^t C_p(t-t')dt' & t < \tau \\ F_p \int_0^\tau C_p(t-t')dt' + K^{trans} \int_\tau^t C_p(t-t') exp\left[-k_{ep}(t'-\tau)\right] dt' & t \geq \tau \end{cases} \tag{3.11}$$

Due to the high number of parameters, the AATH-model fitting is unstable and highly time-consuming [18, 24, 81]. This is explained in detail in chapter 7.

### 3.2.5 Lumped parameter models

In this section the compartmental model of Tofts & Kermode (TK) and its extended version (ETK) are discussed. These are lumped parameter models based on a compartmental representation of the tumor physiology and assuming both the plasma and the EES compartment to be well-mixed. The model equations can be derived by explicitly solving the differential equations governing the 2-compartmental CA exchange. However, it is also feasible to simplify the model equations of a higher order model in accordance to the additional presumptions underlying the TK model. Considering the plasma compartment to be well mixed is equivalent to assuming that the mean transit time of the tracer in the tissue is zero:

$$\begin{aligned} C_t(t) &= \lim_{\tau \to 0} \left[ \frac{\nu_p}{\tau} \int_0^\tau C_p(t-t')dt' + K^{trans} \int_\tau^t C_p(t-t') exp\left[-k_{ep}(t'-\tau)\right] dt' \right] \\ &= \nu_p C_p(t) + K^{trans} \int_0^t C_p(t-t') exp[-\frac{K^{trans}}{\nu_e} t'] dt' \qquad (3.12) \\ &= \nu_p C_p(t) + K^{trans} \int_0^t C_p(t') exp[-\frac{K^{trans}}{\nu_e} (t-t')] dt' \qquad (3.13) \end{aligned}$$

Eq. 3.13 is the standard model equation of the ETK model [17]. The TK model initially neglected the contribution of the intravascular tracer ($\nu_p = 0$), leading to the 2-parameter model equation:

$$C_t(t) = K^{trans} \int_0^t C_p(t') exp[-\frac{K^{trans}}{\nu_e} (t-t')] dt' \qquad (3.14)$$

Finally, from the definition of the extraction fraction in eq. 3.9, the above cited permeability and flow-limited cases can be explained. In the flow-limited case, $F_p << PS$, while in the permeability-limited case, $PS << F_p$. $K^{trans}$ reduces to:

$$K^{trans} = \begin{cases} F_p & F_p << PS \\ PS & PS << F_p \end{cases} \qquad (3.15)$$

In the flow-limited case $K^{trans}$ reflects plasma flow, while in the permeability limited case it identifies with the permeability-surface area product. For intermediate situations $K^{trans}$ mirrors both $F_p$ and $PS$. Therefore it is clear that the lumped parameter model can only assess one of both parameters, or measure their joint effect through $K^{trans}$.

## 3.3 Applications & clinical experience

The potential of pharmacokinetic modeling arises from its ability to non-invasively characterize microvascular physiology in a wide range of pathologies. The pharmacokinetic parameters as described above provide the clinician with additional functional information which can serve as an important tool for

diagnosis, treatment choice or prognosis. In this section an overview will be given of the applications of pharmacokinetic modeling of DCE-MRI data by summarizing a number of important clinical studies in the field. Although the focus is mainly on applications in tumor research, a number of non-tumor applications is mentioned as well. The applications for tumor research are subdivided in tumor detection and characterization, treatment follow-up and the testing of novel anti-angiogenic therapies.

### 3.3.1 Non-tumor applications

Although the main part of this section concerns tumor research, pharmacokinetic modeling has proven its benefits in other diseases in which angiogenesis plays an important role and microvascular changes are induced. As already stated in the historical overview, the first studies concerning pharmacokinetic modeling were performed in patients with multiple sclerosis (MS) [67, 69]. MS is an inflammatory disease in which, due to a disrupture of the blood-brain barrier (BBB), white blood cells enter the extracellullar brain fluid and attack the myelin[1] that protects the neurons of the nervous system. The BBB is the separation between the circulating blood and the extracellullar fluid in the brain. It consists of tight junctions around the capillaries that do not occur in normal circulation and protects the brain of e.g. bacterial infections. As in tumor microvasculature, a disfunctional BBB allows CA extravasation, which does not occur in normal tissue [16]. DCE-MRI and pharmacokinetic modeling have proven to be valuable tools for quantitation of the state of the BBB [16, 67, 82]. No vascular contribution has to be taken into account in the TK model, as the plasma fraction in the brain is mostly negligible [82]. In comparison with brain tumors the permeability of the disfunctional BBB is much smaller and the kinetics of CA-uptake in MS enhancing lesions are much slower. The enhancement curve is therefore permeability limited and $K^{trans}$ is a measure for BBB permeability [16, 82]. However, the associated disadvantage is that long scanning times are required (20 min up to 2 h [16, 67, 82]), which can be unfeasible in clinical practice. For other pathologies, affecting the integrity of the BBB, such as cerebral ischemia[2] [83, 84] or brain tuberculosis[3] [85, 86], a role for pharmacokinetic modeling has been established as well.

In inflammatory diseases in other parts of the body, as rheumatoid arthritis[4] or

[1] myelin provides the insulation surrounding the communication fibers along which nerve cells communicate by sending eletrical signals. In absence of myelin, transmission speed of nerve impulses is reduced, causing the typical MS symptoms

[2] Ischemia denotes a reduced and inadequate blood supply to a tissue and may cause a stroke

[3] Brain tuberculosis is an infectuous disease caused by myobacterium tuberculosis. Mostly tuberculosis affects the lungs, but it can attack the brain as well.

[4] rheumatoid arthritis is a systemic inflammatory disease, that principally affects the joints. It causes inflammation of the synovial membrane, which is the soft tissue delining the joint

atherosclerosis[5], pharmacokinetic modeling has shown to be of great value for diagnosis and treatment follow-up. Inflammation is an important step in the body's vascular defence mechanism against for example bacterial infections. The inflammatory response consists of vasodilation and increased vessel wall permeability, causing enhanced local blood flow and the ability for leukocytes to migrate to the infection. As a result, pharmacokinetic parameters can be used as a marker for inflammatory activity [87]. Vasodilation causes the contribution of the plasma compartment to be non-negligible and therefore most authors use the ETK model. In rheumatoid arthritis, several authors showed a correlation between the pharmacokinetic parameters and widespread clinical outcome measures such as synovial volume [88, 89], in particular for $K^{trans}$. Other studies found a significant reduction in $K^{trans}$ after succesfull therapy [90, 91]. $K^{trans}$ was also proven to be a good measure to differentiate between patients with osteoarthritis and rheumatoid arthritis [92]. In atherosclerosis, pharmacokinetic modeling was shown to be a good non-invasive method for assessing high-risk plaque formation [93]. $K^{trans}$ was identified as a marker for neo-vascularization [93–95], which is believed as an indication for plaque vulnerability. Both $\nu_p$ [96] and $K^{trans}$ [94] were shown to correlate with the invasive histological markers of plaque angiogenesis, such as microvessel density. A recent study found that pharmacokinetic modeling can be used for the detection of inflamed bowel segments in patients with Crohn's disease [97]

### 3.3.2 Cancer detection & tumor characterization

As for several tumor types, the stage of the disease is an important factor for therapy options and survival rate, early detection and treatment of malignant tumors are the best way to beat cancer and offer considerable improvement in outcome. In addition, delayed diagnosis of metastasic spread or recurrence after therapy limits the treatment opportunities that can be offered to a patient [4]. Several studies have suggested a role for pharmacokinetic modeling and DCE-MRI in early tumor detection. The term 'early' should be understood relative to the imaging strategy that is conventionally used for the diagnosis of a given tumor type. It may for instance denote that for a cohort of patients the sensitivity[6] or the specificity[7] of pharmacokinetic modeling & DCE-MRI may be higher than that of the conventional imaging technique, or that the non-invasiveness of the pharmacokinetic modeling technique predominates a potential lower sensitivity and/or specificity.

---

cavities.

[5] atherosclerosis is a progressive systemic disease that is characterized by the formation of plaque in the arterial vessel walls. These plaques can, when ruptured, cause myocardial infarction or stroke. In the vessel wall a chronic inflammatory response arises.

[6] $\text{sensitivity} = \frac{\text{number of true positives}}{\text{number of true positives} + \text{number of false negatives}}$

[7] $\text{specificity} = \frac{\text{number of true negatives}}{\text{number of true negatives} + \text{number of false positives}}$

Prostate cancer is the most common malignancy in men and has the second highest mortality rate. When clinical examination arouses the suspicion of prostate cancer, the diagnosis is usually confirmed by transrectal ultrasound (TRUS) guided biopsy [98]. This technique is characterized by a low sensitivity (39-52%) [99], meaning that a considerable proportion of the patients has to undergo this invasive procedure twice, before their cancer is detected. A non-invasive imaging technique relies on $T_2$-weighted MRI, and shows the lesion as a region of reduced signal intensity. This low $T_2$-signal intensity is however not unique for prostate cancer, but it can occur for other abnormalities such as prostatitis or fibrosis[8], causing a low specificity [98]. Ocak et al. have compared $T_2$-weighted imaging with DCE-MRI and pharmacokinetic modeling for the detection of prostate cancer. Pharmacokinetic modeling showed reduced sensitivity, but a far better specificity, based on $K^{trans}$ or $k_{ep}$ [100]. Similar results were obtained by Kiessling et al. [101]. Other studies suggest that a combination of non-invasive imaging techniques may improve prostate cancer detection and thereby reducing the need for biopsy [98]. Van Dorsten and coworkers use a combination of pharmacokinetic modeling & DCE-MRI with MR spectroscopic imaging [102], while Langer et al. show improved cancer detection by combining $T_2$-weighted MR, DCE-MRI & pharmacokinetic modeling and diffusion weighted MR imaging [103]. Recently, a role for pharmacokinetic modeling (in combination with $T_2$-weighted MR, diffusion-weighted MRI or magnetic resonance spectroscopy) was established in guiding prostate biopsy in patient with a previously negative biopsy [98, 104, 105]. This means that samples from suspicious regions, identified by pharmacokinetic modeling, are added to the randomized biopsy samples, and it has shown to increase the accuracy of the second biopsy [104]. It has been suggested that in the future parametric maps may be fused with real-time TRUS images for targetted biopsy [106]. However, there is no concensus about the optimal imaging strategy [98, 104] and often heuristic methods are used to generate the pharmacokinetic maps [105]. Finally, pharmacokinetic modeling and DCE-MRI have shown their applicability in prostate cancer localisation and in detection of recurrence. Accurate localisation is necessary for adequate prostatectomy planning or radiotherapy treatment [98]. Jackson et al. found higher sensitivity and similar specificity for DCE-MRI and TK-pharmacokinetic mapping in comparison with $T_2$-weighted imaging for prostate cancer localisation. They suggested the use of DCE-MRI and pharmacokinetic modeling for guiding the radiotherapy beam and thereby improving the outcome of radiotherapy [107]. Other studies confirm that the combination of conventional MR-imaging with PK-mapping is more accurate for prostate cancer delineation than conventional $T_2$-weighted imaging alone [100,108]. Finally a role has been suggested for pharmacokinetic modeling in the detection [109] and the treatment guidance [110] of prostate

[8] fibrosis is the formation of excess connective tissue

cancer recurrence after radiotherapy. All these studies mainly employ the TK- or ETK-models, although strong evidence exists that the mean transit time of the tracer in prostate cancer cannot be neglected and values up to 90s have been found [111]. Despite the unstability and mathematical considerations, a number of researchers has tested the AATH model for prostate cancer applications [111–114]. In a pilot study, Buckley et al. found increased plasma flow and EES-space fraction within prostate tumor tissue, when compared to its peripheral zones. Permeability and plasma volume fraction estimates were similar in both regions of interest [112].

Pharmacokinetic modeling has been investigated for lesion characterization in brain tumors as well [64]. Several studies have investigated the potential of the pharmacokinetic parameters to distinguish between different brain tumor types, such as glioma, meningioma, acoustic neuroma[9] or metastases. Andersen & Jensen found that $K^{trans}$ was significantly higher in meningioma than that in glioma or metastates [115]. Zhu et al. found the highest values of $\nu_e$ in acoustic neuroma, intermediate values in meningioma and the smallest values in glioma. These findings agree with results from microscopy studies [116]. Recently, two new applications for pharmacokinetic modeling in brain lesion characterisation were established: Haris et al. found $K^{trans}$ and $\nu_e$ to be useful for disriminating between infective brain lesions and glioma's [117]. Bisdas et al. investigated the feasibility of pharmacokinetic modeling for distinguishing recurrent high-grade gliomas from radiation injury, which is important for the accurate delineation of tumor recurrence and poses a significant problem in neuro-oncology. They found significant higher values of $K^{trans}$ in recurrent glioma's in comparison to radiation induced necrosis sites. They developped a diagnostic method based on a cut-off value for $K^{trans}$, which showed 100% sensitivity and 83 % specificity for detecting recurrent glioma's. A similar method based on the heuristic parameter AUC (area under the curve) had 71 % sensitivity and 71% specificity [118].

The role of pharmacokinetic modeling for the detection and diagnosis of breast cancer, the most common malignancy in women, is somewhat unclear. When clinical examination reveals a suspicious lesion, mammography is the standard imaging modality used for breast cancer diagnosis. The sensitivity of mammography, however, is reported to be low (down to 45% [7]), especially in patients with dense breast tissue. In addition, radiation exposure during mammography examination has to be considered, in particular for high risk women. Therefore, DCE-MRI has been established as a powerfull non-invasive alternative to mammography in breast cancer diagnosis [1], with reported sensitivity values up to 93% [119]. In 2007, the American Association for Cancer Research even recommended annual screening with breast MR imaging

[9]The nomenclature is dependent on the type of cells that start to proliferate. Glioma is a tumor that arises from the glial cells, while meningiomas start in the cells of the meninges. Acoustic neuroma is a tumor of the Schwann cells.

for high-risk women [120]. However, only a minor part of the numerous studies published on the subject perform pharmacokinetic modeling of the DCE-MRI concentration curves. Instead, visual inspection of signal intensity curves or semi-quantitative parameters, as described in chapter 2 are employed. The underlying reason has been discussed in the previous chapter and comes down to the trade-off between spatial resolution, temporal resolution and SNR, when the field of view of the MR-image has to achieve complete coverage of the breast. In addition, a high spatial resolution (1mm in plane, 3mm slice thickness) is required to detect small lesions and for the assessment of lesion morphology [7, 121]. Therefore, most clinically available protocols for breast MR imaging have temporal resolution in the range of 90-120s, which is too low for pharmacokinetic modeling[10]. Furman-Haran et al., did use a 2 min temporal resolution sequence with high spatial resolution for distinguishing between benign fibrocystic changes and malignant lesions [122]. They found high specificity (96%) and sensitivity (93%) for breast cancer detection based on $K^{trans}$, and concluded that pharmacokinetic modeling can significantly improve breast cancer diagnosis. However, the low temporal resolution is a serious drawback for their results. Schabel et al. reduced the spatial resolution to enable pharmacokinetic modeling. With a 9.7-19.7s temporal resolution sequence, they obtained excellent sensitivity and specificity when compared to mammography, based on a classification method of $K^{trans}$ and $k_{ep}$ [123]. Another study found similar results based on $k_{ep}$ alone [45]. Mussarakis et al. reduced the number of slices by pre-selecting a number of suspicious locations and found, with a temporal resolution of 12s, that TK model parameters can improve specificity of conventional MR breast examination [124]. Radjenovic and coworkers investigated the correlation between quantitative DCE-MRI parameters and histological tumor grade[11]. The TK model parameters $K^{trans}$ and $k_{ep}$ exhibited the highest degree of correlation with the tumor grade, in comparison with heuristic quantities. A significant difference in these parameters was found between grade 2 and grade 3 tumor, but not between grade 1 and grade 2 tumors. The latter may again be attributed to the low temporal resolution of their DCE-MRI measurement (32.5s) [125].

### 3.3.3 Treatment response and patient prognosis

In clinical oncology, an increased interest arises for biomarkers that can predict response of a patient to tumor treatment and the corresponding patient outcome. Such biomarkers have the advantage that the therapy can be targetted to those patients that are most likely to benefit, while for the others the associated toxicity of cytotoxic therapies can be avoided. To show

[10] the required temporal resolution is between 1.5-15s, depending on model and protocol. See chapter 1

[11] The grading of a breast cancer is based on microscopically comparing the breast cancer cells to cells of normal breast tissue. Grade 1 has the best progrosis, grade 3 the worst.

how pharmacokinetic modeling can evaluate tumor treatment, fig. 3.2 shows an example of treatment monitoring in two women with a grade 3 breast cancer, adopted from [1]. Both women received 6 cycles of chemotherapy. Before the treatment and after two cycles, pharmacokinetic parameter maps were produced from DCE-MRI investigations. For the first patient, in fig. 3.2 A & B, a strong change in the $K^{trans}$-map can be visually inspected: the transfer constant reduces significanlty across the complete lesion size. After 6 cycles of chemotherapy, this patient had a complete clinical[12] and radiological[13] response to the treatment. For the second patient, in fig. 3.2 C & D, no considerable changes in the transfer constant are seen within the lesion. After the complete chemotherapy treatment, this patient had no clinical or radiological response, and the cancer was still evaluated as grade 3. This example shows the potential of pharmacokinetic model to predict tumor response in an early stage of the chemotherapy treatment. Thereby the treatment can be adapted to increase life expectation and the hazardous effects for the patient of non-effective chemotherapy can be avoided. Tumor therapy may also be evaluated by MRI-derived tumor size change, but the time scale on which tumor size changes is much longer than the time scale on which microvascular changes occur.

A wide range of studies have investigated the potential of pharmacokinetic modeling in chemotherapy treatment evaluation. In breast cancer, Ah-See et al. investigated whether pharmacokinetic modeling of DCE-MRI data pre- and post neoadjuvant chemotherapy treatment could predict final clinical and pathological response. They found that changes in $K^{trans}$ and $k_{ep}$ correlated with both clinical and pathological response. Change in $K^{trans}$ was the best predictor for pathological non-response, correctly identifying 94% of the non-responders and 73% of the responders. The specificity and sensitivity are significantly higher than for change in MRI-derived tumor size change [126]. Vincensini found that the monitoring of $k_{ep}$ may be used for discriminate, at the early stage of the treatment, between lesions that respond well or poorly to therapy [45]. Other examples in breast cancer can be found in [119]. Also for other tumor types, the pharmacokinetic models are able to monitor or predict tumor response to chemotherapy [10,12,21,127–129].

Pharmacokinetic modeling can monitor and predict the radiotherapy treatment response as well [98,130]. Ceelen et al. found a significant reduction in $K^{trans}$ after fractionated radiotherapy in a colorectal tumor model in rats as well as correlation with tumor reoxygenation [131]. Zahra and coworkers showed the predictive value of pharmacokinetic parameters of the ETK model for radiation response in cervical cancer [130]. Also in other tumor types, radiotherapy response may be assessed by pharmacokinetic modeling [2, 10, 21, 132].

[12] clinical response denotes the disappearance of clinical symptoms

[13] radiological response denotes the reduction or disappearance of the lesion on radiological images after treatment

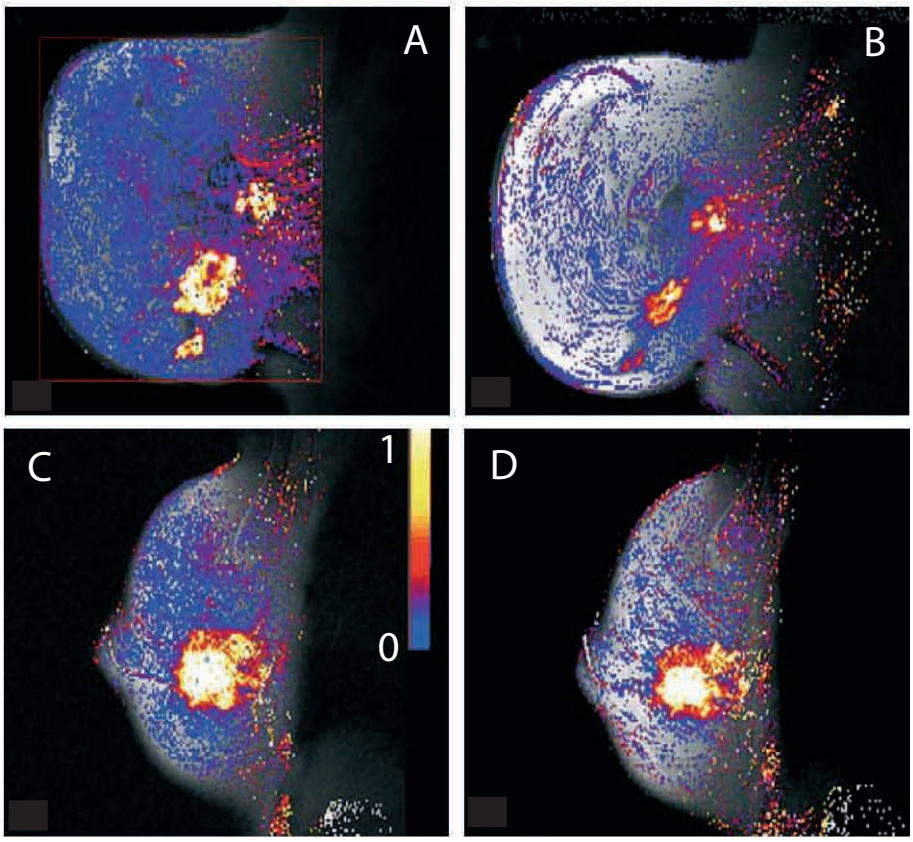


**Figure 3.2:** Example of tumor treatment follow-up with pharmacokinetic modeling. A & C: pre-treatment $K^{trans}$-map (TK-model) of two patients with grade 3 breast cancer. B & D: $K^{trans}$-map in those patients after two cylces of chemotherapy. For the first patient (A & B) a clear change is seen in the $K^{trans}$ across the lesion. This patient showed a complete clinical and radiological response after 6 cycles of chemotherapy. For the second patient (C & D) no significant change can be inspected. After 6 cycles, the cancer was still evaluated as grade 3. The color scale is expressed in $min^{-1}$.

The success of pharmacokinetic modeling in this field may be attributed to its ability to detect hypoxia, which is a known factor in the resistance to radiation treatment [9, 132]. Gulliksrud et al. showed that $K^{trans}$ could distinguish between hypoxic and non-hypoxic tumor regions [133]. Ellingsen et al. confirmed the potential of $K^{trans}$ for assessing the extent of hypoxia in carcinoma of the cervix. They found a strong inverse relationship between $K^{trans}$ and the fraction of radiobiologically hypoxic cells [134].

### 3.3.4 Testing of novel anti-angiogenic cancer treatments

As explained in chapter 1, pharmacokinetic modeling of DCE-MRI data can be used as a biomarker for assessing the effect of anti-angiogenic drugs on the tumor vasculature [2]. The difference in the TK- or ETK-parameters between pre- and post- anti-angiogenic therapy pharmacokinetic modeling assessments is frequently used in phase I and phase II drug development trials, to non-invasely quantify the efficacy of the treatment [14, 129, 135–138].

## 3.4 Arterial input function

Theoretically, the AIF is the plasma CA concentration in the plasma compartment (TK & ETK model) or on the arterial side of the plasma compartment (AATH model). Its knowledge is indispensable for the estimation of the kinetic parameters. In this section an overview is given of the different techniques to measure or determine the AIF. They are subdivided into four categories: a population-averaged or standard AIF, an individually measured AIF, the reference region method and AIF based on joint estimation with pharmacokinetic parameters.

### 3.4.1 Population averaged AIF

A wide range of studies uses a population averaged or standard AIF in the tumor tissue, presuming that the interindividual differences in the AIF are small. Parker et al. proposed a population averaged AIF, by performing DCE-MRI measurements of the AIF in a group of 23 cancer patients after bolus injection of Gd-DTPA-BMA (Dose = 0.1 $mmol\ kg^{-1}$). In this way they obtained 67 different AIF's, whose average was fit to a functional form with 10 free parameters. This best-fit functional was proposed as population averaged AIF and used in a wide range of studies [32, 139]. As in the following chapters, this AIF is frequently used, we explicitly mention the expression:

$$C_b(t) = \sum_{n=1}^{2} \frac{A_n}{\sigma_n\sqrt{2\pi}} exp(-\frac{(t-T_n)^2}{2\sigma_n^2}) + \frac{\alpha\ exp(-\beta t)}{1+exp(-s(t-\tau))} \tag{3.16}$$

$$\begin{aligned} A_1 &= 0.809\ mmol\ min & \sigma_2 &= 0.132\ min \\ A_2 &= 0.330\ mmol\ min & \alpha &= 1.050\ mmol \\ T_1 &= 0.170\ min & \beta &= 0.1682\ min^{-1} \\ T_2 &= 0.365\ min & s &= 38.078\ min^{-1} \\ \sigma_1 &= 0.0563\ min & \tau &= 0.483\ min \end{aligned} \tag{3.17}$$

Remark that this is the blood concentration, as MRI can only assess the concentration in a voxel that contains both blood plasma and blood cells. For practical use in pharmacokinetic modeling, it should be scaled to the plasma concentration by means of the hematocrit value (see table 3.2). Another AIF, that is currently employed in clinical studies, is the Weinmann curve [16, 66, 140]. It was determined by spectroscopic analysis of blood samples taken from healthy volunteers after bolus injection of Gd-DTPA, and fitting them to a sum of two degrading exponentials. As these blood samples cannot be taken with high temporal resolution, it fails to describe the AIF peak:

$$C_p(t) = D \sum_{n=1}^{2} a_i \; exp(-m_i t) \tag{3.18}$$

$$a_1 = 3.99 \; kg \; l^{-1} \qquad m_1 = 0.144 \; min^{-1} \tag{3.19}$$

$$a_2 = 4.78 \; kg \; l^{-1} \qquad m_2 = 0.0111 \; min^{-1} \tag{3.20}$$

D is the administered Gd-DTPA dose in $mmol \; kg^{-1}$. Both AIF's are shown in fig. 3.3. It is clear that the Parker AIF is more realistic, as it includes a first- and second pass peak in the plasma concentration after bolus injection of a CA. In comparison with the other AIF determination methods, assuming a population averaged AIF has the advantage of simplicity, as it does not require additional MR measurements in other regions of interest (see next paragraph). It was shown that the use of a population averaged AIF for the cohort of patients from which it was determined, increases the repeatability and reproducibility of the pharmacokinetic estimates in that population [139, 141]. However, when used for another cohort of patients, no such reproducibility increase could be found [141]. In addition, interindividual differences in the AIF induce bias in the pharmacokinetic estimates. For the ETK-model for instance, Cheng found that an error in the AIF peak amplitude causes an inversely proportional error in $K^{trans}$ and $\nu_p$, while $\nu_e$ is relatively unaffected. Assuming a biexponential AIF, as the Weinmann curve, resulst in a consistent 20% underestimation of $K^{trans}$ and a severe underestimation of $\nu_p$ [27]. Identical results were found by Kershaw & Cheng for the AATH model [24].

### 3.4.2 Individually measured AIF

By monitoring the signal intensity in a large feeding artery of the tissue of interest, the AIF can be individually measured in every patient. It can be expected that an individual measured AIF closely resembles the true AIF. However, for co-measurement of tissue and blood concentrations a number of technical considerations has to be taken into account. As explained in the previous chapter, inflow effects occur that induce overestimation of the true

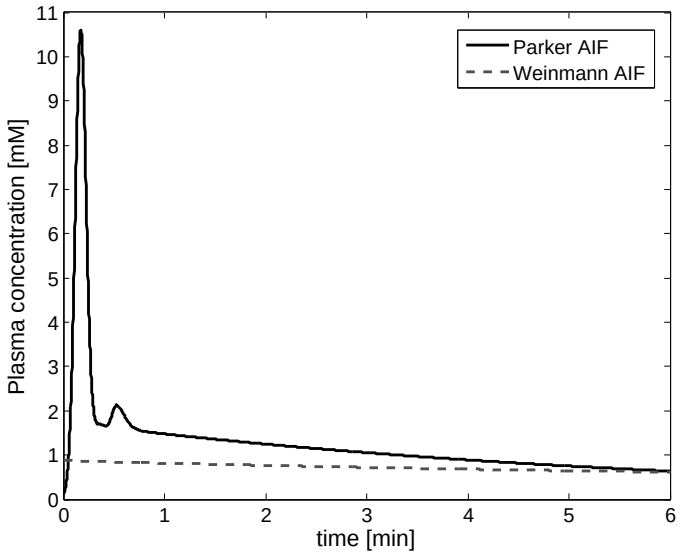


**Figure 3.3:** Parker AIF (Hematocrit = 0.4) and Weinmann AIF (Dose = 0.1 $mmol\ kg^{-1}$)

AIF concentration and may cause errors up to 40% in $K^{trans}$ [60]. These inflow effects are dependent on the repetition time of the sequence, the employed flip angle and on the orientation of the blood flow with respect to the imaging slice [22, 60, 62]. This implies that when the AIF is individually measured, the effect of the choice of the pulse sequence parameters on the AIF measurement accuracy has to be considered. Recently, Cron and coworkers have proposed a method for measuring the AIF derived from phase MR images, which are relatively unaffected by inflow effects. They could however not shown increased $K^{trans}$-reproducibility with a phase-derived AIF compared to a magnitude-derived AIF [142]. In addition, the concentration range that has to be measured in tumor tissue (0-2mM of a small Gd-chelate as Gd-DTPA) is much smaller than the typical blood concentrations (0-10 mM). In chapter 4 & 5, it is shown that improper pulse sequence design may lead to very high concentration noise on the AIF peak concentration. This is for instance observed in the study of Parker et al, and may explain why the repeatability of the pharmacokinetic estimates is higher with a population averaged AIF, as cited in the previous section [139]. It emphasizes again that the pulse sequence design has to be adapted to the AIF determination strategy. In the case of an individual measured AIF, the required temporal resolution of the DCE-MRI measurement is highly dependent on the AIF, rather than on the measured

tissue concentration[14]. Meng et al. showed that when DCE-MRI data are acquired with limited temporal resolution, individually measured AIF is not significantly better than population averaged AIF in predicting the biopsy results in prostate cancer [143].

### 3.4.3 Reference region method

The technical difficulties for co-measurement of the AIF and the inaccuracies when using a standard AIF, have led to the development of the reference region (RR) method [144]. Instead of monitoring the signal intensity in an artery, the signal variation in a reference tissue, mostly a muscle, is measured. As in the tumor tissue, the concentration curve is calculated in the reference tissue. By assuming that the pharmacokinetic parameters in the reference tissue are known from literature, the AIF in the reference tissue can be calculated from its tissue concentration curve [145]. However, interindividual variability in the pharmacokinetic parameters of the reference tissue causes the method to have low reproducibility [146,147]. Therefore a double reference region method [148] and a multiple reference region method [149] have been developped, that do not require a presumption about the pharmacokinetic parameters in the reference tissue. AIF's determined from the multiple reference region method have been shown to given better pharmacokinetic model fits and equally good reproducibility, when compared modeling with the Parker population averaged AIF [141]. No blood concentration measurement have to be performed when using a RR-method, which has important implications for protocol design: the required temporal resolution is only dependent on the tissue behaviour and the DCE-MRI pulse sequence settings may be designed for monitoring concentrations between 0-2mM. These methods have only recently been established and require additional research to the precision and accuracy of the resulting pharmacokinetic estimates.

### 3.4.4 Joint estimation of AIF and PK parameters

The principle idea of joint estimation of the AIF and pharmacokinetic parameters is to develop an acceptable functional form for the AIF, with a number of free parameters, that is joinly fit to the tissue concentration curve with the pharmacokinetic parameters. However, as can be seen from the Parker AIF parametrization in eq. 3.16, a realistic functional form contains a high number of extra parameters. For the TK model 12 parameters would have to be fit from the tissue concentration curve in each voxel, which is practically infeasible. Very recently, a number of authors therefore developped method for blind estimation of the AIF based on clustering of the tissue concentration

[14] in the next section it is explained how the temporal resolution depends on the tissue concentration curves

curves [150–152]. In the method of Fluckiger et al. for instance, the average curve in a cluster of tissue concentration curves is fitted to an initial estimate of the AIF, i.e. an initial estimate for the parameters in the functional form. With the resulting kinetic parameter estimates held fixed, the best possible parameters of the functional form are then estimated and compared to the initital estimate. This procedure is repeated untill it converges [150]. Just as for population averaged AIF determination, these methods have the advantage that no protocol requirement have to be met for AIF measurement. In addition, decreased biases and uncertainties in pharmacokinetic estimates were shown when compared to a population averaged AIF strategy [152]. Similar to the multiple tissue RR-method, these AIF determination strategies are recently developped and require additional investigation.

## 3.5 Limitations and challenges

### 3.5.1 Accuracy

As explained above, the errors in the AIF are a first source of bias in the pharmacokinetic parameters [24, 27, 143]. The MR-related errors, such as $B_1$-inhomogeneity, incomplete spoiling, flip angle deviation from its nominal value, errors in $T_{10}$, etc. cause errors in the calculated concentration curve, that on their turn induce bias in the pharmacokinetic parameters. Schabel & Parker have investigated the accuracy of concentration measurement in SPGRE-pulse sequences in the presence of these errors [30], while Di Giovanni et al. investigated the influence of these errors on the TK model parameters accuracy. In the presence of realistic $B_1$-field inhomogeneity at 3T in a breast coil, they found errors up to 66% in $K^{trans}$ and 74% in $\nu_e$. $T_{10}$-errors caused by incomplete spoiling or $B_1$-field inhomogeneity in the multiple flip angle method (see chapter 2), induce $K^{trans}$- and $\nu_e$-bias up to 531% and 233% respectively. This shows the importance of reducing the MR-related errors by the correction methods mentioned in chapter 2.

The temporal resolution of the DCE-MRI measurement has an important influence on the accuracy of the pharmacokinetic estimates. Lopata et al. showed that the TK and ETK-model are low-pass filters, with a cut-off frequency of $k_{ep} = K^{trans}/\nu_e$ [23]. To avoid nyquist induced bias, the sampling frequency should be twice the highest $k_{ep}$ in the tissue of interest. In the above cited study, Di Giovanni and coworkers found a systematically increasing bias from 0% to 48% in $K^{trans}$, when the temporal resolution of the DCE-MRI protocol is reduced from 10s to 70s. $\nu_e$ is not significanlty influenced. Similar results were found by Henderson et al. [29]. However, when the AIF is measured individually, a correct identification of the AIF peak will be the decisive factor for the temporal resolution [27, 29] as explained

in the previous section. For the AATH model, Kershaw & Cheng advice 1.5s as minimal temporal resolution to keep bias in all AATH-parameter beneath 5%. If bias in the mean transit time may exceed 10%, a temporal resolution of 6s may be used [24]. This effect is mainly attributed to the instable and inaccurate fitting procedure that are currently available for the AATH model [26]. In chapter 7, we introduce a new stable and fast fitting procedure, that may weaken the necessary temporal resolution demands.

### 3.5.2 Precision & reproducibility

Galbraith et al. investigated the reproducibility of pharmacokinetic modeling by performing paired examinations in a group of 21 patients with different tumor types. They concluded that for a single patient, $K^{trans}$-changes of -45% or +83% could be considered as statistically significant [66]. Padhani et al. found similar results in a group of 19 patients with prostate cancer [140]. These studies suggest a low reproducibility for kinetic modeling. As explained in chapter 1, a number of studies have investigated the influence of the temporal resolution [23, 26], leading to a range of practical recommendations (1.5s-15s). Obviously the concentration noise level was shown to correlate with the uncertainty on the pharmacokinetic estimates [23]. Recently Schabel & Parker showed that this concentration noise level not only depends on the SNR of the DCE-MRI measurement but also on the pulse sequence settings [30]. In chapter 2, the trade-offs in DCE-MRI were discussed. It was shown that, when spatial resolution and spatial coverage are fixed, reducing temporal resolution unevitably reduces the SNR or requires a change in repetition time. This link between temporal resolution and concentration noise has not been investigated to our knowledge, and will be discussed in chapter 8. The flip angle, however, can be changed without compromising SNR or temporal resolution. For SPGRE pulse sequences, Schabel & Parker showed the existence of a flip angle minimizing the concentration noise for a single concentration, but they did not assess the influence on the pharmacokinetic parameter precision [30]. All these examples show again the lack of standardized and thoroughly investigated DCE-MRI protocols and the absence of a framework to evaluate the influence of the trade-off within DCE-MRI. In addition, no statistical framework exists to construct accurate confidence intervals for the pharmacokinetic parameters. Galbraith et al. proposed experimentally-derived reproducibility statistics to evaluate statistical significance of kinetic parameter changes, but these are only useful if standardized protocols are introduced and evaluated [66]. Kershaw et al. used bootstrap error analysis to assess the precision of the pharmacokinetic estimates [113]. Orton investigated confidence intervals constructed from least-square analysis, and found these to be inaccurate and overconfident [35]. Therefore, a standardized post-processing technique is necessary as well [19,21,37], in particular for evaluating pre- and post- therapy kinetic parameter changes.

### 3.5.3 Validation and model selection

Due to the lack of a golden standard for pharmacokinetic parameter measurement, it remains difficult to assess the true physiological significance of the estimated parameters. As explained in chapter 1, a number of authors have found correlations between the pharmacokinetic estimates and invasive histological markers for angiogenesis, as microvessel density or VEGF-expression [10, 21, 32, 38], while others could not establish a significant association [10, 21, 32, 153]. Another validation strategy consists of the comparing pharmacokinetic estimates obtained from different imaging modalities, to assess the degree to which the reported parameter values are dependent on the physiology and not on the imaging technique. Naish et al. compared pharmacokinetic parameters from modeling DCE-MRI- and DCE-CT data with the ETK model. They found that $K^{trans}$ is a robust parameter with excellent agreement between DCE-MRI and DCE-CT analysis. $\nu_p$ is significantly higher for DCE-CT, while only low values of $\nu_e$ showed reasonable agreement [154]. Results from a similar study by Kierkels et al. confirm these findings [40]. The discrepancies may be due to different protocol design or imaging artefacts in the DCE-CT and DCE-MRI, which emphasizes again the need for standardized measurement protocols and post-processing techniques, in order to enable fair comparison between imaging modalities.

The discrepancies may also be attributed to the failure of the compartmental models to describe the kinetics of the CA adequately. Buckley investigated the agreement between the pharmacokinetic parameter of the TK-, the ETK- and the AATH model on the one hand and input parameter of a realistic distributed patway model for tracer kinetics on the other hand [18]. He found that the TK-model and ETK-model systematically overestimate $K^{trans}$, while the ETK model underestimates $\nu_p$. The AATH-parameters show the highest degree of agreement with the input parameter, but $\nu_p$ remains underestimated. This study confirms the general thesis that higher-order models describe the true physiological processes better. The cost, however, is that a higher data quality is required for the AATH model [24]. In addition the estimation of a high number of parameters renders the AATH-model fitting unstable and the uncertainties on the AATH parameters are increased [21, 22, 24, 26]. It is a general rule in curve fitting, that a higher number of parameters in the model reduces the minimal sum-of squares (better model fit), but may enhance the uncertainties on the estimated parameters. Recently, Naish et al. compared the ETK model and the AATH model for lung tumor DCE-MRI, with Akaike's information criterion. They found that in most cases the AATH model is the best description [155]. Nevertheless, no guidelines are available in literature for model selection.

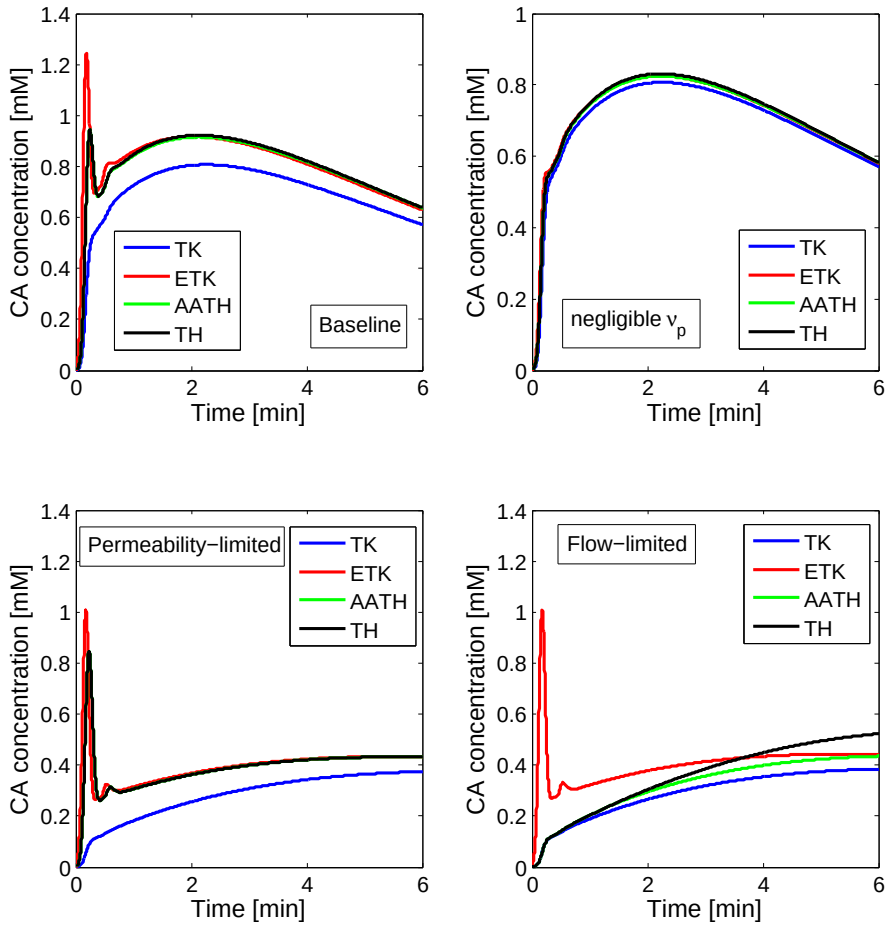


**Figure 3.4:** A: model curves for the TH-model, AATH-model, ETK-model and TK-model for a parameter set representative of a breast tumor (($F_p = 0.57min^{-1}$, $PS = 0.33min^{-1}$, $\nu_p = 0.06$, $\nu_e = 0.45$, Parker AIF). B-D similar curves with only one pharmacokinetic parameter changed (B: $\nu_p$=0.01, C: $PS = 0.05\ min^{-1}$, D: $F_p = 0.05\ min^{-1}$.

With a very straightforward example, the importance of model selection can be made clear. In fig. 3.4A, the tissue concentration curves (Parker AIF) have been simulated with the tissue homogeneity model (black), the AATH model (green), the ETK model (red) and the TK model (blue), for a set of pharmacokinetic parameters representative of a breast tumor ($F_p = \ 0.57 min^{-1}$, $PS = 0.33\ min^{-1}$, $\nu_p = 0.06$, $\nu_e = 0.45$ [18]. It may be assumed that the TH-model is the best description of the true physiology. For this baseline breast tumor case, the AATH model is a very good approximation of the TH-model and will yield accurate pharmacokinetic estimates. The TK- and ETK-model however significantly differ from the TH-model curve and it may be noticed that overestimation of $K^{trans}$ and underestimation of $\nu_p$ will occur, as predicted by [18]. In fig. B, $\nu_p$ was reduced to 0.01, while all other parameters were kept constant to simulate a tissue in which the plasma fraction is negligible. Now all curve approximately coincide. In such cases, use of the AATH- or ETK-model unnecessarily reduces the precision of $K^{trans}$ and $\nu_e$[15], without improving their physiological accuracy. The TK-model is recommended to use when plasma fraction is negligible. In fig. C a permeability-limited case is shown (PS= 0.05 $min^{-1}$, other parameters remain constant). When $PS << F_p$, TK-model parameters are highly inaccurate and underestimation of $K^{trans}$ occurs. The ETK or AATH model have to be used instead. Fig. 3.4 D plots the corresponding flow-limited case ($F_p = 0.05\ min^{-1}$, other parameters remain constant). ETK-parameters are strongly biased, and the validity of the AATH-model is reduced. Although it may seem that the AATH-model remains the best description, the flow-limited case is equivalent to an extraction fraction close to one (eq. 3.9). In such case of low flow and high permeability, the AATH model fitting was shown to be unstable, and resulted in PS-overestimation up to 152% [18, 24]. The TK-model should be used instead for acceptable pharmacokinetic parameter reproducibility and stability of the fitting procedure. Remark that in both the permeability and flow-limited case $K^{trans} = 0.05\ min^{-1}$.

## 3.6 Conclusion

The 2-, 3- and 4-parameter models, that are currently used in DCE-MRI literature, can all be derived from the TH-model, by making subsequent assumptions about the tumor physiology. The TK-model and the ETK-model have shown their applicability both in tumor research or for other pathologies that affect the microvascular network of the host tissue. The AATH model is lesser used because of the mathematical complications in the fitting procedure. Generally, a higher order model requires increased data quality. Nevertheless no consensus exists in literature about the necessary protocol design for the dif-

[15] For now, we can only assume this based on the general rule in fitting, that an increased number of model parameters gives better model fits but worse parameter precision. However in chapter 8 this statement is proven and quantified

ferent pharmacokinetic models. Optimal protocol design is dependent upon the AIF determination strategy as well. In addition, no standardized post-processing techniques are avalaible, to characterize for instance the precision of the pharmacokinetic estimation. This prevents the intercomparison of results from different scanning sites and raises questions about the statistical significance of pre- and post- treatment kinetic parameter changes. Finally, no clear recommendations exists for model selection. Parameters from higher order models have been shown to be better reflections of their true physiological counterparts, but typically exhibit higher parameter uncertainties. By means of a simple example, this trade-off between physiological significance and parameter reproducibility is enlighted:

- small $\nu_p$: TK model
- Permeability-limited: AATH or ETK-model
- Flow-limited: TK-model
- intermediate case: preferentially AATH model, also ETK-model

# Chapter 4

# Accuracy and Precision of Contrast Agent Concentration

## 4.1 Introduction

In this chapter the conversion of MR-signal intensity to contrast agent (CA) concentration is enlightened and the accuracy and the precision of the resulting concentration values are discussed. As explained in chapter 2, the majority of the quantitative DCE-MRI studies employs spoiled gradient echo pulse sequences (SPGRE) for the monitoring of CA concentration, for their ability to combine good spatial and temporal resulution with acceptable signal-to-noise ratio (SNR) [42]. Therefore this chapter is devoted to the conversion methods for SPGRE-pulse sequences only. Throughout this chapter, 4 SPGRE pulse sequence designs from literature, with a wide range in SPGRE-parameters and using 3 different CA's, are used as examples to illustrate the main results. Details from these study design are mentioned in table 4.1.

The rationale of this chapter is found in the interaction mechanisms between the tissue and the CA. Firstly, in contrast to nuclear medicine or CT tracer methodologies, contrast enhanced MRI does not measure the signal directly from the tracer itself, but rather the effect of the CA on the local relaxation times. Secondly, the presence of the CA causes a change in both the longitudinal and transverse relaxation times, which affect the signal intensity in a different and non-linear manner. Therefore the signal intensity is not linearly related to the amount of tracer in the tissue and non-linear conversion methods are necessary. For SPGRE-pulse sequences several conversion methods exist in literature, which are all based on the relative signal enhancement, a concept

explained in section 4.2. The most early studies dealing with pharmacokinetic modeling of DCE-MRI data, assumed a linear relationship between the signal enhancement and the CA concentration [16, 47, 88]. Obviously, this method was shown to cause severe errors in the pharmacokinetic parameters [33]. Currently, many authors employ a non-linear method for signal conversion, based on the assumption that the change of the transverse relaxation rates should not be taken into account for physiological CA concentrations. This assumption is based on the the fact that for pharmacokinetic modeling, pulse sequences are designed to be $T_1$-weighted ($T_E << T_2^*$) [18, 19, 90, 107]. This implies that the $T_1$-induced signal intensity change, caused by the presence of the CA, predominates the similar $T_2^*$-induced signal intensity change. The advantage of this approach is that an analytical solution exists, linking a measured signal intensity to a single concentration. Although the assumption of negligible $T_2^*$-relaxation proves to be valid for the typical CA concentrations found in tumour tissue, it is shown to break down at the high arterial concentration that have to be measured for the monitoring of the arterial input function (AIF). The most accurate method involves a numerical solution of the SPGRE equations, accounting for both $T_1$- and $T_2^*$-relaxation caused by the CA. However, due to its mathematical complexity it is hardly used in clinical practice [49]. In this chapter, a fourth and new conversion method is proposed, relying on a first order approximation of the $T_2^*$-relaxation. This method yields an analytical relationship between signal enhancement and CA concentration as well and is therefore easy to perform in any clinical setting. However, when comparing the accuracy of the different conversion methods both in vivo and by simulations, this first-order method is found to reduce CA concentration error severely, in particular for arterial concentrations. These conversion methods are explained in section 4.3 and their accuracy is compared in section 4.4.

Another important consequence of the non-linear relationship between signal intensity and CA concentration, concerns the concentration precision. For DCE-MRI studies, MR signal intensity is assumed to be gaussian distributed [156]. The noise variance of this distribution is constant and therefore independent of the CA concentration [157]. However, when this signal intensity is converted to a CA concentration by a non-linear conversion method, the concentration precision varies with CA concentration itself. As a result, the uncertainty on specific CA concentration is unacceptably high, even at high signal-to-noise ratio in the dynamic MR imaging. The understanding of the concentration distribution and in particular the knowledge of the concentration uncertainty is of crucial importance for a well-considered design of the DCE-MRI experiment (see chapter 5). In addition this distribution has to be taken into account when fitting the concentration data to the pharmacokinetic models and it highly affects the confidence intervals of the pharmacokinetic parameters (see chapter 6). Therefore in section 4.5, the concentration distribution is derived and validated in vitro.

**Table 4.1:** SPGRE pulse sequence parameters and contrast agents for the DCE-MRI studies of Parker et al. (PS1) [139], Hodgson et al. (PS2) [90], Jackson et al. (PS3) [107] and Padhani et al. (PS4) [19].

| Studie name | $T_R$ [ms] | $T_E$ [ms] | FA [°] | Contrast agent | $C_{max}$ [mM] |
|---|---|---|---|---|---|
| PS1 | 4 | 0.82 | 20 | Gd-DTPA-BMA | 22.4 |
| PS2 | 4.5 | 2 | 30 | Gd-DOTA | 19.9 |
| PS3 | 7 | 1.1 | 35 | Gd-DTPA-BMA | 24.5 |
| PS4 | 35 | 5 | 70 | Gd-DTPA | 11.5 |

## 4.2 Relative signal enhancement and maximal measurable concentration

The relationship between CA concentration C and MR signal intensity, S, for SPGRE-pulse sequences is given by eq. 4.1 and eq. 4.2. $R_1$ and $R_2^*$ are the longitudinal and transverse relaxation rates respectively, the inverse of the $T_1$ and $T_2^*$ relaxation times. $r_1$ and $r_2$ are the relaxivity coefficients, $\alpha$ is the flip angle, $T_R$ and $T_E$ are the pulse sequence repetition and echo times respectively. $M_0$ is scaling factor comprising both equilibrium magnetization and system gain. $R_{10}$ and $R_{20}^*$ are the native relaxation rates of the tissue of interest. $R_{10}$ is assumed to be known from a series of pre-contrast scans (see chapter 2).

$$\begin{cases} S(R_1, R_2^*) = M_0 sin(\alpha) \frac{1-E_1}{1-cos(\alpha)E_1} E_2^* \\ E_1 = exp(-T_R R_1) \\ E_2^* = exp(-T_E R_2^*) \end{cases} \tag{4.1}$$

$$\begin{cases} R_1 = R_{10} + r_1 C \\ R_2^* = R_{20}^* + r_2 C \end{cases} \tag{4.2}$$

All conversion methods employ the relationship between the CA concentration and the relative signal enhancement $\Xi$:

$$\Xi = \frac{S - S_0}{S_0} \tag{4.3}$$

$$= \frac{(E_1(C) - 1)(E_{10} cos(FA) - 1)}{(E_{10} - 1)(E_1(C) cos(FA) - 1)} E_2'(C) - 1 \tag{4.4}$$

$$E_2'(C) = \frac{E_2}{E_{20}} = exp(-T_E r_2 C) \tag{4.5}$$

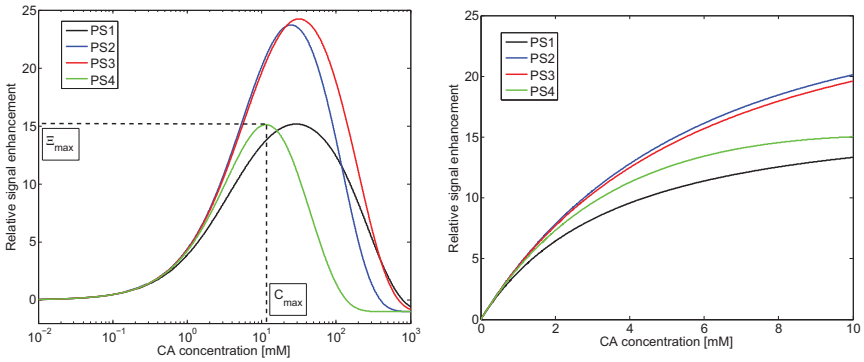


**Figure 4.1:** Relative signal enhancement versus Gd-DTPA-concentration ($r_1 = 4.1$ $s^{-1}mM^{-1}$, $r_2 = 4.6$ $s^{-1}mM^{-1}$) for 4 SPGRE pulse sequences (table 4.1) in blood ($T_{10}$= 1250 ms). Left a broad concentration range is depicted on a logarithmic scale, right the signal enhancement in a physiologically relevant range is enlarged. For PS4 the maximal enhancement and the maximal measurable concentration are illustrated.

By using Ξ, eq. 4.5 shows that the knowledge of $M_0$ or $R_{20}^*$ is irrelevant for the calculation of the CA concentration. Both parameters are gathered in the pre-contrast signal intensity $S_0$, making their separate estimation unnecessary.

Fig. 4.1 shows the variation of Ξ with the CA concentration for the four pulse sequences from table 4.1. Ξ is confined within -1, at the high concentration limit, and $\Xi_{max}$ at $C_{max}$ (designated for PS4). For Ξ-values between 0 and $\Xi_{max}$, eq. 4.4 has two possible solutions, one above $C_{max}$ and one below $C_{max}$. This suggests that whenever the concentration can rise above $C_{max}$, CA concentration can no longer be determined unambiguously. Therefore $C_{max}$ is designated the maximal measurable concentration and it puts an upperbound on the allowed concentration range in a quantitative DCE-MRI study. $C_{max}$ can be interpreted in terms of signal weighting as well: for concentrations beneath $C_{max}$, the MR-signal is $T_1$-weighted. In this concentration range, the $T_1$-induced signal intensity increase prevails the $T_2^*$-induced decrease and the signal intensity rises with increasing concentration. For concentrations above $C_{max}$, the $T_1$-induced signal increase becomes predominated by the $T_2^*$-induced signal distortion and the signal intensity decreases with increasing concentration. The MR-signal is $T_2^*$-weighted.

The knowledge of the maximal measurable concentration in quantitative DCE-MRI studies is highly significant. Not only is it required for the selection of one of the two possible solutions of the numerical method, it is of crucial importance for the evaluation of the accuracy (section 4.4) and the precision

(section 4.5) of the measured concentrations as well. In addition, in chapter 5, its knowledge is shown to be indispensable for flip angle optimization in DCE-MRI studies. The concept of a maximal measurable concentration for SPGRE-pulse sequences was initially proposed by Schabel & Parker [30]. For clinical practice however, their analysis is somewhat complicated[1] and an easy-to-perform determination method should be available. The exact values of $C_{max}$ and $\Xi_{max}$ depend on the pulse sequence settings, as can be seen from fig. 4.1, but also on the CA relaxivity coefficients and, at least theoretically, on the tissues native relaxation rate $R_{10}$. As $C_{max}$ corresponds with the maximum of the $\Xi$-curve, it can be derived by equating the signal derivative with respect to the concentration to zero. This signal derivative can be calculated as:

$$\begin{aligned}\frac{dS}{dC} &= \frac{\partial S}{\partial R_1}\frac{\partial R_1}{\partial C} + \frac{\partial S}{\partial R_2^*}\frac{\partial R_2^*}{\partial C} \\ &= M_0 T_R r_1 E_2^* \left[\frac{E_1 sin(FA)(1-cos(FA))}{(1-cos(FA)E_1)^2} - \gamma\frac{sin(FA)(1-E_1)}{(1-cos(FA)E_1)}\right] \qquad (4.6)\end{aligned}$$

$$\gamma = \frac{r_2^* T_E}{r_1 T_R} \qquad (4.7)$$

From eq. 5.11 it is clear that $C_{max}$ corresponds with $E_{1mm}$, the minimal value of $E_1$ that can be measured unambiguously:

$$E_{1mm} = exp(-T_R R_{1mm}) \qquad (4.8)$$

$$R_{1mm} = R_{10} + r_1 C_{max} \qquad (4.9)$$

$E_{1mm}$ depends solely on the flip angle and the parameter $\gamma$:

$$E_{1mm} = \frac{\gamma(1+cos(\alpha)) + (1-cos(\alpha)) - \sqrt{(1+\gamma^2)(1-cos(\alpha))^2 + 2\gamma sin(\alpha)^2}}{2\gamma cos(\alpha)} \qquad (4.10)$$

This enables a contour plot presentation of $T_R R_{1mm} = -ln(E_{1mm})$, from which for every SPGRE-pulse sequence design and with the knowledge of the CA characteristics, the maximal measurable $R_1$ can be read off (fig. 4.2). $C_{max}$ can be calculated from eq. 4.9, given the native $R_1$ of the tissue of interest. For every pulse sequence under consideration, table 4.1 contains the $C_{max}$-values for their respective CA's in tumour tissue. Figure 4.3 shows the influence of the native longitudinal relaxation rate on the maximal measurable concentration. It is clear that in view of the large $R_{1mm}$-values in comparison with the physiological $R_{10}$-values, this native relaxation rate will not significantly affect the maximal measurable concentration. The influence of the repetition time on $C_{max}$ is difficult to asses from eq. 4.9 or fig. 4.2.

[1] Schabel & Parker assume a general relationship between CA concentration and relaxation rates, instead of a linear relationship as in eq. 4.2.

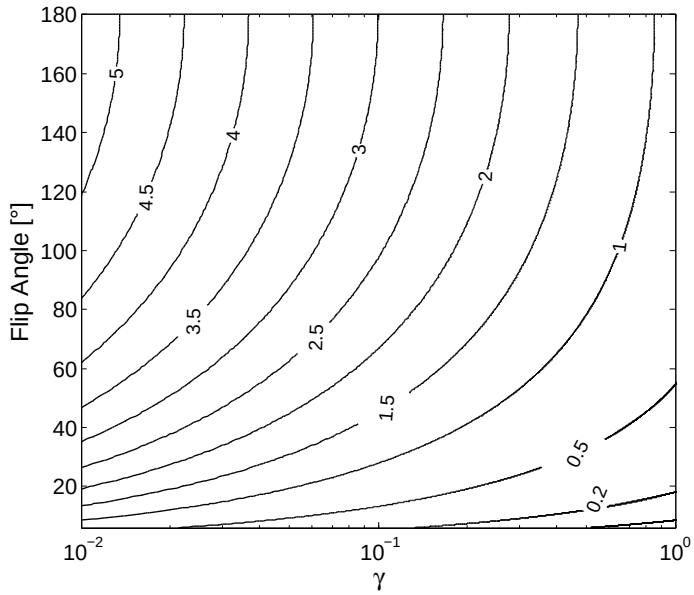


**Figure 4.2:** Contour plot of $R_{1mm}T_R$ as a function of the flip angle FA and the dimensionless variable $\gamma = \frac{r_2 T_E}{r_1 T_R}$. $R_{1mm}$ is the maximum measurable longitudinal relaxivity rate and can be used for determining the maximum measurable contrast agent concentration $C_{max}$.

From fig. 4.3b, plotting $C_{max}$ versus $T_R$ for the three pulse sequence in table 4.1, it can be seen that increasing $T_R$ decreases the maximal measurable concentration. Furthermore, both smaller $T_E$ and larger flip angles enlarge the maximal measurable concentration range.

## 4.3 Contrast agent determination methods for SPGRE-pulse sequences

In this section an overview is given of the conversion methods currently employed in DCE-MRI literature to calculate the CA concentration from the SPGRE signal intensity. The problem statement is as follows: given the pre-contrast signal intensity $S_0$ and the pre-contrast relaxation rates $R_{10}$ pixelwise, and with the knowledge of the CA characteristics $r_1$ and $r_2$ and the pulse sequence settings $T_R$, $T_E$ and $\alpha$, how can the CA concentration be determined from the measured relative signal enhancement, by using eq. 4.4.

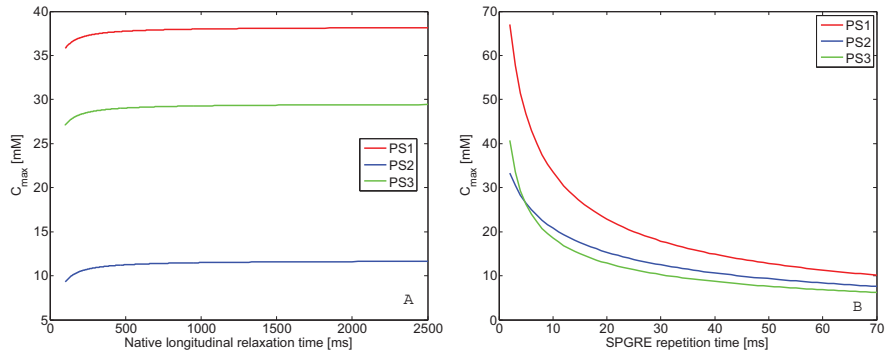


**Figure 4.3:** A. Variation of the maximal measurable Gd-DTPA concentration ($r_1$ = 4.1 $s^{-1}mM^{-1}$, $r_2$ = 4.6 $s^{-1}mM^{-1}$) versus the native longitudinal relaxation time for three SPGRE pulse sequences (table 4.1). B. Variation of the maximal measurable Gd-DTPA concentration versus SPGRE repetition time for the three pulse sequences.

### 4.3.1 Numerical method

The most accurate method for the conversion of signal intensity to CA concentration is the numerical conversion method. The method relies on finding a numerical solution $C_{num}$ of eq. 4.4. As explained in the previous section, two analytical solutions exist for this equation, one above and one below $C_{max}$. Therefore, the initial value for the numerical solver should be well-considered and it should be checked whether $C_{num}$ does not exceed $C_{max}$. To our knowledge, however, this method is solely used in a recent DCE-MRI study [49].

### 4.3.2 Method neglecting $T_2^*$-relaxation

In clinical practice, it is preferred to have a one-on-one relationship between the relative signal enhancement and the CA concentration. Such a closed-form solution of eq. 4.4 can be obtained by assuming that the $T_2^*$-relaxation of the SPGRE signal intensity, caused by the presence of the CA, can be neglected. In this case $E_2 \approx E_{20}$ and eq. 4.4 can be solved analytically to yield an approximated solution $C_{app}$ for the CA concentration:

$$C_{app} = \frac{1}{r_1 T_R} log\left[E_{10}\frac{1 + cos(\alpha)(\Xi(E_{10} - 1) - 1)}{\Xi(E_{10} - 1) + E_{10}(1 - cos(\alpha))}\right] \tag{4.11}$$

This method was proposed by Zhu et al. [64] and it is used in a majority of the quantitative DCE-MRI studies [18, 19, 90, 107, 158].

### 4.3.3 First order correction for $T_2^*$-relaxation

This section describes the work presented in [34]. Although the $T_2^*$-neglecting conversion method is easy in use and widespread accepted in the DCE-MRI community, it breaks down at the high arterial concentrations that have to be measured for the monitoring of the AIF ( [34], section 4.4). At these concentration values, the assumption that $E_2^* \approx E_{20}^*$ is no longer valid, and $C_{app}$ severely underestimates the true CA concentration. Therefore in this section, a new closed-from approximated solution of eq. 4.4 is derived, that accounts for a first order approximation of $T_2^*$-relaxation. To do so, a variable $\Phi$ is defined, that can be calculated from the measured signal enhancement:

$$\Phi = \frac{(1+\Xi)(E_{10}-1)}{E_{10}cos(FA)-1} \tag{4.12}$$

$$\tag{4.13}$$

Eq. 4.4 can now be rewritten:

$$\Phi = \frac{E_1 - 1}{E_1 cos(FA) - 1} E_2' \tag{4.14}$$

Solving this equation for $E_1$ and taking the natural logarithm yields:

$$T_R r_1 C = log(E_{10}) + log\left[\frac{cos(FA)\Phi - E_2'}{\Phi - E_2'}\right] \tag{4.15}$$

To account for $T_2^*$-relaxation, the right hand term in eq. 4.15 is approximated by a first order taylor expansion around $T_E r_2 C = 0$, which agrees with the assumption that $E_2^* \approx E_{20}^*$. This yields the final first order solution for the CA concentration $C_{fo}$:

$$C_{fo} = \frac{\kappa_1}{r_1 T_R - r_2 T_E \kappa_2} \tag{4.16}$$

$$\kappa_1 = log\left[E_{10}\frac{cos(FA)\Phi - 1}{\Phi - 1}\right] \tag{4.17}$$

$$\kappa_2 = \frac{1}{cos(FA)\Phi - 1} - \frac{1}{\Phi - 1} \tag{4.18}$$

When $T_E = 0$ or $r_2 = 0$, $C_{fo}$ is identical to $C_{app}$. In comparison with the $T_2^*$-neglecting method, our method thus requires the calculation of one extra parameter $\kappa_2$ and the knowledge of $T_E$ and $r_2$ for determining the CA concentration [34].

### 4.3.4 Method assuming signal linearity

Several early studies, concerning pharmacokinetic modeling of SPGRE-measured concentration data use a linear relationship between relative signal

enhancement and the CA concentration. The validity of the method is constrained to concentrations for which $T_R r_1 C << 1$ and $T_E r_2 C << 1$ in tissues where $T_R << T_{10}$. Under these circumstances the exponentials in eq. 4.4 can be linearly approximated to yield the linear approximation for the CA concentration:

$$C_{lin} = \frac{1}{T_{10} r_1} \Xi \tag{4.19}$$

The validity of this conversion method can be seen on the right panel of fig. 4.1. For small concentrations (< 1mM) the relative signal enhancement appears to be independent of the pulse sequence settings and proportional to the CA concentration. For higher concentrations, however, the accuracy of this methods drops swiftly and $C_{lin}$ is seen to underestimate the true concentration values severely. This is confirmed by the study of Heilmann et al., who found errors up to 60% in the pharmacokinetic parameters when using a linear conversion method [33]. Therefore, this method will not be further investigated in the rest of this chapter.

## 4.4 Contrast agent accuracy

In this section the accuracy of the approximated conversion methods, $C_{app}$ and $C_{fo}$, are investigated theoretically by means of simulations. Remark that we have only investigated the inaccuracies caused by the conversion methods. For inaccuracies in the CA concentration caused by the MR-related errors as mentioned in section 2.7, we refer to [30]. A small in vivo study measuring the AIF in mice, was performed and the results of these approximated methods are compared with the results of the numerical method.

### 4.4.1 Simulations

A simulation program was written in Matlab (Mathworks, Ma) to compare the performance of the $C_{app}$- and $C_{fo}$-expressions[2], in both blood and tumor tissue, for the 4 DCE-MRI studies from table 4.1. In blood, the simulations were performed for a typical arterial concentration range, 0-10 mM of the concerned Gd-chelates. In tumor tissue, a concentration range up to 2 mM is sufficient [19, 90, 107, 139]. For blood a $T_{10}$-value of 1250ms is assumed [44], while for tumor tissue $T_{10}$ is set to 675 ms [45]. For both conversion equations, the knowledge of $T_{20}^*$ or $M_0$ is abundant. Appropriate $r_1$- and $r_2$-values in both tissues are selected from literature ( [44], or table 2.2). For every concentration within the concerned ranges, the SPGRE signal intensity is computed. Contrast agent concentration is recalculated

[2]In simulations, $C_{num}$ would automatically equal the simulation input value

from the relative signal enhancement with eq. 4.11 or with eq. 4.16 respectively.

Fig. 4.4 shows the procentual underestimation of the CA concentration by the $C_{app}$- (dotted lines) and $C_{fo}$ expressions (full lines) for the 4 pulse sequences under consideration. The peak concentrations in blood are severely underestimated by $C_{app}$. For an actual concentration of 10mM, the true concentration is underestimated ranging from 17.5% for PS1 up to 43% for PS4, showing that of the neglection of $T_2^*$-relaxation is no longer valid at these high concentrations. $C_{fo}$ reduces the concentration error over the complete range. For concentration beneath 5mM, $C_{fo}$ differs less than 1% of the true concentration for PS1-PS3, while for PS4 the error is reduced with a factor ten. For 10mM, error is decreased up to 6-fold for PS1, while for PS4 our method renders inaccurate as well at high concentrations. In tumor tissue, the error reduction by using the $C_{fo}$-expression is comparable, but the errors associated with $C_{app}$ are much smaller. $C_{fo}$ can be considered as identical to the numerical method for concentration calculation in tumor tissue, while neglecting $T_2^*$-relaxation causes concentration errors ranging from 1% for PS1 to 6% for PS4.

From fig. 4.4 it is clear that the concentration range, in which a conversion method preserves an acceptable accuracy, depends strongly on the pulse sequence parameters. Therefore, in fig. 4.5 the errors associated with $C_{app}$ (dotted lines) and $C_{fo}$ (full lines) are plotted against the concentration relative to the maximal measurable concentration $C_{max}$ ($T_{10}$=1250 ms). Values of $C_{max}$ are mentioned in table 4.1. The two sets of lines for the 4 pulse sequences under investigation nearly coincide. This observation indicates that for the evaluation of the accuracy of the conversion methods, a procentual concentration value relative to $C_{max}$ rather than an absolute concentration boundary has to be used. Our method remains 5% accurate for concentrations up to 45%-50% of $C_{max}$. Afterwards the accuracy drops swiftly and $C_{max}$ is underestimated up to 35%. As $C_{max}$ for PS4 equals 11.5mM, this explains why our method fails above 6mM in blood (fig. 4.4). For the $T_2^*$-neglection method, errors of 5% already occur at 14-17.5% of $C_{max}$. To investigate the influence of the choice of $T_{10}$ on these boundary values for accurate concentration conversion, we have simulated similar curves as in fig. 4.5 for $T_{10}$ = 200 ms and $T_{10}$ = 675 ms. As no significant shift in the curves could be seen, these results are not shown in the figures. Nevertheless they indicate that the relative boundary values obtained above are independent of $T_{10}$.

### 4.4.2 in vivo AIF measurement

The approximated conversion methods $C_{app}$ and $C_{fo}$ were compared with the numerical conversion method in vivo, by measuring the arterial input function in 2 nude mice (athymic nu/nu, Harlan, The Netherlands). Before MR examination, both animals were sedated with an intraperitoneal injection

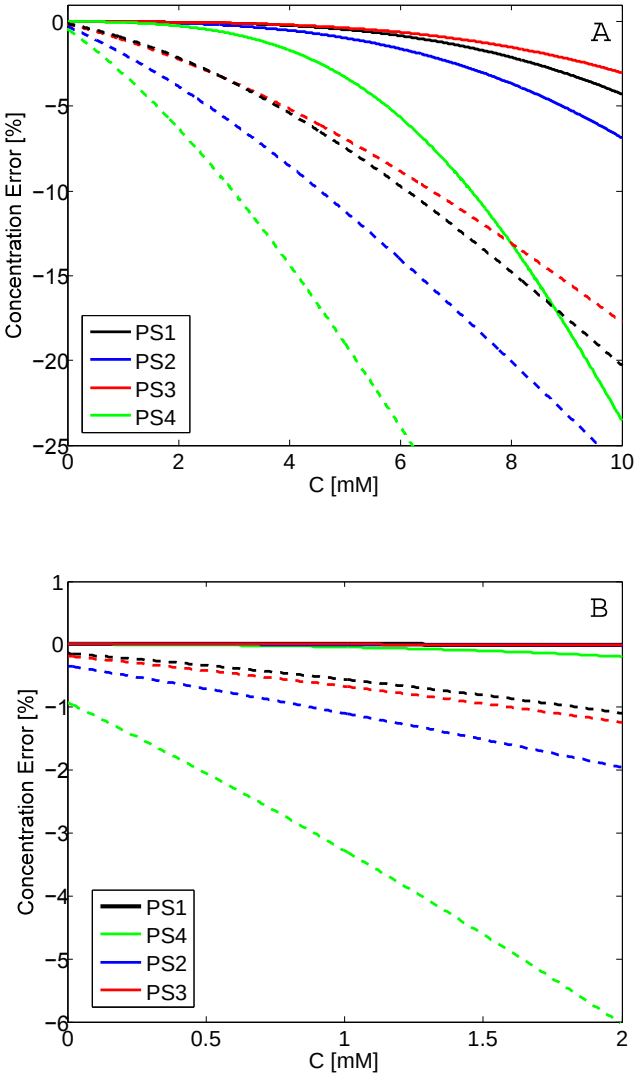


**Figure 4.4:** Procentual error in contrast agent concentration when calculated with a $T_2^*$-relaxation neglecting method (eq. 4.11, dotted lines) or with a method comprising a first order correction for $T_2^*$-effects (eq. 4.16, full lines) for 4 different pulse sequences. Pulse sequences details can be found in table 4.1. A. for typical CA concentrations in arterial blood. B. for typical CA concentrations in tumor tissue.

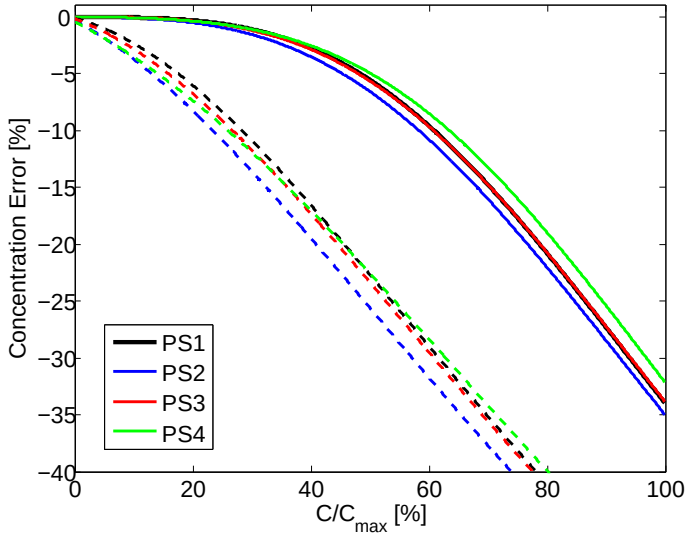


**Figure 4.5:** Procentual concentration error versus concentration relative to maximal measurable concentration, for the $T_2^*$-relaxation neglecting method (eq. 4.11, dotted lines) and the conversion method comprising a first order correction for $T_2^*$-relaxation (eq. 4.16, full lines). Pulse sequence details and $C_{max}$-values are mentioned in table 4.1.

of ketamine/xylazine. Dynamic MR imaging was performed on a Siemens Symphony 1.5T scanner. 3D SPGRE images ($T_R/T_E$ = 6.78/2.78 ms) were acquired with a 384 x 384 x 60 matrix of 0.3 x 0.3 x 2 mm voxels in 9 minutes/dataset. A total of 4 pre-contrast scans was obtained with nominal flip angles of 8°, 12°, 20° and 30° for $T_{10}$ mapping. The dynamic series consisted of 9 scans with a flip angle of 12° at 5, 20, 35, 50, 65, 80, 95, 110 and 120 minutes after the injection of a Gd-DOTA bolus (0.1 mmol/kg, Dotarem, Guerbet, France). Postprocessing is done in Matlab (Mathworks, Natick, Ma). The AIF is extracted manually in the aorta ascendens. Signal intensities from the dynamic series are converted to Gd-DOTA concentrations with eq. 4.4, eq. 4.11 and eq. 4.16 respectively. $S_0$ is obtained from the pre-contrast scan with FA=12°. $T_{10}$ is calculated from the pre-contrast scans [50].

Fig. 4.6 shows the AIF calculated with three conversion methods, for the signal intensity measured in the aorta descendens of two mice. The maximal measurable Gd-DOTA concentration in blood for the associated MR-settings is for both mice 6.6 mM. The measured peak concentrations of 1.7 and 1.9 mM, are underestimated by 12% and 14% respectively with $C_{app}$ and by 0.5% and 0.9% respectively with $C_{fo}$. This is in very good agreement with the results of the simulations: the respective peak concentration are 26% and 29% of $C_{max}$. These values are within the range, predicted from our simulation, in which the $C_{fo}$-expression remains 5% accurate, but outside the similar range for the $C_{app}$-expression. Concentrations beneath 0.5 mM are measured equally accurate with the three conversion methods.

### 4.4.3 Consequences for pharmacokinetic modeling

In this section we have investigated the errors in CA concentration measurement with SPGRE pulse sequences caused by the neglection of $T_2^*$-relaxation, and we have proposed an easy-to-perform method comprising a first order correction for $T_2^*$-effects. Our simulations show that the concentration range for which a given conversion method is accurate, is strongly dependent on the pulse sequence parameters employed in the study. However, when expressing this range as relative to the maximal measurable concentration, this variation largely dissappears, and coarse relative boundaries can be determined, that are valid for any study design. The $T_2^*$-neglecting method, based on the assumption that $E_2^* \approx E_{20}^*$, produces 5% accurate concentration values, for CA concentration up to only 14-17.5% of $C_{max}$. While for most pulse sequences, this range covers the physiological concentrations found in tumor tissue, it does not comprise the typical blood concentrations encountered when measuring the arterial input function. Nevertheless many DCE-MRI studies use the $T_2^*$-neglecting method to convert the signal intensity variation into concentration curves as it yields an analytical solution linking a relative signal enhancement to a single CA concentration [18, 19, 64, 90, 107, 158]. The newly proposed method, comprising a first order correction for $T_2^*$-relaxation,

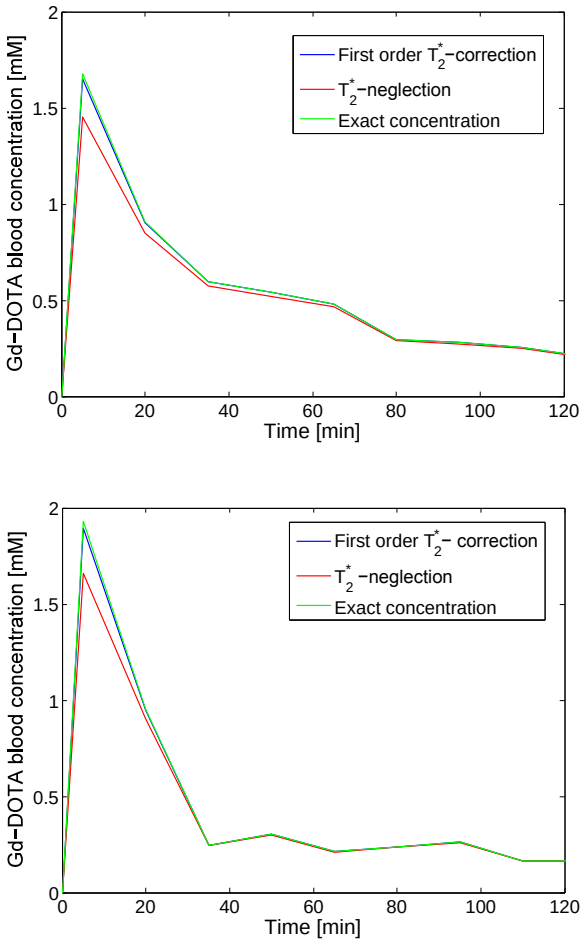


**Figure 4.6:** Gd-DOTA arterial input functions, calculated from the SPGRE signal intensity in the aorta descendens of two mice, with 3 different conversion methods ($T_R/T_E = 6.78/2.78$, FA $= 12°$). The conversion methods are described in the text.

combines the simplicity of the $T_2^*$-neglecting method, with the accuracy of the exact method for CA concentrations up to 45-50% of $C_{max}$. In tumor tissue, our method can be regarded as identical to the numerical conversion method, while for 3 pulse sequences under consideration [90, 107, 139], blood concentrations up to 10mM can be calculated with 5% accuracy. For the pulse sequence of Padhani et al. [19], the 5% accuracy limit is at 5.6 mM as a consequence of the lower $C_{max}$-value. Schabel & Parker recently showed that concentration values above 50% of $C_{max}$ are subject to high uncertainties, i.e. they cannot be precisely determined, even at high signal-to-noise ratios. As a heuristic optimization method for pulse sequence parameters, they advice that the largest concentration to be measured is at most 50% of $C_{max}$, for acceptable concentration uncertainty. In this approach, our first order method can be of great value for improving the accuracy of the concentration calculation, with the same simplicity of the widespread accepted $C_{app}$-method. The only cost of applying the $C_{fo}$-expression is that it requires the knowledge of the echo time $T_E$ and the tranverse relaxation coefficient $r_2$ in the tissue of interest. This $r_2$-value can, however, be found in literature [44] or determined from an in vitro experiment, as it is performed in many studies to determine $r_1$ [30, 107]

The simulation results are confirmed by the results from the in vivo AIF measurement in mice. The measured peak concentrations are respectively 26% and 29% of the corresponding $C_{max}$. Therefore, the $T_2^*$-neglecting method fails with concentration underestimation ranging up to 14%, while our first order approximation yields accurate concentration values when compared with the exact conversion method. Incorrect determination of the AIF, and in particular of the peak concentration, has been acknowlegded as an important error source affecting the accuracy of the kinetic parameters [50, 89, 139, 141]. Cheng et al. found that the relative error in the transendothelial transfer constant $K^{trans}$ is roughly inversely proportional to the relative error in the AIF amplitude [27]. This suggests that a 15% underestimation of the AIF peak, that can result from neglecting $T_2^*$-decay for all pulse sequences under consideration, causes a 15% overestimation of $K^{trans}$. This emphasizes the importance of incorporating $T_2^*$-relaxation for the determination of the AIF, which can easily be done with our first order method.

## 4.5 Contrast agent precision

In this section, the precision of the MR-measured concentration values is investigated. Consider a voxel containing a concentration $C_{real}$. In the previous section, it was shown that the mean concentration, calculated from relative signal enhancement approximately equals $C_{real}$, under the condition that an appropriate conversion method is employed and that the MR-related errors are

minimized. However, as a result of the noise on the MR-signal intensity, an uncertainty is present on the calculated concentrations. In this section an analytical expression is derived for this uncertainty and the type of distribution of the calculated concentration is investigated in an in vitro experiment. This section contains results presented in [25].

### 4.5.1 Theoretical derivation

Consider again the voxel containing a CA concentration $C_{real}$, corresponding with a MR signal intensity $S_{real}$. In practice, the measured MR-signal S arising from that voxel can be described by a gaussian distribution with mean $S_{real}$ and standard deviation $\sigma_S$ [159]:

$$f_S(S \mid S_{real}, \sigma_S) = \frac{1}{\sqrt{2\pi}\sigma_S} e^{-\frac{(S-S_{real})^2}{2\sigma_S^2}} \tag{4.20}$$

The noise standard deviation $\sigma_S$ is a constant for a given pulse sequence design (see section 2.3.3), independent of $S_{real}$ and thus independent of the CA concentration [157]. If the noise in the dynamic series is the only error source under consideration (thus neglecting the noise on the pre-contrast-signal $S_0$) and concentration is calculated from the relative signal enhancement, the standard theory of error propagation predicts the variance of the concentration distribution:

$$\sigma_C^2 = \sigma_S^2 \left[\frac{dC}{dS}\right]^2 \tag{4.21}$$

### 4.5.2 In vitro validation

To test this concentration uncertainty expression (eq. 4.21) and to investigate whether the resulting concentration distribution remains gaussian, in vitro experiments were performed with a dilution series of Gd-DOTA in deionized water at room temperature ($r_1$ and $r_2$ from [44] or table 2.2) in a typical tissue concentration range from 0 to 2 mM on a 1.5T Symphony scanner (Siemens, Germany). 11 vials, approximately 1 cm in diameter and 7 cm in length (0.000, 0.020, 0.050, 0.075, 0.10, 0.20, 0.40, 0.50, 0.75, 1.0, 2.0 mM), were placed in the magnet bore parallel to the main magnetic field to reduce susceptibility-induced image distortion at the air-fluid interface. 3 sets of 50 subsequent images were captured with the in-house IR-SPGRE pulse sequence (see section 2.4.3). Each set had a distinctive inversion time ($T_I$ = 412-560-700 ms, $T_R$=5000 ms, $T_E$=3.42 ms, FA = 12°, imaging matrix 192 x 192, spatial resolution 0.5 mm x 0.5 mm, slice thickness 7.5 mm). Different inversion times were considered since the signal intensity derivative with respect to the concentration of the IR-SPGRE sequence (eq. 2.28) is most sensitive to variations in this parameter. For every image set, $M_0$ and $R_{10}$ were calculated from a fit of the mean measured signal intensities in the vials to the signal

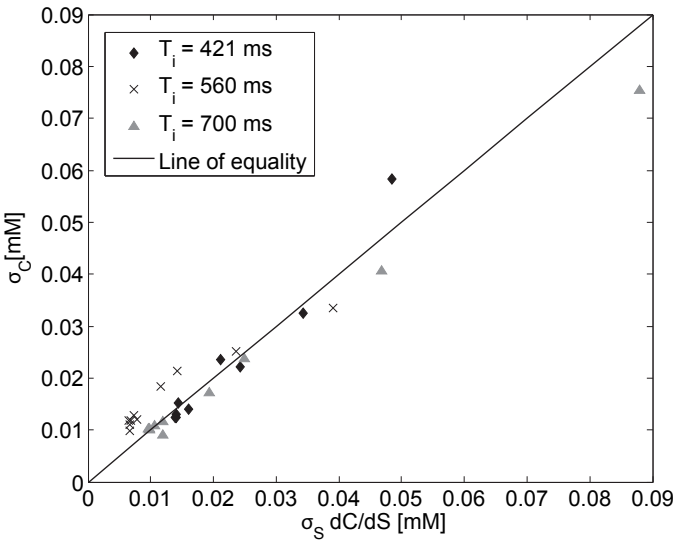


**Figure 4.7:** Experimental concentration uncertainty plotted against uncertainty predicted by eq. 4.21. ($T_R$ = 5000 ms, FA = 12°, $T_E$ = 3.42 ms, $r_1 = 3.5\ mM^{-1}s^{-1}$).

intensity equation. $S_0$ was estimated as the average signal intensity in the water filled vial. With these values the distribution of 200 signal intensities in every vial, stemming from 4 voxels in 50 subsequent images, was transformed into a concentration distribution. Concentration calculation was performed in Matlab, based on the relative signal enhancement, with the numerical method as described above. The chosen voxels were located centrally in the vials to exclude partial volume effect at the boundaries. The resulting concentration distribution of every vial was tested for gaussianity with a Kolmogorov-Smirnov test [160]. The experimental standard deviation is plotted against the standard deviation predicted by eq. 4.21. For every image set, Pearsons correlation coefficient between experimental and theoretical standard deviation is calculated. The noise variance $\sigma_S^2$ for every image set is determined as the average variance of the different signal distributions. The inverse derivative in of IR-SPGRE signal equation is calculated analytically and evaluated in the vial concentrations.

The measured standard deviations $\sigma_C$ of the concentration distributions are plotted against the theoretical values according to eq. 4.21, in fig. 4.7. Pearson's correlation coefficient between both values is above 0.95 for the three image sets, showing experimental validity of eq. 4.21 for the IR-SPGRE

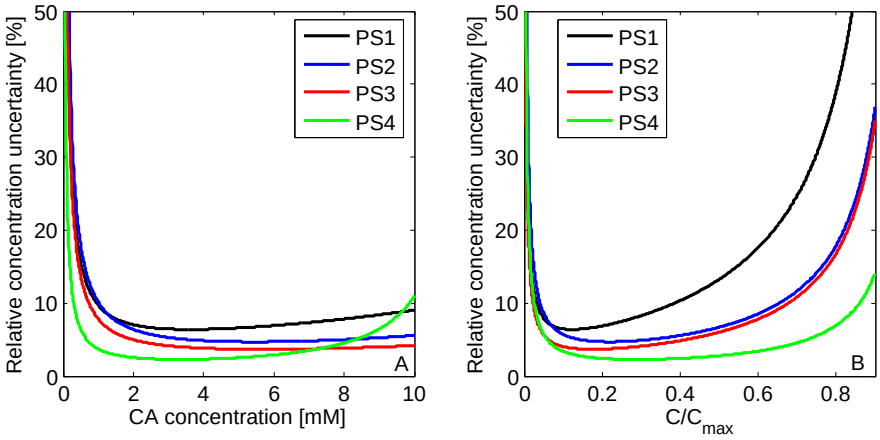


**Figure 4.8:** Relative concentration uncertainty for 4 pulse sequences (table 4.1) plotted versus CA concentration (A) and versus CA concentration relative to maximal measurable CA concentration (B).

sequence. From a kolmogorov-smirnov test, all concentrations distributions did not significantly differ from gaussian at the 5%-level (p>0.43). Mean concentration values of the distributions were within -8% and +6% of the preassumed vial concentrations. These results indicate that eq. 4.22 is a valid assumption for the concentration distribution:

$$f_C(C \mid C_{real}) = \frac{1}{\sqrt{2\pi}\sigma_C} e^{-\frac{(C-C_{real})^2}{2\sigma_C^2}} \tag{4.22}$$

$$\sigma_C = \sigma_S \left[\frac{dS}{dC}\right]^{-1}_{C=C_{real}} \tag{4.23}$$

Although the in vitro results were obtained with an IR-SPGRE sequence, there is no reason to doubt the validity of this distribution for SPGRE-pulse sequences.

### 4.5.3 Consequences for pharmacokinetic modeling

In fig. 4.8A the relative concentration uncertainty ($\sigma_C/C$) for the 4 pulse sequences from table 4.1 are plotted against the absolute CA concentration ($M_0/\sigma_S = 200$, $T_{10}/T_{20}^*$=916/200 ms). Small concentrations (< 0.1mM) exhibit high relative uncertainties for all 4 pulse sequences under consideration. The noise levels on the SPGRE signal intensity are of the same order of magnitude as the signal changes in this concentration range, making precise

determination impossible. Higher concentrations have lower uncertainties, but the concentration range that can be measured with acceptable precision is clearly dependent on the pulse sequence settings. At the current SNR ($M_0/\sigma_S$), this range could roughly be estimated as 0.1 to 10mM for PS4, and as 0.5 to beyond 10mM for PS1-PS3. In chapter 5, the influence of the pulse sequence parameters on this range is investigated and a simple procedure is proposed to find the optimal of the flip angle for precise determination of a given concentration range. Fig. 4.8B shows the relative concentration uncertainty as a function of the concentration relative to $C_{max}$. Again some general conclusions may be drawn: for concentrations above 50-60% of the maximal measurable concentration, a steep increase is seen in their relative uncertainties. This is in accordance with the findings of Schabel & Parker [30], who proposed $C_{max}/2$ as an upper limit for concentrations to be measured with acceptable precision. Schabel & Parker, however, also take into account the uncertainty on the pre-contrast signal intensity $S_0$, which results in lower precision values for concentrations calculated from the relative signal enhancement than those obtained by eq. 4.23 and in fig. 4.8. Throughout this work, this $S_0$-uncertainty is consistently neglected. Generally, the pre-contrast signal intensity is measured a number of times, denoted $N_B$, and the average $S_0$-value over $N_B$ images is taken to calculate the relative signal enhancement. This average value has an standard deviation given by $\sigma_S/\sqrt{N_B}$. Therefore by increasing $N_B$, a high $S_0$-precision can be achieved, and the validity of eq. 4.23 is preserved.

Other consequences for pharmacokinetic modeling are discussed in the next chapters. In chapter 6 a new estimator is proposed for the fitting of pharmacokinetic models to DCE-MRI measured concentration data, as the commonly used least square estimator is not optimal for data with varying variance. It is shown that the concentration distribution (eq. 4.22 & eq. 4.23) has to be taken into account when calculating confidence intervals on the estimated pharmacokinetic parameters. Furthermore, in chapter 8, it is observed that SPGRE pulse sequences operating at a reduced repetition time, but with corresponding higher temporal resolution (see eq. 2.21), do not necessarily produce more precise pharmacokinetic estimates. This effect is induced by the higher concentration uncertainty when $T_R$ is reduced, and can be seen for concentrations beneath 5mM in fig. 4.8: concentration uncertainty is higher in pulse sequences with a smaller repetition time. Finally, it should be mentioned that the concentration precision is only dependent on the conversion method used. The accuracy of the MR-measured concentration is dependent on the conversion method and on a number of MR-related errors, that reduce the accuracy of the SPGRE signal intensity equation. The precision, however, is not changed by these errors, but is only reliant on the method used for conversion. This is an important remark for the rest of this work, as for precision analysis of pharmacokinetic modeling estimates, these errors do not have to be considered.

# Chapter 5

# Flip angle optimization for dynamic contrast-enhanced MRI studies with spoiled gradient echo pulse sequences

## 5.1 Introduction

### 5.1.1 Concentration noise

In the previous chapter the concentration uncertainty has been analysed and discussed. It was shown that the noise on the MR signal intensity is transformed to concentration noise, whose extent depends on the pulse sequence design and the CA concentration itself. In this chapter, the derived analytical uncertainty expression is further investigated for SPGRE pulse sequences. In chapter 2, it was explained that the choice of SPGRE pulse sequence settings comprises a trade-off between field of view, spatial and temporal resolution and signal-to-noise ratio (SNR). However, a freedom exists in the choice of the flip angle, that has been exploited by other authors for optimizing the SNR [42] or the $T_1$-dependent contrast [161]. The flip angle also influences the concentration uncertainty, and an unappropriate choice may unnecessarily cause higher concentration noise levels, leading to reduced pharmacokinetic parameter precision [23]. Evelhoch was the first to propose a well-considered flip angle selection to facilitate concentration measurement with SPGRE-pulse sequences, but he did not quantify his idea [31]. Schabel & Parker recently demonstrated the existence of a flip angle that minimizes concentration uncer-

**Table 5.1:** Left: overview and description of the 6 parameters that influence the value of the optimal flip angle. Right: Dimensionless quantities used throughout this chapter and their ranges.

| Parameter(s) | Description | Dimensionless quantity | Range |
|---|---|---|---|
| $\Delta C$ | concentration range to be measured | $\gamma$ | 0.01-1 |
| $r_1, r_2$ | CA relaxivity coefficients | $R_{10}T_R$ | 0.001-1 |
| $T_R$, $T_E$ | SPGRE-pulse sequence parameters | $\Delta R_1 T_R$ | 0-10 |
| $R_{10}$ | native relaxation rate | $R_1 T_R$ | 0.001-10 |

tainty for a single concentration [30]. In their analysis this optimal flip angle depends on the longitudinal and transverse relaxivity coefficients of the CA, the native relaxation rates of the tissue of interest and the number of pre-contrast scans. Consequently every study design requires a separate computational optimization procedure to find the optimal flip angle. Moreover, as the optimal angle is highly dependent on the CA concentration as well, it is difficult to select from this analysis a single flip angle that is suitable for the complete CA concentration range typically encountered in kinetic modeling studies (0-10mM). This chapter therefore gives an overview of the procedure that we have proposed in [162], to select the optimal flip angle for pharmacokinetic modeling studies employing SPGRE-pulse sequences.

### 5.1.2 Aim & methodology

In this study it is aimed to find the optimal flip angle $\alpha_{opt}$ in a DCE-MRI study with a SPGRE sequence, given the sequence parameters, the tissue(s) of interest and the expected CA concentration range therein. The chapter begins with an overview of the literature concerning flip angle optimization for SPGRE-sequences, namely the ernst angle for maximizing SNR and the pelc angle for optimizing $T_1$-dependent contrast between tissues. Afterwards, our analysis starts by deriving a theoretical expression for the flip angle $\alpha_C$ that minimizes concentration uncertainty for a single concentration in a SPGRE-measurement. It is shown that this flip angle is only dependent on two dimensionless variables. When $T_2^*$-effects caused by the presence of the CA can be neglected, our analysis predicts that minimizing concentration uncertainty is equivalent to maximizing the local $T_1$-contrast. It will be shown that, for physiological CA concentrations occuring in most human tissues, $\alpha_C$ can be approximated by the pelc angle, which is only dependent on 1 dimensionless variable. An optimization procedure is then proposed for finding the best suitable flip angle $\alpha_{opt}$ for the imaging of a complete concentration range. Exploiting the pelc approximation, it is demonstrated that $\alpha_{opt}$ can be estimated from two dimensionless variables and can easily be deduced

from our contour plots for any study design. To test the consequences of this optimal flip angle selection for kinetic parameter reproducibility, kinetic modeling simulations are performed. Finally an in vivo study, in which test animals are scanned at different SPGRE flip angles, is reported as a proof of concept.

It is important to mention, that in order for flip angle optimization to be feasible, a linear relationship between the $R_1$ and $R_2^*$-relaxation rates and the CA concentration has to be assumed (see section 2.5). Proportionality coefficients are $r_1$ and $r_2$, the longitudinal and tranverse relaxivity coefficients respectively:

$$R_1 = R_{10} + r_1\ C \tag{5.1}$$
$$R_2^* = R_{20}^* + r_2\ C \tag{5.2}$$

The challenge of flip angle optimization is not in its mathematical derivation, but rather in the identification of those variables which have a significant influence on its value. From the analysis in chapter 4, the precision of a SPGRE measured concentration is dependent on 7 parameters[1]: the concentration itself, the flip angle $\alpha$, $r_1$ & $r_2$, the repetition time $T_R$ & the echo time $T_E$, $R_{10}$ and the SNR. As the flip angle has no influence on the SNR[2], its optimal value for the measurement of a concentration range, $\Delta C$, is therefore dependent upon 6 parameters, which are all summed in table 5.1. The merit of the analysis in this chapter is mainly in the identification of 3 dimensionless parameters, all combinations of the 6 variables in table 5.1, from which optimal flip angle selection can be performed based on 2 contour plots: $\gamma = \frac{r_2 T_E}{r_1 T_R}$ is a measure for the $T_2^*$-effects caused by the presence of the CA, relative to the associated $T_1$-effects. $R_{10}T_R$ is the product of the repetition time with the native longitudinal relaxation rate. $\Delta R_1 T_R = r_1 \Delta C\ T_R$ is the product of the repetition time with the total change in longitudinal relaxation rate, caused by the presence of the CA. These parameters are also mentioned in table 5.1, together with their ranges. To find these relevant ranges for the dimensionless variables, 10 recently published DCE-MRI studies were examined which are summarized in table 5.2 [18, 19, 37, 65, 66, 90, 135, 139, 141, 163]. These studies employ 3 different CA's, whose $r_1$- and $r_2$ -relaxivity coefficients are obtained at 1.5T from the study of Rohrer et al. ( [44] or table 2.2). In the ten studies, $\gamma$ varies between 0.010 and 0.62. Taking into account the increasing $r_2/r_1$ ratio at increasing field strengths [44], the range for $\gamma$ was set from 0.01 - 1. Vincensini et al. measured the native longitudinal relaxation times in normal

[1] When CA concentration is calculated by means of the relative signal enhancement, $N_{pre}$, the number of pre-contrast scans has to be accounted for. However as explained in the previous chapter this is neglected. In section 5.7 the consequences are discussed. Remark that $R_{20}^*$ is of no interest when relative signal enhancement is used (see chapter 4)

[2] Remind that we have defined the SNR as $M_0/\sigma_S$, on which the flip angle has no influence. Other authors define the SNR as the measured signal intensity divided by $\sigma_S$, which is of course influenced by the flip angle.

glandular tissue and in benign and malignant breast lesions. They found that $T_{10}$ varied between 375 and 1800 ms [45]. The results from Buckley et al. in prostate tumors and muscle were all within this range [18]. Given the $T_R$-values in table 5.2, 0.001 - 1 is a safe range for $R_{10}T_R$. The concentration range that occurs in a DCE-MRI study depends to a large extent on the determination method for the arterial input function (AIF). As explained in chapter 3, the AIF describes the concentration variation in the tumor capillaries and has to be known in advance to estimate the kinetic parameters. If the AIF is to be measured individually, Gd-DTPA concentrations up to 10 mM in blood can be expected [21]. However, if the reference region method (RR) is employed [145,164], a standard population averaged AIF [19,66] is used, or the AIF is jointly estimated with the kinetic parameters [150], tissue concentrations up to 2 mM should be measured (see section 3.4). Therefore, an appropriate range for $\Delta R_1 T_R$ is set to 0-10. The fourth dimensionless parameter that is mentioned in table 5.1 and used throughout this chapter, $R_1 T_R$, is the sum of $R_{10}T_R$ and $\Delta R_1 T_R$ (eq. 5.1). Its range is therefore set to 0.001-10. For other contrast agents with higher $r_1$-relaxivity coefficients, these values hold as the injected dose and resulting peak concentrations will typically be lower [165].

**Table 5.2:** SPGRE-pulse sequence parameters and contrast agent (CA) for 10 recent DCE-MRI studies [65, 66, 90, 112, 135, 139–141, 163, 166].

| Study | $T_R$ [ms] | $T_E$ [ms] | CA | $\gamma$ | $\alpha$ [°] |
|---|---|---|---|---|---|
| Batchelor | 5.7 | 2.73 | Gd-DTPA | 0.54 | 10 |
| Buckley | 2.5 | 0.86 | Gd-DTPA-BMA | 0.42 | 30 |
| Galbraith | 80 | 9 | Gd-DTPA | 0.13 | 70 |
| Hodgson | 4.5 | 2 | Gd-DOTA | 0.53 | 30 |
| Padhani | 35 | 5 | Gd-DTPA | 0.16 | 70 |
| Parker | 4 | 0.82 | Gd-DPTA-BMA | 0.25 | 20 |
| Pickles | 7.6 | 4.2 | Gd-DTPA | 0.62 | 30 |
| Schwenzer | 3.91 | 1.45 | Gd-DTPA | 0.42 | 20 |
| Yang | 7.8 | 1.7 | Gd-DTPA-BMA | 0.26 | 60 |
| Yankeelov | 200 | 1.8 | Gd-DTPA | 0.010 | 30 |

Three of the studies from table 5.2 were used in practical examples throughout this chapter (Batchelor, Yang & Parker). Especially the study of Parker et al. was of particular interest from our point of view: they aimed to find a population averaged AIF by performing a total of 67 blood concentration measurements in the aorta or in the iliac arteries in a population of 23 cancer patients. Gd-DTPA-BMA blood concentrations up to 10mM were found. At every time point they analysed the standard deviation of the calculated blood concentrations, which is suitable to compare to our theoretical results.

## 5.2 Flip angle optimization in SPGRE-pulse sequences

In this section an overview is given of the well known flip angles in MR-literature for maximizing signal intensity and $T_1$-dependent contrast in SPGRE pulse sequences.

### 5.2.1 Maximizing SPGRE signal intensity

The flip angle, maximizing SPGRE signal intensity in a tissue is known as the ernst angle [42]. It can be derived by setting the derivative of the SPGRE signal intensity equation with respect to the flip angle to zero and depends on the repetition time and the tissue's longitudinal relaxation time.

$$\alpha_E = acos(E_1) \tag{5.3}$$
$$E_1 = exp(-T_R/T_1) \tag{5.4}$$

If the SNR is defined as the ratio of the measured signal intensity S to the noise standard deviation $\sigma_S$, the ernst angle maximizes the SNR. Throughout this work however, SNR is defined as $M_0/\sigma_S$, $M_0$ being the proportionality factor of the SPGRE signal intensity (eq. 2.27), on which the flip angle has no influence.

### 5.2.2 Maximizing contrast-to-noise ratio

When the radiological investigation aims at distinguishing two or more tissues with different $T_1$-values, it is useless to maximize the SNR. Instead, the signal difference between the two tissue should be maximized, i.e. the contrast-to-noise ratio, to facilitate radiological interpretation on greyscale images. The optimal flip angle in this case has been derived by the analysis of Buxton, Pelc and Haselhoff [161, 167, 168]. Suppose an optimal distinction should be visible between tissues with longitudinal relaxation times $T_{1a}$ and $T_{1b}$. When the tissues have comparable $T_2^*$ and proton density or when their influence can be neglected, the signal difference or contrast is given by:

$$\Delta S = sin(\alpha)\left[\frac{1-E_{1a}}{1-cos(\alpha)E_{1a}} - \frac{1-E_{1b}}{1-cos(\alpha)E_{1b}}\right] \tag{5.5}$$

with $E_{1a}$ and $E_{1b}$ similarly defined as in eq. 5.4. An analytical expression exists for the flip angle maximizing this contrast [168]:

$$\alpha_d = acos\left[\frac{-\bar{E_1}^2 + \bar{E_1} - 1 + \delta^2 + \sqrt{\bar{E_1}^4 - (2\delta^2+2)\bar{E_1}^2 + \delta^4 - \delta^2 + 1}}{\bar{E_1} - 2\bar{E_1} - \delta^2}\right] \tag{5.6}$$

$$\bar{E_1} = \frac{E_{1a} + E_{1b}}{2} \tag{5.7}$$

$$\delta = \frac{E_{1a} - E_{1b}}{2} \tag{5.8}$$

In practive however, optimization is required for tissues with similar relaxation times, which under sub-optimal conditions, are difficult to distinguish from one another. Taking the limit for $\delta \rightarrow 0$ of eq. 5.6 yields:

$$\alpha_{Pelc} = acos\left[\frac{2E_1 - 1}{2 - E_1}\right] \tag{5.9}$$

This is the pelc flip angle that maximizes local $T_1$-contrast [161, 167], i.e. for which $\partial S/\partial T_1$ is maximal. Pelc showed that this expression, with $E_1$ evaluated in the average $T_1$-value of the two tissues under investigation, is a sufficient approximation of eq. 5.6. Even if the difference in the $T_1$-values ,$\Delta T_1$, equals the average of the $T_1$-values, the contrast loss remains less than 1%. Therefore, this pelc angle is widely used to optimize $T_1$-dependent contrast between tissues in SPGRE-sequences.

## 5.3 Flip angle optimization for a single concentration

In this section a theoretical expression is derived for $\alpha_C$, the flip angle maximizing concentration precision for a fixed concentration. A practical example is used to demonstrate the potential of flip angle optimization and to show (again) the existence of a maximal measurable concentration. Afterwards, the expression for the concentration uncertainty, as derived in chapter 4, is repeated and used to calculate $\alpha_C$. Finally, it is shown that the pelc angle is a sufficient approximation for $\alpha_C$. Although $\alpha_C$ is not the final goal of this chapter, the theoretical expression and in particular the pelc angle approximation will be exploited when deriving $\alpha_{opt}$

### 5.3.1 Practical example

Flip angle optimization for a single concentration aims at minimizing the concentration uncertainty for that given concentration, thereby enabling its most precise measurement. It differs from the flip angle optimization for $T_1$-dependent contrast in the sense that $T_2^*$-relaxation, caused by the presence of CA, has to be accounted for. In fig. 5.1 the normalized signal intensity is plotted for the pulse sequence of Batchelor (table 5.2) versus the concentration at 3 different flip angles. At C = 1mM the concentration uncertainty is evaluated graphically. While the signal noise $dS$ is equal in all three cases, the concentration noise is severely reduced for the flip angle of 25°, in comparison with 10° or 60°. This straightforward example proves that a proper flip angle

selection is indispensable for DCE-MRI, although it has only been discussed in 2 studies [30, 31]. Secondly, fig. 5.1 shows again the existence of a flip angle dependent maximal measurable concentration $C_{max}$, above which the CA concentration cannot be determined unambiguously. This maximal measurable concentration has been discussed in the previous chapter (section 4.2) and the contour plot (fig. 4.2) that was derived is an important element in the final flip angle optimization strategy. For now it is not clear why this maximum measurable relaxivity rate plot is necessary for our optimal flip angle analysis. In the following it will be shown that $\alpha_{opt}$ can be accurately selected without taking into account $R_2^*$-effects. Therefore it will have to be verified that the $R_1$-relaxivity rate in the study does not exceed the $R_{1mm}$, the maximal measurable longitudinal relaxivity rate, at the optimal flip angle and the corresponding $\gamma$.

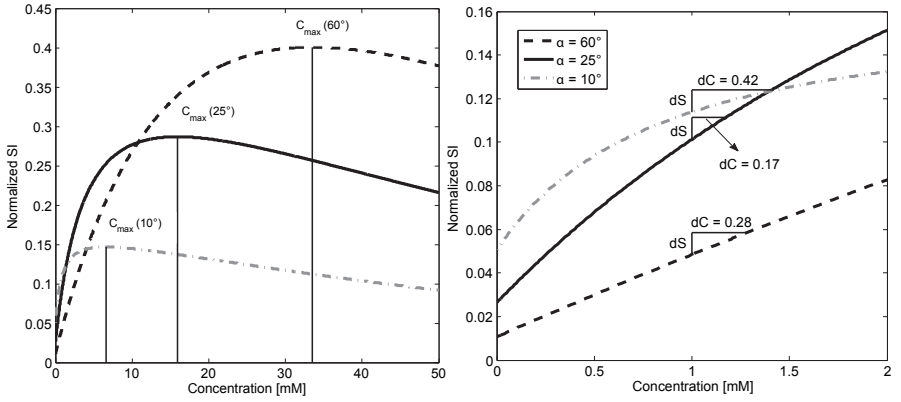


**Figure 5.1:** Left: normalized signal intensity versus CA concentration ($T_{10}/T_{20}^*$=916/200 ms, Gd-DTPA, $T_R/T_E$ = 5.7/2.73 ms) for three different flip angles with indication of the maximal measurable concentration $C_{max}$. Right: graphical analysis of the concentration uncertainty for C = 1 mM, at the three flip angles. $dC$ is expressed in mM (dS = 0.01).

### 5.3.2 Concentration uncertainty

When finite SNR is considered as the only error source, the concentration uncertainy is given by (see chapter 4):

$$\sigma_C = \sigma_S \left[\frac{dS}{dC}\right]^{-1} \tag{5.10}$$

$$\frac{dS}{dC} = M_0 T_R r_1 E_2^* \left[\frac{E_1 sin(\alpha)(1-cos(\alpha))}{(1-cos(\alpha)E_1)^2} - \gamma \frac{sin(\alpha)(1-E_1)}{(1-cos(\alpha)E_1)}\right] \tag{5.11}$$

$$\gamma = \frac{r_2^* T_E}{r_1 T_R} \tag{5.12}$$

With $E_1$ as defined in eq. 5.4 and $E_2^* = exp(-R_2^* T_E)$. $\gamma$ comprises the ratio of transverse to longitudinal relaxivity rate changes for any CA concentration and is therefore a measure of $R_2^*$-effects relative to $R_1$-effects. If SNR is defined as $\frac{M_0}{\sigma_S}$, eq. 5.10 can be rewritten as:

$$\sigma_C = \frac{1}{SNR}\ \frac{1}{T_E r_2 E_2^*}\gamma\left[\frac{E_1 sin(\alpha)(1-cos(\alpha))}{(1-cos(\alpha)E_1)^2} - \gamma\frac{sin(\alpha)(1-E_1)}{(1-cos(\alpha)E_1)}\right]^{-1} \tag{5.13}$$

### 5.3.3 Optimal $\alpha_C$

The flip angle $\alpha_C$, minimizing concentration uncertainty for a single concentration in a given tissue of interest, can be derived by differentiating eq. 5.11 with respect to $\alpha$ and equating this expression to zero :

$$\frac{d[dS/dC]}{d\alpha} = 0 \tag{5.14}$$

By factorizing the signal derivative as in eq. 5.11, it can easily be seen that $\alpha_C$ is only dependent on the 2 dimensionless parameters $\gamma$ and $R_1 T_R$. After some mathematics (see appendix), $\alpha_C$ can be determined from:

$$cos(\alpha_C) = \frac{-E_1(E_1+1) + \gamma(1-E_1)(1+E_1^2) + (1-E_1)\sqrt{9E_1^2 - 2\gamma E_1(1-E_1^2) + \gamma^2(1-E_1^2)^2}}{2E_1(E_1 - 2 + \gamma(1-E_1))} \tag{5.15}$$

In fig. 5.2A $\alpha_C$ is depicted in a contour plot versus $\gamma$ and $R_1 T_R$. For every study design, summarized in the parameter $\gamma$, and every tissue of interest and CA concentration, summarized in $R_1 T_R$, $\alpha_C$ can be read off fig. 5.2A. Fig. 5.2B shows the corresponding minimum values of the dimensionless variable $SNR \cdot \sigma_C \cdot T_E r_2 E_2^*$ as determined from eq. 5.13, from which minimal $\sigma_C$ for the particular concentration can be calculated if SNR, $T_E$, $r_2$ and $R_{20}^*$ are known. The dashed vertical line shows the variation in $\alpha_C$ and the concentration uncertainty along the complete concentration range in the study of Parker, 0-10 mM in blood, for the corresponding $\gamma$-value of 0.25 (table 5.2). $\alpha_C$ varies between 7.2° for the lowest concentrations, and 55° for the peak concentrations, showing the need for further optimization to find the best suitable value of the flip angle $\alpha_{opt}$, which is located between these boundaries.

### 5.3.4 Pelc angle as approximation for $\alpha_C$

In the limit for $\gamma = 0$, eq. 5.15 reduces to:

$$cos(\alpha_C) = \frac{2E_1 - 1}{2 - E_1} \tag{5.16}$$

which is identical to the pelc angle for optimizing $T_1$-dependent contrast. This can be expected on physical grounds as $\gamma \to 0$, corresponds to $r_2/r_1 \to 0$ or

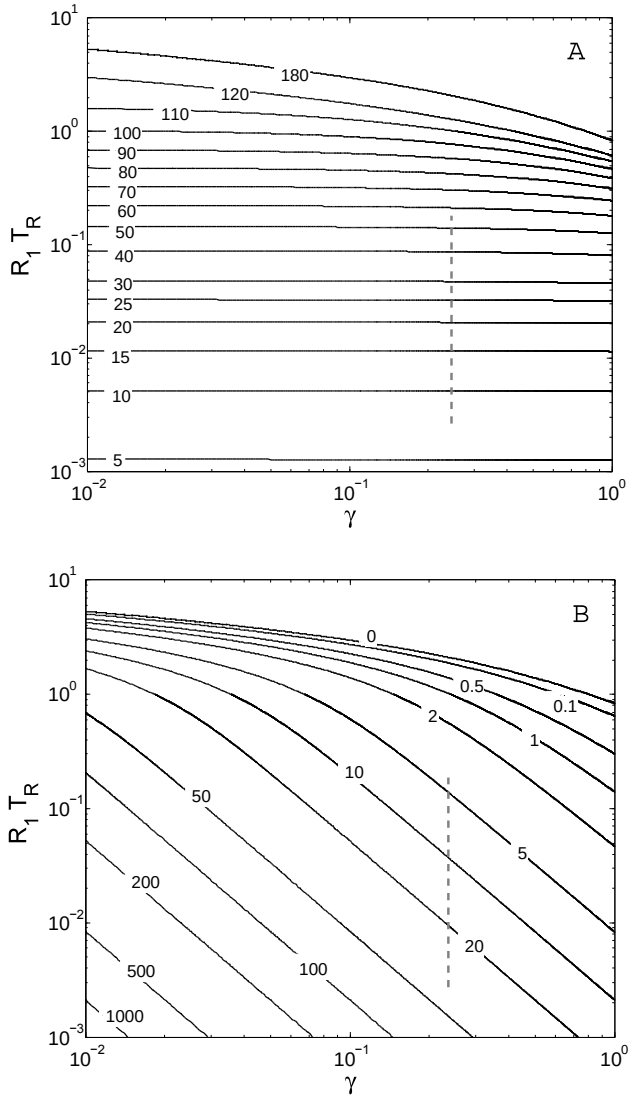


**Figure 5.2:** A: contour plot of $\alpha_C$, the flip angle maximizing concentration precision for a single concentration in a tissue, as a function of the dimensionless variables $\gamma = \frac{r_2 T_E}{r_1 T_R}$ and $R_1 T_R$; B: corresponding minimum values of $SNR \cdot \sigma_C \cdot T_E r_2 E_2^*$

**Table 5.3:** Several properties of the DCE-MRI studies

| Study | $C_{crit}$ [mM] [a] | $\alpha_{opt}^{ex}$ [°] [b] | $\alpha_{opt}$ [°] [b] | $\Delta\sigma_C$ [%] [c] | $\alpha_{opt}^{ex}$ [°] [b] | $\alpha_{opt}$ [°] [b] | $\Delta\sigma_C$ [%] [c] |
|---|---|---|---|---|---|---|---|
| | | 2mM in tumor tissue | | | 10 mM in blood | | |
| Batchelor | 33 | 23.6 | 23.4 | 108 | 47.6 | 45.5 | -[d] |
| Buckley | 89 | 15.9 | 15.9 | 30 | 32.3 | 31.8 | 1 |
| Galbraith | 5.9 | 76.9 | 74.9 | 1 | -[e] | -[e] | -[e] |
| Hodgson | 49 | 19.9 | 19.8 | 13 | 39.8 | 38.6 | 7 |
| Padhani | 12 | 55.0 | 54.1 | 6 | 97.2 | 90.3 | 33 |
| Parker | 80 | 20.1 | 20.0 | 0 | 40.2 | 39.6 | 65 |
| Pickles | 22 | 27.2 | 26.8 | 1 | 55.4 | 51.7 | 72 |
| Schwenzer | 59 | 19.5 | 19.4 | 0 | 39.3 | 38.4 | 62 |
| Yang | 40 | 27.9 | 27.7 | 50 | 54.9 | 53.3 | 1 |
| Yankeelov | 6.0 | 99.6 | 99.0 | 741 | -[e] | -[e] | -[e] |

[a] $C_{crit}$ is the concentration at which the pelc angle approximation of $\alpha_C$ fails

[b] $\alpha_{opt}^{ex}$ is the optimal flip angle calculated based on eq. 5.18. $\alpha_{opt}$ is the approximation of the optimal flip angle based on (eq. 5.22).

[c] $\Delta\sigma_C$ is the average percentage decrease in concentration uncertainty by using the optimal flip angle instead of the flip angle employed in the study.

[d] For the flip angle in the study of Batchelor, 10 mM is above the maximal measurable concentration in blood.

[e] No flip angle optimization is possible for 10mM for this study

$T_E/T_R \rightarrow 0$. In both hypothetical cases the $T_2^*$-weighting of the SI is negligible in comparison with the $T_1$-weighting. The derivative of the signal to the concentration is then proportional to the derivative of the signal towards $R_1$ (eq. 5.11) and minimizing the concentration uncertainty is equivalent to maximizing the local $T_1$-contrast $dS/dT_1$. From fig. 5.2A no $\alpha_C$ variation with $\gamma$ is seen, unless for high $R_1T_R$-values ($> 1$). This indicates that the pelc flip angle may be a sufficient approximation for the exact $\alpha_C$, unregarded the $\gamma$-value. Fig. 5.3 shows the percentage deviation of the pelc flip angle from the exact $\alpha_C$ for different values of $\gamma$ (A) and the associated percentage loss in $dS/dC$ (B). The difference between the exact $\alpha_C$ and its approximation is marginal for small $R_1T_R$ and rises up to 30% for high $\gamma$-values and large $R_1T_R$. The associated change in dS/dC however, remains negligible up to a critical $R_1T_R$-value where it begins to rise steeply to 100%. For the 10 different DCE-MRI protocols, table 5.3 contains the critical concentration $C_{crit}$ where the decrease in dS/dC, caused by using the pelc angle instead of the exact $\alpha_C$, exceeds 10%. This concentration was determined in a tissue with $T_{10} = 1250$ ms, which corresponds with the $T_1$ value of blood, as the highest concentrations are to be expected in arteries. It is clear that these critical concentrations fairly exceed the expected physiological concentrations in human tissues, except for the two studies with the highest $T_R$ (Yankeelov & Galbraith). However both studies measured only tissue concentrations (0-2mM) and did not perform AIF measurement in blood [37, 66]. Therefore it may be concluded that for the 10 studies reported in table 5.2 and 5.3, the pelc angle is a sufficient approximation for $\alpha_C$, irrespective the $\gamma$-value of the study. Although this implies that $\gamma$ and its associated $T_2^*$-effects have no significant influence on $\alpha_C$, they highly affect the exact $\sigma_C$-values as can be seen from fig. 5.2B.

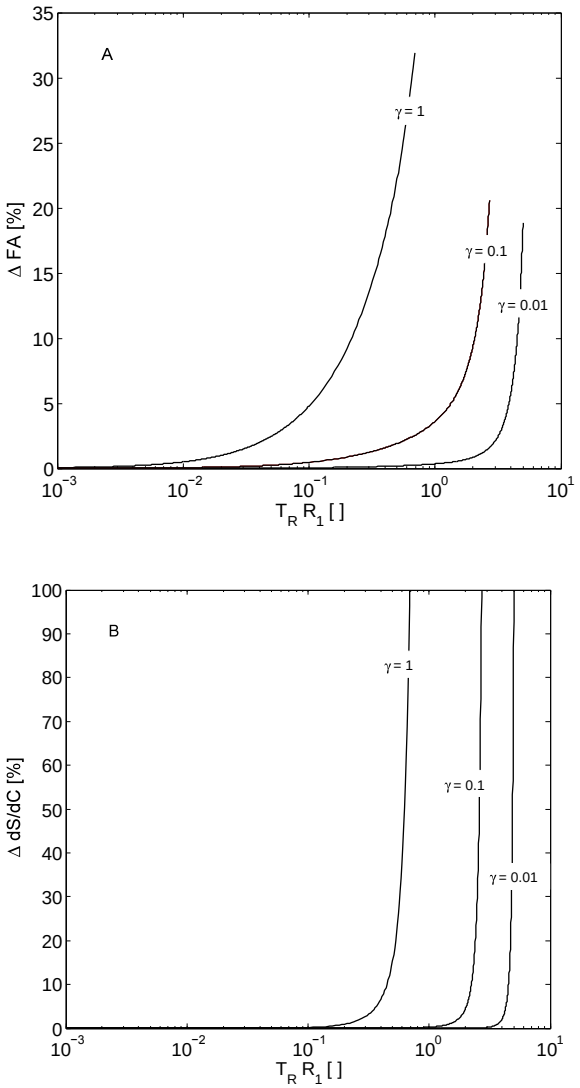


**Figure 5.3:** A. percentage deviation between the pelc approximation for $\alpha_C$ and its exact value as a function of $R_1 T_R$ for different values of $\gamma$. B. corresponding relative loss in dS/dC.

## 5.4 Flip angle optimization for a concentration range

### 5.4.1 Optimal flip angle $\alpha_{opt}$

In this section the optimal choice for the flip angle $\alpha_{opt}$ is derived when performing a contrast enhanced MRI study, given the expected concentration range and

the tissue(s) of interest. In order to find this optimal value for a given concentration range, the average relative contrast with respect to the maximum possible contrast $\rho$ is introduced:

$$\rho = \frac{1}{\Delta C} \int_0^{\Delta C} \frac{dS/dC'(\alpha)}{dS/dC'(\alpha_{C'})} dC' \tag{5.17}$$

$\Delta C$ is the upper bound of the expected concentration range, $\alpha_C$ is the optimal flip angle for an individual concentration as predicted by eq. 5.15 or eq. 5.16. By maximizing $\rho$ with respect to $\alpha$, any concentration within the expected range will be imaged with the smallest possible uncertainty. In other words, the signal difference (in time or in space) between two voxels with slightly different concentrations will be as high as possible for any concentration in that given range. From eq. 5.11, it can be seen that eq. 5.17 does not contain $E_2^*$-factors. This implies that $\rho$ can be rewritten with $E_1$ as the new integration variable. Leaving behind the explicit dependency of $\alpha_C$ to $E_1$, $\rho$ becomes:

$$\rho = \frac{1}{r_1 T_R \Delta C} \int_{E_1^{min}}^{E_1^{max}} \frac{sin(\alpha)\left[(1-cos(\alpha))E_1 - \gamma(1-E_1)(1-cos(\alpha)E_1)\right]\left[1-cos(\alpha_C)E_1\right]^2}{E_1 sin(\alpha_C)\left[(1-cos(\alpha_C))E_1 - \gamma(1-E_1)(1-cos(\alpha_C)E_1)\right]\left[1-cos(\alpha)E_1\right]^2} dE_1 \tag{5.18}$$

$$E_1^{min} = exp(-T_R(R_{10} + r_1\Delta C) = exp(-T_R R_1^{max}) \tag{5.19}$$

$$E_1^{max} = exp(-T_R R_{10}) = exp(-T_R R_1^{min}) \tag{5.20}$$

$E_1^{min}$ and $E_1^{max}$ are the expected minimum and maximum values for $E_1$ in the study, derived from the maximum and minimum $R_1$-relaxivity rates, $R_1^{max}$ and $R_1^{min}$ respectively. The best suitable value for the flip angle is again derived by differentiating eq. 5.18 with respect to $\alpha$ and equating this derivative to zero. As $\alpha_C$ is function of $E_1$ and $\gamma$, it can be seen from eq. 5.18 that $\alpha_{opt}$ will depend on $E_1^{min}$, $E_1^{max}$ and $\gamma$. Finding $\alpha_{opt}$ for any study design thus requires computational optimization based on numerical integration of the above integral. However, from the previous section it is known that in normal physiological situations, the pelc-expression for $\alpha_C$ differs only weakly from the exact $\alpha_C$-value and that the associated contrast loss is negligible. Therefore the $R_1$- and $R_2^*$-dependencies will be decoupled in the rest of the analysis. $R_2^*$-effects and the associated parameter $\gamma$ will only be used to calculate the minimum value of $E_1$ that can be measured unambiguously, while its effects on optimal flip angle will be neglected. For this latter purpose, only $R_1$-influence will be taken into account, which was already justified for a single concentration. Neglecting $R_2^*$-effects is equivalent to setting $\gamma$ to zero and inserting eq. 5.16 for $\alpha_C$ in eq. 5.18 for $\rho$:

$$\rho = \frac{1}{r_1 T_R C} \int_{E_1^{min}}^{E_1^{max}} \frac{dS/dC'(\alpha)}{E_1 dS/dC'(\alpha_{C'}(E_1))} dE_1 \tag{5.21}$$

$$= \frac{4}{3\sqrt{3}} \frac{sin(\alpha)(1-cos(\alpha))}{log(E_1^{max}/E_1^{min})} \int_{E_1^{min}}^{E_1^{max}} \frac{\sqrt{1-E_1^2}(1+E_1)}{(1-cos(\alpha)E1)^2 E_1} dE_1 \quad (5.22)$$

$sin(\alpha_C)$ is evaluated as the positive square root of $(1-cos(\alpha_C)^2)$, as in the flip angle range of 0 to $\pi$ the sine is always positive. The integral in eq. 5.22 can be evaluated analytically, avoiding the need for numerical integration. The primitive function is however very complicated and of little practical interest and is therefore not mentioned. It was calculated by using the Symbolic Math Toolbox in Matlab (Mathworks MA). For every ($E_1^{min}$, $E_1^{max}$)-pair expression 5.22 can be maximized with respect to $\alpha$, and the resulting $\alpha_{opt}$ can be depicted in a contour plot. Fig. 5.4A is a contour plot of $\alpha_{opt}$ as a function of the $R_1^{min}T_R$ and $\Delta R_1 T_R$, as obtained by maximizing eq. 5.22. Fig. 5.4B shows the corresponding maximum value of $\rho$ calculated with eq. 5.22. This value only comprises the $T_1$-effects caused by varying concentration and is therefore an overestimation of the real value of $\rho$ (eq. 5.18). $\alpha_C$ can now be regarded as a special case of $\alpha_{opt}$, for $\Delta R_1 T_R = 0$. Fig. 5.4A also states that when $R_1^{min} < \Delta R_1/2$, the tissue of interest is of little importance for the selection of the optimal flip angle.

### 5.4.2 Validity of decoupling presumption

Table 5.3 contains the exact values $\alpha_{opt}^{ex}$ for the optimal flip angle based on numerical integration of eq. 5.18 for the 10 DCE-MRI studies under consideration and for the 2 concentration ranges of the corresponding contrast agents mentioned in the introductory section. The approximate values of $\alpha_{opt}$ determined with eq. 5.22 and fig. 5.4 are given as well. For the typical concentration range found in tumor tissue, both values are in good agreement. For two studies [37] [66], 10mM is above the maximum measurable concentration $C_{max}$ for the corresponding $\gamma$. For the 8 others, the difference between the approximated and exact value of $\alpha_{opt}$ grows with increasing concentration, as can be expected from enhanced $T_2^*$-effects. However, the maximum difference (7%) [19] remains small. It may therefore be concluded that fig. 5.4 yields a sufficient approximation for the optimal flip angle, provided that at this flip angle, given the $\gamma$-value of the study, the expected concentration range does not exceed $C_{max}$. The average percentage increase $\Delta\sigma$ in $\sigma_C$ by using the flip angle employed in the study (table 5.2) instead of $\alpha_{opt}$, for the 2 concentration ranges is also mentioned in table 5.3. For the study of Batchelor et al., the maximum measurable concentration at a flip angle of 10° is smaller than 10 mM. From these values it is clear that unadapted flip angle choice causes a severe and unnecessary uncertainty increase on the concentration curve up to 741%.

### 5.4.3 Robustness and trade-off of optimization criterion

Fig. 5.5 is based on the study of Parker et al. and assumes an arterial concentration range (0-10mM). Fig. 5.5A shows the ratio between the concentration

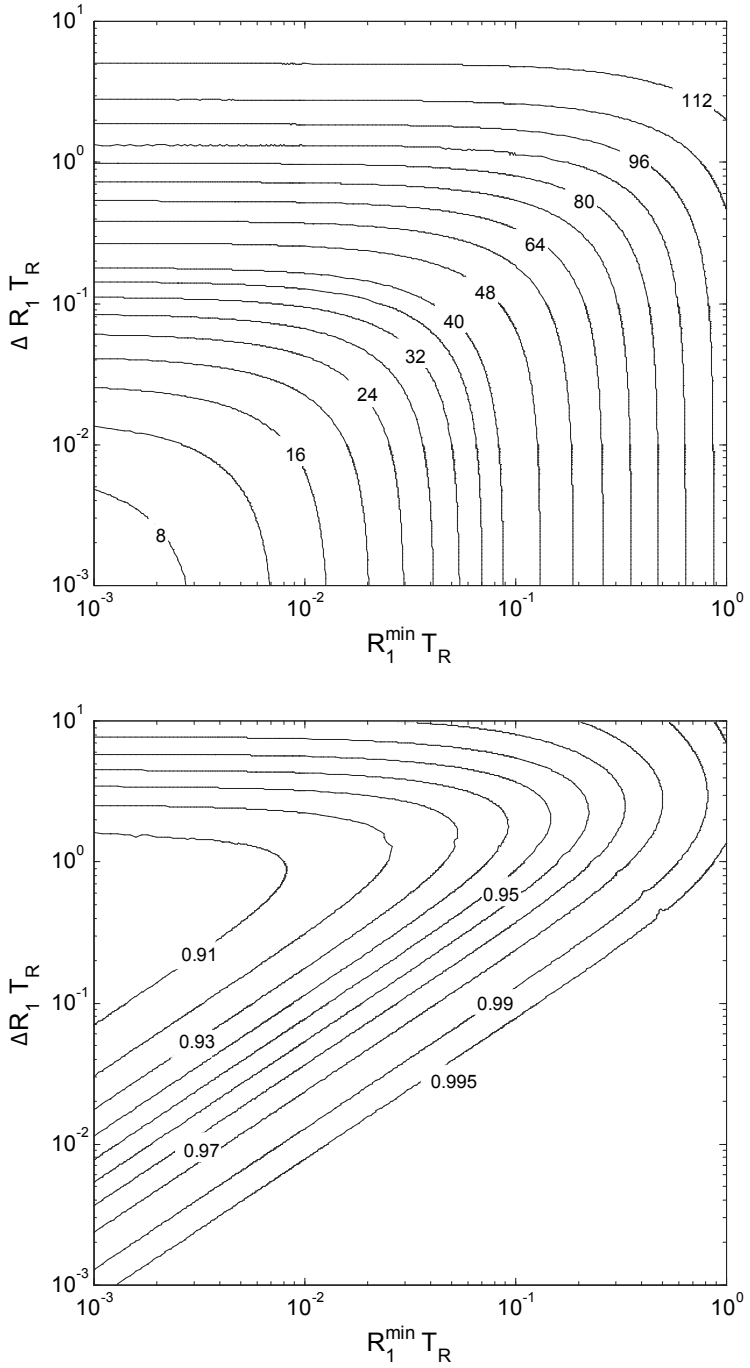


**Figure 5.4:** A. Contour plot of the best suitable flip angle $\alpha_{opt}$ for a concentration range in a tissue of interest in function of $R_1^{min}T_R$ and $\Delta R_1 T_R$. B. Contour plot of the optimization variable $\rho$ (eq. 5.21).

uncertainty at the optimal flip angle of 40.2° (table 5.3) to the uncertainty at several other flip angles, as a function of concentration. The flip angles are 20°, employed in the study itself, and 7.2° and 55°, the optimal flip angles $\alpha_C$ for the minimum and maximum concentration in the range according to fig. 5.2. The figure shows the trade-off that is made by the optimization criterion. Flip angles beneath $\alpha_{opt}$ are better for the smallest concentrations, but cannot reasonably depict the higher part of the concentration range. Flip angles exceeding $\alpha_{opt}$ cause better concentration precision for the higher concentrations in the range at the expense of poorer precision for the smallest concentrations. Eq. 5.21 integrates these sacrifices into one parameter $\rho$. $\rho$ is plotted against the flip angle in fig. 5.5B, for the study of Parker et al. The broad maximum of this $\rho$ vs. flip angle curve shows that our method is robust to misestimation of the concentration range. According to fig. 5.4 an over- or underestimation will lead to an corresponding over- or underestimation of $\alpha_{opt}$. This robustness to misestimation of $\alpha_{opt}$ or the concentration range, is mirrored in the $\Delta\sigma$-values of table 5.3 as well. For the study of Padhani et al., a 27% overestimation of $\alpha_{opt}$ (70° instead of 55°) causes a mere 6% average $\sigma_C$-increase. A 12% underestimation of $\alpha_{opt}$ in the study of Galbraith et al., leads to a $\sigma_C$-increase of only 1%.

## 5.5 Kinetic modeling simulations

A simulation environment in Matlab (Mathworks, MA) was written, to assess the influence of the proposed flip angle selection on the reproducibility of the kinetic parameters in a typical DCE-MRI experiment. For three of the DCE-MRI studies mentioned above [135, 139, 141], two different approaches were investigated: kinetic modeling with an individually measured AIF and kinetic modeling with a standard (or population averaged) AIF. The kinetic model employed in the simulations is the Tofts model with vascular contribution [16]. Kinetic parameters are the transendothelial transfer constant $K^{trans}$ ($min^{-1}$), the interstitial space fraction $\nu_e$, and the plasma fraction $\nu_p$. The tissue concentration varies according to eq. 5.23.

$$C_t(t) = \nu_p C_p(t) + K^{trans} \int_0^t C_p(t')\ exp\left[-\frac{K^{trans}}{\nu_e}(t-t')\right] dt' \qquad (5.23)$$

In the simulations, $10^4$ kinetic parameters combinations are randomly selected from a physiologically relevant range ($K^{trans}$ = 0.05 - 1 $min^{-1}$, $\nu_e$ = 0.05 - 0.5 , $\nu_p$ = 0.03 - 0.15). As AIF the population averaged parametrized curve derived by Parker was used (haematocrit was set to 0.45, [139] or eq. 3.16). For every kinetic parameter combination the tissue concentration curve is calculated according to eq. 5.23, with a temporal resolution of 0.1 s (to avoid aliasing errors). This tissue concentration curve is sampled with the temporal resolution $\Delta t$ and for the total scan time $T_{scan}$ of the DCE-MRI study under investigation ($\Delta t/T_{scan}$ = 5/250 s for Batchelor, 2/360s for Yang, 5/375s

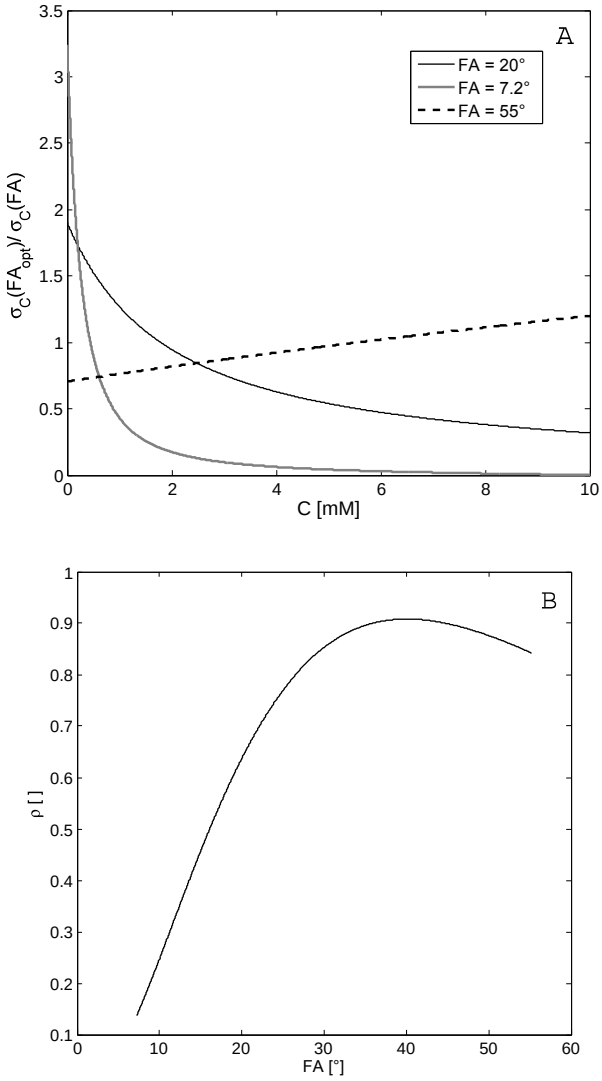


**Figure 5.5:** A: ratio of concentration uncertainty at optimal flip angle to uncertainty at different flip angles as a function of concentration for the study of Parker et al. ($\alpha_{opt}$ = 40.1°, $T_R/T_E$=4/0.82 ms, Gd-DPTA-BMA concentration range = 10 mM in blood, $T_{10}$=1250 ms). B: variation of optimization variable $\rho$ vs. flip angle.

for Parker). To mimic a pixelwise variation in the native longitudinal relaxation time, $T_{10}$ is randomly selected from the range 600 ms - 1000 ms. Using the pulse sequence parameters $T_R$ and $T_E$ from the study, the signal intensity curves are calculated for Gd-DTPA for a given flip angle according to SPGRE equation (eq. 2.27). After the addition of white Gaussian noise (SNR = 600), the noise contaminated signal curves are recalculated to tissue concentration curves [30]. For the standard AIF approach, the kinetic parameters are determined from a fit of this concentration curve to the Tofts model with the standard AIF from Parker et al. [139]. For the patient-specific AIF approach, the procedure is repeated for the AIF measurement. Assuming a $T_{10}$ of 1250 ms for blood [44], the signal intensity curve is calculated, contaminated with white Gaussian noise and recalculated to a concentration curve. The latter is used in the fit procedure to estimate the kinetic parameters. The reproducibility of a kinetic parameter $\theta$ for a given flip angle is then evaluated by the mean relative error MRE:

$$MRE(\alpha) = \frac{100}{N} \sum_{i=1}^{N} \frac{|\hat{\theta}_i(\alpha) - \theta_i|}{\theta_i} \tag{5.24}$$

N being the number of simulations ($10^4$). The flip angle values for which the MRE is simulated, are chosen as the $\alpha_{opt}$-values for a concentration range varying between 0 and 10 mM (and for the pulse sequence settings of the considered DCE-MRI study). For the standard AIF approach this $\alpha_{opt}$ is determined with $T_{10}$ set to its maximal value in tissue (1000 ms in this simulation), for the individually measured AIF approach $T_{10}$ is set to 1250 ms (the value in blood). This is in agreement with the flip angle optimization algorithm that will be proposed in section 5.7. It should be mentioned that MRE is a measure for the kinetic parameters reproducibility in the kinetic parameter range under investigation, as we did not consider other error sources (such as partial volume effect or inflow effects, $B_1$-field inhomogeneities, errors in $T_{10}$, errors in the AIF,...). The only parameter that was changed in the simulations is the flip angle. Therefore, the noise in the concentration-time curve will solely depend on the flip angle and MRE is a measure for the resulting kinetic parameter reproducibility.

For three DCE-MRI studies from table 5.2, fig. 5.6 shows the evolution of the mean relative error in a physiological relevant kinetic parameter range as a function of the flip angle. However, this flip angle is displayed on the abcis axis as the concentration range for which the DCE-MRI experiment has been optimized. This enables us to check the validity and the robustness of our optimization strategy and to make more practical recommendations about the concentration ranges. For the individually measured AIF approach, this $\alpha_{opt}$ is calculated in blood ($T_{10}$ = 1250 ms), while for the standard AIF approach, the maximal $T_{10}$-value (1000 ms) in the simulations is used to determine $\alpha_{opt}$. The variation of this optimal flip angle with the expected concentration range

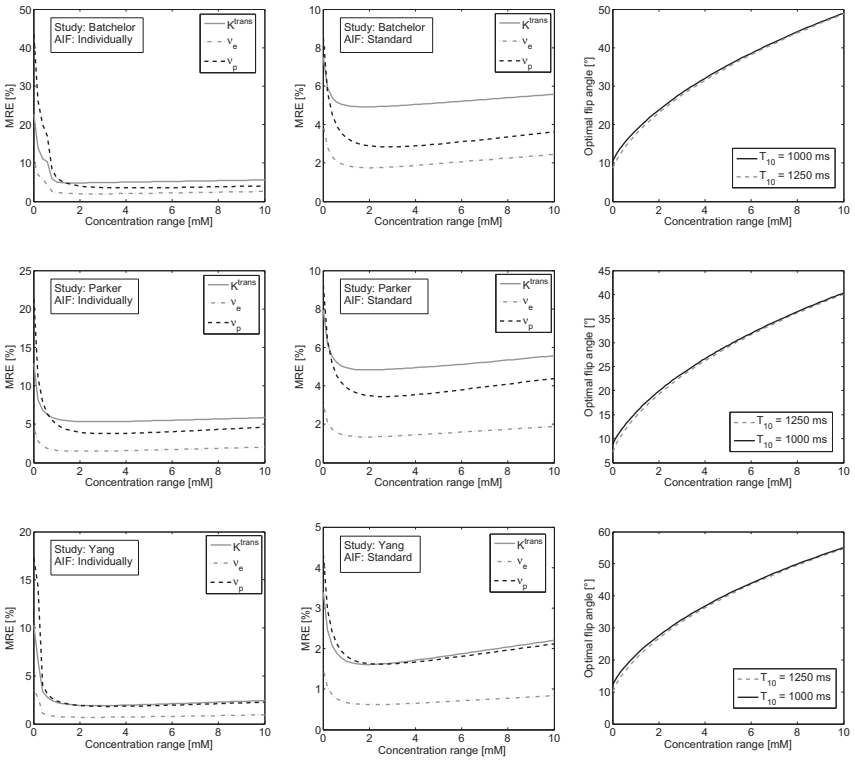


**Figure 5.6:** Results of the kinetic modeling simulations for the settings of three DCE-MRI studies. Mean relative error as a function the flip angle. This flip angle is expressed as the concentration range for which it is the optimal value (see text). The relationship between the flip angle and the concentration range is plotted in the third column. Two approaches are investigated: kinetic modeling with a individually measured AIF and kinetic modeling with a standard AIF.

is plotted for each of the three studies in the right column of fig. 5.6. When the AIF is measured together with the tissue concentration curves, flip angle optimization is indispensable for kinetic modeling, with MRE reductions up to 82% for $K^{trans}$, 82% for $\nu_e$ and 92% for $\nu_p$. The minimum of the MRE-curve is broad, implying that the optimization procedure for kinetic modeling purposes is very robust to the a priori expected concentration range. Moreover a flip angle optimization for a concentration range between 2-6 mM results in an almost equal reproducibility in the kinetic parameter range under consideration. This is in very good agreement with the true concentration range to be measured

**Table 5.4:** Mean kinetic parameter values and their mean 95% confidence intervals over the tumor region in three mice

| | | Mean kinetic parameter values | | | Mean 95% confidence intervals | | |
|---|---|---|---|---|---|---|---|
| $\alpha$ [°] | $\Delta C$ [mM] [a] | $K^{trans}$ $[min^{-1}]$ | $\nu_e$ [] | $\nu_p$ [] | $K^{trans}$ [%] | $\nu_e$ [%] | $\nu_p$ [% ] |
| 15 | - [b] | 0.41 | 0.4 | 0.055 | 10.9 | 11.1 | 32.1 |
| 24 | 0.57 | 0.25 | 0.32 | 0.046 | 6.2 | 6.7 | 15.7 |
| 54 | 5.6 | 0.31 | 0.29 | 0.042 | 10.5 | 10.2 | 29.4 |

[a] $\Delta C$ is the concentration range for which the employed flip angle is optimized, with $T_{10}$ set to its mean value over the tumor region

[b] The flip angle of 15° is smaller than the $\alpha_{Pelc}$-value of the average $T_{10}$ in the tumor

for this AIF (0-6.5 mM). For the standard AIF approach, MRE-reductions are smaller, up to 53% for $K^{trans}$, 59% for $\nu_e$ and 67% for $\nu_p$. The minimum of the curve is more narrow, but the optimization strategy remains robust. A concentration range of 1-3 mM can be considered as a practical recommendation for kinetic modeling with this standard AIF and for this kinetic parameter range. Again, this is in agreement with the true tissue concentration range to be measured in the kinetic parameter range under consideration (0-2.5 mM). Our simulations thus confirm that our optimization strategy, in which concentration uncertainty is minimized, results in optimal reproducibility of the kinetic parameter estimates. As predicted by the results from table 5.3, the flip angle in the study of Batchelor et al. is too small, while for the study of Yang et al. the flip angle is too high. The study of Parker et al. seems to be well developed for kinetic modeling purposes. However, these statements are only valid when the true AIF resembles the AIF used in the simulations.

## 5.6 In vivo demonstration

Three Male athymic nude mice were grown in plastic cages with free access to tap water and standard pellet food. A HT29 (human colorectal cancer) cell line was cultured and 1 million cells suspended in 0.1 ml of saline were injected subcutaneously in the hind leg of the mice. Scans were performed after two weeks, when the tumors had a diameter around one centimetre. Mice were anaesthetised with intraperitoneal injection of ketamine and xylazine. A catheter was placed in the tail vein before positioning in the magnet bore. Gd-DOTA was administered in bolus through this catheter (dose = 0.2 mmol/kg).

MRI measurements were performed on a Siemens Symphony 1.5 T scanner. A 2-D SPGRE pulse sequence ($T_R/T_E$ = 15 ms/ 4.1 ms, FOV = 10 cm x 10 cm, matrix size = 128 x 128, slice thickness = 5 mm) was employed, with a different flip angle for each animal ($\alpha$ = 15° - 24° - 54°). To avoid differences in the calculation of the $T_{10}$-map, each animal underwent 3 series

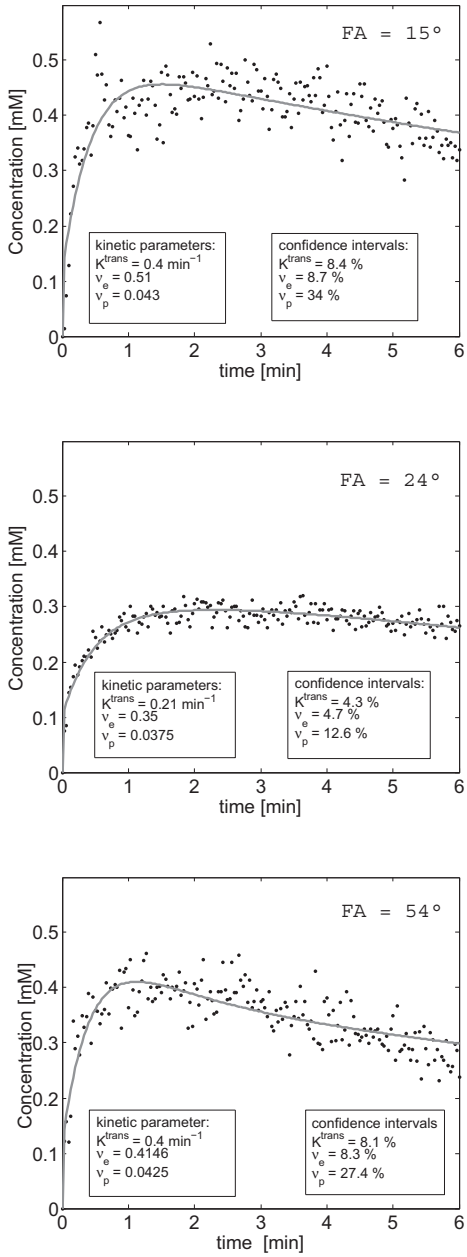


**Figure 5.7:** In vivo measured concentration curves (black points) with a SPGRE pulse sequence ($T_R/T_E$ = 15/4.1 ms, Gd-DOTA) in the tumor of three mice at different flip angles. The fit to the TK model is also shown (grey full line). Kinetic parameter estimates and their respective 95% confidence intervals are mentioned.

of pre-contrast measurements with the three flip angles ($\alpha = 15° - 24° - 54°$, 25 images/series). The $T_{10}$-map of the tumor was calculated with a method described by Cheng et al. [50]. After contrast injection, a dynamic series was started with one of the three flip angles in which 185 images were captured with a temporal resolution of 2s. Postprocessing of the images was done in Matlab. Concentration curves were calculated for every pixel in the region of interest around the tumor, based on the relative signal enhancement $(S - S_0)/S_0$ [30] and the $T_{10}$-map. $S_0$ was determined as the mean signal intensity from the pre-contrast series with the identical flip angle as the dynamic series. In vivo Gd-DOTA relaxivities were taken from literature (table 2.2 or [44]). The bolus arrival time was manually determined. The fitting of the concentration curves to the kinetic model (eq. 5.23) was performed in Matlab, with a standard AIF for Gd-DOTA from literature [169]. Pixels with a $R^2$-value smaller than 0.5 were removed from the analysis. To assess the reproducibility of the kinetic parameter estimates, the 95% confidence intervals were calculated for each parameter with a method described in the next chapter.

Fig. 5.7 shows three concentration curves, measured in three different test animals at different flip angles (these concentration curves were selected as they exhibit the highest $R^2$-value over the region of interest in each animal). The fit to the Tofts kinetic model, the estimated kinetic parameter values and their percentage confidence intervals are also mentioned in the figures. Table 5.4 contains the mean kinetic parameter values for the complete tumor region and their mean percentage confidence intervals. In addition the concentration range is mentioned, for which the employed flip angle is the optimal flip angle (calculated with $T_{10}$ set as the average value of the tumor region). From visual inspection of fig. 5.7 it can be seen that the flip angle of 24° results in the smallest concentration uncertainties. This is explained by the concentration ranges $\Delta C$ in table 5.4. A flip angle of 24° is optimal for a concentration range of 0.57 mM in the tumor, while the other flip angles are suboptimal for the measured concentration ranges. Although the average kinetic parameter values are not identical in the three animals, it is clear from both fig. 5.7 and table 5.4 that flip angle optimization can reduce the confidence intervals of the kinetic parameter estimates as a consequence of the reduced concentration uncertainty on the measured curves.

## 5.7 Optimization strategy: overview and critical analysis

### 5.7.1 Optimization overview

Clinical relevance of kinetic parameters is crucially dependent on their precision and the associated reproducibility of the complete DCE-MRI & kinetic

modeling technique. Increasing noise variance on measured concentration values has been shown to decrease $K^{trans}$-precision [23]. This concentration uncertainty, arising from the non-linear signal intensity equation, is highly dependent on the sequence parameters and the CA concentration itself [30]. Mostly the sequence parameters are determined as a trade-off between temporal and spatial resolution, field of view and SNR. However for SPGRE-pulse sequences, a freedom is introduced by the flip angle of the excitation pulse. A typical DCE-MRI investigation comprises a multiplicity of parameters and variables, from native relaxation times of the tissue of interest and CA relaxivity coefficients to the pulse sequence parameters and CA concentration ranges (see table 5.1). Many of these can be calculated, measured or estimated before the DCE-MRI investigation starts, and can therefore be used to select the best suitable value for the flip angle. We have distinguished between $\alpha_C$, the flip angle minimizing concentration uncertainty for a single concentration in the tissue of interest, and $\alpha_{opt}$, the best suitable flip angle for a complete concentration range in the tissue of interest. $\alpha_C$ can be considered as a specific case of $\alpha_{opt}$, and therefore we will restrict our discussion to $\alpha_{opt}$.

Our analysis has shown that for the selection of $\alpha_{opt}$, the multiplicity of DCE-MRI variables can be reduced to a set of 3 dimensionless quantities. $R_1^{min}T_R$ and $\Delta R_1 T_R$ comprise the $R_1$-range the study wants to cover and its associated effects, while $\gamma = \frac{r_2 T_E}{r_1 T_R}$ is a measure for the $R_2^*$-induced signal decrease that will accompany any change in $R_1$. It was demonstrated that $R_1$- and $R_2^*$-effects may safely be decoupled for physiological concentration ranges in most human tissues, leading to a straightforward procedure to determine the optimal flip angle:

1. Calculate/estimate $R_1^{min}T_R$ and $\Delta R_1 T_R$ for the study
2. Extract $\alpha_{opt}$ from the contour plot in fig. 5.4A
3. Calculate $\gamma$ and determine $R_{1mm}T_R$ for $\alpha_{opt}$ from the corresponding contour plot in chapter 4 (fig. 4.2)
4. Verify that $R_1^{min}T_R + \Delta R_1 T_R < R_{1mm}T_R$

If this latter condition is not satisfied, the decoupling presumption no longer holds and a computational optimization method based on eq. 5.18 is imposed or it is impossible to measure the premised $R_1$ unambiguously at the given $\gamma$-value. However, this situation is only likely at high $T_R$-values and arterial CA concentrations. Our results from table 5.3 show that this procedure provides sufficient estimates for the optimal flip angle for the typical tissue (0-2mM) and arterial (0-10 mM) concentration ranges in the 10 DCE-MRI studies from table 5.2. For the two studies with the highest $T_R$ [37, 66], the condition in step (iv) is not satisfied for an arterial concentration range. In these cases, a reduction of $T_R$ or a narrowing of the intended concentration range is necessary to allow flip angle optimization. A realistic complication of

this procedure may occur when the flip angle is restricted by specific absorption rate (SAR) guidelines or slice profile considerations [42]. If 2D-spatially selective RF-pulses are employed, the slice profile at high flip angle may become increasingly non-uniform, diminishing the accuracy of SPGRE signal intensity equation (see section 2.7 or [51]). In this case a suboptimal flip angle value can be derived using fig. 5.2. By determining upper and lower bounds for the flip angle, from the $\alpha_C$-values of $R_1^{min}T_R$ and $R_1^{max}T_R$ in fig. 5.2A (similar to the dotted line), a trade-off can be made between concentration uncertainty and SAR or slice profile restrictions.

### 5.7.2 Potential and shortcomings of flip angle optimization

A possible difficulty of the described method lies in the determinination of appropriate values of $R_1^{min}T_R$ and $\Delta R_1 T_R$ a priori. $R_1^{min}$ can be determined from the maximum $T_{10}$ in the tissue of interest. However, when $\Delta R_1/2 > R_1^{min}$, it was shown that the native relaxivity rates of the tissue of interest do not have a significant influence on $\alpha_{opt}$. This is of particular interest in blood, where for Gd-DTPA concentrations above 0.4-0.5 mM, $\alpha_{opt}$ solely depends on the expected concentration range. This latter statement is confirmed by the optimal flip angle variation with the concentration range in the right column of fig. 5.6 for the two AIF determination strategies. If only one tissue of interest is imaged, $\Delta R_1$ can be calculated from the expected concentration range and the relaxivity coefficient of the CA under investigation. When the AIF is determined from the MRI-images or the reference region method is used, multiple tissues are subject of the DCE-MRI investigation. $R_1^{max}$ is then to be calculated separately in every tissue of interest based on the various concentration ranges and the native $T_1$ and $\Delta R_1$ is set to the maximum difference between $R_1^{max}$ and $R_1^{min}$. The expected concentration range is difficult to determine as it will depend on unknown physiological characteristics that may vary across various patients and different pathologies. However, as numerous studies have described the concentration curves found in many tumor types, reasonable estimates of the ranges can be made [10, 21]. In addition, fig. 5.5 and the $\Delta\sigma_C$ values from table 5.3 have shown that our method is robust for misestimation of the concentration range. This statement is reinforced by our kinetic modeling simulations, which are designed in accordance with the algorithm above ($T_{10}$ set to its maximal value for the calculation of $\alpha_{opt}$). It should however be kept in mind that $\alpha_{opt}$ is determined as a trade-off between uncertainty on low and high concentrations in the expected range. Extending the range impels higher $\alpha_{opt}$-values, at the expense of increased uncertainty on the lowest CA concentrations (fig. 5.5). Our simulations also indicate that a flip angle optimization in accordance with our algorithm effectively enhances the reproducibility of the kinetic parameter estimates. In combination with the robustness of our technique, the simplicity of the algorithm and the lack

of computational optimization methods, our $\alpha_{opt}$ can be considered as a very good a priori selection for the flip angle.

As mentioned in the introduction, it is useful to compare our results to those of Parker et al., who measured the standard deviation on every time point of their population averaged AIF. They found very good reproducibility of the second pass peak and the AIF tail (1-2mM), but they encountered a 50% standard deviation on the first pass averaged peak concentration of 6mM [139]. Neglecting interindividual differences in the AIF peak, this is in agreement with our findings as we predicted that the employed flip angle of 20° is optimal for measuring concentration up to 2mM (table 5.3). Arterial concentration (up to 10mM) should be measured at a 40°-flip angle, which would decrease $\sigma_C$ at 6mM by 87%.

The in vivo measurements performed in this study can be considered as a proof-of-concept of our optimization algorithm. It is clear that the reproducibility of the kinetic estimates, expressed as the 95% confidence intervals [35], can be reduced by using an optimized value for the flip angle. These confidence intervals could be reduced with 43% for $K^{trans}$, 39% for $\nu_e$ and 51% for $\nu_p$. Although this reduction can partially be caused by a better model validity of the Tofts model for the measured concentration curves or by the unequal averages of the kinetic parameters in the different animals, fig. 5.6 confirms that the reduced concentration noise is the main cause for the increased reproducibility. A more rigorous validation of the proposed optimization strategy, with a higher number of subjects, should be performed with a study similar to the one of Galbraith [66]. A similar study could also incorporate the individually measured AIF strategy, which we could not investigate in our mice experiments. Comparison of our simulation results with the outcome of the in vivo measurements is difficult, as it concerns another AIF and consequently different concentration ranges. However, both results confirm that $\nu_p$ is the most senstitive parameter to the flip angle optimization.

Obviously, the exact values of $\alpha_{opt}$ are determined by the optimization criterion (eq. 5.21). Other criterions could be employed, such as minimizing the average absolute or relative concentration uncertainty in a given range. Apart from being severely influenced by $T_2^*$-effects (eq. 5.11), the corresponding $\alpha_{opt}$ would not account equally for every single concentration in the range. In our criterion, every concentration has a maximum weight of 1. As in DCE-MRI no a priori information about the particular concentrations to be measured is available (apart from the range), the criterion assures any concentration to have the highest possible precision. It therefore provides the most suitable flip angle to be chosen in advance. Moreover, we claim that other optimization strategies will be less robust to the choice of the concentration range, due to unequal weights of the different concentrations in that range. In the theoretical analysis we have considered finite SNR as the only error source. In

comparison to Schabel & Parker [30], no uncertainty on the pre-contrast signal intensity $S_0$ was taken into account. $S_0$ is used in practice to determine the CA concentration from signal intensity and tissue of interest native relaxation rates. $S_0$ uncertainty leads to a concentration detection limit, beneath which no CA concentration values can be measured and affects $\sigma_C$ for small CA concentrations ($< 0.1$ mM). Therefore the optimal flip angle for these concentration values will also depend on $S_0$ and the $\sigma_C$-values resulting from our analysis will be an underestimation. However, our approach can be justified as the $S_0$ uncertainty can be reduced as low as necessary by increasing the number of pre-contrast scans. Also, including this error source in our analysis would for instance make $\alpha_C$ subject to $\gamma$, $R_1T_R$, $R_{10}T_R$ and the number of pre-contrast scans, imposing the need for computational optimization for any study design. It should however be kept in mind that our optimal flip angle is only valid for concentration ranges that sufficiently exceed the detection limit, available from Schabel & Parker [30]. Moreover it should be mentioned that the use of $\alpha_{opt}$ will not enhance the accuracy of the kinetic parameters. Bias in kinetic estimates is caused by many error sources, such as partial volume or inflow effects, errors in $r_1$ or $r_2$ [30, 44], misestimation of $T_{10}$ [50] or improper knowledge of the AIF [141], etc. These errors do not disappear when using an optimized flip angle. However, the reproducibility of the kinetic estimates can be increased by using an optimal flip angle without making other sacrifices. For several kinetic modeling applications, this reproducibility is far more important than the accuracy of the kinetic parameters. For instance, in therapy evaluation by comparing pre- and post-therapy kinetic parameter values [131, 135], an increased reproducibility can severely enhance the sensitivity of the combined DCE-MRI and kinetic modeling technique. Flip angle optimization in DCE-MRI can therefore be an important step towards a more widespread clinical acceptance of quantitative DCE-MRI [21].

# Appendix: Mathematical derivations

## Flip angle $\alpha_C$

To obtain $\alpha_C$ the eq. 5.14 has to be solved. Omitting all factors independent of $\alpha$ in eq. 5.11, renders eq. 5.14 equivalent to:

$$\frac{d}{d\alpha}\left[\frac{E_1 sin(\alpha)(1-cos(\alpha))}{(1-cos(\alpha)E_1)^2} - \gamma\frac{sin(\alpha)(1-E_1)}{(1-cos(\alpha)E_1)}\right] = 0 \tag{5.25}$$

If we set $x = cos(\alpha)$, this yields a quadratic equation in $x$:

$$\begin{aligned} x^2\left[E_1(E_1-2)+\gamma E_1(1-E_1)\right] \; + \\ x\left[(1+E_1)E_1-\gamma(1-E_1)(1+E_1^2)\right] \; + \\ \left[(1-2E_1)E_1+\gamma E_1(1-E_1)\right] \;=\; 0 \end{aligned} \tag{5.26}$$

The discriminant of this quadratic equation can be simplified:

$$D = (1 - E_1)^2(9E_1^2 - 2\gamma E_1(1 - E_1^2) + \gamma^2(1 - E_1^2)^2) \tag{5.27}$$

The two solutions for x are given by:

$$x^{\pm} = \frac{-E_1(E_1 + 1) + \gamma(1 - E_1)(1 + E_1^2) \pm \sqrt{D}}{2E_1((E_1 - 2) + \gamma(1 - E_1))} \tag{5.28}$$

Now it should be investigated which of both solution can only attain values between -1 and +1. However, it is easier to state that physically, in the limit for $\gamma \to 0$, the solution should be identical to the pelc expression:

$$\lim_{\gamma \to 0} x^{+} = \frac{1 - 2E_1}{E_1 - 2} \tag{5.29}$$

$$\lim_{\gamma \to 0} x^{-} = 1 \tag{5.30}$$

$x^+$ is therefore the only solution of eq. 5.14.

# Chapter 6

# Estimators for pharmacokinetic modeling & confidence intervals for pharmacokinetic parameters

## 6.1 Introduction

### 6.1.1 Post-processing protocol

One of the main issues in pharmacokinetic modeling of DCE-MRI data is the absence of a standardized post-processing protocol [2, 19, 21]. Such protocol should comprise both an appropriate estimation method and a procedure to generate accurate confidence intervals for the kinetic parameters. An estimator is nothing more than a mathematical expression that is minimized with respect to a set of parameters, to obtain the most likely values for those parameters. The most familiar is the least square estimator (LSQ), that minizes the sum of squared differences between the observed concentrations and the model concentrations. It is employed by most authors for its simplicity and robustness [66, 140]. LSQ estimation is optimal for data that exhibit homoskedastic, i.e. with equal variance, gaussian noise. Several authors, however, have shown that when accurate conversion methods are used to calculate CA concentration from MR signal intensity, the variance of the CA concentration is heteroskedastic, i.e. varies with the concentration values itselves [25, 30]. This was confirmed by our analysis in chapter 4. For such heteroskedastic data, LSQ estimation may not be optimal, and the resulting

uncertainty on the kinetic parameters may be lower when maximum likelihood (MLM) estimation is used. A MLM estimator obtains best-fit values for the kinetic parameters by maximizing the likelihood function of the observation. This likelihood function accounts for the varying concentration variance and physically represents the probability that the measured concentration data truly occur. Generally, MLM estimators deliver the most precise estimates of the model parameters and their advantages have been demonstrated in other MRI related fitting problems [170]. In literature, several authors have investigated the influence of the estimation technique on the accuracy and the precision of the kinetic parameters. However, they mainly focussed on the joint estimation of the kinetic parameters and the arterial input function (AIF) [150] or the bolus arrival time [35, 113, 171]. None of these studies incorporates the heteroskedasticity of the concentration data.

The second and even more significant part of a standardized post-processing protocol is the construction of accurate confidence intervals for the kinetic parameter estimates. CI's are of crucial importance in several applications that compare pre- and post-treatment kinetic parameters, in order to reliably evaluate therapy or to demonstrate the anti-angiogenic effect of new vascularization targeting compounds. The statistical significance of an observed kinetic parameter change is totally dependent on an accurate estimation of the CI's for that parameter. In addition they are indispensable for the intercomparison of kinetic modeling results from different scanning sites [2], especially as we have shown that noise on the concentration curve is dependent on the SPGRE pulse sequence parameters. Nevertheless, the construction of CI's for kinetic parameter estimates remains uninvestigated in literature.

The aim of this chapter is to investigate the use of MLM estimation for the fitting of pharmacokinetic models to DCE-MRI data. It starts with a practical example to illustrate the heteroskedasticity of the concentration data and to demonstrate the advantages of a MLM estimator. Afterwards in section 6.2 an overview is given of the current estimators for pharmacokinetic modeling. In section 6.3 an expression is derived for the MLM estimator based on the statistical distribution of MR-measured concentrations as obtained in chapter 4. The performance of this estimator is compared to LSQ by means of simulations. Section 6.4 describes and evaluates the practical calculation methods of confidence intervals for both the LSQ and MLM estimators. Finally, in section 6.5 the sensitivity of both estimators to errors in DCE-MRI parameters, such as flip angle or native relaxation time, is investigated.

### 6.1.2 Practical example

MLM estimation takes into account the varying variance of the CA concentrations. As this variance strongly depends on the pulse sequence parameters,

**Table 6.1:** SPGRE-pulse sequence parameters, temporal resolution and total scan time for the studies of Batchelor et al. [135], Parker et al. [139] and Yang et al. [141]

| Study | Study name | $T_R$ [ms] | $T_E$ [ms] | $\alpha$ [°] | $\Delta t$ [s] | $T_{scan}$ [s] |
|---|---|---|---|---|---|---|
| Batchelor | PS1 | 5.7 | 2.73 | 10 | 5 | 250 |
| Parker | PS2 | 4 | 0.82 | 20 | 5 | 375 |
| Yang | PS3 | 7.8 | 1.7 | 60 | 2 | 360 |

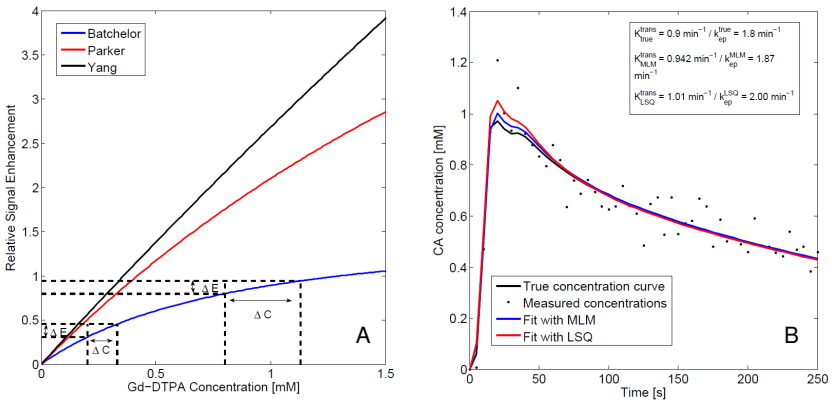


**Figure 6.1:** A. Relative signal enhancement versus Gd-DTPA concentration ($T_{10}$ = 675 ms.) for three SPGRE pulse sequence designs [135, 139, 141]. Heteroskedasticity is illustrated for PS1: identical noise levels on the signal intensity cause different noise levels on the concentration values. B. Practical example of the advantage of the MLM estimator. From the true concentration curve, a signal intensity curve is calculated and sampled (pulse sequence parameters and AIF from Parker et al. [139]). After the addition of gaussian noise these signal intensities are converted to the measured concentrations. These concentrations are fit to the TK model with both MLM and LSQ. MLM provides better estimates of the true kinetic parameter values because the highly noisy peak concentrations are given less weight.

the performance of MLM and LSQ is compared for three different pulse sequences from recent DCE-MRI literature [135, 139, 141]. All three studies employ a SPGRE pulse sequence, whose parameters are mentioned together with other pulse sequence properties in table 6.1. These pulse sequences

are chosen because their resulting concentration data will exhibit a different degree of heteroskedasticity: fig. 6.1A shows the variation of the relative signal enhancement E with the CA concentration in a physiologically relevant concentration range (0 mM to 1.5 mM) [1]. Due to the non-linear behaviour of the SPGRE signal intensity equation, the calculation of the CA concentration from noisy signal intensity curves causes heteroskedastic concentration data: while signal intensity uncertainty is unrelated to the CA concentration (i.e. $\Delta E$ is constant), the concentration uncertainty $\Delta C$ strongly depends on the CA concentration itself. It can be graphically inspected that PS1 (Batchelor) exhibits the highest degree of heteroskedasticity for physiological concentrations. The extent of heteroskedastity in PS2 (Parker) is mediocre, while PS3 (Yang) no heteroskedasticity is apparent from fig. 6.1A.

Fig. 6.1B shows a practical (simulation) example of the consequences of heteroskedasticity for the TK model (pulse sequence parameters from PS2, AIF from [139]). The black dots are the concentration values, calculated from the measured signal intensity in a tissue with [$K^{trans}$, $k_{ep}$]=[0.9 $min^{-1}$,1.8 $min^{-1}$]. From visual inspection the heteroskedasticity of the curve can be seen, with higher noise variances near the peak concentration. The MLM estimator ([$K^{trans}$, $k_{ep}$]=[0.942 $min^{-1}$, 1.87 $min^{-1}$]) considerably improves the kinetic parameter estimates in comparison with the LSQ estimator ([$K^{trans}$, $k_{ep}$]=[1.01 $min^{-1}$, 2.00 $min^{-1}$]). The MLM fitted curve resembles the true curve better, in particular around the peak. This example suggests the importance of employing a MLM estimator for DCE-MRI data.

### 6.1.3 Nomenclature & quantities

For clarity, table 6.2 contains an overview of the different symbols used throughout this chapter.

## 6.2 Overview of estimators for pharmacokinetic modeling

### 6.2.1 Least square estimator

Most DCE-MRI studies employ a LSQ-estimator to obtain best-fit values of the pharmacokinetic parameters. Suppose a DCE-MRI experiment measures n concentration values, $C_i = C_1..C_n$, on n time points, $t_i = t_1..t_n$, that should be fit to a kinetic model $C_T(t)$. The LSQ estimator minimizes the sum of squared residuals $ssq$ with respect to the parameter vector $\boldsymbol{\theta}$.

[1] it may be recalled from chapter 4 that the CA concentration is calculated from the relative signal enhancement

**Table 6.2:** Symbols

| Symbol | Definition |
|---|---|
| $\boldsymbol{C}$ | measured concentration vector |
| $C_T(t, \boldsymbol{\theta})$ | General pharmacokinetic model |
| $\boldsymbol{\theta}$ | Parameter vector |
| $L(\boldsymbol{C} \mid \boldsymbol{\theta})$ | Likelihood function |
| $\sigma_S$ | Signal intensity standard deviation |
| $\sigma_C$ | Concentration standard deviation |
| $\boldsymbol{\Sigma}$ | covariance matrix |
| $F_{ij}$ | Fisher matrix elements |

$$ssq(\boldsymbol{\theta}) = \sum_{i=1}^{n} [C_i - C_T(t_i, \boldsymbol{\theta})]^2 \tag{6.1}$$

The success of LSQ is mainly due to its high robustness and its simplicity for implementation. LSQ is the maximum likelihood estimator for data with homoskedastic gaussian error terms.

### 6.2.2 Bayesian fitting method

Orton et al. have proposed a bayesian estimation method for fitting DCE-MRI data to a pharmacokinetic model. The theory is based on the calculation of the a posteriori distribution of the parameter vector $\boldsymbol{\theta}$, given the measured concentration vector $\boldsymbol{C}$, $p(\boldsymbol{\theta}|\boldsymbol{C})$. This calculation requires the knowledge of the conditional distribution for the concentration vector $\boldsymbol{C}$ given $\boldsymbol{\theta}$, $p(\boldsymbol{C}|\boldsymbol{\theta})$, and a prior distribution for $\boldsymbol{\theta}$, $p_{prior}(\boldsymbol{\theta})$, which are both assumed to be known. According to Bayes' rule, the a posteriori distribution of $\boldsymbol{\theta}$ can then be calculated as:

$$p(\boldsymbol{\theta}|\boldsymbol{C}) = \frac{p(\boldsymbol{C}|\boldsymbol{\theta})p_{prior}(\boldsymbol{\theta})}{p(\boldsymbol{C})} \tag{6.2}$$

$$p(\boldsymbol{C}) = \int p(\boldsymbol{C}|\boldsymbol{\theta})p_{prior}(\boldsymbol{\theta})d\boldsymbol{\theta} \tag{6.3}$$

After marginalization of $p(\boldsymbol{\theta}|\boldsymbol{C})$, the best-fit values of the pharmacokinetic parameters are obtained as those values for which the marginal distribution attain their maximum. This fitting method has the advantage that, apart from the kinetic parameters, it can achieve a robust estimate of the onset time. In addition, it has shown to reduce bias when compared to LSQ and the

confidence intervals as determined from the marginal distribution were proven to be highly accurate [35]. Furthermore, the theory can be adapted to include the heteroskedastic distribution of the concentration data. Nevertheless, the implementation of the procedure, in particular the calculation of the integral in eq. 6.3, is complicated and requires numerical integration, which is susceptible to errors.

## 6.3 Maximum likelihood estimator

In this section, a maximum likelihood estimator is derived for the concentration distribution as obtained in chapter 4. Afterwards the performance of this estimator is compared to the LSQ estimator by means of simulations.

### 6.3.1 Theoretical derivation

Consider again a series of n measured concentration values, $\boldsymbol{C} = C_1...C_n$, on time points $t_1...t_n$, that have to be fit to a kinetic model equation $C_T(t_i, \boldsymbol{\theta})$. The MLM estimator aims at finding the best-fit values for the parameter vector $\boldsymbol{\theta}$ by maximizing the likelihood function $L(\boldsymbol{C} \mid \boldsymbol{\theta})$. This likelihood function is a function of the parameter vector, and denotes the probability that the joint observation of $C_1...C_n$ truly occurs. Mathematically, it is the product[2] of the individual probability distributions of each measured concentration, $f_C(C_i \mid C_T(t_i, \boldsymbol{\theta}))$. As shown in chapter 4, these individual probability distribution are gaussian, with expectation value $C_T(t_i, \boldsymbol{\theta})$ and with variance $\sigma_C = \sigma_S \left[\frac{dS}{dC}\right]^{-1}$, evaluated in $C_T(t_i, \boldsymbol{\theta})$.

$$L(\boldsymbol{C} \mid \boldsymbol{\theta}) = \prod_{i=1}^{n} f_C(C_i \mid C_T(t_i, \boldsymbol{\theta})) \tag{6.4}$$

$$f_C(C_i \mid C_T(t_i)) = \frac{1}{\sqrt{2\pi}\sigma_C} e^{-\frac{(C_i - C_T(t_i, \boldsymbol{\theta}))^2}{2\sigma_C(t_i, \boldsymbol{\theta})^2}} \tag{6.5}$$

$$\sigma_C(t_i, \boldsymbol{\theta}) = \sigma_S \left[\frac{dS}{dC}\right]_{C=C_T(t_i, \boldsymbol{\theta})}^{-1} \tag{6.6}$$

By taking the natural logarithm of the likelihood function [3], it can easily be shown that maximizing $L(\boldsymbol{\theta})$ is equivalent to minimizing:

$$-log\left[L(\boldsymbol{\theta})\right] = \sum_{i=1}^{n} \frac{(C_i - C_t(t_i, \boldsymbol{\theta}))^2}{2\sigma_C(C_t(t_i, \boldsymbol{\theta}))^2} - log\left[\frac{1}{\sigma_C(C_t(t_i, \boldsymbol{\theta}))}\right] \tag{6.7}$$

[2] As the measurements of the concentrations are independent of each other

[3] the so-calles log-likelihood function

By defining the SNR as $M_0/\sigma_S$ and using equation 6.6, this can be rewritten as:

$$-2log\left[L(\boldsymbol{\theta'})\right] = \sum_{i=1}^{n}\left[C_i - C_T(t_i,\boldsymbol{\theta})\right]^2\left[\frac{dS'}{dC_T(t_i,\boldsymbol{\theta})}\right]^2 SNR^2 - 2log\left[\frac{dS'}{dC_T(t_i,\boldsymbol{\theta})}SNR\right] \tag{6.8}$$

$\frac{dS'}{dC_T(t_i,\boldsymbol{\theta})}$ denotes the derivative of the normalized signal intensity (i.e. $S/M_0$) with respect to the CA concentration, evaluated in $C = C_T(t_i,\boldsymbol{\theta})$. $\boldsymbol{\theta'}$ is the extended parameter vector, as the MLM estimator requires the additional estimation of the SNR. For example, for the TK model, the MLM estimator finds the best fit values for $K^{trans}$ and $\nu_e$, by minimizing eq. 6.8 with respect to $K^{trans}$, $\nu_e$ and SNR.

### 6.3.2 Simulations

A simulation environment in Matlab (Mathworks, Ma) was written to compare the performance of the MLM and LSQ estimator for the fitting of a measured concentration curve to 2 kinetic models, the TK-model (eq. 6.9) and the extended TK model (eq. 6.10):

$$C_T^{TK}(t) = K^{trans}\int_0^t C_p(t')exp[-k_{ep}(t-t')]dt' \tag{6.9}$$

$$C_T^{ETK}(t) = \nu_p Cp(t) + K^{trans}\int_0^t C_p(t')exp[-k_{ep}(t-t')]dt' \tag{6.10}$$

In comparison with the model equation from chapter 3, the parameter $k_{ep} = K^{trans}/\nu_e$ will be used throughout this chapter, instead of the physiological parameter $\nu_e$. The reason is that many studies have proposed clinical applications by the use of $K^{trans}$ or $k_{ep}$, rather then $\nu_e$. Therefore the accurate and precise estimation of $k_{ep}$ and its confidence intervals may be of greater interest to the DCE-MRI community. The parameter vectors for both models and for both estimator are summarized in table 6.3.

For the TK model, tissue curves were generated from eq. 6.9, for 4 combinations of $K^{trans}/k_{ep}$ (1.2/2.4, 1.2/6, 0.3/0.6, 0.3/1.5). Physiologically these kinetic parameter combinations are representative of tissues with a high (1.2 $min^{-1}$) and a low (0.3 $min^{-1}$) transendothelial transfer constant both combined with a large ($\nu_e = 0.5$) and a small ($\nu_e = 0.2$) EES fraction. For the ETK model, these 4 parameter couples were all combined with a large ($\nu_p = 0.1$) and a small ($\nu_p = 0.05$) plasma volume fraction. As AIF the parametrized form of the population averaged AIF obtained by Parker et al. was used ( [139] or eq. 3.16). Hematocrit was assumed to be 0.4. The tissue curves were generated with a temporal resolution of 0.5 s, to avoid errors caused by aliasing. From these tissue concentration curves, signal intensity curves were calculated for three pulse sequences from recent DCE-MRI literature [135,139,141]. All three

**Table 6.3:** Parameter vectors estimated from MLM and LSQ for TK model and ETK model

| model | LSQ | MLM |
|---|---|---|
| TK model | [$K^{trans}$, $k_{ep}$] | [$K^{trans}$, $k_{ep}$, SNR] |
| ETK model | [$K^{trans}$, $k_{ep}$, $\nu_p$] | [$K^{trans}$, $k_{ep}$, $\nu_p$, SNR] |

studies adopted SPGRE pulse sequences (signal intensity equation can be found in chapter 2), with parameters as mentioned in table 6.1. White gaussian noise is added to the signal intensity curves, and a sampling procedure is performed with the temporal resolution of the corresponding pulse sequence set-up, for the duration of $T_{scan}$ (table 6.1). SNR ($M_0/\sigma_S$) is set to 400. The resulting noisy signal intensity curve is reconversed to a noisy tissue concentration curve by means of the relative signal enhancement, as explained in chapter 4. This noisy concentration curve is fitted to the corresponding model with both estimators. For the MLM estimator the signal intensity derivatives with respect to the concentration are adopted from chapter 4. This procedure is repeated $10^4$ times for every kinetic parameter combination and the performance of the estimators for a parameter $\theta$ is compared based on their relative root mean squared error (m is the number of simulations):

$$rmse(\theta) = 100\% \frac{\sqrt{\sum_{i=1}^{m} (\hat{\theta}_i - \theta)^2}}{\theta} \tag{6.11}$$

Table 6.4 contains the rmse-values for both estimators at the kinetic parameter combinations under consideration for the TK model. Overall, MLM is never worse than LSQ and can lead to significant reduction in rmse-values. In particular, in highly permeable/perfused tissues, rmse-reduction up to 17% for $K^{trans}$ and 13% for $k_{ep}$ can be achieved with MLM. For small $K^{trans}$ the rmse-improvement with MLM is less. In general, the advantages of the MLM estimators are mostly pronounced for PS1 followed by PS2. For the particular case of $K^{trans}/k_{ep} = 1.2/6\ min^{-1}$, fig. 6.2 shows the boxplots of the simulated distribution of relative estimation errors $\frac{\hat{\theta}-\theta}{\theta}$. It is clear that for the three pulse sequences MLM reduces the standard deviation of this distribution and the estimation bias, thereby increasing both the precision and the accuracy of the kinetic parameter estimates. For the ETK model, table 6.5 contains the rmse-values. MLM never performs worse than LSQ and rsme reductions up to 11% for $K^{trans}$ and 14% for $k_{ep}$ and $\nu_p$ can be achieved (PS1). Again, MLM causes rmse-reduction for PS1 and PS2 in particular, while the estimates from PS3 are minimally affected by the use of MLM. This can be understood from fig. 6.1A, as the degree of heteroskedasticity of the data evolve from high in PS2, over mediocre in PS2, to very low in PS3. As expected the MLM estima-

**Table 6.4:** Root mean squared error values for the TK model

| Study | True values | $K^{trans}$ | | $k_{ep}$ | |
|---|---|---|---|---|---|
| | $K^{trans}/k_{ep}$ | LSQ | MLM | LSQ | MLM |
| | $[min^{-1}]/[min^{-1}]$ | [%] | [%] | [%] | [%] |
| PS1 | 1.2/2.4 | 7.3 | 6.3 | 7.2 | 6.3 |
| | 1.2/6 | 16.8 | 13.9 | 17.3 | 15.2 |
| | 0.3/0.6 | 4.6 | 4.6 | 6.7 | 6.7 |
| | 0.3/1.5 | 8.3 | 8.2 | 9.0 | 8.8 |
| PS2 | 1.2/2.4 | 4.8 | 4.6 | 4.8 | 4.6 |
| | 1.2/6 | 14.0 | 13.4 | 13.0 | 12.4 |
| | 0.3/0.6 | 3.6 | 3.6 | 4.5 | 4.5 |
| | 0.3/1.5 | 8.6 | 8.5 | 9.1 | 9.0 |
| PS3 | 1.2/2.4 | 2.9 | 2.8 | 3.0 | 3.0 |
| | 1.2/6 | 6.5 | 6.4 | 6.8 | 6.7 |
| | 0.3/0.6 | 3.0 | 3.0 | 3.8 | 3.8 |
| | 0.3/1.5 | 6.9 | 6.9 | 7.4 | 7.4 |

tor is most usefull for the most heteroskedastic pulse sequences. The boxplots for the ETK model are not shown because the results are similar to fig. 6.2 with improvements in both accuracy and precision of the kinetic parameter estimates.

## 6.4 Confidence intervals for pharmacokinetic parameters

### 6.4.1 Correlation matrix & Cramer-Rao lower bounds

CI's of kinetic modeling estimates are obtained based on the estimation of the covariance matrix $\mathbf{\Sigma}$. For the Tofts model under consideration, a 95% CI for the parameter $\theta_j$ can be constructed using the diagonal elements of the covariance matrix:

$$CI_{95} = \hat{\theta}_j \pm 1.96{\Sigma_{jj}}^{1/2} \tag{6.12}$$

The practical calculation of the covariance matrix depends on the estimator. For maximum likelihood estimators, the covariance matrix can be calculated as the inverse of the Fisher information matrix (FIM). The FIM is a concept of estimation theory, that in the particular case of kinetic modeling, emphasizes how much information about the kinetic parameter vector is carried by the observation of the n measured concentrations. It was first introduced by Edgeworth & Fisher, while H. Cramer and C.R. Rao showed that the diagonal elements of the inverse FIM express an under bound on the variance of an estimated parameter [172]. As MLM estimators exhibit the lowest possible uncertainty among all estimators, the inverse FIM is used as an estimate for

**Table 6.5:** Root mean squared error values for the ETK model

| Study | True values | $K^{trans}$ | | $k_{ep}$ | | $\nu_p$ | |
|---|---|---|---|---|---|---|---|
| | $K^{trans}/k_{ep}/\nu_p$ | LSQ | MLM | LSQ | MLM | LSQ | MLM |
| | $[min^{-1}]/[min^{-1}]/-$ | [%] | [%] | [%] | [%] | [%] | [%] |
| PS1 | 1.2/2.4/0.1 | 11.5 | 10.9 | 9.8 | 8.8 | 18.2 | 16.1 |
| | 1.2/2.4/0.05 | 10.2 | 10.2 | 8.8 | 8.4 | 25.7 | 24.8 |
| | 1.2/6/0.1 | 33.7 | 30.1 | 24.9 | 21.4 | 19.4 | 16.7 |
| | 1.2/6/0.05 | 29.3 | 26.7 | 21.3 | 18.7 | 30.3 | 28.0 |
| | 0.3/0.6/0.1 | 7.2 | 7.0 | 8.5 | 8.4 | 10.9 | 9.8 |
| | 0.3/0.6/0.05 | 6.2 | 6.2 | 7.9 | 7.9 | 13.9 | 13.4 |
| | 0.3/1.5/0.1 | 14.1 | 13.3 | 12.4 | 11.7 | 11.2 | 10.1 |
| | 0.3/1.5/0.05 | 11.9 | 11.7 | 10.8 | 10.5 | 15.5 | 14.8 |
| PS2 | 1.2/2.4/0.1 | 6.3 | 6.2 | 5.5 | 5.3 | 9.1 | 9.0 |
| | 1.2/2.4/0.05 | 6.5 | 6.1 | 5.4 | 5.3 | 16.3 | 16.2 |
| | 1.2/6/0.1 | 19.7 | 18.9 | 15.5 | 14.7 | 10.8 | 10.6 |
| | 1.2/6/0.05 | 18.9 | 18.4 | 15.1 | 14.5 | 19.8 | 19.6 |
| | 0.3/0.6/0.1 | 4.8 | 4.8 | 5.1 | 5.1 | 6.7 | 6.5 |
| | 0.3/0.6/0.05 | 4.6 | 4.6 | 5.0 | 5.0 | 11.9 | 11.9 |
| | 0.3/1.5/0.1 | 11.4 | 11.3 | 10.3 | 10.1 | 7.1 | 6.9 |
| | 0.3/1.5/0.03 | 11.0 | 10.9 | 10.2 | 10.1 | 12.8 | 12.7 |
| PS3 | 1.2/2.4/0.1 | 3.8 | 3.8 | 3.4 | 3.3 | 5.9 | 5.9 |
| | 1.2/2.4/0.05 | 3.8 | 3.8 | 3.3 | 3.3 | 11.5 | 11.5 |
| | 1.2/6/0.1 | 10.4 | 10.3 | 8.2 | 8.2 | 7.5 | 7.5 |
| | 1.2/6/0.05 | 10.4 | 10.4 | 8.1 | 8.1 | 15.9 | 15.9 |
| | 0.3/0.6/0.1 | 3.7 | 3.7 | 4.1 | 4.0 | 4.9 | 4.9 |
| | 0.3/0.6/0.05 | 3.7 | 3.7 | 4.1 | 4.1 | 9.2 | 9.2 |
| | 0.3/1.5/0.1 | 8.7 | 8.7 | 8.1 | 8.1 | 5.2 | 5.2 |
| | 0.3/1.5/0.05 | 8.6 | 8.6 | 8.1 | 8.1 | 10.4 | 10.4 |

the covariance matrix with MLM estimation. The mathematical expression of its elements, for an observed concentration vector $\boldsymbol{C}$, is given by:

$$F_{ij} = E\left[\frac{d\ [log\ L(\boldsymbol{C} \mid \boldsymbol{\theta})]}{d\theta_i}\frac{d\ [log\ L(\boldsymbol{C} \mid \boldsymbol{\theta})]}{d\theta_j}\right] \tag{6.13}$$

L is the likelihood function as described in eq. 6.4, whose explicit dependence on the measured concentration vector $\boldsymbol{C}$ is mentioned. In the framework of FIM, $\boldsymbol{C}$ should be regarded as a statistical variable and E denotes the expectation value among all possible values of $\boldsymbol{C}$. $\theta_i$ and $\theta_j$ are the individual elements of the kinetic parameter vector. For kinetic modeling estimates of DCE-MRI data, the FIM-elements reduce to (the mathematical derivation can be found in the appendix or in [25]).

$$F_{kl} = \sum_{i=1}^{n}\frac{dC_T(t_i,\boldsymbol{\theta})}{d\theta_k}\frac{dC_T(t_i,\boldsymbol{\theta})}{d\theta_l}(2\alpha_i^2 + \frac{1}{\sigma_C(t_i,\boldsymbol{\theta})^2}) \tag{6.14}$$

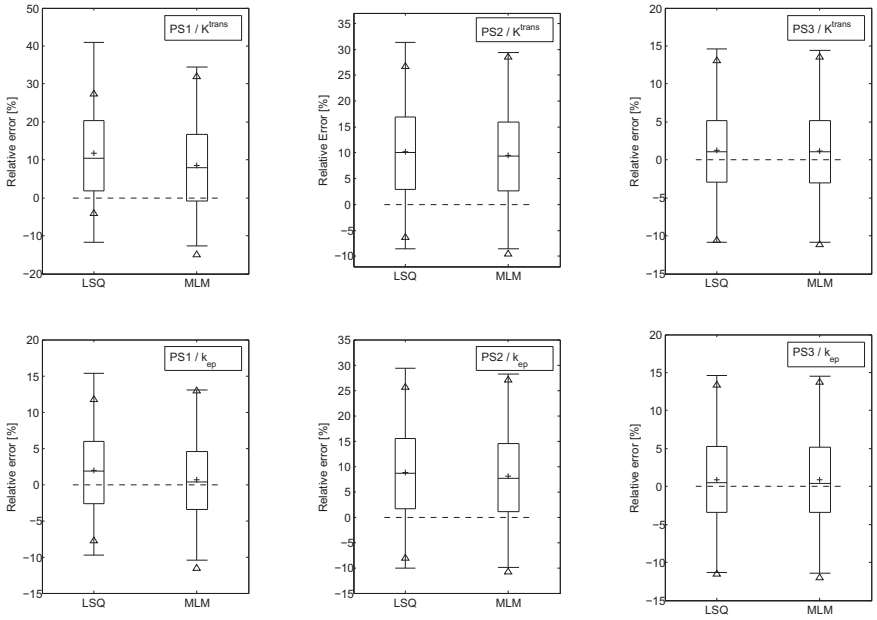


**Figure 6.2:** Boxplots of the relative error distribution (m = 10000) for the $K^{trans}$- and $k_{ep}$-parameters fitted from the Tofts model without vascular contribution. The simulation input values were $K^{trans}/k_{ep}$=1.2/6 $min^{-1}$. The error bars denote the 2.5%- and 97.5%-percentiles, the boxes indicate the quartiles and the plus is the mean value of the relative errors. The triangles show the average lower- and upperbounds of the MLM and LSQ constructed confidence intervals.

$$\alpha_i \quad = \quad \frac{d^2S/dC^2}{dS/dC}_{C=C_T(t_i,\boldsymbol{\theta})} \tag{6.15}$$

which in the framework of the MLM estimator can be rewritten as:

$$F_{ij} = \sum_{i=1}^{n} \frac{dC_T(t_i,\hat{\boldsymbol{\theta}})}{d\hat{\theta}_i} \frac{dC_T(t_i,\hat{\boldsymbol{\theta}})}{d\hat{\theta}_j} \left[ 2 \left( \frac{d^2S'/dC_T^2(t_i,\hat{\boldsymbol{\theta}})}{dS'/dC_T(t_i,\hat{\boldsymbol{\theta}})} \right)^2 + \left( \frac{dS'}{dC_T(t_i,\hat{\boldsymbol{\theta}})} S\hat{N}R \right)^2 \right]$$

S' is again the normalized signal intensity. $dC_T(t_i)/d\hat{\theta}_i$ denotes the derivative of the tissue concentration with respect to the kinetic parameter $\theta_i$, evaluated in the best-fit value $\hat{\theta}_i$.

**Table 6.6:** Observed coverages for the TK model

| Study | True values | $K^{trans}$ | | $k_{ep}$ | |
|---|---|---|---|---|---|
| | | LSQ | MLM | LSQ | MLM |
| | $[min^{-1}]/[min^{-1}]$ | [%] | [%] | [%] | [%] |
| PS1 | 1.2/2.4 | 80.2 | 95.5 | 84.0 | 95.0 |
| | 1.2/6 | 67.2 | 94.2 | 74.1 | 94.8 |
| | 0.3/0.6 | 95.4 | 95.2 | 95.5 | 95.3 |
| | 0.3/1.5 | 92.3 | 94.8 | 93.2 | 94.5 |
| PS2 | 1.2/2.4 | 86.2 | 93.2 | 88.6 | 93.6 |
| | 1.2/6 | 79.4 | 88.7 | 84.1 | 90.7 |
| | 0.3/0.6 | 94.6 | 94.9 | 95.1 | 95.1 |
| | 0.3/1.5 | 93.6 | 94.1 | 94.3 | 94.4 |
| PS3 | 1.2/2.4 | 93.9 | 94.8 | 94.1 | 94.9 |
| | 1.2/6 | 94.3 | 95.2 | 94.0 | 94.7 |
| | 0.3/0.6 | 95.3 | 95.3 | 95.1 | 95.2 |
| | 0.3/1.5 | 94.8 | 95.0 | 94.5 | 94.7 |

The covariance matrix for MLM estimates is therefore:

$$\boldsymbol{\Sigma}_{MLM} = \boldsymbol{F}^{-1} \tag{6.16}$$

### 6.4.2 Confidence intervals for least square

For LSQ estimators, most statistical software uses the hessian of $ssq$, evaluated in the $\hat{\boldsymbol{\theta}}$, as an estimate of the correlation matrix:

$$\begin{aligned} \boldsymbol{\Sigma}_{LSQ} &= \hat{\sigma}^2 \left[ \frac{\frac{1}{2}\delta^2 ssq}{\delta \hat{\boldsymbol{\theta}}^2} \right]^{-1} \\ \hat{\sigma}^2 &= \frac{ssq(\hat{\theta})}{n-p} \end{aligned} \tag{6.17}$$

$\hat{\sigma}^2$ is an estimate of the variance of the error terms, p is the number of parameters estimated. It can be checked that this formula concurs with the inverse of the FIM for homoskedastic gaussian concentration data, for which LSQ would be the maximum likelihood estimator.

### 6.4.3 Simulations

For the simulations described in the previous section, the 95%-CI's of the kinetic parameter estimates are calculated based on eq. 6.12 and eq. 6.17 & 6.16 for LSQ and MLM estimates respectively. For both parameters the coverage is calculated, i.e. the procentual number of simulations for which the

**Table 6.7:** Observed coverages for the ETK model

| Study | True values | $K^{trans}$ | | $k_{ep}$ | | $\nu_p$ | |
|---|---|---|---|---|---|---|---|
| | $K^{trans}/k_{ep}/\nu_p$ | LSQ | MLM | LSQ | MLM | LSQ | MLM |
| | $[min^{-1}]/[min^{-1}]/-$ | [%] | [%] | [%] | [%] | [%] | [%] |
| PS1 | 1.2/2.4/0.1 | 77.7 | 95.1 | 81.9 | 95.3 | 71.6 | 91.9 |
| | 1.2/2.4/0.05 | 80.9 | 94.3 | 82.7 | 94.5 | 71.0 | 94.2 |
| | 1.2/6/0.1 | 64.2 | 94.2 | 67.0 | 93.7 | 59.6 | 93.9 |
| | 1.2/6/0.05 | 68.0 | 94.9 | 71.1 | 94.0 | 69.2 | 94.1 |
| | 0.3/0.6/0.1 | 92.4 | 94.1 | 94.2 | 94.6 | 80.8 | 94.1 |
| | 0.3/0.6/0.05 | 94.7 | 94.7 | 95.0 | 94.9 | 94.3 | 95.0 |
| | 0.3/1.5/0.1 | 88.1 | 94.9 | 91.3 | 94.5 | 71 | 94.15 |
| | 0.3/1.5/0.05 | 90.6 | 94.4 | 91.9 | 94.5 | 84.2 | 94.0 |
| PS2 | 1.2/2.4/0.1 | 87.6 | 93.9 | 88.1 | 94.1 | 96.5 | 94.5 |
| | 1.2/2.4/0.05 | 87.5 | 93.5 | 87.9 | 93.8 | 89.5 | 94.0 |
| | 1.2/6/0.1 | 84.1 | 93.9 | 84.3 | 93.0 | 85.0 | 94.2 |
| | 1.2/6/0.05 | 85.6 | 93.8 | 85.0 | 93.0 | 87.7 | 94.5 |
| | 0.3/0.6/0.1 | 93.9 | 95.0 | 94.3 | 94.5 | 90.7 | 94.9 |
| | 0.3/0.6/0.05 | 94.2 | 94.5 | 94.4 | 94.5 | 93.3 | 94.5 |
| | 0.3/1.5/0.1 | 92.8 | 95.0 | 94.0 | 95.1 | 89.8 | 94.9 |
| | 0.3/1.5/0.05 | 94.2 | 94.9 | 93.9 | 94.9 | 91.4 | 94.4 |
| PS3 | 1.2/2.4/0.1 | 93.7 | 94.8 | 93.2 | 94.6 | 93.6 | 94.6 |
| | 1.2/2.4/0.05 | 93.7 | 94.7 | 93.3 | 94.6 | 93.8 | 94.5 |
| | 1.2/6/0.1 | 92.8 | 94.5 | 93.4 | 94.3 | 93.2 | 94.5 |
| | 1.2/6/0.05 | 93.0 | 94.6 | 94.5 | 95.0 | 93.6 | 95.2 |
| | 0.3/0.6/0.1 | 95.3 | 95.4 | 95.7 | 95.5 | 93.4 | 94.7 |
| | 0.3/0.6/0.05 | 95.1 | 95.1 | 94.7 | 94.8 | 95.5 | 95.5 |
| | 0.3/1.5/0.1 | 95.0 | 95.0 | 94.9 | 95.1 | 94.6 | 95.3 |
| | 0.3/1.5/0.05 | 94.9 | 95.0 | 94.6 | 94.6 | 94.0 | 94.5 |

true value of the parameter is contained within the constructed CI's.

The observed coverages of the 95%-CI's, calculated with eq. 6.17 and eq. 6.16 respectively, are mentioned in table 6.6 for the TK model. It is clear that the LSQ procedure consistently overestimates its own precision. The extent of this overestimation grows in tissues with high $K^{trans}$ or as the temporal resolution of the protocol decreases. The CI's for the MLM estimator exhibit coverages close to the expected 95%, with minimal dependence on the value of $K^{trans}$ or on the temporal resolution of the employed protocol. Significant overestimation of the precision of the MLM estimate is seen in only one specific case ($K^{trans}/k_{ep} = 1.2/6$, PS2). However, this effect is due to a bias in the estimated parameters, as can be seen from fig. 6.2. PS2 exhibits the highest bias in both $K^{trans}$ and $k_{ep}$ and therefore the probability that the true value is contained within the calculated CI is below 95%. In fig. 6.2 the average boundaries of the 95% CI's are depicted by triangles. A very good agreement between these boundaries and the 2.5 % and 97.5 % percentiles of the error distribution can be seen for MLM, also for the 1.2/6 $min^{-1}$ combination. This implies that even in this biased case, the CI is an excellent measure for the reproducibility of the experiment. The LSQ-constructed intervals are too small and can lead to erroneous conclusions when used as reproducibility measures for comparing pre- and post-treatment kinetic modeling results. For the ETK model, the observed coverages are mentioned in table 6.7. Again, LSQ calculated CI's severely overestimate the precision of the kinetic parameter estimates and are highly dependent on the kinetic parameter values and the pulse sequence settings. On the contrary, MLM calculated CI's are highly reliable and minimally dependent on pulse sequence or kinetic parameter value. In addition for this extended model, LSQ fails in delivering reliable CI's for $\nu_p$ even at small $K^{trans}$-values. Similar to the rmse-values, the use of MLM calculated CI's is most advantageous for PS1 and PS2. However, even for PS3 significant improvements in the CI's can be achieved with MLM.

## 6.5 Error sensitivity

From eq. 6.8 it is clear that the MLM estimator requires a number of parameters as the flip angle $\alpha$, the native longitudinal relaxation rate $R_{10}$ and the relaxivity coefficients $r_1$ and $r_2$, all abundant for LSQ estimation. As explained in chapter 2, it is characteristic for DCE-MRI that these parameters are subject to errors, as they cannot be determined with infinite accuracy nor precision. Therefore, an evaluation of the sensitivity of both estimators to these errors is imposed. Although these parameters are abundant for the LSQ procedure itself, their values are required for the conversion of signal intensity to CA concentration and errors will affect the LSQ estimates as well [30]. To assess for instance the sensitivity to errors in the flip angle, the simulations of sec-

tion 6.3.2 are repeated: for the three pulse sequences under consideration and the different kinetic parameters combinations, $10^3$ signal curves infected with white gaussian noise are simulated as described above. Each of these curves is recalculated to a concentration curve with the real value of the flip angle from table 6.1 ($\alpha_r$), but also with 8 erroneous values ($\alpha_{er}$ = 0.9, 0.925, 0.95, 0.975 , 1.025, 1.05, 1.075 and 1.1 times $\alpha_r$ ). The resulting concentration curves are fitted to the corresponding kinetic model with the 2 estimators. For the MLM estimator, the corresponding $\alpha_{er}$ is used in the estimation procedure. The sensitivity of each estimator to a given error in the flip angle is quantified by of the mean relative distance MRD between the estimate at $\alpha_{er}$ and the estimate at $\alpha_r$. For the TK model this relative distance can be expressed as:

$$MRD(\alpha_{er}, \alpha_r) = \frac{1}{m} \sum_{i=1}^{m} \sqrt{\left[\frac{\hat{K}_i(\alpha_{er}) - \hat{K}_i(\alpha_r)}{K}\right]^2 + \left[\frac{\hat{k}_i(\alpha_{er}) - \hat{k}_i(\alpha_r)}{k}\right]^2} \tag{6.18}$$

in which for the compactness of the notation K and k are used for $K^{trans}$ and $k_{ep}$ respectively. m is the number of simulations ($10^3$). The MRD is an objective measure for the shift in the kinetic parameter couple caused by the error in the flip angle. By dividing every term by $K^{trans}$ or $k_{ep}$, it is assured that every parameter is equally accounted for. For the ETK model an extra term in the sum of eq. 6.18 is added for $\nu_p$. For $R_{10}$, $r_1$ and $r_2$, the procedure is identical. The errors in the flip angle and in $R_{10}$ are varied between -10% and +10% of the true values, to cover reported error ranges with various measurement techniques [30, 50, 51, 57]. For $r_1$ and $r_2$ the errors are varied between -25% and 25% of their true value [44, 173].

Fig. 6.3 shows the sensitivity of the kinetic parameter estimates to errors in the flip angle, for the MLM (crosses) and LSQ (circles) estimators applied to the TK model (dotted black lines) and the ETK (full grey lines). The pulse sequences and the kinetic parameter combinations are mentioned in the figure legends. The errors are expressed in terms of the mean relative distance between an estimate at the true flip angle and the estimate at the erroneous flip angle (eq. 6.18). For the three pulse sequences and the kinetic parameters couples under consideration the MLM estimator is less sensitive to errors in the flip angle. The sensitivity reduction is the highest for PS1, for which it ranges up to 37% for the ETK model and up to 25% for the TK model. For PS2 and PS3, the sensitivity reduction is less, but MLM never performs worse than LSQ. In general, the advantage of MLM is more pronounced as the sensitivity of the pulse sequence to flip angle errors increases. In addition, fig. 6.3 states that the ETK model is more sensitive to errors in the flip angle than its TK-counterpart. If both models would be equally sensitive, the ratio of their MRD would be approximately $\sqrt{3}/\sqrt{2} \approx 1.22$. For the other kinetic parameters couples, not shown in the figures, the sensitivity reduction with MLM is smaller, but MLM does not perform worse than LSQ. Fig. 6.4

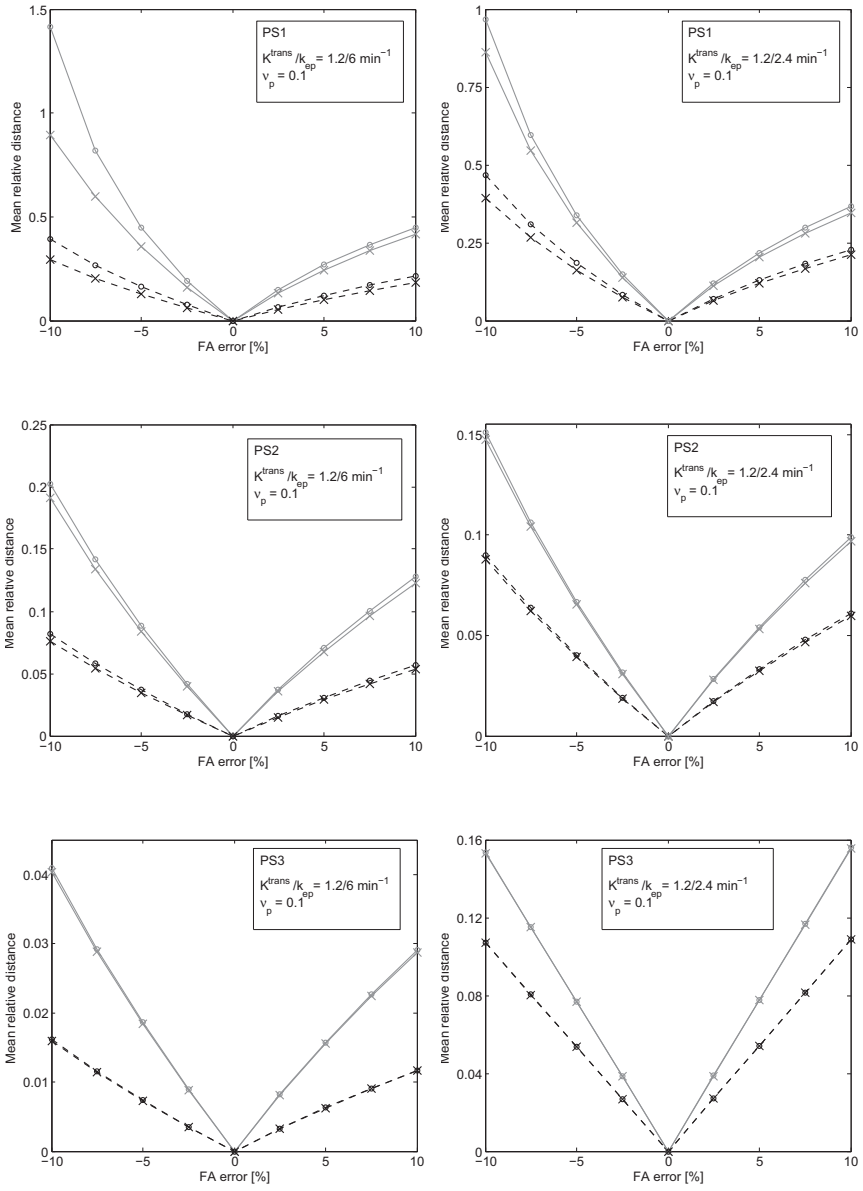


**Figure 6.3:** Mean relative distance between the kinetic parameter set estimate at the true flip angle and the kinetic parameter estimate at the erroneous flip angle, as a function of the relative flip angle error. LSQ-sensitivity is denoted with open circles, MLM-sensitivity with crosses. The full grey lines represent the results for the ETK model, the dotted black lines show the sensitivity of the TK model.

shows for PS1, the sensitivity of the kinetic parameters estimates to errors in the native relaxation rate $R_{10}$, and in the relaxivity coefficient $r_1$ and $r_2$. Again, MLM estimates are less sensitive to these error sources than their LSQ counterparts. The results of PS2 and PS3 are not shown, because the trends for errors in $R_{10}$, $r_1$ and $r_2$ are similar than for errors in the flip angle (fig. 6.3): a smaller sensititivy reduction is seen for PS2 and MRD is almost equal for PS3. The sensitivity reduction with MLM is again most pronounced for the pulse sequences that are most senstive to a given error source.

## 6.6 Relevance & shortcomings of MLM in post-processing

Clinical acceptance of DCE-MRI & kinetic modeling studies is greatly depending on two important issues: the reproducibility of the results and the ability to compare the results from different scanning sites. This latter issue has been reported by several authors [12, 19, 21] and is mainly caused by the use of different imaging acquisition techniques, different determination methods for the AIF and lack of convention regarding post-processing of DCE-MRI data (concentration calculation, fitting process, CI's,...). In recent literature, advances have been made regarding the AIF determination method [139,141,150]. In addition, a great number of studies has improved the accuracy of the CA concentration calculation by using SPGRE-signal intensity based conversion techniques [30], thereby making the kinetic parameter results less dependent on the employed pulse sequence settings [33]. In this work we have investigated the influence of the fitting process for DCE-MRI concentration data converted from SPGRE pulse sequence intensity and the construction of CI's for the kinetic parameter estimates. Our results show a higher reproducibility and an increased accuracy of the kinetic parameter values than with a conventional LSQ estimator. Moreover, as it has an overall smaller rmse, the MLM estimator renders the kinetic parameter estimates as independent as possible of the pulse sequence settings and the employed DCE-MRI protocol [25]. This statement is enforced by our error analysis, proving that MLM-estimates are less sensitive to errors in the DCE-MRI parameters. However, the most important finding regarding the comparability issue, is the reliable CI construction with MLM. Our results not only show that LSQ consistently underestimates its own uncertainty, but also that the observed coverages are stronlgy dependent on the pulse sequence settings and the DCE-MRI protocol. MLM constructed CI's closely cover the expected 95% and their coverages are minimally dependent on the pulse sequence. This enables a statistically justified comparison of kinetic modeling results from different scanning sites. A reliable CI estimation is of crucial importance for several DCE-MRI applications as well. For therapy evaluation or for the testing of novel anti-angiogenic drugs an underestimation

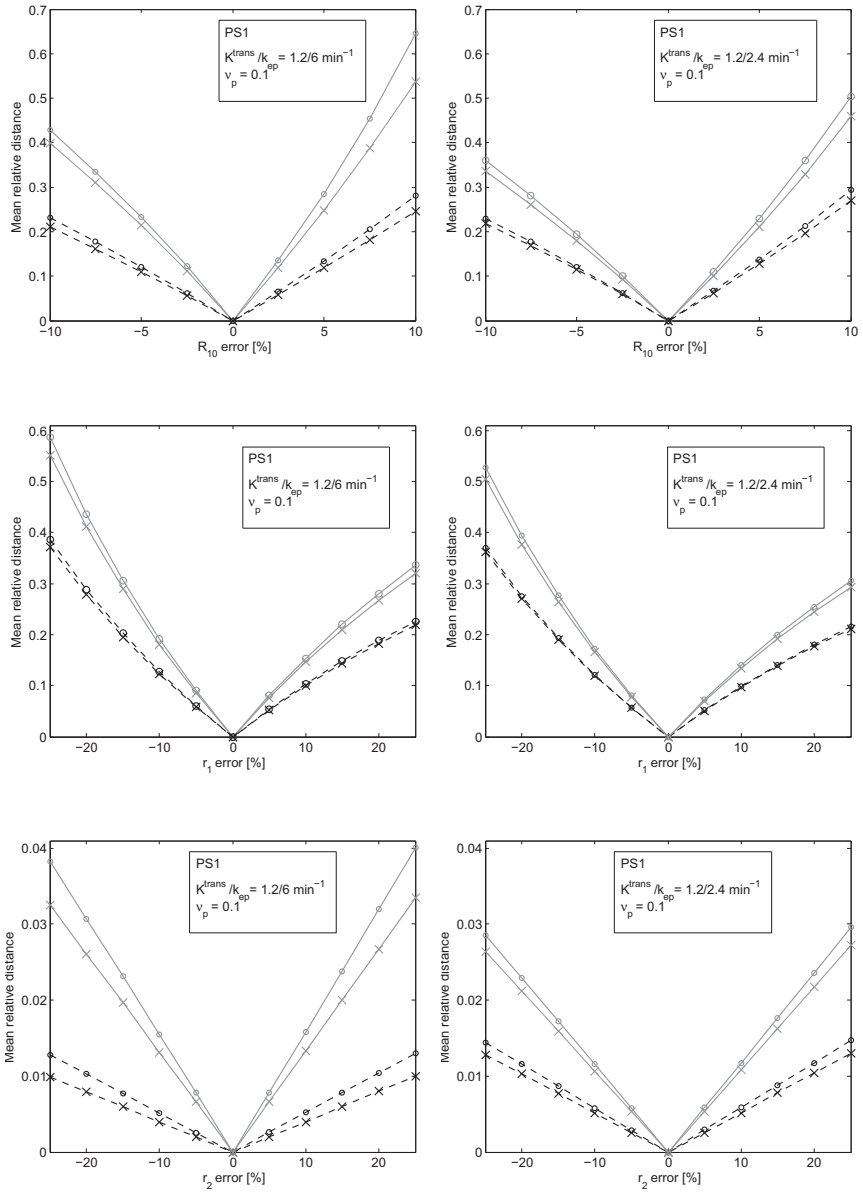


**Figure 6.4:** Mean relative distance between the kinetic parameter set estimate at the true value of $R_{10}/r_1/r_2$ and the kinetic parameter estimate at the erroneous value of the concerned parameter, versus the relative parameter error. LSQ-sensitivity is denoted with open circles, MLM-sensitivity with crosses. The full grey lines represent the results for the ETK model, the dotted black lines show the sensitivity of the TK model.

of the kinetic parameter uncertainty may lead to erroneous conclusions, in particular as LSQ CI's are mainly unreliable for highly permeable/perfused tissues (high $K^{trans}$), typically occuring in pathological lesions. Therefore we claim that our MLM estimator, and in particular our method for CI construction, can be of great value as a part of a cross-site standardization of post-processing techniques in DCE-MRI and kinetic modeling. This standardization has been acknowledged by many authors as a essential step towards a widespread acceptance of quantitative DCE-MRI in clinical practice [12,19,21].

The rmse-reductions and the error sensitivity reductions obtained with the MLM estimator are most important for PS1 and PS2. For the rmse, this can easily be explained by fig. 6.1. The extent of heteroskedastiticy of the concentration data is much higher for PS1 than for PS2, while for PS3 the concentration data can be approximated as homoskedastic. The MLM estimator accounts for the heteroskedasticity by dividing the contribution of a measured concentration with a $[dS/dC]^2$-factor. This reduces the weight of the highly noisy data and causes the rmse-reduction. The error sensitivity reduction is caused by this factor as well. For a complete analysis of the concentration bias, caused by an error in an imaging parameter, we refer to Schabel & Parker [30]. However, it is easy to see that the concentration error associated with an error in an imaging parameter $\beta$ (flip angle, $R_{10}$, $r_1$ or $r_2$) is proportional to $dC/d\beta = dC/dS.dS/d\beta$. Therefore, the MLM estimator gives lesser weights to the concentrations that are most sensitive to those errors. Our results show that the error reduction with MLM is more pronounced for the pulse sequences that are most sensitive to these errors. This implies that the advantages of the MLM estimator are depending on the pulse sequence parameters. However, MLM never has a worse performance, nor is it more sensitive to errors in the DCE-MRI parameters. In addition, a small but significant improvement in the CI's is seen in both fig. 6.2, table 6.6 and table 6.7 for PS3. Therefore we state that the use of MLM is beneficial for all SPGRE pulse sequence design. In previous work, a reduction of the $K^{trans}$-uncertatinty up to 30% was shown for a IR-SPGRE sequence with MLM [25], which demonstrates the applicability of the MLM estimator for other types of pulse sequences.

It is difficult to compare our results with other studies regarding estimators for DCE-MRI data. We have focussed on the implications of the concentration data distribution, while other authors did not consider this issue. Orton et al. investigated a bayesian estimator for Tofts modeling of concentration data, but assumed a homoskedastic concentration distribution [35]. Fluckiger et al. developped a method for the joint estimation of the AIF and the kinetic parameters [150]. In their simulations, gaussian noise with constant standard deviation was added to the tissue concentration curves. When these estimation methods are used for heteroskedastic concentration data, we claim that our MLM estimator can be used as a part of these techniques. Other

studies, investigating the reproducibility [174] or the error sensitivity [36] of kinetic parameters, with (heteroskedastic) concentration data stemming from SPGRE-pulse sequence signal intensity, may also benefit from the use of the MLM estimator. A drawback of the MLM estimation method is its more difficult implementation when compared to LSQ. The dS/dC factor can be found in [30]. As initial values for the minimization, identical parameter values as with LSQ can be used. The formula for the CI's is difficult to implement and should be embedded in post-processing software, as it is done for the LSQ CI construction. Furthermore our study has not considered the influence of heteroskedastic concentration noise on the AIF, on the CI's for kinetic parameters. When the AIF is measured together with the tissue concentration curves, this effect may broaden the CI's significantly and should be investigated in future work[4]. However, our results are directly applicable to those studies using population averaged AIF's or employing the reference region method. Finally, it should be mentioned that in vivo comparison of these estimators is useless, as no golden standard for kinetic parameter measurement is available, nor can the accuracy of the CI's be investigated in a clinical study.

Finally, our results have demonstrated that the ETK model is more sensitive to errors in the DCE-MRI parameters, in comparison with its non-vascular counterpart. Although, this statement is independent of the estimator, we wish to point attention to this result, as (to our knowledge) it has not been demonstrated before in DCE-MRI literature. Comparison of the rmse-values of table 6.4 and table 6.5 shows that the kinetic parameter estimates form the ETK are less reproducible as well. However, Buckley showed that the inclusion of a vascular contribution in the kinetic model can significantly improve the physiogical interpretation of the kinetic parameters [18]. These findings implie that a trade-off in the selection of kinetic models is enforced, between the physiogical relevance on the one hand and the error sensitivity and reproducibility on the other hand. This should be subject of further investigation.

## Appendix: derivation of Fisher information matrix elements

The Cramer-Rao inequality is a theorem from estimation theory that expresses a lower bound on the variance of an estimator for a model parameter. This so called Cramer Rao lower bound (CRLB) was first derived by Harald Cramer and Calyampudi Radhakrishna Rao. The inequality theorem states that for a set of parameter estimators, the difference between the covariance matrix and

[4]Preliminary simulation results suggest that when an appropriate flip angle optimization is used, the accuracy of the MLM constructed CI's remains high, even in the case of individually measured AIF.

the inverse of the Fischer matrix (FIM) is positive semi-definite. For practical use, this means that the minimal variance of an unbiased estimator equals the corresponding diagonal element of the inverse of the Fischer matrix. In this chapter we have used this Cramer-Rao unequality and stated that the inverse of the FIM is a good estimate for the covariance matrix.

Consider a parameter vector $\boldsymbol{\theta} = [\theta_1 \ \ \theta_2 \ ... \ \theta_n]$ and a corresponding likelihood function for the response variable $\boldsymbol{x}$, $L(\boldsymbol{\theta} \mid \boldsymbol{x})$. Let $\hat{\boldsymbol{\theta}}$ be an estimator for $\boldsymbol{\theta}$. If $\hat{\boldsymbol{\theta}}$ is an unbiased estimator the Cramer-Rao inequality theorem states that the covariance matrix $\Sigma_{\hat{\theta}}$ of $\hat{\boldsymbol{\theta}}$ satisfies:

$$\boldsymbol{\Sigma}_{\hat{\boldsymbol{\theta}}} \geq F(\boldsymbol{\theta})^{-1} \tag{6.19}$$

$F(\boldsymbol{\theta})$ is the Fischer Information Matrix, defined as:

$$F_{ij} = E\left[\frac{d\ [log\ L(\boldsymbol{x} \mid \boldsymbol{\theta})]}{d\theta_i} \frac{d\ [log\ L(\boldsymbol{x} \mid \boldsymbol{\theta})]}{d\theta_j}\right] \tag{6.20}$$

E denotes the expectation value operator over all possible measurements of $\boldsymbol{x}$. The matrix inequality in eq. 6.19 is to be understood as $\boldsymbol{\Sigma}_{\hat{\boldsymbol{\theta}}} - F(\boldsymbol{\theta})^{-1}$ being positive semi-definite.

For the case of the DCE-MRI concentration measurement combined with Tofts kinetic modeling the reponse variable $\boldsymbol{x}$ is the measured concentration vector $\boldsymbol{C}$. The likelihood function of this series of observations $\boldsymbol{C} = [C_i]$ on time points $t_i$, i=1..n, that should be fit to a kinetic model $C_T(t_i)$, is given by:

$$L(\boldsymbol{C} \mid \boldsymbol{\theta}) = \prod_{i=1}^{n} \frac{1}{\sqrt{2\pi}\sigma_i} exp\left[-\frac{(C_i - C_{ti})^2}{2{\sigma_i}^2}\right] \tag{6.21}$$

$$C_{ti} = C_T(t_i, \boldsymbol{\theta}) \tag{6.22}$$

$$\sigma_i = \sigma_S \frac{1}{dS/dC}_{C=C_{ti}} \tag{6.23}$$

S is the signal intensity equation of the pulse sequence employed in the study. $C_{ti}$ has been defined to simplify the notation of $C_T(t_i, \boldsymbol{\theta})$.The derivative of the logarithm of the likelihood function L to a model parameter can be calculated as:

$$\frac{d\ [log\ L(\boldsymbol{C} \mid \boldsymbol{\theta})]}{d\theta_k} = \tag{6.24}$$
$$\sum_{i=1}^{n} -\frac{1}{\sigma_i}\frac{d\sigma_i}{d\theta_k} + \frac{(C_i - C_{ti})}{{\sigma_i}^2}\frac{dC_{ti}}{d\theta_k} + \frac{(C_i - C_{ti})^2}{{\sigma_i}^3}\frac{d\sigma_i}{d\theta_k}$$

With eq. 6.23 the derivative of $\sigma_i$ to $\theta_k$ can be written as:

$$\frac{d\sigma_i}{d\theta_k} = -\sigma_i \alpha_i \frac{dC_{ti}}{d\theta_k} \tag{6.25}$$

$$\alpha_i = \frac{d^2S/dC^2}{dS/dC}_{C=C_{ti}} \tag{6.26}$$

$$\frac{dC_{ti}}{d\theta_k} = \frac{dC}{d\theta_k}_{C=C_{ti}} \tag{6.27}$$

With eq. 6.25, eq. 6.24 can be rewritten as:

$$\frac{d\ [log\ L(\boldsymbol{C} \mid \boldsymbol{\theta})]}{d\theta_k} = \sum_{i=1}^{n} \beta_{ik} \tag{6.28}$$

$$\beta_{ik} = \frac{dC_{ti}}{d\theta_k}(\alpha_i + \frac{C_i - C_{ti}}{{\sigma_i}^2} - \frac{(C_i - C_{ti})^2}{{\sigma_i}^2}\alpha_i) \tag{6.29}$$

According to eq. 6.20 the elements of the Fischer matrix are:

$$F_{kl} = E\left[\sum_{i=1}^{n}\sum_{j=1}^{n} \beta_{ik}\beta jl\right] \tag{6.30}$$

$$= \int \cdots \int L(\boldsymbol{\theta} \mid \boldsymbol{C}) \sum_{i=1}^{n}\sum_{j=1}^{n} \beta_{ik}\beta_{jl}\ dC_1\ \ldots dC_n \tag{6.31}$$

$$= \sum_{i=1}^{n}\sum_{j=1}^{n}\prod_{m=1}^{n} \int f_m(C_m \mid C_{tm})\beta_{ik}\beta_{jl}\ dC_m \tag{6.32}$$

In eq. 6.31, $L(\boldsymbol{C} \mid \boldsymbol{\theta})$ is the likelihood function of the series of observations $\boldsymbol{C}$ (eq. 6.21). It is the product of the individual gaussian probability functions $f_m(C_m \mid C_{tm})$ (eq. 6.5). For every $m \neq i, m \neq j$ the integral in eq. 6.32 is 1, due to normalization of the gaussian distribution. The product reduces to a multiplication of two integrals over $dC_i$ and $dC_j$, as long as $j \neq i$. When $j = i$ only one factor remains. Therefore the summation should be split up into two parts:

$$F_{kl} = \sum_{i=1}^{n}\sum_{j=1, j\neq i}^{n} \int f_i(C_i \mid C_{ti})\beta_{ik}\ dC_i \int f_j(C_j \mid C_{tj})\beta_{jl}\ dC_j + \sum_{i=1}^{n} \int f_i(C_i \mid C_{ti})\beta_{ik}\beta_{il}\ dC_i \tag{6.33}$$

Since the central moment of uneven order of the normal distribution is zero, the double sum in the first part of eq. 6.33 can be reduced to:

$$\begin{aligned} &= \sum_{i=1}^{n} \sum_{j=1, j\neq i}^{n} \left( \alpha_i \frac{dC_{ti}}{d\theta_k} (1 - \frac{{\sigma_i}^2}{{\sigma_i}^2}) \right) \left( \alpha_j \frac{dC_{tj}}{d\theta_l} (1 - \frac{{\sigma_j}^2}{{\sigma_j}^2}) \right) \\ &= 0 \end{aligned} \tag{6.34}$$

The Fischer matrix element reduces to:

$$\begin{aligned} F_{kl} = \sum_{i=1}^{n} \int f_i(C_i \mid C_{ti}) \frac{dC_{ti}}{d\theta_k} \frac{dC_{ti}}{d\theta_l} \Bigg[ & \frac{(C_i - C_{ti})^2}{\sigma_i^4} \\ & + \alpha_i^2 (1 - 2\frac{(C_i - C_{ti})^2}{\sigma_i^2} + \frac{(C_i - C_{ti})^4}{\sigma_i^4}) \\ & + 2\alpha_i \frac{(C_i - C_{ti})}{\sigma_i^2} (1 - \frac{(C_i - C_{ti})^2}{\sigma_i^2}) \Bigg] dC_i \end{aligned} \tag{6.35}$$

The central moment of fourth order equals $3\sigma_i^4$. The Fischer matrix element is:

$$\begin{aligned} F_{kl} &= \sum_{i=1}^{n} \left[ \alpha_i^2 \frac{dC_{ti}}{d\theta_k} \frac{dC_{ti}}{d\theta_l} (1 - 2 + 3) + 0 + \frac{dC_{ti}}{d\theta_k} \frac{dC_{ti}}{d\theta_l} \frac{1}{\sigma_i^2} \right] \\ &= \sum_{i=1}^{n} \frac{dC_{ti}}{d\theta_k} \frac{dC_{ti}}{d\theta_l} (2\alpha_i^2 + \frac{1}{\sigma_i^2}) \end{aligned} \tag{6.36}$$

These matrix elements are derived in a model independent manner. They are valid for any kinetic model, unregarded the number of parameters. Moreover, eq. 6.36 can be used for different MR-sequences, as long as the resulting concentration distribution is gaussian and its variance satisfies eq. 6.23.

# Chapter 7

# A stable and fast procedure for the fitting of DCE-MRI data to the AATH model

## 7.1 Introduction

In chapter 2, an overview was given of the models that are currently used in clinical DCE-MRI studies. The compartmental models, as reviewed and standardized by Tofts et al. [16, 17], enable the estimation of 2 or 3 pharmacokinetic parameters describing the physiology of the tissue of interest. In the 2-parameter model, $\nu_e$ is the extracellullar extravascular space fraction and $K^{trans}$ $[min^{-1}]$ is the transendothelial transfer constant. The latter describes the joint effect of the plasma flow $F_p$ through, and the permeability $PS$ of the tumours microvascular network (see chapter 2). The 3-parameter compartmental model contains the plasma volume fraction $\nu_p$ as well, to include the non-negligible contribution of the CA in the capillaries [16]. These 2- and 3 parameters models have been intensively investigated in literature and have shown their applicability in many tumour types [119, 131]. Nevertheless, it was shown that due to the simplified model assumptions, the physiologic parameters one aims to measure are inaccurate [18]. A potential modeling error is the assumption, inherent to the compartimental models, that the mean transit time $\tau$ of the blood in the tumor is zero. Several studies revealed non-negligible values in various tumour types, up to 90s in prostate cancer [111] (see table 7.1). Another major disadvantage of the compartmental model is the inability to achieve separate estimation of the plasma flow and the permeability. It can only assess their joint effect through $K^{trans}$.

The tissue homogeneity model (TH model) is a 4-parameter description of the

capillary exchange mechanisms [78]. It enables estimation of both blood flow and permeability and takes into account the finite transit time. The model equations however, can only be solved in the Laplace or Fourier space, making time domain fitting methods impossible. Very recently a fitting method in fourier space was developped and tested [81]. An adiabatic approximation for the TH model was derived in 1998 by St-Lawrence and Lee and enables the separate estimation of $\nu_e$, $\nu_p$ and both the plasma flow $F_p$ and the permeability surface area product $PS$ [79, 80]. Several studies showed the benefits of this 4-parameter model over the 2- of 3-parameter models [26, 155]. In addition Buckley found that the AATH model provides the most accurate estimates of the true physiological parameters [18]. However, the model fitting has been shown to be highly unstable [18, 24, 79, 81]. Due to intercorrelations between the parameters, multiple local minima are apparent in the least square cost function and a large amount of initial estimates for the kinetic parameters are necessary to find the global minimum. In general 2 fitting methods exist. The first one uses multiple initial estimates for the mean transit time and allows all four parameters to vary freely, while the second method employs several fixed values for the mean transit time, and allows variation of the 3 others parameters only. As a result of the multiple and often unstable minimization procedures that have to be performed in these procedures, the AATH model fitting is highly time consuming.

In this chapter a new fitting procedure for the AATH model is proposed and compared to the currently used fitting procedures by means of simulations. The chapter starts by giving an overview of these current estimation methods for the AATH model. By means of a practical example, the instability of these procedures is illustrated and a number of observations is made, which lay the foundation of the newly proposed fitting method in section 7.3. In section 7.4, the set-up and the results of the simulations to compare the fitting methods are explained. Finally in section 7.5 the potential and the shortcomings of our new method are discussed.

## 7.2 Current status of AATH model fitting procedures

### 7.2.1 Practical implementation of AATH model

The AATH model [79] allows the separate estimation of 4 physiological parameters: $F_p$ is the plasma flow [$min^{-1}$ [1]], $PS$ is the permeability-surface area product [$min^{-1}$], $\nu_e$ is the interstitial space fraction and $\nu_p$ is the plasma volume fraction. To describe the model mathematically, 4 more variables are defined:

[1] if for simplicity the tissue density is assumed to be 1 g/ml

**Table 7.1:** An overview of the studies using the AATH model to fit DCE-MRI [18,24, 26,111–113,155] or DCE-CT data [114]. The pathology and the employed fitting method are mentioned as well. The $\tau$-grid describes the different $\tau$-values used in the respective fitting methods. Kershaw (2010) has investigated both fitting methods. The mean $\tau$-value found in the clinical studies is mentioned as well.

| Study | Pathology | Fitting method | $\tau$-grid | mean $\tau$ [$s$] |
|---|---|---|---|---|
| Henderson(2000) | breast cancer | FMTF | 60 values in 1-60s | 24 |
| Buckley (2002) | simulation study | MMTF | - | - |
| Buckley (2004) | prostate cancer | MMTF | - | - |
| Kershaw (2006) | prostate cancer | MMTF | 30 values in 0.6-90s | 19 |
| Jeukens (2006) | prostate cancer | FMTF | 50 values in 6-70s | 25 |
| Naish (2009) | lung cancer | FMTF | 30 values in 2-60s | 21 |
| Kershaw (2009) | prostate cancer | MMTF | - | 60 |
| Kershaw (2010) | simulation study | MMTF | 30 values in 0.6-90s | - |
| | | FMTF | 90 values in 0.6-90s | |

the extraction fraction E, the mean capillary transit time $\tau$, the endothelial transfer constant $K^{trans}$ and the transfer constant between interstitial space and plasma $k_{ep}$. The relationships between these variables and the physiological quantities above are given in eq. 7.1.

$$\begin{aligned} E &= 1 - exp(-\frac{PS}{F_p}) \\ \tau &= \frac{\nu_p}{F_p} \\ K^{trans} &= EF_p \\ k_{ep} &= \frac{EF_p}{\nu_e} \end{aligned} \tag{7.1}$$

The impulse answer of the AATH model is given by eq. 7.2:

$$H(t) = \begin{cases} 0 & t < 0 \\ F_p & 0 < t \leq \tau \\ K^{trans} exp(-k_{ep}(t-\tau)) & t > \tau \end{cases} \tag{7.2}$$

It may be clear from these equations that in practice the parameters $F_p$, $K^{trans}$, $k_{ep}$ and $\tau$ can be estimated. The other parameters are calculated from eq. 7.1. The parameters that are reported differ between different studies. In this work we only report the results for the physiological parameters. The tissue concentration curve is determined as the convolution of the AIF with this impulse answer (eq. 7.3), which in practice, is calculated as a discrete sum

(eq. 7.4).

$$C_t(t) = C_p(t) \otimes H(t) = \int_0^t C_p(t')H(t-t')dt' \tag{7.3}$$

$$C_t(t_j) = \sum_{m=1}^{j} C_p(m)H(j-m+1)\Delta \tag{7.4}$$

In eq. 7.4, $t_j = (j-1)\Delta$, are the discrete times at which a DCE-MRI-image is captured. $\Delta$ is the time step between 2 subsequent DCE-MRI images. By choosing this way of indexing, it is ensured that our equations are directly transferrable to mathematical programs as Matlab. The best-fit values of the AATH parameters are determined by minimizing the sum of squared differences (ssq) between the measured concentration curve and the convolution expression:

$$ssq = \sum_{j=1}^{n} [C(t_j) - C_t(t_j)]^2 \tag{7.5}$$

$C(t_j)$ is the CA concentration measured at time point $t_j$. n is the number of DCE-MRI images taken in the dynamic series.

### 7.2.2 Multiple minima in parameter space

To illustrate the difficulties encountered in the fitting of the AATH model, an example concentration curve is used throughout this chapter, shown in fig. 7.1b. Figure 7.1a shows the simulated concentration curve, generated from the tissue homogeneity model with pharmacokinetic parameters representative for a breast tumor [18] and with the Parker AIF [139]. Parameters are mentioned in table 7.2. The noisy concentration curve in fig. 7.1b is obtained by sampling this simulated curve ($\Delta t$ = 2s) and contaminating it with white gaussian noise (SD = 0.05).

It is impossible to illustrate the existence of multiple minima of the ssq-cost function in the 4-dimensional AATH parameter space. Therefore, fig. 7.1c shows the cost function in a 1-dimensional cross section of the parameter space, formed by the straight line adjoining the global minimum and a randomly chosen local minimum. The parameter vector $\hat{\boldsymbol{\theta}}_{gl}$, corresponding with the global minimum, was found by minimizing the sum of squared differences between of the noisy concentration curve and the AATH model equation (eq. 7.5) with the simulation input parameters (table 7.2) as initial estimates for the minimization algorithm (standard Matlab library Nelder-Mead simplex algorithm). For the local minimum, $\hat{\boldsymbol{\theta}}_{loc}$, the simulation input parameters were used as starting values as well, except for the starting value of $\nu_p$, which was tripled. The pharmacokinetic parameters corresponding to both minima are mentioned in table 7.2. In fig. 7.1c, u is the parameter describing the straight

line according to $\boldsymbol{\theta} = \hat{\boldsymbol{\theta}}_{\boldsymbol{gl}} + u(\hat{\boldsymbol{\theta}}_{\boldsymbol{loc}} - \hat{\boldsymbol{\theta}}_{\boldsymbol{gl}})$. The global minimum ($u = 0$) and the local minimum ($u = 1$) are designated in fig. 7.1c. It is clear that even in this small cross section of the complete AATH parameter space, several minima occur. Depending on the initial values, used in the minimization algorithm, different results will present, which can be highly divergent. To find the global minimum of the cost function, the currently used fitting procedures (see next section) explore multiple starting points across the AATH parameter space.

To find a solution for this fitting problem, it is interesting to recognize the cause of the occurence of local minima. Firstly, as with any model containing a high[2] number of parameters, parameter intercorrelation occurs [18,24,26]. Parameter intercorrelation is the phenomenom for which different parameter combinations lead to approximately identical tissue concentration curves, making curve fitting a hazardous task [3]. The occurence of parameter intercorrelation for the AATH model can be seen on fig. 7.1b, where the curves for the global (red) and local minimum (green) are plotted together. Only a small curve shift around the peak concentration can be inspected, although the parameters are highly different. This intercorrelation is an intrinsic disadvantage of the AATH model.

However, in the case of the AATH model, the instability of the curve fitting is caused by the model evaluation method as well. Most authors evaluate the model concentrations by an explicit calculation of the discrete convolution in eq. 7.4 [24, 26, 114, 155]. Although the analytical convolution in eq. 7.3 is continuous in the parameter $\tau$, its discrete counterpart in eq. 7.4 is not. This can be seen in fig. 7.1d, plotting the variation of the AATH concentration at 2 fixed time points versus the mean transit time. Whenever $\tau$ crosses a multiple of the temporal resolution $\Delta$, a jump in the concentration occurs. This implies that for values of $\tau$ that are not a multiple $\Delta t$, the convolution expression is inaccurate. It also explains the discontinuities observed in the cost function in fig. 7.1c. Moreover, the local minimum $\hat{\boldsymbol{\theta}}_{loc}$, found by the minimization algorithm, is clearly a consequence of such discontinuity. Several other similar minima can be observed in fig. 7.1c. This proves that this convolution expression, that is often used as a practical determination method for the AATH model concentrations is inaccurate and partly responsible for the instability and occurence of local minima.

In view of these inaccuracies when $\tau$ is not a multiple of $\Delta$, it is interesting to investigate the variation of the ssq cost function with the mean transit time.

[2]The term 'high' indicates a number of parameters that is larger than in other models that also succeed in fitting a measured curve with an acceptable goodness-of-fit.

[3]Remark that parameter intercorrelation does not necessarily induce low parameter precision. The latter is due to a broad minimum of the cost function in parameter space, because one or more parameters only affect the cost-function in a minor way. Parameter intercorrelation indicates that a change in a given parameter can be corrected by a change in an other parameter, leading to multiple minima in the cost function. However, no conclusions can be drawn about the broadness of these minima, and thus about the precision of the parameters

**Table 7.2:** Parameter set used for the generation and corresponding to a global and a local minimum of the curve in fig. 7.1b.

| | $F_p$ $[min^{-1}]$ | $PS$ $[min^{-1}]$ | $\nu_e$ | $\nu_p$ |
|---|---|---|---|---|
| Simulation values | 0.57 | 0.33 | 0.45 | 0.060 |
| Global minimum | 0.61 | 0.33 | 0.46 | 0.065 |
| Local minimum | 0.37 | 0.35 | 0.41 | 0.11 |

In fig. 7.1e, the cost function for the fixed $\tau$ fitting method is plotted (more explanation can be found in the next section): for every $\tau$-value, the optimal values of the other 3 parameter are determined, that minimize the ssq cost function. This minimal value of the cost function is then plotted against $\tau$ and the minimum of this curve is regarded as the global minimum. The corresponding parameters are chosen as the best fit-values. However, when inspecting fig. 7.1e, no variation can be seen between $\tau = 3\Delta$ and $\tau = 4\Delta$ ($\tau$-input value is 6.31s in the example, $\Delta$ =2s). Therefore in fig. 7.1f, this part of the cost function, subtracted with its minimal value, is enlarged. The differences are in the order of $10^{-8}$, which is precisely the tolerance value on the cost function, that stops the iterations of the Nelder-Mead simplex minimization algorithm. When this tolerance value is changed, the differences change as well and remain in the order of the tolerance value. Therefore these differences are not significant, and it is proven that an estimate of $\tau$ is only precise up to a multiple of $\Delta$. This will be used in the new fitting procedure.

### 7.2.3 Fixed mean transit time fitting procedure (FMTF)

FMTF performs multiple fits to the AATH model at different fixed $\tau$-values in which only $F_p$, $K^{trans}$ and $k_{ep}$ are allowed to vary. The fixed $\tau$-values are typically varied in steps of 0.01 min, beginning from a lower limit up to an upper bound that depends on the pathology. Finally, the fit with the lowest ssq-value among all fixed $\tau$-values is regarded as global minimum. For the minimization procedure at a specific fixed $\tau$-value, the initial values of $F_p$, $K^{trans}$ and $k_{ep}$ are determined as follows: a non-linear fit of the concentration curve to the TK model equation is performed. The resulting best fit-values for $k_{ep}$ and $K^{trans}$ are used in both algorithms as starting points for these respective parameters. For $F_p$, an initial value of 0.5 times the best-fit value for $K^{trans}$ is chosen, which corresponds with an initial estimate of 0.5 for the extraction fraction. To avoid parameter intercorrelation induced stability problems in the fitting algorithm, many authors use bounded optimization algorithms. All parameters are assumed to be non-negative, or even have lower limit of $10^{-4}$ in their respective units [24]. The extraction fraction E and $\nu_e$

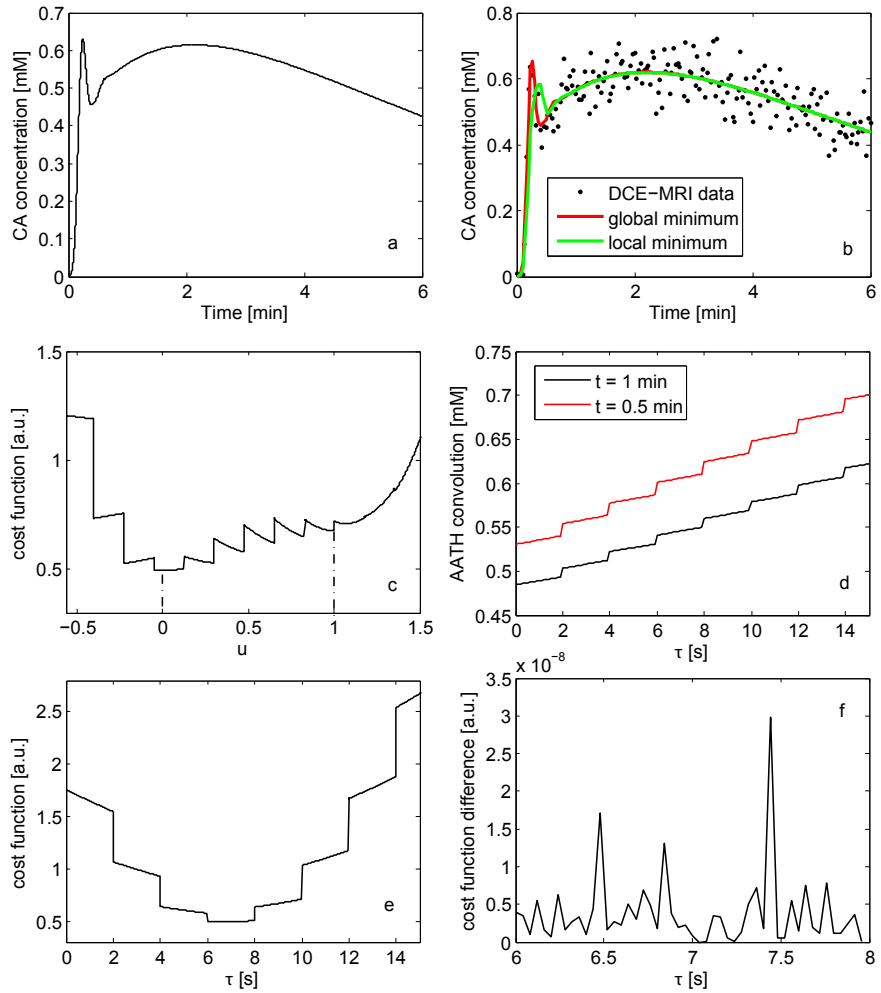


**Figure 7.1:** a: Simulated concentration curve from TH model and Parker AIF, representative for a breast tumor. Parameters are mentioned in table 7.2. b: Noisy concentration curve (black dots) and the fitted AATH model curves in the global minimum and in a local minimum of the cost function. AATH fit parameters of the global and local minimum are mentioned in table 7.2. c: 1-dimensional cross section of the ssq cost function, obtained by adjoining the global and the local minimum along a straight line described by the parameter u. d: variation of the AATH concentration at two fixed time points versus the mean transit time. e: variation of the ssq cost function with the mean transit time. f: cost function minus its minimal value, plotted in a $\tau$-interval with the width of the temporal resolution.

are physiologically and physically bounded to be smaller than 1. For $F_p$ an upper bound of 10 $min^{-1}$ was proposed [24,113]. Table 7.1 mentions a number of studies that employed the FMTF method, together with the corresponding $\tau$-grid.

### 7.2.4 Multiple mean transit time initial values fitting procedure (MMTF)

The MMTF method performs multiple fits to the AATH model equation for multiple initial values for $\tau$, with the initial values for the other parameters as defined in the previous section. When for a given initial value of $\tau$, a minimum has been reached, the fit is restarted with the optimal parameter values from this minimum changed by 5%, to decrease the influence of local minima. The fit with the smallest ssq is again chosen as the global minimum. In table 7.1 the studies employing MMTF fitting are mentioned with the different choices for the $\tau$-initial values. As with the FMFT method, the pharmacokinetic parameters are restricted, and bounded minimization methods are used. In contrast to the FMTF method, MMTF allows all 4 parameters to vary freely in the minimization algorithm.

Recently Kershaw & Cheng [24] compared FMTF and MMTF estimation for the fitting of concentration data, simulated with the TH-model. They found that FMTF reduces the median error in the extraction fraction and decreases the interquartile range of alle parameters, especially for $\tau$. This observation implies that we only have to compare our new fitting procedure with the FMTF method, as it is the better of both available methods. However, we do not agree with the simulations set-up of Kershaw & Cheng. Their simulation input values for $\tau$ were all beneath 75s. While for the FMTF method, the maximal possible $\tau$ is determined by the upper bound of the $\tau$-grid (90s for Kershaw & Cheng, see table 7.1), for the MMTF their upper bound for $\tau$ in the bounded optimization algorithm was 300s. This set-up is beneficial for the FMTF method, as any global minimum with a $\tau$-value above 90s in the MMTF method, cannot be found by the FMTF method, but always leads to an apparent worse resemblance with the true input parameters. Therefore, our newly proposed fitting method is compared with both fitting procedures, but with similar upper bounds for $\tau$.

## 7.3 Recursive grid based fitting procedure (RGBF)

### 7.3.1 Overview

Our new fitting procedure is inspired on the findings in section 7.2.2, that the precision of the $\tau$-parameter for the convolution based fitting procedures is bounded by the temporal resolution $\Delta$. In other words, a fitting procedure that considers multiples of $\Delta$ as the only possible values for the mean transit time, will not necessarily perform worse than the currently used procedures. Therefore, the new fitting method is based on the fast calculation of a ssq-grid in [$\tau$, $k_{ep}$]-space. In this section, a structured overview is given of the different steps in the RGBF-procedure, which is also shown in fig. 7.2. The mathematical details are explained in the next section.

- Grid construction: a grid in [$\tau$, $k_{ep}$]-space is constructed. In $\tau$-direction the resolution equals the temporal resolution $\Delta$. Minimal $\tau$ is $\Delta$, while the maximal $\tau$ can depend on the pathology. To cover the majority of the studies in table 7.1, it is set to 90 s for the rest of this chapter, but it can easily be adapted. In $k_{ep}$-direction, $k_{ep}$ varies in steps of 0.015 $min^{-1}$ from a minimal value of 0.03 $min^{-1}$ to a maximal value of 7.5 $min^{-1}$. Again, upper- and lower bound can be adapted according to the pathology. Fig. 7.2 shows the grid in [$\tau$, $k_{ep}$]-space.
- Grid filling: in every node of the grid 3 parameters are calculated. Firstly, the optimal values of $K^{trans}$ and $F_p$ at the specific grid point are calculated by linear regression. With these parameters, the ssq is calculated for every node. The practical aspects of this grid filling are explained in the next section.
- Global minimum selection: the node with the smallest ssq-value is chosen as the global minimum. The corresponding parameters are regarded as the best-fit values.

### 7.3.2 Linear regression and recursion formula

The fast calculation of the ssq-grid is based on the following analytical expression for the AATH model which can be derived from eq. 7.3 and eq. 7.2:

$$C_t(t) = \begin{cases} F_p \int_0^t C_p(t-t')dt' & t < \tau \\ F_p \int_0^\tau C_p(t-t')dt' + K^{trans} \int_\tau^t C_p(t-t') exp\left[-k_{ep}(t'-\tau)\right] dt' & t \geq \tau \end{cases} \tag{7.6}$$

This can be rewritten as:

$$C_t(t) = F_p \; x_1(\tau, t) + K^{trans} \; x_2(\tau, k_{ep}, t) \tag{7.7}$$

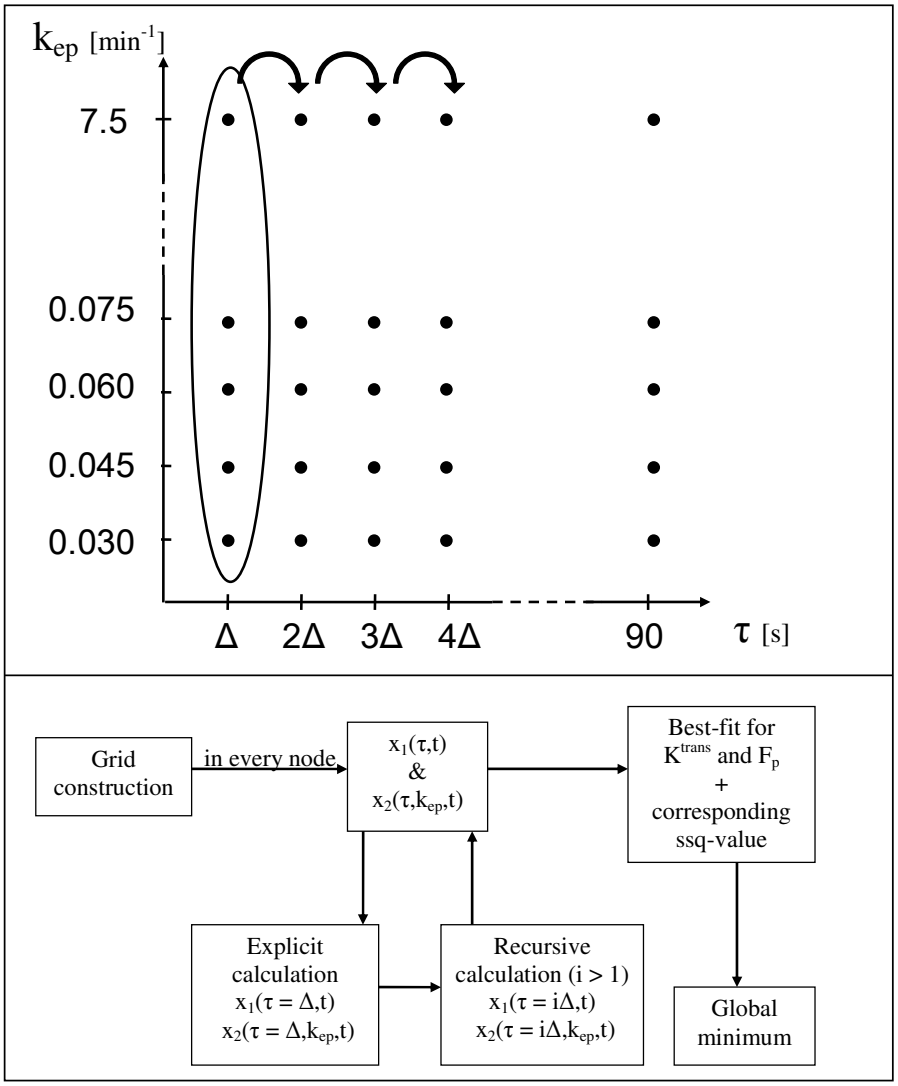


**Figure 7.2:** Above: grid in $[\tau,\ k_{ep}]$ for the recursive grid based fitting procedure (RGBF). In $\tau$-direction the resolution equals the temporal resolution $\Delta$. Only in the first column of the grid, $x_1$ and $x_2$ are calculated explicitly. In the neighbouring columns the recursion relations are used for fast $x_1$- and $x_2$-calculation. Below: Schematic overview of the different steps in the RGBF.

This equation shows that if $\tau$ and $k_{ep}$ are fixed, $K^{trans}$ and $F_p$ can be estimated from standard linear regression to the measured concentrations, with $x_1$ and $x_2$ as independent variables. This estimation can be performed analytically, with the standard matrix formulas for linear regression, and does not require time-consuming and unstable minimization procedures or selection of appropriate initial estimates. For a given gridpoint [$\tau$, $k_{ep}$], the best-fit values are given by:

$$\begin{bmatrix} \hat{F}_p \\ \hat{K}^{trans} \end{bmatrix} = (X^T X)^{-1} X C_t \tag{7.8}$$

with X being a $2 \times n$ matrix containing the $x_1$- and the $x_2$-vectors for that specific gridpoint, as its column vectors. From eq. 7.6, the analytical expressions for $x_1$ and $x_2$ can be derived:

$$t < \tau \quad \begin{cases} x_1(\tau, t) & = \int_0^t C_p(t - t')dt' \\ x_2(\tau, k_{ep}, t) & = 0 \end{cases} \tag{7.9}$$

$$t \geq \tau \quad \begin{cases} x_1(\tau, t) & = \int_0^\tau C_p(t - t')dt' \\ x_2(\tau, k_{ep}, t) & = \int_\tau^t C_p(t - t') exp\left[-k_{ep}(t' - \tau)\right] dt' \end{cases} \tag{7.10}$$

However, if $x_1$ and $x_2$ have to be determined based on a discretisation of eq. 7.9 and 7.10, little or no computational time would be gained in comparison with the other estimation procedures. Therefore a recursion based procedure was developped for the fast determination of $x_1$ and $x_2$ over the complete grid. It starts with the discrete calculation $x_1(\Delta, t)$ (independent of $k_{ep}$) and of $x_2(\Delta, k_{ep}, t)$. In addition a third variable is determined, $x_3(k_{ep}, t)$, required for the recursion relationship of $x_2$:

$$x_1(\Delta, j) = \frac{C_p(j) + C_p(j-1)}{2}\Delta \tag{7.11}$$

$$x_2(\Delta, k_{ep}, j) = e^{k_{ep}(t-\Delta)} \sum_{m=1}^{j-1} \frac{C_p(m)e^{k_{ep}m\Delta} + C_p(m-1)e^{k_{ep}(m-1)\Delta}}{2}\Delta \tag{7.12}$$

$$x_3(k_{ep}, j) = \frac{C_p(j)e^{k_{ep}j\Delta} + C_p(j-1)e^{k_{ep}(j-1)\Delta}}{2}\Delta \tag{7.13}$$

The values of $x_1(i\Delta, j)$ and $x_2(i\Delta, k_{ep}, j)$, $i \geq 2$, can be calculated based on the following recursion relationship:

$$\begin{cases} x_1(i, j) = x_1(i-1, j) & j \leq i \\ x_1(i, j) = x_1(i-1, j) + x_1(1, j-i+1) & j > i \end{cases} \tag{7.14}$$

$$\begin{cases} x_2(i, j) = x_2(i-1, j) & j \leq i \\ x_2(i, j) = x_2(i-1, j)e^{k_{ep}\Delta} - x_3(k_{ep}, j-i+1)e^{k_{ep}(i-j+1)} & j > i \end{cases} \tag{7.15}$$

Fig. 7.2 shows an schematic overview of these different steps. The proof of these recursion relations is given in the appendix.

**Table 7.3:** Ranges for the physiological parameters $F_p$, $PS$, $\nu_e$ and $\nu_p$, from which the simulation input values were selected. The ranges for the other parameters $E$, $K^{trans}$, $k_{ep}$ and $\tau$ were manually calculated from the physiological parameters

| Parameter | min | max |
|---|---|---|
| $F_p$ $[min{-}1]$ | 0.15 | 1 |
| $PS$ $[min^{-1}]$ | 0.01 | 0.8 |
| $\nu_e$ | 0.1 | 0.6 |
| $\nu_p$ | 0.03 | 0.15 |
| E | 0.095 | 1 |
| $K^{trans}$ $[min^{-1}]$ | 0.073 | 0.55 |
| $k_{ep}$ $[min^{-1}]$ | 0.12 | 5.5 |
| $\tau$ [s] | 1.8 | 60 |

## 7.4 Comparison of fitting procedures

### 7.4.1 Simulation setting

A simulation environment was written in Matlab (Matworks, Ma) to compare the performance of the fitting procedures. $10^4$ parameter combinations were selected from the ranges mentioned in table 7.3. For every parameter combination the tissue concentration was simulated according to the tissue homogeneity model, with a method as described in [24]. As AIF, the parametetrized form of the population averaged AIF, measured by Parker et al. was used [139]. To avoid errors caused by aliasing, a temporal resolution of 0.1 s was used for the generation of each curve, after which it is sampled with a temporal resolution of 2s, for a total scan time of 360s (identical to the protocol of [141]). The sampled curve is infected with white gaussian noise, with a standard deviation of 0.05 and fitted to the AATH-model with each of the three fitting methods. Their performance is compared for a parameter $\theta$ by means of the mean relative error:

$$MRE = \frac{1}{n}\sum_{i=1}^{n}\frac{\mid \hat{\theta}_i - \theta_i \mid}{\theta_i} \tag{7.16}$$

$\theta_i$ is the simulation input value for the parameter $\theta$ in the $i^{th}$ simulation. $\hat{\theta}_i$ is the corresponding estimate. n is the number of simulations. These simulations were repeated for 4 other values of the temporal resolution ($\Delta t$=1-2-3-4-5 s). For the FMTF and MMTF method, all parameters were constrained to be non-negative. Physiologically $\nu_e$ has to be smaller than 1. Upper bounds for

$PS$ and $F_p$ were set to 1.2 $min^{-1}$ and 10 $min^{-1}$ respectively. As mentioned above (section 7.2.4), other authors demand E<1, and do not consider an upper bound on $PS$. When comparing their results to the simulation input values they typically evaluate $F_p$, E, $\nu_e$ and $\nu_p$/ or $\tau$ [24]. $PS$-comparison is avoided because when the estimated value of E is close to 1 (due to instability reasons, this occurs frequently in flow-limited situations [18], see eq. 7.1 ), $PS$ becomes physiologically senseless or is impossible to calculate at all. However, in this work we wish to evaluate the physiological parameters $F_p$, $PS$, $\nu_p$ and $\nu_e$. Therefore, instead of demanding that E<1, an upper bound has to be imposed on $PS$ to keep its value calculable. For the FMTF method, the $\tau$-grid varies from 0.6s to 90s in steps of 0.6s. To enable a fair comparison (as explained in the previous section), the value of $\tau$ is bounded in the MMTF method between 0.6 and 90 (maximal input value of $\tau$ is 60s, see table 7.3). The grid for the RGBF procedure was designed as in fig. 7.2: in $\tau$-direction the grid step is $\Delta$, going from $\tau = \Delta$ to $\tau$=90s, again to enable a fair comparison with the other fitting procedures. In $k_{ep}$-direction, the grid step, is 0.015 $min^{-1}$, going from 0.03 $min^{-1}$ to 7.5 $min^{-1}$. Remark that this $k_{ep}$-grid is well-designed to comprise all possible $k_{ep}$-values in the simulations (table 7.3). For the RGBF method, the constraining of $F_p$, $PS$ and $\nu_e$ is identical as in the other methods.

The simulations as described in the previous paragraph are bulk simulations, i.e. the mean relative error comprises information about the average performance of the fitting procedures in a relevant parameter range. However, MRE of such a bulk simulation does not provide insight into the accuracy and precision of individual kinetic parameter estimates. To assess the influence of the RGBF-procedure on the accuracy and precision of the AATH-parameters, the simulations were repeated for 4 fixed kinetic parameter sets. The parameter set were chosen to be representative for a brain tumor, a breast tumor, a lung tumor and a prostate tumor. The values are mentioned in table 7.4. For each kinetic parameter set $10^3$ simulations were performed and the parameter error is depicted in a box plot.

### 7.4.2 Results

The MRE-values for the simulations with $\Delta t = 2s$, are mentioned in table 7.5. RGBF severely reduces the MRE for all parameters (58% for $F_p$, 25% for $PS$, 14% for $\nu_e$ and 22% for $\nu_p$). In addition RGBF is much faster than the other fitting procedures, with a reduction of 70% in computational time. The influence of the temporal resolution of the data on the performance of the fitting procedures is shown in fig. 7.3. The mean computational time for one fit is plotted in fig. 7.4 against the temporal resolution. From these graphs is it indisputable that our RGBF has a superior performance compared to the currently used MMTF- or FMTF-methods, unregarded of the temporal resolution of the data.

**Table 7.4:** Pharmacokinetic parameters in 4 different tumor types. Values adopted from [18, 113, 155].

| Pathology | $F_p$ $[min^{-1}]$ | $PS$ $[min^{-1}]$ | $\nu_e$ | $\nu_p$ | $\tau$ [s] |
|---|---|---|---|---|---|
| Brain tumor | 1.2 | 0.34 | 0.4 | 0.08 | 4 |
| Breast tumor | 0.57 | 0.33 | 0.45 | 0.06 | 6.3 |
| Lung tumor | 0.16 | 0.067 | 0.11 | 0.06 | 22.5 |
| Prostate tumor | 0.21 | 0.24 | 0.35 | 0.12 | 34.3 |

**Table 7.5:** MRE-values and mean computational time for the investigated fitting procedures ($\Delta t$ =2s, $T_{scan}$=360 s, $\sigma = 0.05$)

| Fitting method | $F_p$ | PS | $\nu_e$ | $\nu_p$ | mean time[s] |
|---|---|---|---|---|---|
| MMTF | 14.7 | 17.6 | 5.6 | 19.3 | 11.8 |
| FMTF | 14.2 | 17.3 | 5.5 | 18.5 | 18.8 |
| RGBF | 6.1 | 13.2 | 4.8 | 15.0 | 3.4 |

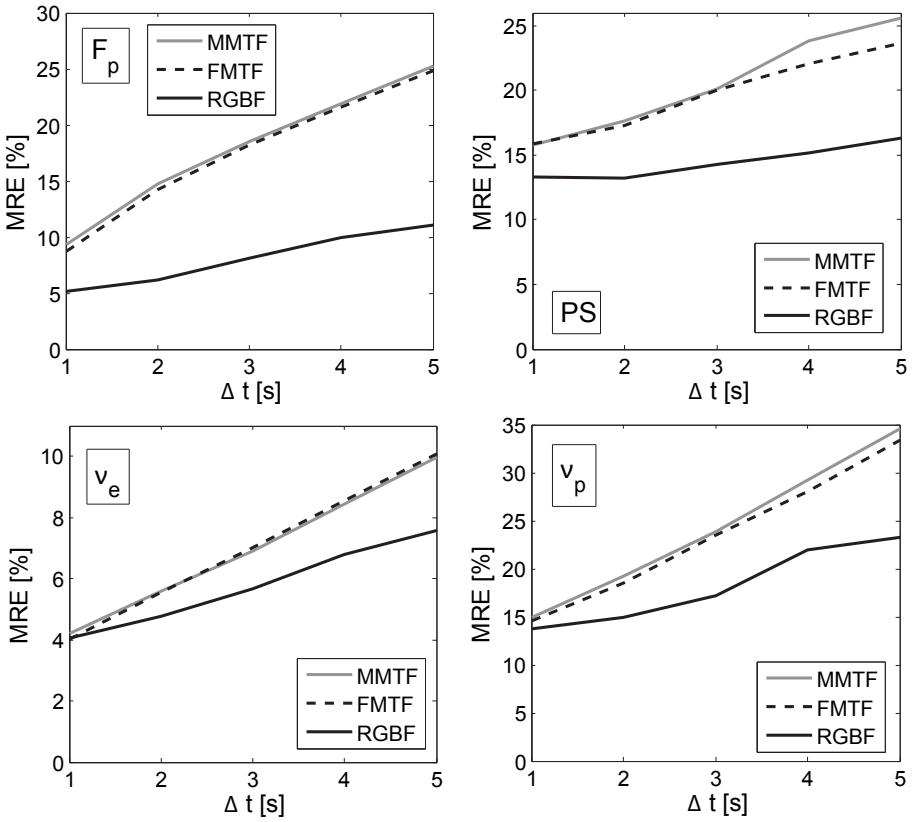


**Figure 7.3:** Comparison of the three fitting procedures at different temporal resolution. The mean relative error is plotted for the 4 physiological parameters of the AATH model against the temporal resolution.

Fig. 7.5 shows the boxplots of the AATH-parameter error, for 4 kinetic parameter combinations representative of different pathologies (table 7.4). In all cases, bias (both median and mean error) in $F_p$ is strongly reduced by the RGBF-method. In particular when $\tau$ is small (breast & brain, see table 7.4), $F_p$-estimates from MMTF or FMTF exhibit biases of 20%. These errors disappear with the RGBF-method in all pathologies, but for small $\tau$ this goes at the cost of a higher interquartile range. The estimation of $PS$ is benefitted as well from using the RGBF-method, with consistent reductions in mean and median error and interquartile range in all pathologies. For $\nu_e$, RGBF corrects for bias in breast and brain tumors, while in the other pathologies its performance is comparable to the other fitting procedures. Finally, $\nu_p$-bias is

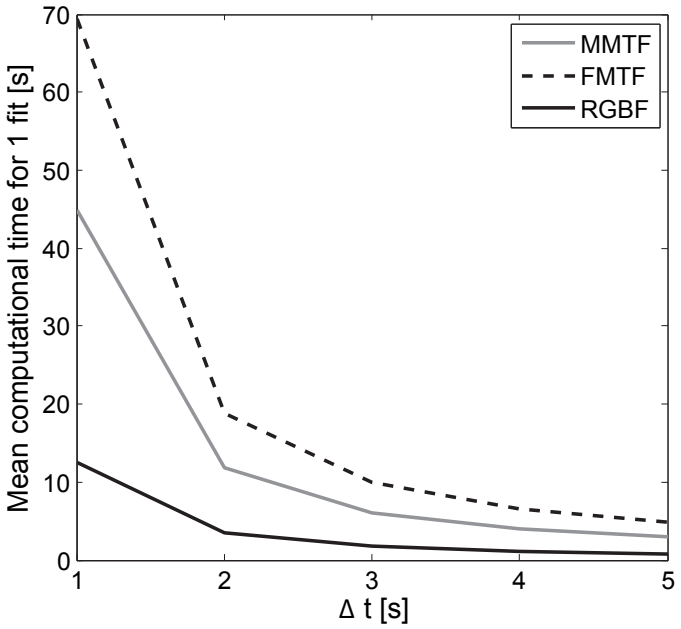


**Figure 7.4:** Comparison of the mean computational time needed to perform 1 fit, at different temporal resolutions.

decreased in all pathologies and a reduction in interquartile range is apparent when $\tau$ is small (brain & breast).

## 7.5 Potential & shortcomings

A growing clinical interest exists for the AATH-model [26, 111–113, 155]. The model has the ability to obtain separate estimations of blood flow and permeability, where conventional pharmacokinetic models can only assess their joint effect through $K^{trans}$. By the inclusion of finite mean transit time, it has been shown that the model is able to obtain statistically more significant fits to the measured concentration curves [155] and that its parameters display a higher degree of correlation with their true physiogical counterparts [18]. However, the model fitting is confronted with parameter intercorrelations and instability. We have identified the practical evaluation method for the AATH concentrations as the main cause of these instabilities. The discrete convolution, currently used by the majority of the investigators as practical evaluation method for the AATH concentrations, is discontinuous in the

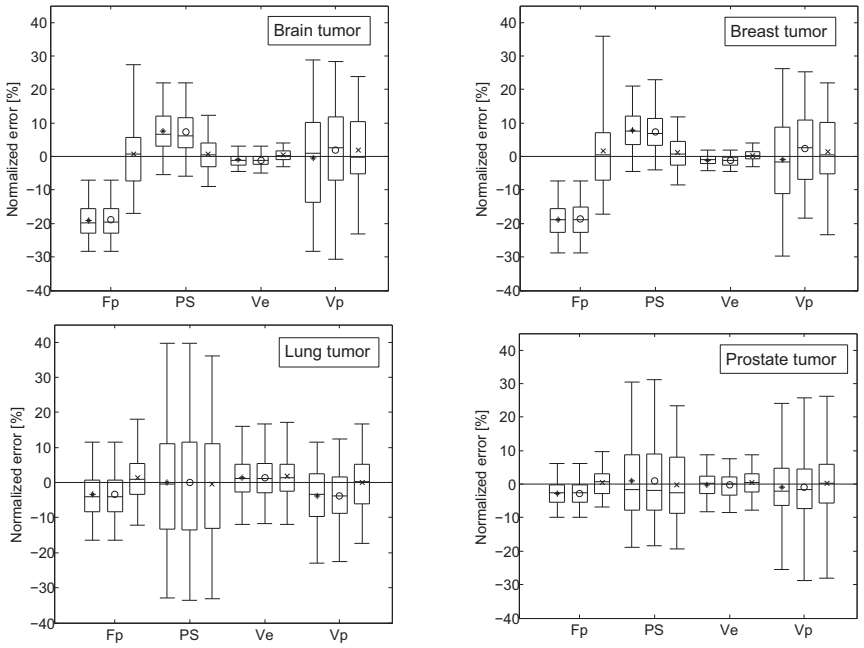


**Figure 7.5:** Boxplots of the relative error distribution for the AATH parameters, fitted with the MMTF- ($*$) , the FMTF- ($\circ$) or the RGBF-method ($\times$) respectively. The error bars denote the 2.5% and 97.5percentiles. The upper- and lower bounds of the boxes indicate the quartiles. The middle line in the boxes is the median error. The signs ($*$,$\circ$ or $\times$) denote the mean error. Kinetic parameter values for the different tumor types are mentioned in table 7.4.

parameter $\tau$. The resulting concentrations are inaccurate when $\tau$ is not a multiple of the time step $\Delta t$. As a consequence, many local minima that occur in the ssq-cost function and the fitting procedures have been developped that scan a high number of regions of the parameter space, to find a global minimum. These fitting procedure are therefore highly time-consuming. From our simulations, the calculation of a kinetic parameter map for a tumor with 1000 voxels and DCE-MRI scan with temporal resolution of 1s, lasts between 13 and 19 hours depending on the applied fitting procedure. In addition, these fittings procedures require high data quality. Kershaw and Cheng recently showed for the FMTF procedure that in order to ensure minimal bias ($<5\%$) a temporal resolution of 1.5s combined with high SNR is requires [24]. From the trade-offs discussed in chapter 2, it is recalled that this kind of DCE-MRI experiment design may be unfeasible, when an acceptable spatial resolution is

required in the pathology. These practical considerations prevent the AATH model, despite its high physiological significance, to become generally accepted as improved pharmacokinetic model and to reveal its potential by clinical studies. It should not be doubted that the development of a fast, stable and accurate fitting procedure for the AATH model, will effectively enhance its clinical relevance.

Our recursive grid based fitting procedure has proven to be superior to the other available fitting methods: mean relative error is reduced severely in bulk simulations, up to 58% for $F_p$; computational time is reduced up to 70%. Single value simulations show that both accuracy and precision of the pharmacokinetic parameters benefit from the use of the RGBF-method. For $F_p$, bias almost disappears although for low $\tau$-values this goes at the cost of decreased precision. This effect, however, has been observed by Garpebring et al. as well, when testing their fourier domain fitting procedure for the TH-model[4] [81]. For $\nu_p$ and $PS$ both the accuracy and the precision are enhanced by the RGBF procedure. For $\nu_e$, RGBF mostly affects the accuracy. The succes of our RGBF-method is founded on the exclusion of all instabilities in $\tau$-direction. One of the problems when discretizing the AATH model equation is the appearance of $\tau$ as a limit in the integral of eq. 7.6. The accuracy of such discrete evaluation method is the highest when $\tau$ is a multiple of $\Delta$, the time step. The local minima in $\tau$-direction, located in between multiples of $\Delta$, are often caused by the inaccuracies of the discrete evalution method, rather than by true resemblance with the AATH model. The RGBF method avoids this issue by excluding all values of $\tau$ that are not multiples of $\Delta$. Only those values of $\tau$ are considered, for which a high accuracy of the concentration evaluation method is assured. The disadvantage is that the complete parameter space has to be scanned, as no search algorithm can be used to find the minimal ssq-value. However, the RGBF procedure reduces the 4-dimensional parameter space to a 2-dimensional grid, by exploiting the linearity of the $K^{trans}$ and $F_p$-parameters in the AATH model equations. Furthermore, the recursion relationship reduces the compuational time to fill the 2D-grid, to the time needed to fill a 1D-line in $k_{ep}$-direction. Thereby, the speed of the procedure has been increased with approximately $\tau_{max}/\Delta$. Remark that the MRE-reduction could be achieved without the recursion relationship as well, but for the example quoted in the previous paragraph (tumor with 1000 voxels), it would require approximately 12.5 days. With the recursion relationship, the time needed is around 3 hours.

It is difficult to compare our MRE-results of the MMTF and FMTF procedures to the of Kershaw & Cheng [24], as they employed a different AIF, a different kinetic parameter range, and most importantly other parameter constraints

[4]It is commonly known that biased estimators may have lower standard deviation than their unbiased counterparts.

(see section 7.2.4). However, the reported errors are in the same order of magnitude, and similar bias in $F_p$ and $\nu_p$ are found. As mentioned above, our new fitting method will not require the same high data quality as reported by Kershaw & Cheng. Future studies should adress this issue. Garpebring et al. compared their fourier domain method to the MMTF method, but used an interpolation technique to increase the accuracy of the AATH convolution. Remark that by adequately constraining the parameter values, only small difference can be observed between MMTF and FMTF procedures, and no conclusions can be made about the superiority of one of both. This consistent constraining of the parameter values is one the strong points of our study and supports the superiority of our RGBF-procedure.

Nevertheless, our study has a number of shortcomings that should be mentioned. First of all, the influence of the grid size in $k_{ep}$ was not investigated. As this grid step imposes an upper bound on the precision of the $k_{ep}$-estimates, but affects the speed of the RGBF-method as well, it comprises a trade-off that should be investigated further. Finally, the input data of our simulations is homoskedastic, and not representative of true DCE-MRI data. This chapter is only a proof-of-concept and the inclusion of the heteroskedastic data distribution can easily be investigated in future work.

## 7.6 Conclusion

A new fast and stable fitting procedure has been developped for the AATH model that overcomes the often cited fit instability problems and can mark the beginning of an increased clinical acceptance of the model.

## Appendix: formal proof of the recursion relationship

In this appendix, a mathematical proof of the recursion relationships for $x_1$ and $x_2$ is provided. For a thorough understanding, we define $\tau_i$ and $t_j$, respectively the $\tau$-value and the time point corresponding with the indices $i$ and $j$:

$$\tau_i = i\Delta \tag{7.17}$$

$$t_j = (j-1)\Delta \tag{7.18}$$

The $j$-indexing scheme was chosen that $j = 1$ corresponds with $t = 0$, which is in agreement with the Matlab-indexing. If $t_j < \tau_i$, eq. 7.9 has to used for the calculation of $x_1(i,j)$ and $x_2(i,j)$. If $t_j \geq \tau_i$, eq. 7.10 should be employed. Therefore the proof is subdivided into three cases: $j < i$, $j = i$ and $j > i$.

- $j < i$

  If $j < i$, $t_j$ is both smaller than $\tau_i$ and $\tau_{i-1}$. Therefore, both $x_1(i,j)$ and $x_1(i-1,j)$ have to be calculated with eq. 7.9. As eq. 7.9 does not depend on $\tau$, it is proven that:

$$\begin{aligned} x_1(i,j) &= \int_0^t C_p(t-t')dt' && (7.19)\\ &= \int_0^{(j-1)\Delta} C_p((j-1)\Delta - t')dt' && (7.20)\\ &= x_1(i-1,j) && (7.21) \end{aligned}$$

  For $x_2$ a similar argumentation can be used: both $x_2(i,j)$ and $x_2(i-1,j)$ are 0. The recursion relationships are proven for $j < i$

- $j = i$

  In this case, $t_j < \tau_i$, but $t_j = \tau_{i-1}$. Nothing changes for $x(i,j)$, which still agrees to eq. 7.20. However, $x_1(i-1,j)$ has to be calculated with eq. 7.10:

$$\begin{aligned} x_1(i-1,j) &= \int_0^{\tau_{i-1}} C_p(t-t')dt' && (7.22)\\ &= \int_0^{(i-1)\Delta} C_p((j-1)\Delta - t')dt' && (7.23)\\ &= \int_0^{(j-1)\Delta} C_p((j-1)\Delta - t')dt' && (7.24)\\ &= x_1(i,j) && (7.25) \end{aligned}$$

  $x_2(i,j)$ remains 0 in this case. As $t_j = \tau_{i-1}$, $x_2(i-1,j) = 0$ when calculated with eq. 7.10. The recursion relationships are proven for $j = i$.

- $j > i$

  Firstly an expression is derived for $x_1(1, j-i+1)$. As $j > i$, $t_{j-i+1} > \tau_1$. Therefore $x_1(1, j-i+1)$ is calculated according to eq. 7.10:

$$\begin{aligned} x_1(1,j-i+1) &= \int_0^{\Delta} C_p((j-i)\Delta - t')dt' && (7.26)\\ &= \int_{(j-i-1)\Delta}^{(j-i)\Delta} C_p(u)du && (7.27) \end{aligned}$$

(7.28)

The last expression is obtained by substituting $u = (j-1)\Delta - t'$ in the integral. For $x_1(i,j)$, eq. 7.10 has to be used as well, as $t_j > \tau_i$:

$$\begin{aligned}
x_1(i,j) &= \int_0^{\tau_i} C_p(t_j - t')dt' && (7.29)\\
&= \int_0^{i\Delta} C_p((j-1)\Delta - t')dt' && (7.30)\\
&= \int_0^{(i-1)\Delta} C_p((j-1)\Delta - t')dt' + \\
&\quad \int_{(i-1)\Delta}^{i\Delta} C_p((j-1)\Delta - t')dt' && (7.31)\\
&= x_1(i-1,j) + \int_{(j-i-1)\Delta}^{(j-i)\Delta} C_p(u)du && (7.32)\\
&= x_1(i-1,j) + x_1(1,j-i+1) && (7.33)
\end{aligned}$$

Eq. 7.32 has been derived from eq. 7.31 by using that (first term) $t_j > \tau_{i-1}$ as well, and therefore eq. 7.10 is valid for $x_1(i-1,j)$ and (second term) by substituting $u = (j-1)\Delta - t'$.

Similarly, for $x_2(i,j)$, eq. 7.10 has to be used:

$$\begin{aligned}
x_2(i,j) &= \int_{\tau_i}^{t_j} C_p(t_j - t')exp\left[-k_{ep}(t' - \tau_i)\right]dt' && (7.34)\\
&= \int_{\tau_{i-1}}^{t_j} C_p(t_j - t')exp\left[-k_{ep}(t' - \tau_{i-1} - \Delta)\right]dt' - \\
&\quad \int_{\tau_{i-1}}^{\tau_i} C_p(t_j - t')exp\left[-k_{ep}(t' - \tau_i)\right]dt' && (7.35)\\
&= e^{k_{ep}\Delta}x_2(i-1,j) - y(i,j) && (7.36)\\
y(i,j) &= \int_{(i-1)\Delta}^{i\Delta} C_p((j-1)\Delta - t')exp\left[-k_{ep}(t' - i\Delta)\right]dt' && (7.37)\\
&= \int_{(j-i-1)\Delta}^{(j-i)\Delta} C_p(u)exp\left[-k_{ep}((j-i-1)\Delta - u)\right]du && (7.38)\\
&= e^{k_{ep}(i-j+1)\Delta}\int_{(j-i-1)\Delta}^{(j-i)\Delta} C_p(u)exp\left[k_{ep}u\right]du && (7.39)\\
&= e^{k_{ep}(i-j+1)\Delta}\int_{t_{j-i}}^{t_{j-i+1}} C_p(u)exp\left[k_{ep}u\right]du && (7.40)\\
&= e^{k_{ep}(i-j+1)}x_3(k_{ep}, j-i+1) && (7.41)
\end{aligned}$$

The recursion relationship is now proven for $j > i$ as well.

# Chapter 8

# Protocol optimization for pharmacokinetic modeling: influence of total scan time and temporal resolution

## 8.1 Introduction

To our knowledge, all studies investigating the influence of protocol design on kinetic parameter estimation, use a simulation methodology to assess the accuracy and the precision of the kinetic parameters, in absence of a validation standard. Typically, a (simplified) simulation set-up is as follows: a tissue concentration curve is generated according to a given kinetic model, sampled and infected with white gaussian noise with constant variance. This distorted curve is then fit to the kinetic model under consideration and the best-fit values are compared to the input values used for curve generation. To assess accuracy, the simulation is repeated $m$ times for a fixed kinetic parameter set, and the average of the $m$ best-fit values is compared to the true values. The variance of the $m$ best-fit values is a measure for kinetic parameter precision. The higher $m$, the better the statistical power of the simulation set-up. This procedure has two major disadvantages. First of all, to get sigificant results, m has to be in the order of $10^2 - 10^3$ for every kinetic parameter set under investigation. Therefore, it is very time-consuming, and it is difficult to perform simulations for a wide range of kinetic parameters or investigate multiple protocol designs. Therefore, most of these studies are in fact case-studies, in which the influence of one single parameter or error source (temporal resolution, accuracy of the AIF, noise level, injection protocol,... ) is investigated for one single kinetic model. Although these studies are of great

value for assessing kinetic parameter accuracy, the reproducibility of pharmacokinetic modeling and the design of standardized protocol may be difficult without a generalized framework. Secondly, only a limited number of studies effectively investigate the influence of the pulse sequence parameters [28, 36]. Nevertheless, pulse sequence parameters have a major influence on the kinetic parameter precision as they determine the concentration noise levels at fixed SNR (see chapters 3, 5& 6). In addition, pulse sequence parameters are coupled to spatial resolution, SNR and temporal resolution. The repetition time for instance has an important influence on temporal resolution and their common relationship is dependent on the sampling strategy of k-space (see chapter 2). It minimal value is determined by the field-of-view, the spatial resolution and the bandwidth. In chapter 2, it was shown that strategies to adapt the temporal resolution, such as partial fourier sampling, inevitably affect the SNR as well. These trade-offs between temporal resolution, spatial resolution and SNR have only been taken into account in a minority of the simulation studies [28].

Our Cramer-Rao Lower bound (CRLB) framework, that was proposed in chapter 6 to predict the confidence intervals on the kinetic parameters, has the ability to investigate the influence of any parameter on the kinetic parameter precision by one single calculation, instead of multiple simulations. CRLB describe how noise on the MR signal vs. time curve is transported throughout the different processing steps (concentration calculation, fit procedure) to uncertainty on the kinetic parameters and naturally incorporate the temporal resolution of the scans, the SNR of the MR images, the total scan time and the non-linearities between signal enhancement and CA concentration. They are therefore of particular interest for investigating the reproducibility of the DCE-MRI protocol and to make recommendations for protocol optimization. As they have been derived in chapter 6 in a model-independent manner, they can be implemented for any kinetic model and model comparison becomes feasible. However, CRLB can only assess kinetic parameter precision. Accuracy and estimation bias, due to error sources of improper protocol design or MR-related errors, should be investigated by the case studies mentioned above. Nevertheless, kinetic parameter precision and more general the reproducibility of DCE-MRI and pharmacokinetic modeling is of crucial importance for increasing the clinical acceptance of several promising applications, as was shown by the example in chapter 1. In particular for the testing of novel anti-angiogenic therapy, treatment follow-up, or cancer characterization, an optimized protocol with high reproducibility is indispensable. In addition, on mathematical grounds, the accuracy of a parameter cannot be discussed without acceptable precision.

In this chapter the CRLB methodology is employed for protocol optimization and precision analysis of kinetic parameter estimates. It contains an expanded version of the work proposed in [25]. The chapter starts with the introduction

and the validation of the CRLB methodology in section 8.2. In section 8.3, the influence of the kinetic parameters values themselves and the SNR in the DCE-MRI measurements on the kinetic estimates precision in the TK model are analysed. Total scan time and temporal resolution are investigated in section 8.4 and section 8.5 respectively. In section 8.6 the relevance of flip angle optimization, in accordance with chapter 5, is examined. Finally the precision of the ETK-parameters and TK-parameters is compared in section 8.7 and some practical recommendations are formulated in section 8.8.

## 8.2 Cramer-Rao lower bounds methodology

### 8.2.1 Fisher matrix elements

In chapter 6 it was confirmed that the maximum likelihood estimator (MLM) exhibits the smallest possible variance on kinetic parameter estimates. These underbounds on the uncertainty are called the CRLB. In practice, CRLB are calculated as the diagonal elements of the inverse fisher matrix. The fisher matrix elements ,$F_{kl}$, for a DCE-MRI experiment measuring $n$ CA concentrations time points $t_i$, with signal intensity variation $S(C)$ and given SNR ($M_0/\sigma_S$), and for a general kinetic model $C_T(\boldsymbol{\theta})$, with a parameter vector $\boldsymbol{\theta}$, were derived in the appendix of chapter 6 :

$$F_{kl} = \sum_{i=1}^{n} \frac{dC_{Ti}}{d\theta_k} \frac{dC_{Ti}}{d\theta_l} (2\alpha_i^2 + \frac{1}{\sigma_i^2}) \tag{8.1}$$

$$\alpha_i = \frac{d^2S/dC^2}{dS/dC}_{C=C_{Ti}} \tag{8.2}$$

$$\sigma_i = \frac{1}{SNR} \left[ \frac{dS'}{dC} \right]^{-1}_{C=C_{Ti}} \tag{8.3}$$

For simplicity of notation, $C_T(t_i)$ are written as $C_{Ti}$. $\frac{dC_{Ti}}{d\theta_k}$ denotes the derivative of the kinetic model equation to the $k^{th}$ element of the parameter vector $\boldsymbol{\theta}$, evaluated in $C_{Ti}$. $S'$ is the normalized signal intensity ($S/M_0$). Remark that for $\alpha_i$ it does not matter whether $S$ or $S'$ is used.

### 8.2.2 Validation by simulations

As mentioned in the introduction, kinetic parameter precision is mostly assessed by repeated simulations. To justify the CRLB-methodology used in this chapter, the results from such simulations are compared to the results from the CRLB framework. As in chapter 6 the validity of CRLB for calculating kinetic parameter confidence intervals has already been shown for three SPGRE-pulse sequences, an IR-SGPRE sequence has been used in this section [131]. Pulse

**Table 8.1:** Protocol parameters for the pulse sequences of Ceelen et al. (PS1) [131], Galbraith et al. (PS2) [66] and for 1 self-defined pulse sequence (PS3). For the IR-SPGRE pulse sequences, inversion time was 560 ms.

| Study | Pulse sequence | $\Delta t$ [s] | $T_{scan}$ [s] | $T_R$ [ms] | $T_E$ [ms] | $\alpha$ [°] |
|---|---|---|---|---|---|---|
| PS1 | IR-SPGRE | 1.1 | 550 | 1100 | 4.12 | 12 |
| PS2 | SPGRE | 12 | 360 | 80 | 9 | 70 |
| PS3 | IR-SPGRE | 1.1 | 360 | 1100 | 3.42 | 12 |

sequence details are found in table 8.1 (PS1). The validation was performed for Gd-DTPA as CA ($r_1$ and $r_2$-values can be found in [44] or table 2.2) and for the TK model:

$$C_T^{TK}(t) = K^{trans} \int_0^t C_p(t') exp[-k_{ep}(t-t')]dt' \tag{8.4}$$

For a given $K^{trans}$ and $\nu_e$, tissue concentration curves were generated according eq. 8.4 with a temporal resolution of 0.1 s and with the AIF as modelled by Weinmann (see eq. 3.18, dose = 0.1 $mmol\ kg^{-1}$). These curves are sampled with the temporal resolution and for the total scan time of PS1. From these sampled curves, signal intensity curves are generated according to the signal equation of IR-SPGRE pulse sequences (see chapter 2). $T_{10}$ was set to 675 ms [45]. After adding gaussian noise with fixed standard deviation (SNR = $M_0/\sigma_S = 100$) to the signal curve, the concentration-time curve is recalculated and fitted to the TK model with the MLM estimator as described in chapter 6. This procedure is repeated $10^3$ times for every kinetic parameter couple. The standard deviation of the resulting kinetic parameter distributions is compared to the uncertainty values predicted by the CRLB. To calculate the CRLB's, the fisher matrix elements are implemented in Matlab, with the signal intensity and TK model derivatives calculated analytically and accordingly implemented. The CRLB vs. simulations comparison is performed for $K^{trans}$ varying between 0.02 and 1.2 $min^{-1}$ combined with $\nu_e$=0.3 and $\nu_e$ = 0.5, covering ranges from other simulation [23,175] or clinical studies [45,66] with Gd-DTPA.

Fig. 8.1 shows the standard deviations $\sigma_K$ and $\sigma_\nu$ on the simulated kinetic parameters' distribution obtained with the MLM estimator, and the CRLB for PS1. The uncertainties are shown for a LSQ estimator as well. It is clear that the MLM obtained standard deviation concurs with the minimal standard deviation as predicted by the CRLB for both kinetic parameters. This confirms that the results from CRLB analysis are identical to those obtained from repeated simulations and justifies the use of the CRLB for protocol

optimization. In addition, the advantage of using MLM estimation instead of LSQ is illustrated for IR-SPGRE pulse sequences, with $\sigma_K$-reductions up to 30% for high $K^{trans}$ (1.2 $min^{-1}$) and $\nu_e$ (0.5). Both $\sigma_K$ and $\sigma_v$ of the LSQ estimator evolve in a similar manner as the CRLB, implying that CRLB can be used to make predictions about the precision of kinetic parameter estimates with LSQ-estimators as well.

### 8.2.3 Validation by comparison with literature

Clinical validation CRLB is a laborious task. It requires the experimental estimation of the standard deviation on the kinetic parameters, which can be achieved by performing paired examinations on test subjects. Several difficulties emerge however: firstly, an almost identical patient localisation is required, to ensure that the DCE-MRI errors (flip angle deviation from its nominal value, partial volume effects, error in $T_{10}$,...) are approximately equal in both examinations. Although this is difficult in clinical studies, it may be feasible in an animal model. In test animals, however, the fast growing implanted human tumor cell line may undergo significant vascular changes in the time period between the paired examinations, as at least 24h-48h interscan time may be needed, to ensure total Gd-clearance and for toxicity (of both sedative and Gd-complex) reasons. In clinical studies these problems may be sidestepped by performing a ROI-analysis instead of pixel-by-pixel validation. A second problem is posed by the AIF. CRLB assume a single AIF, although it is unlikely that AIF is identical in both examinations. Therefore the CA injection protocol and all physiological factors influencing the shape and the amplitude of the AIF (heart rate, blood pressure, injection site, ...) should be identical. Again, this problem can be partially avoided by assuming a fixed standard AIF, as the cost of reduced accuracy of the kinetic parameters. Nevertheless, Cheng showed that the error in $K^{trans}$ scaled linearly with the underestimation of the AIF peak [27]. Therefore, when the error in the AIF is not identical for both of the paired examinations, a change in $K^{trans}$ will occur, that cannot be explained by the CRLB.

Taking into account the above considerations, no in vivo validation of the CRLB was performed. Instead, the results of an experimental kinetic modeling reproducibility study from literature are compared with the predicted reproducibility from CRLB analysis. In an often cited paper, Galbraith et al. tested the reproducibility of kinetic parameters in tumors and muscles by means of statistical analysis of paired examinations in a group of 16 patients [66]. They employed the TK model (eq. 8.4) with a population-averaged Weinmann AIF and performed a whole ROI analysis. As measure for kinetic parameter reproducibility, the within-patient coefficient of variation (wCV) and the ratio of between patient variance to within patient variance were used:

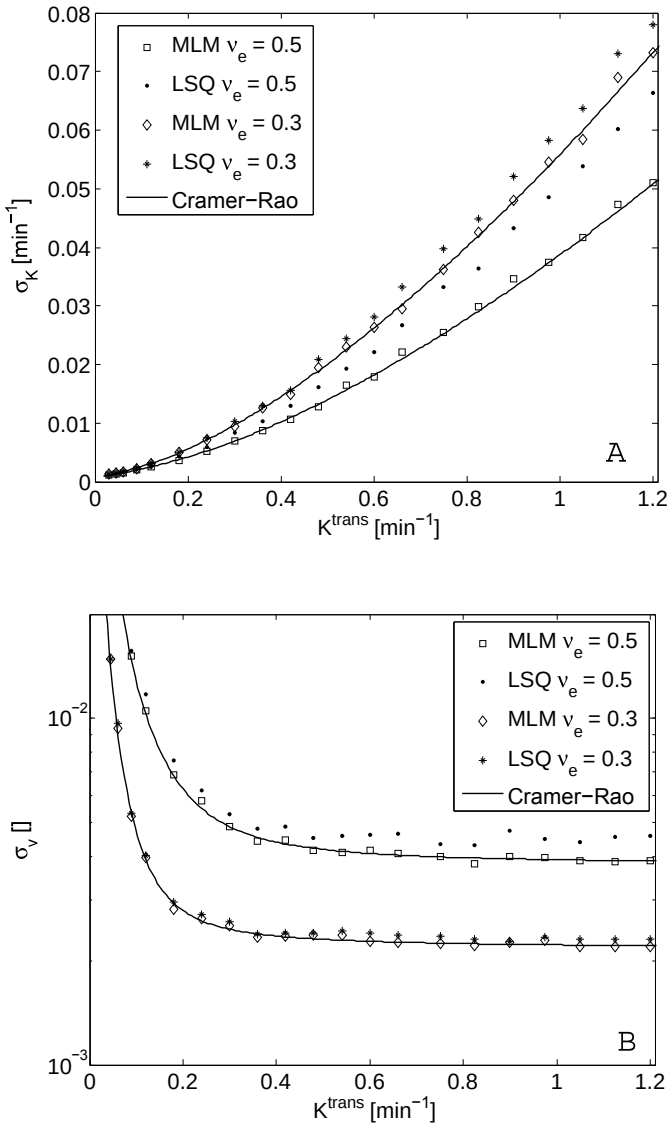


**Figure 8.1:** Standard deviation $\sigma_K$ (A) and $\sigma_\nu$ (B) of the LSQ- and MLM-estimators, versus $K^{trans}$ and for 2 values of $\nu_e$ (data points), and Cramer-Rao lower bounds on $\sigma_K$ and $\sigma_\nu$ calculated with eq. 8.1 (solid line). Other simulation parameters are mentioned in the text.

**Table 8.2:** Reproducibility statistics for the data of Galbraith et al. [66].

| Parameter | p-value for Kendall's $\tau$ | wCV | Variance ratio |
|---|---|---|---|
| $K^{trans}_{muscle}$ | 5.94 $10^{-5}$ | 36.7 % | 2.54 |
| $K^{trans}_{tumor}$ | 0.0016 | 8.9% | 6.19 |
| $\nu_{muscle}$ | 0.1254 | 5.6% | 6.46 |
| $\nu_{tumor}$ | 0.3502 | 2.2 % | 17.66 |

$$wCV = \frac{\sqrt{\frac{\sum d^2}{N}}}{\mu_\theta} \tag{8.5}$$

d is difference in the kinetic parameter $\theta$ between the paired examinations, N is the number of patients and $\mu_\theta$ is the mean kinetic parameter value in the group of patients. By digitizing figure 1 from Galbraith et al. the mean [$K^{trans}$, $\nu_e$]-couples over both examinations for the 16 patients in the study were obtained, in tumor and in muscle respectively. With these values and the protocol parameters for the SPGRE-pulse sequence employed by Galbraith (table 8.1, PS2), the absolute values of $\sigma_K$ and $\sigma_v$ in tumor and muscle were simulated with the CRLB-expressions. wCV and the variance ratio were calculated for both kinetic parameters in both tissues by substituting $\sigma_\theta$ for d in eq. 8.5. Kendall's $\tau$ for correlation between $\sigma_\theta$ and $\theta$ was determined as well. For muscle a $T_{10}$-value of 1008 ms was assumed [30].

Fig. 8.2 shows the absolute values of the standard deviation on the kinetic parameters for the 16 patients in the reproducibility study as predicted by CRLB (SNR = 100). Table 8.2 contains the p-value for the hypothesis that a correlation is existing between the size of a kinetic parameter and its standard deviation, based on kendall's $\tau$ correlation coefficient. From these values and from fig. 8.2, it is obvious that (at the 5%-level) $\sigma_K$ depends strongly on the value of $K^{trans}$ for both muscle and tumor, whereas $\sigma_v$ shows no significant correlation with the size of $\nu_e$. Table 8.2 contains the wCV and the variance ratio as well. For this cohort of patients, CRLB predicts that both kinetic parameters are more reproducible in tumor than in muscle. Within the same tissue, $\nu_e$ is the most reproducible parameter.

The experimental results from Galbraith et al. are very similar: they found a significant correlation between the difference in $K^{trans}$-estimates of paired examinations and the size of the mean $K^{trans}$. For $\nu_e$ no such correlation could be found. In their group of patients, they determined $\nu_e$ as the more reproducible kinetic parameter in tumors and demonstrated a worse

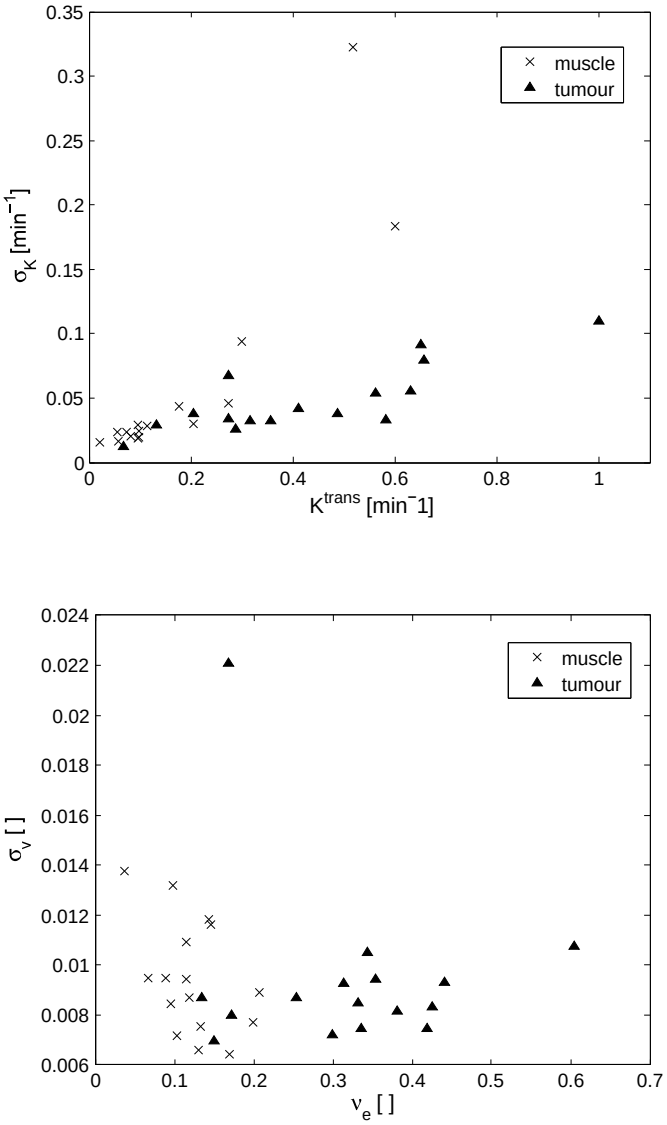


**Figure 8.2:** Absolute values of the standard deviation on the kinetic parameters $\sigma_K$ and $\sigma_v$ for the kinetic parameter couples in the study of Galbraith et al. Protocol details are mentioned in table 8.1.

kinetic parameter reproducibility in muscle in comparison with tumor [66]. These findings are in excellent agreement with the theoretical CRLB-based reproducibility analysis of fig. 8.2 and table 8.2, which can be considered as proof-of-concept of the CRLB framework.

## 8.3 Tofts & Kermode model: Influence of kinetic parameter value and SNR

In this section the reproducibility of the TK-model parameters, $K^{trans}$ and $\nu_e$ is investigated. As most clinical studies have identified $K^{trans}$ as the most important or decisive for clinical applications, its reproducibility is the main concern of this section. Throughout the rest of this chapter, as a measure for kinetic parameter uncertainty, the coefficient of variation of kinetic parameter, $c_\theta = \sigma_\theta/\theta$, is used. As a measure for precision, its inverse value is employed.

Before analysing the influence of total scan time and the trade-off's concerning temporal resolution, the precision of the kinetic parameters is investigated for 2 fixed pulse sequences from DCE-MRI literature [66, 131]. Pulse sequence type and parameters are mentioned in table 8.1 (PS1 & PS2). CRLB are calculated for $K^{trans}$ and $\nu_e$ varying in the physiologically relevant range of 0.02-1.2 $min^{-1}$ and 0.1-0.5 respectively [23, 26, 175]. The Weinmann AIF for Gd-DTPA is used and the native $T_1$-relaxation time $T_{10}$ was set to 675 ms [45]. To evaluate the influence of the SNR of the MR-measurement on the kinetic parameter precision, SNR is varied between 5 and 200.

Fig. 8.3 A & B plot the coefficient of variation $c_K$ or the relative standard deviation on $K^{trans}$ as a function of the kinetic parameter values for PS1 and PS2 respectively. It is clear that $K^{trans}$-precision is highly dependent on the kinetic parameters themselves. An increase in $K^{trans}$-uncertainty is seen for both low $K^{trans}$ and high $K^{trans}$, the latter being strongly dependent on the $\nu_e$-value: higher EES-volumes allow more reproducible determination of $K^{trans}$. A similar trend can be observed for $\nu_e$, whose coefficient of variation is shown in fig. 8.3 C & D (with logarithmic axis, due to the large range): an increase in uncertainty is observed at both low and high $K^{trans}$. Again at high $K^{trans}$, higher EES volumes exhibit higher precision, while al low $K^{trans}$, small EES volumes have higher precision. Lopata and coworkers investigated the frequency response of the TK-model and found that it acts as a low-pass filter with a cut-off frequency given by $k_{ep} = K^{trans}/\nu_e$ [23]. This denotes that of all frequencies present in the arterial input function, those above $K^{trans}/\nu_e$ are attenuated and explains the observations in fig. 8.3 A-D: At high $K^{trans}$ combined with increasing $\nu_e$, i.e. high cut-off frequencies, the temporal resolution of the pulse sequences under investigation fails to adequately sample the increased frequencies in the concentration curve, causing high uncertainties.

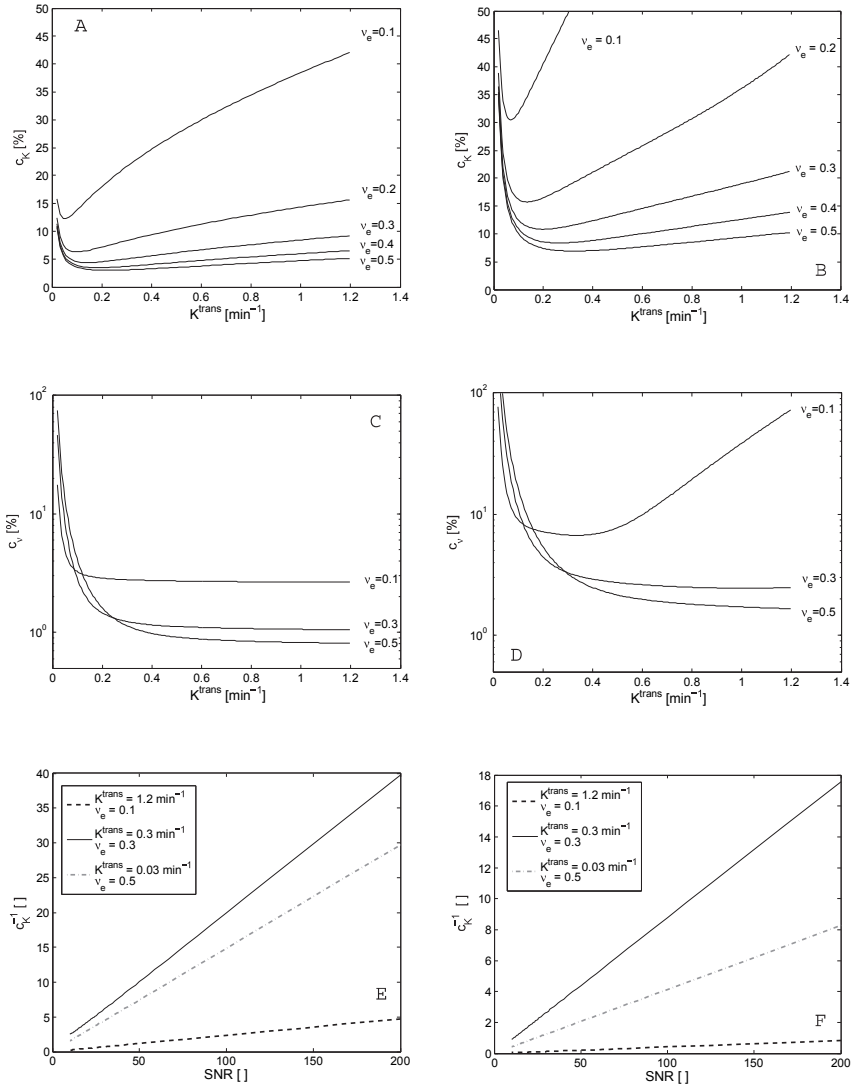


**Figure 8.3:** A-B: Coefficient of variation for $K^{trans}$ as a function of $K^{trans}$ and for different values of $\nu_e$ for PS1 (A) and PS2 (B). C-D: Coefficient of variation for $\nu_e$ as a function of $K^{trans}$ and for different values of $\nu_e$ for PS1 (C) and PS2 (D). E-F: $K^{trans}$-precision, expressed as the inverse of the uncertainty, versus ratio for 3 different kinetic parameter couples for PS1(E) and PS2(F).

This statement is reinforced by the observation that the uncertainty increase at high $K^{trans}$ and low $\nu_e$ is most pronounced for the pulse sequence with the smallest temporal resolution (PS2). At low $K^{trans}$, combined with high $\nu_e$, i.e. when the cut-off frequency is small, the total scan time of the pulse sequences under investigation fails to cover[1] an adequate part of the frequency spectrum of the concentration curve, causing increased uncertainties. Again, this statement is confirmed when comparing the extent of the uncertainty increase of both pulse sequences under investigation in fig. 8.3. Finally, fig. 8.3E & F plots the variation of the $K^{trans}$-precision (expressed as the inverse of the coefficient of variation) with SNR. For three kinetic parameter couples, it is clear that the kinetic parameter precision is proportional to the SNR of the MR-measurement. The proportionality factor is however strongly dependent on the kinetic parameter values and the pulse sequence design. Similar SNR in the MR-signal is converted to smaller kinetic parameter precision by PS2 in comparison with PS1, due to longer total scan time, higher temporal resolution and different concentration uncertainties. This shows that noise propagation in kinetic parameter estimation is highly influenced by the protocol design.

## 8.4 Total scan time

The influence of the total scan time $T_{scan}$ on kinetic parameter uncertainty is analysed by doubling $T_{scan}$ for PS1 and PS2 and inspecting the ratio of $\sigma_K$ at both scan times. To investigate whether $T_{scan}$ requirements are dependent on the studies pulse sequence equation, the pulse sequence parameters or the temporal resolution, a third pulse sequence (PS3) was defined (table 8.1). It is identical to PS1, but the total scan time corresponds to PS2. For PS3, scan time was again doubled and the uncertainty ratio was analysed. From these results, it will be clear that increasing total scan time always enhances kinetic parameter precision. Therefore, to make practical recommendations about the total scan time needed for precise determination of the kinetic parameters, we introduce the concept of precision efficiency:

$$\Gamma = \frac{1}{\sigma_K \; T_{scan}} \tag{8.6}$$

$\Gamma$ describes the average precision per total scan time unit. Minimal necessary scan time for a kinetic parameter couple [$K^{trans}$, $\nu_e$] will be derived by maximizing $\Gamma$ for PS1.

Fig. 8.4A shows the ratio $\frac{\sigma_K(T_{scan})}{\sigma_K(2T_{scan})}$ for PS1-PS3, as a function of $K^{trans}$. As expected from the previous section, the influence of $T_{scan}$ is primarily on the precision of low $K^{trans}$ combined with high $\nu_e$-values. $K^{trans}$-precision in rapidly enhancing tissues, with small fractional EES-volume is for both PS1

[1]The smallest frequency in the sampled signal is $1/T_{scan}$

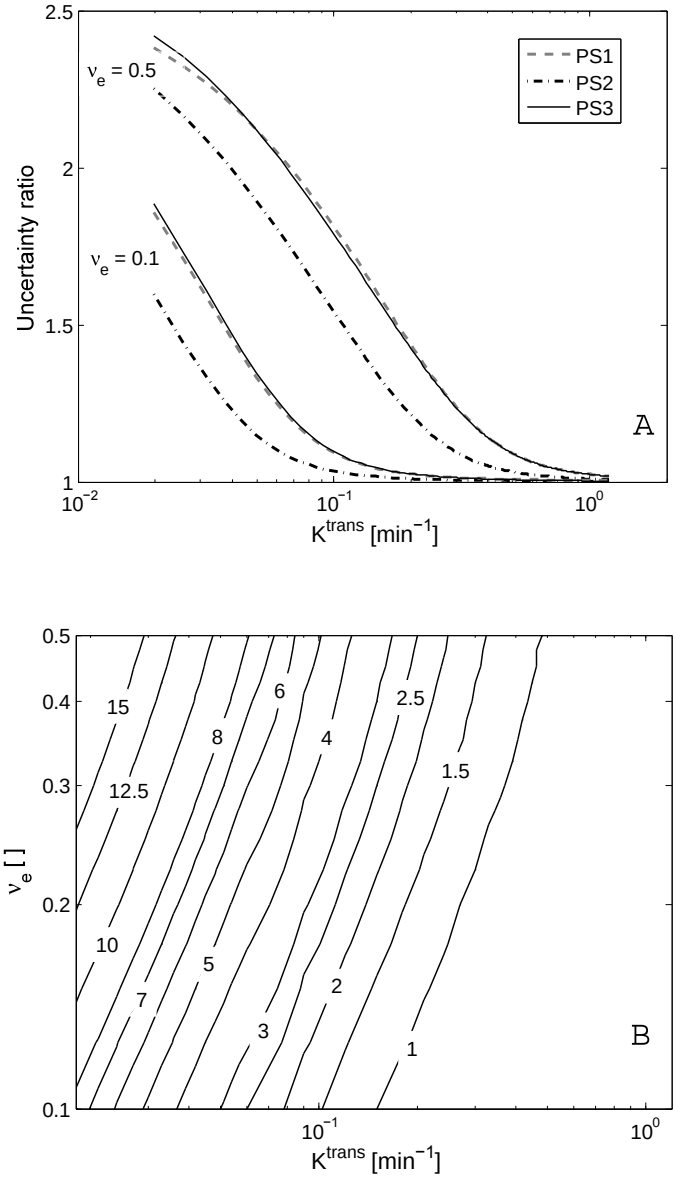


**Figure 8.4:** A: Ratio of the $K^{trans}$-uncertainty for the scan time from table 8.1 to the uncertainty for the double scan time, versus $K^{trans}$ for $\nu_e$=0.1 and $\nu_e = 0.5$. B: contour plot of most efficient scan time (in minutes) as a function of $K^{trans}$ and $\nu_e$.

**Table 8.3:** Protocol parameters for the SPGRE pulse sequences of Padhani et al. (PS4) [19], Yang et al. (PS5) [141] and Batchelor et al. (PS6) [135]. SNR of PS4 is assumed to be 400. SNR of the other pulse sequences was calculated based on the scalingrelationship in eq. 8.7.

| Study | $\Delta t$ [s] | $T_R$ [ms] | $T_E$ [ms] | $\alpha$ [°] | $\Delta x/\Delta y/\Delta z$ [mm] | $B_0$ [T] | SNR |
|---|---|---|---|---|---|---|---|
| PS4 | 10 | 35 | 5 | 70 | 0.98/1.3/10.0 | 1.5 | 400 |
| PS5 | 2 | 7.8 | 1.7 | 60 | 1.2/2.7/8.0 | 1.5 | 508 |
| PS6 | 5.04 | 5.7 | 2.73 | 10 | 2.9/2.0/2.1 | 3 | 359 |

and PS2 scarcely influenced by doubling total scan time. It is interesting to see that the uncertainty ratio curves for PS1 and PS2 are parallel for both $\nu_e$-values. This indicates that the influence of $T_{scan}$ depends solely on the kinetic parameter value. This is confirmed by the uncertainty ratio curve of PS3. It is practically identical to the one of PS2, though pulse sequence, pulse sequence parameters and temporal resolution differ. Increasing scan time from 360 s to 720 s reduces $\sigma_K$ equally for PS2 and PS3, unregarded the other protocol parameters. Total scan time requirements can therefore be deduced independent of other protocol parameters and are only relying on the kinetic parameter values. Fig. 8.4B is a contour plot of the scan time maximizing precision efficiency (eq. 8.6) for PS1. Low $K^{trans}$ combined with high $\nu_e$ again need the longest $T_{scan}$. Increasing $T_{scan}$ above the values from fig. 8.4 still decreases $K^{trans}$-uncertainty, but the precision increase is smaller than the increase in total scan time and therefore no longer efficient. For this particular case of Tofts modeling of Gd-DTPA concentration curves, a scan time of 15 minutes is sufficient to achieve high $K^{trans}$-precision in the complete kinetic parameter range under consideration.

## 8.5 Temporal resolution

To estimate the influence of temporal resolution on kinetic parameter precision, we have simulated the CRLB for three different DCE-MRI protocols from literature. The details of these three studies [19, 135, 141], employing very different temporal resolutions, are mentioned in table 8.3. However, while total scan time can be prolonged without affecting any other imaging parameter, this is not the case for the temporal resolution. In chapter 2, it was discussed that a trade-off exists between temporal resolution, spatial resolution and SNR. Therefore to compare the kinetic parameter precision in the DCE-MRI protocols with differing temporal resolution, we have used the scaling relationship [42](see chapter

2):

$$SNR \propto B_0 \frac{\Delta x \Delta y \Delta z \sqrt{N_x N_y NEX}}{\sqrt{BW}} \tag{8.7}$$

$\Delta x \Delta y \Delta z$ is the product of the three voxel dimensions (the voxels volume). NEX is the number of averages, and is directly proportional to $\Delta t$. In the case of partial fourier imaging NEX can be smaller than one [42]. For the three pulse sequences (PS4-PS6) under investigation, the voxel dimensions were available and a fair comparison of the SNR could be made (NEX=1), assuming identical field of view and bandwidth. For PS4 a SNR of 400 was assumed, and the SNR of PS5-PS6 is calculated based on the scaling relationship above (table 8.3). The total scan time of the protocols was set to 15 min, to exclude any effects from non-sufficient scan time. The CRLB are simulated for both the Weinmann AIF and the Parker AIF and $T_{10}$ was set to 675 ms [45].

Fig. 8.5 & fig. 8.6 show for the Parker AIF and the Weinman AIF respectively, the procentual $K^{trans}$-uncertainty for $\nu_e = 0.1$ and $\nu_e = 0.5$ respectively, as a function of $K^{trans}$ for three pulse sequences (PS4-PS6). Despite having the highest temporal resolution and SNR, PS5 does not yield the most precise $K^{trans}$, except for high $K^{trans}$ low $\nu_e$ combinations. Moreover, the pulse sequence with the smallest temporal resolution has the best performance of the three pulse sequences under consideration for a large kinetic parameter range. For PS6, this could be understood from the lower SNR in the MR-measurement, but for PS5 this is a surprising and contra-intuitive observation. As we have assumed a fixed scan time of 15 minutes for the three protocols, the data curve acquired with PS5 or PS6 always contains more data points than the corresponding data curve of PS4. This lower kinetic parameter precision can only be caused by higher concentration uncertainty on these data points. Fig. 8.5 and fig. 8.6 C & D plot the procentual concentration uncertainty as a function of time for two kinetic parameter couples, whose reproducibility is higher in PS4. Concentration uncertainty is considerably lower in PS4. Compared to PS6, this reduced noise level on the concentration curve induces more reproducible kinetic parameter estimates over the complete range. Compared to PS5, small $K^{trans}$/ high $\nu_e$ combinations, the higher concentration uncertainty in PS5 is not cancelled out by the extra amount of information. For high $K^{trans}$/small $\nu_e$-couples however, the higher temporal resolution becomes the decisive factor and despite of the higher concentration uncertainty, kinetic parameter precision is better with PS5. This is in accordance with the analysis in the previous section. As SNR in PS5 is higher than in PS4, the higher concentration uncertainty can only emerge from the non-linear conversion of MR signal to CA concentration. These results show the effects of the non-linear conversion between MR signal and CA concentration and indicate that due to the strong link between temporal resolution and repetition time, protocols with higher temporal resolution do not necessarily deliver more precise kinetic parameter estimates.

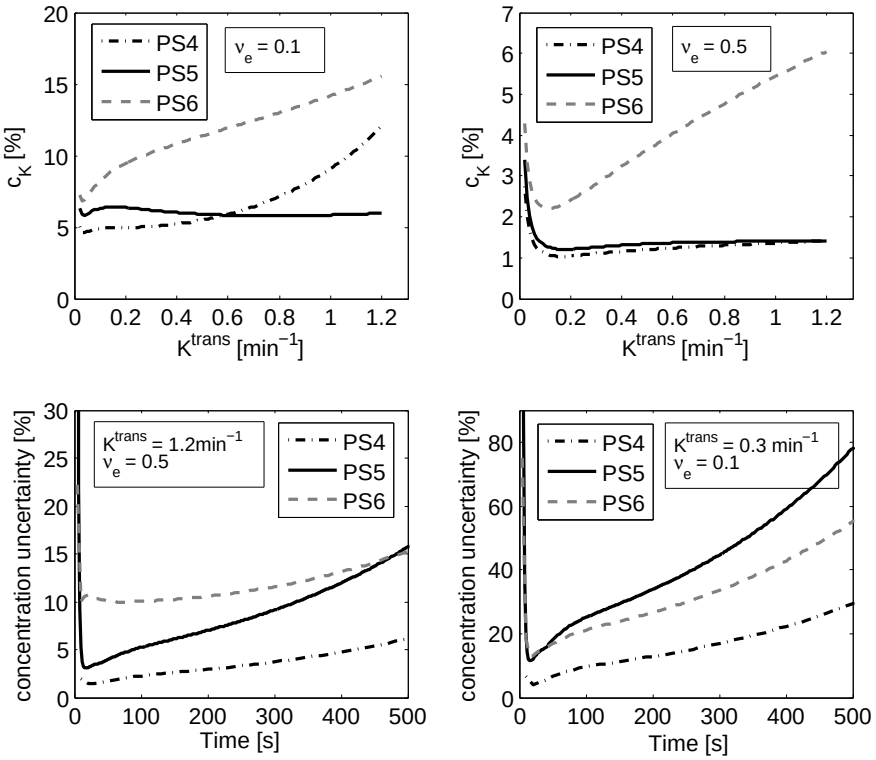


**Figure 8.5:** A-B: coefficient of variation for $K^{trans}$ as a function of $K^{trans}$ for three pulse sequences with different temporal resolution and SNR (table 8.1) with the Parker AIF. C-D: procentual concentration uncertainty vs. time for the three pulse sequences for two kinetic parameter combinations.

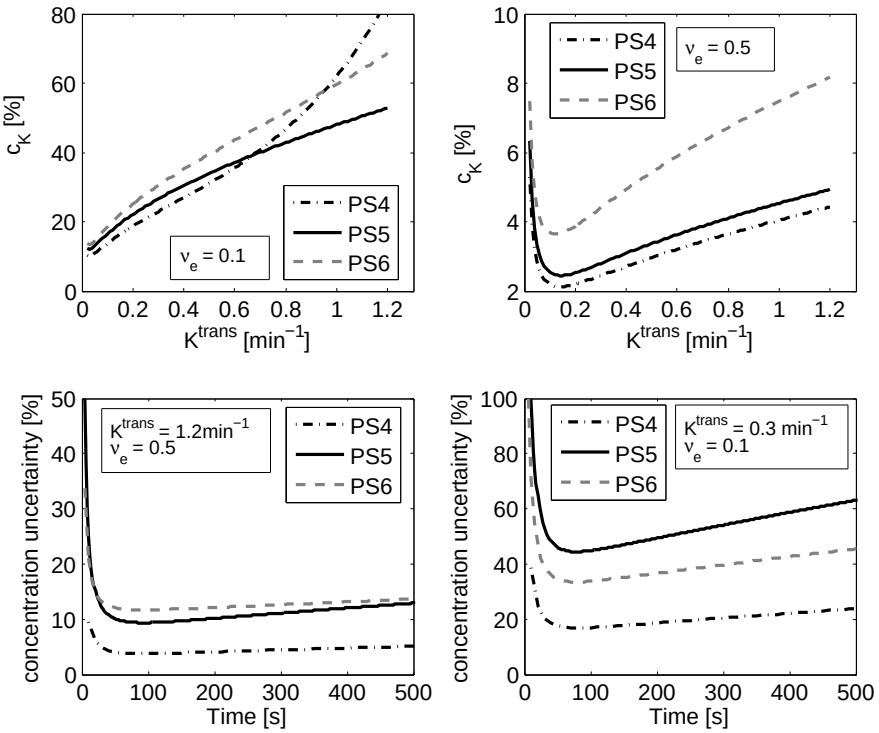


**Figure 8.6:** A-B: coefficient of variation for $K^{trans}$ as a function of $K^{trans}$ for three pulse sequences with different temporal resolution and SNR (table 8.1) with the Weinmann AIF. C-D: procentual concentration uncertainty vs. time for the three pulse sequences for two kinetic parameter combinations.

Another interesting issue that can be adressed with the CRLB framework, is the trade-off between temporal resolution and SNR. As explained in chapter 2, this trade-off is comprised in the value of the parameter NEX. In this section the influence of NEX is investigated: is it usefull to increase SNR at the expense of a reduced temporal resolution, or on the contrary, should temporal resolution be kept as high as possibile, unregarded of the inevitable SNR sacrifices. Therefore, kinetic parameter uncertainty is calculated with the CRLB for PS4-PS6, for $\Delta t$ between 1s and 25s. NEX is then calculated based on the baseline temporal resolution of the corresponding DCE-MRI protocol and SNR is adapted according to the scaling relationship above. While in practice, NEX can only adopt a limited number of values (0.5, 0.75, 1 , 2,...), this analysis is of great value to assess the trade-off between SNR

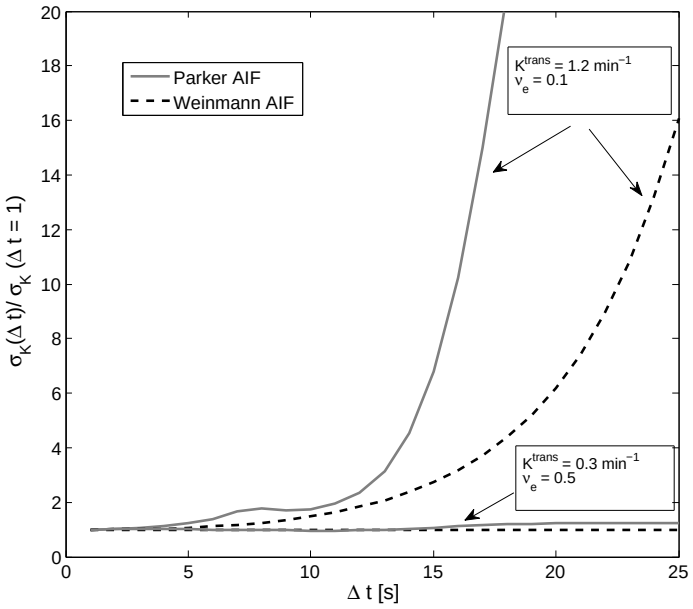


**Figure 8.7:** Ratio of $K^{trans}$-uncertainty at varying temporal resolution, to the uncertainty at a temporal resolution of 1 s, for two different kinetic parameter combinations and two different AIF's (PS4). Temporal resolution is changed by changing NEX, and SNR is adapted according to eq. 8.7. For PS5-PS6 the result is almost identical.

and temporal resolution.

Figure 8.7 shows the ratio of $K^{trans}$-uncertainty at varying temporal resolution, to the uncertainty at a temporal resolution of 1 s, for PS4 and at two kinetic parameter couples and for two different AIF's. As the temporal resolution requirements strongly depend on the value of the kinetic parameter themselves, it is important to evaluate this trade-off for both a high $K^{trans}$/small $\nu_e$-couple (1.2 $min^{-1}$/0.1) as for low $K^{trans}$/high $\nu_e$-couple (0.3 $min^{-1}$/0.5). For the other protocols, the figures are not shown, because they are almost identical. The figure indicates that when pulse sequence parameters ($T_R$, FA, $T_E$,...) are fixed, temporal resolution should be reduced as small as possible (e.g. by partial fourier acquisition), despite the higher SNR in the MR images. The curves for high $K^{trans}$/low $\nu_e$ break down at $\Delta t = 12s$ and $\Delta t = 15s$ for the Parker and Weinmann AIF respectively. As this is seen for the other pulse sequences as well, these values can be considered as a lower limit for the temporal resolution for the kinetic parameter range under consideration. At higher values of $\Delta t$, high $K^{trans}$/small $\nu_e$-couples can no

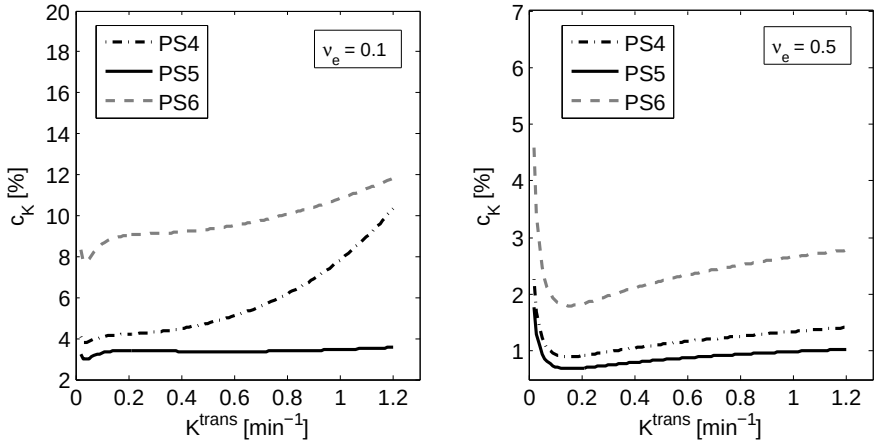


**Figure 8.8:** Coefficient of variation for $K^{trans}$ versus $K^{trans}$ for the three pulse sequences of table 8.3, with optimal flip angle for measuring a 0-2mM concentration range (Parker AIF).

longer be precisely determined, even at high SNR in the MR-images.

## 8.6 Flip angle optimization

Fig. 8.8 is a copy of fig. 8.5, but the flip angle in the three pulse sequences is adapted to its optimal value to measure a 2mM concentration range of Gd-DTPA in the tissue of interest as predicted from the analysis in chapter 5 (55° for PS4, 28° for PS5, 23.6° for PS6). First of all, it is clear that the use of the optimal flip angle effectively reduces the uncertainty on the kinetic parameters (up to 30% for $K^{trans}$ measured with PS4), confirming the results of the simulations in chapter 5. Secondly, fig. 8.8 shows that, under optimal flip angle conditions, PS5 delivers more precise kinetic parameters estimates over the complete range under consideration, which is not the case for the suboptimal flip angle conditions of fig. 8.5. This results shows flip angle optimization can annihilate the effect of increased concentration uncertainty at lower repetition times. As technological improvements enable smaller repetition time and corresponding higher temporal resolution in DCE-MRI, this trend should be accompanied by a robust flip angle optimization to avoid the unwanted and contra-intuitive effects of higher concentration uncertainties.

## 8.7 Extended Tofts & Kermode model

In this section the precision of the ETK-model parameters, $K^{trans}$, $\nu_e$ and $\nu_p$ is investigated by means of the CRLB. A physiologically relevant range for $\nu_p$ is given by 0.01-0.2. [16, 17]. For the pulse sequence settings of PS4 and PS5, fig. 8.9 plots the coefficient of variation for $\nu_p$, and the ratio of $K^{trans}$- and $\nu_e$-uncertainty in the ETK to the uncertainty in the TK model, versus $\nu_p$, for three different $K^{trans}/\nu_e$-couples. It is clear that by incorporating an extra parameter in the model fitting, the uncertainty of $K^{trans}$ and $\nu_e$ increases in a similar way. This increase is most important for the kinetic parameter couples that are most sensitive to the temporal resolution and rises slowly with increasing $\nu_p$. Small $\nu_p$ ($<$0.03) cannot be determined with acceptable precision, unregarded the pulse sequence or the value of the other kinetic parameters. $\nu_p$-uncertainty decreases with increasing $\nu_p$ or decreasing $K^{trans}$. These observations prove that it is statistically useless to employ the ETK-model for fitting DCE-MRI data when the plasma fraction is smaller than 0.03.

## 8.8 Conclusion & practical recommendations

Our CRLB framework has the potential to efficiently simulate the effect of all protocol parameters on the kinetic parameter precision. Thereby it accounts for the effect of the pulse sequence parameter on concentration uncertainty, the influence of temporal resolution and total scan time. CRLB describe how noise on the MR signal intensity is propagated throughout the entire post-processing protocol to uncertainty on the kinetic parameters. We have validated our CRLB-framework by means of simulations and by comparison with an experimental reproducibility study. Combined with the relationships between temporal resolution, pulse sequence parameters and SNR, the CRLB-framework can be used to optimize any DCE-MRI protocol. In this chapter we have performed such optimizations for a cartesian k-space sampling strategy, which has led to a number of practical recommendations for DCE-MRI protocol design:

- $K^{trans}$-uncertainty is proportional to the SNR in MR-measurement. This implies that higher kinetic parameter precision may be obtained at higher field strengths. In chapter 2, however, it was mentioned that at higher field strengths a number of MR-related errors becomes more prominent. Unless these errors can be avoided or corrected for, this imposes a trade-off in pharmacokinetic modeling between precision and accuracy.

- The necessary total scan time is solely dependent on the kinetic parameter range under consideration. The lowest $k_{ep}$-values that

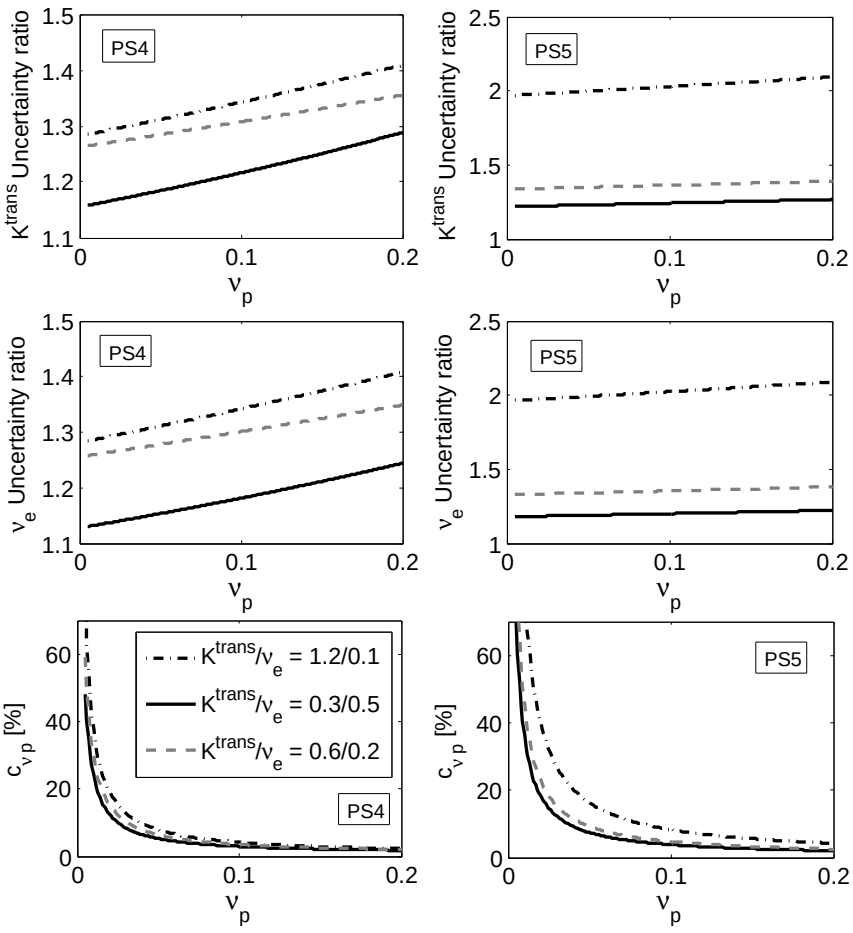


**Figure 8.9:** Above: Ratio of $K^{trans}$ in the ETK-model to the uncertainty in TK model plotted versus $\nu_p$ for PS4 and PS5 and for three $K^{trans}/\nu_e$-couples. Middle: Identical plot for $\nu_e$. Below: Coefficient of variation of $\nu_p$ versus $\nu_p$ for PS4 and PS5 and for three $K^{trans}/\nu_e$-couples. For clarity, the legend is only mentioned in one figure.

have to be measured with acceptable precision, determine the necessary scan time. Practical recommendations for total scan time can be obtained from fig. 8.4. 15 min is adviced for the kinetic parameter range under consideration ($K^{trans}$=0.02-1.2 $min^{-1}$ and $\nu_e$ = 0.1-0.5).

- The influence of temporal resolution on the precision of the kinetic parameter is difficult to assess, due to the trade-off between temporal resolution, spatial resolution, spatial coverage and SNR. However, when the spatial resolution, field of view and pulse sequence parameters are fixed, it is useful to increase spatial resolution by for instance partial fourier sampling. The trade-off between SNR and temporal resolution tends to the side of the latter.

- Technological developments enable shorter repetition times. Reducing $T_R$ increases concentration uncertainty wich may annihilate the effect of the increased temporal resolution. We therefore advice that the trend in DCE-MRI, in which enhanced temporal resolution is obtained by reducing the repetition time, should be accompanied with flip angle optimization as proposed in chapter 5.

- The necessary temporal resolution is determined by the highest $k_{ep}$ values in the tissue of interest. For pharmacokinetic modeling in the kinetic parameter range under consideration with the Parker AIF or the Weinman AIF, $\Delta t$ should not exceed 12s or 15s respectively.

- Under a similar DCE-MRI protocol, the parameters of the ETK model are less reproducible then their TK-counterparts. When estimation reveals a $\nu_p$-value beneath 0.03, this value is irreproducible and the TK-model should be used instead.

A drawback of the CRLB-framework is that it cannot assess the bias of the pharmacokinetic estimates. Influence of the protocol parameters on MR-related error sources, as mentioned in chapter 2, is not taken into account. Furthermore, when the AIF is measured individually by monitoring the signal intensity in feeding artery of the tissue of interest, CRLB may still predict the precision of the pharmacokinetic estimates, but their accuracy can be severely violated by insufficient sampling of the AIF peak [27].

# Chapter 9

# Conclusions & Perspectives

In this conclusive chapter, a number of important realizations in this work is summarized and it is explained how they may contribute to assess the three main limitations of pharmacokinetic modeling as listed in chapter 1. We start by outlining the main innovations of our work. Afterwards the three main limitations are discussed separately. Throughout the sections, a number of perspectives and opportunities for future research are mentioned.

## 9.1 Innovations

The main innovation that is introduced in this work, is the inclusion of a concentration distribution and corresponding concentration uncertainty, that depends upon the pulse sequence parameters and the CA concentration itself. The derivation of this distribution, as mentioned in chapter 4, lays the foundation of the majority of the results in the following chapters. Although, this pulse sequence dependent and heteroskedastic concentration noise, was proposed by Schabel & Parker [30] in 2008 for SPGRE pulse sequences, to our knowledge, the consequences for pharmacokinetic modeling have not been assessed. However, the neglection of the link between pulse sequence parameters and concentration uncertainty is not so surprising. Firstly, it may be remembered that at the start of pharmacokinetic modeling around 1990, a linear relationship between signal enhancement and CA concentration was assumed for the conversion of signal intensity to CA concentration ( [16,33] or section 4.3.4). The use of the non-linear conversion methods has only gained interest in the last decade. When the linear conversion method is employed, the concentration noise is not significantly dependent on the pulse sequence parameters, but only on $T_{10}$ and $r_1$ (eq. 4.19), rendering it homoskedastic in a given voxel. Heteroskedasticity and pulse sequence parameter dependence only occurs when non-linear conversion methods are employed. Secondly,

heteroskedasticity is not easily detected by visual inspection, as may be clear from the concentration curve examples throughout this work. The inclusion of the concentration distribution and the assessment of its consequences for pharmacokinetic parameters is therefore a logic step in DCE-MRI research, that follows from the increasing use of non-linear conversion methods.

We have shown that the dependence of the concentration uncertainty on the pulse sequence parameters and on the true CA concentration itself comprises a number of challenges and opportunities for DCE-MRI protocol design and post-processing of DCE-MRI data. It implies a number of trade-off considerations in DCE-MRI protocol design, and it explains the contra-intuitive observation that protocols with higher SNR and higher temporal resolution yield less precise pharmacokinetic estimates (chapter 8). The latter phenomenom has never been observed before in any simulation study, and shows the importance of accounting for the concentration distribution in pharmacokinetic modeling. In addition, the dependence of the concentration uncertainty on the pulse sequence parameters offers the opportunity to tune the pulse sequence parameters for precise determination of a fixed concentration range, thereby enhancing the reproducibility of pharmacokinetic modeling without the need for technological improvements (chapter 5). Although flip angle optimization had been introduced by Schabel & Parker, our framework is more general, more practical in use and its consequences for pharmacokinetic modeling were investigated. Futhermore, for a fixed protocol design, the heteroskedasticity of the concentration curve has important consequences for the post-processing algorithms. The LSQ-estimator is not optimal and a MLM-estimator should be used instead. For the construction of confidence intervals on the kinetic parameters, the heteroskedasticity should be accounted for, to avoid severe overestimation of the precision of the kinetic estimates (chapter 6). The latter is of course of crucial importance for promising applications of pharmacokinetic modeling as treatment follow-up and the testing of novel anti-angiogenic therapies, and was never before investigated. It may be concluded that the inclusion of this varying concentration distribution is not a second-order effect, but a natural step in the evolution of quantitative DCE-MRI, that has a significant influence on protocol design on post-processing techniques.

In this work, we have mainly focussed on the SPGRE-pulse sequence, as it is abundantly used in pharmacokinetic modeling studies. However, the effect of the heteroskedastic concentration noise has to be evaluated for other pulse sequences as well. We claim that the proposed frameworks in this work, are perfectly capable for protocol optimization and post-processing of other pulse sequences. First of all, our CRLB-framework has been derived based on 1 single assumption ($\sigma_C \sim dC/dS$), which comprises the standard theory of error propagation and whose validity should not be doubted for other pulse sequences. The flip angle optimization is based on the maximization of the parameter $\rho$ (eq. 5.17). For SPGRE-pulse sequences it was shown that

this leads to a decoupling of $T_1$ and $T_2^*$-effects, thereby enabling a contour plot depiction of the optimal flip angle. For other pulse sequences, a similar methodology can be followed, starting from the flip angle $\alpha_C$ for a single concentration, to the maximization of $\rho$. It will of course depend on the pulse sequence properties whether decoupling and contour plot depiction are possible, or whether computational optimization is imposed . For IR-SPGRE pulse sequences for instance, the framework may enable optimization of the flip angle at fixed inversion time or vice versa, optimization of the inversion time (within it boundaries), at fixed flip angle. These are important perspectives for further research, for which our work lays the foundation.

The other important innovation of our work is the stable and fast fitting procedure for the AATH model. The well-known fitting problems have already been reported by Henderson and coworkers in 2000, which was the first study to use the AATH model for separate estimation of plasma flow and permeability in tumors [26]. Despite this huge advantage over the TK- or ETK-model, who can only assess the joint effect of $F_p$ and $PS$ through $K^{trans}$, the number of published studies with the AATH model is almost negligible when compared to those employing the TK- or ETK-model. The main reasons for this are the mathematical fitting complications and instabilities that effectively restrict the clinical use of the AATH-model. Apart from the development of the two fitting procedures as mentioned in chapter 7, the AATH-fitting has not been assessed, untill very recently Garpebring et al. proposed a fourier domain method for TH-model fitting. Therefore, it should not be doubted that our new fitting procedure, that improves both the accuracy and the precision of the AATH parameters and reduces the necessary computational time, will enhance the clinical acceptance of the AATH model. As the parameters of the AATH model were shown to exhibit the best correlation with their physiological counterparts [18], the recursive-based fitting procedure may contribute to an experimental validation of pharmacokinetic modeling, and it can be an important step in the clinical acceptance of the complete pharmacokinetic modeling technique. The fitting procedure can be of interest for the DCE-CT community as well [114].

## 9.2 DCE-MRI protocol

Throughout this work, a number of protocol recommendations has been formulated, that we aim to summarize in this section. In chapter 3, it was shown that protocol requirements are dependent upon the AIF determination strategy. Each of these strategies has a number of advantages, but also introduces additional error sources or imposes more severe protocol requirements. For optimal accuracy of the pharmacokinetic parameters, the AIF should be measured individually. However, this may be complicated due to technological

(inflow effects, too low temporal resolution,...) or physiological (absence of a major artery in the field of view, dispersion, partial volume effects,...) limitations. The other strategies, as reviewed in chapter 3, suffer from inter-individual difference in the AIF (population averaged strategy) or in reference region pharmacokinetic parameters (single reference region method), or require the estimation of additional AIF parameters (multiple reference region & joint estimation of AIF). We therefore think that the DCE-MRI community should not try to find the optimal AIF determination strategy, but should rather aim at developping standardized protocols for each AIF determination method.

### 9.2.1 Generalities

Flip angle optimization should be part of every DCE-MRI protocol. The tuning of the flip angle to the other SPGRE-parameters and the premised concentration range is costless (no trade-off) and has been shown to increase the precision of the pharmacokinetic estimates in both chapter 5 and chapter 8. As technological developments enable smaller repetition times, a trend exists in DCE-MRI to increase the temporal resolution by reducing $T_R$. This trend should be accompanied by flip angle optimization, to avoid unexpected kinetic parameter precision decrease caused by increased concentration noise under these circumstances. As mentioned in chapter 5, the premised concentration range depends on the pathology and the AIF, and is a parameter that should be well-considered. The necessary total scan time is dependent on the minimal $k_{ep}$, for which precise estimation is necessary. This minimal value is related to the pathology as well, but also to the kinetic parameters of the healthy tissue of interest. Although we have only shown the relationship between $k_{ep}$ and $T_{scan}$ for the TK-model, the result should not be doubted for the other models. All models exhibit a very similar long-term behaviour, as is shown in fig. 3.4, that is mainly determined by $k_{ep}$. Finally, in chapter 8, the importance of field of view and spatial resolution was mentioned. A 50% reduction of the spatial resolution for instance, allows a doubling of the temporal resolution at a higher SNR. Therefore the loss in anatomical information is traded for increase kinetic parameter precision (and possibly accuracy). All these considerations prove the obvious statement that DCE-MRI protocol design is highly dependent on the pathology and the tissue of interest. Breast DCE-MRI or prostate DCE-MRI have unequal field of view, require distinctive spatial resolution and are sensitive to different error sources. For every pathology, adapted DCE-MRI protocols should be developped and in particular the trade-off between spatial and temporal resolution should be investigated by the corresponding medical community.

### 9.2.2 Individually measured AIF

When the AIF is measured by monitoring the signal intensity in a large feeding artery of the tissue of interest, the minimal temporal resolution is determined by an accurate sampling of the AIF peak (tyically 1-5s) [24,27]. The repetition should be reduced as low as technically possible, not only to obtain the highest temporal resolution, but also to reduce the inflow effects [60]. At this low repetition time, flip angle optimization is indispensable. The flip angle should be optimized for a typical concentration range of 0-10 mM of the Gd-chelates mentioned in table 2.2. We did not assess the effect of this flip angle on the inflow effects, but as it may be significant [21], it should be investigated in future research. In addition, for an arterial concentration range, even at low repetition time, the optimal flip angles are relatively large (see table 5.3) imposing the need for slice profile or SAR considerations. In chapter 5, we have formulated an alternative optimization strategy if the flip angle is constrained to lower values. The effect of reducing NEX (partial fourier acquisition) should be further investigated. We know that it increases the precision of the pharmacokinetic estimates for a population averaged AIF, but the increased noise level on the individually measured AIF may reduce the reproducibility of the technique.

### 9.2.3 Population averaged AIF

If a population averaged AIF is employed, the conclusions from chapter 8 are all valid. Temporal resolution should be below 12s or 15s for the Parker or Weinmann AIF respectively and determines the precision of the highest $k_{ep}$-value to be measured. Flip angle should be optimized for 0-2mM concentration range in the tissue interest. Increasing the temporal resolution by reducing NEX, effectively enhances the kinetic parameter precision.

### 9.2.4 Other AIF strategies

When the reference region method is used or the AIF is jointly estimated from the tissue concentration curves, a number of extra parameters has to be estimated [148–150]. As these techniques are relatively new, the effect of the temporal resolution should be further investigated. It is impossible to reconstruct or fit a swiftly varying AIF, from low temporal resolution data, imposing the need for more rapid sampling when compared to the population averaged approach. For the same reason, the trade-off between temporal resolution and SNR might still tend to the side of the temporal resolution, but this should be investigated further. Flip angle optimization should be performed for a typical tissue concentration range of 0-2mM.

### 9.2.5 Trade-off between accuracy and precision

During this work a number of conflicting interests has emerged concerning the accuracy and the precision of the pharmacokinetic estimates. For instance, DCE-MRI at higher field strenghts increases the SNR and may be of particular interest for breast imaging, for which the required spatial resolution and spatial coverage, cause limited temporal resolution or low SNR. At 3T, increased SNR can increase the precision of the pharmacokinetic estimates. However, the extent of $B_1$-field inhomogeneities at 3T is much higher and imposes a severe drawback on the accuracy of the pharmacokinetic estimates [36]. Another example concerns incomplete spoiling, which may be reduced at the cost of a higher temporal resolution [61]. The AIF determination strategy comprises the same trade-off. Population averaged AIF have been shown to increase the repeatability of pharmacokinetic estimates [139] but their accuracy is infected by intra-individual differences in the AIF [27]. According to the optimization criterion in chapter 5, flip angle optimization for the arterial concentrations when individually measuring the AIF, increases the concentration uncertainty for the tissue concentrations. This may decrease the precision of the resulting pharmacokinetic parameters, who are typically considered as highly accurate for this AIF determination strategy. All these examples show that in pharmacokinetic modeling a trade-off between parameter accuracy and parameter precision exists. Parameter precision is important for applications as treatment follow-up or the testing of anti-angiogenic therapies, while parameter accuracy may be interesting for other applications as tumor detection and tumor characterization. Optimized protocol design should consider this trade-off and different standardized protocols should be developped for different applications.

## 9.3 Model selection

One of the shortcomings of our work, is that we did not succeed in proposing clear guidelines for model selection. We can only summarize some general observations that were made throughout the different chapters. Remark that a difference exists between the accuracy of a parameter and its agreement with the true physiological quantity it aims to measure. The accuracy of a parameter is optimal when all error sources are minimized. However, even in the absence of error sources, a difference may exist between the estimated parameter and its true physiological counterpart, caused by the invalidity of the model assumptions. Generally, when fitting multiple models to identical data, the parameters of the higher order models exhibit better correlations with the true physiological parameters [18], as higher-order models have less strict assumptions. However, this goes at the cost of increased uncertainties, which we have observed when comparing the ETK- and the TK-parameters at a fixed protocol design. Kershaw & Cheng found a similar uncertainty increase

for the AATH-parameters, altough our new fitting procedure may reduce the absolute differences [24]. In addition, in chapter 6, an increased error sensitivity was observed for the parameters of the ETK-model when compared to the TK-model. In combination with the example from chapter 3 we may conclude that when ETK-modeling, reveals a $\nu_p$-value beneath 0.03-0.05, the TK model should be used instead. The reason is that the estimated $\nu_p$-value has very limited precision, and that the ETK-values for $K^{trans}$ and $\nu_e$ are less reproducible, more prone to MR-related errors than their TK-counterpart, who exhibit identical physiological relevance. For the AATH-model, no such analysis was made, but it should be subject of further investigation. The development of our new AATH-fitting procedure was ment as a first step to perform such an investigation and can comprise an important step in further validation of pharmacokinetic modeling.

## 9.4 Post-processing

We have contributed to the development of standardized post-processing techniques by deriving an accurate first-order corrected conversion method for SPGRE-signal intensity [34], by proposing and testing a MLM-estimator for pharmacokinetic modeling together with a highly accurate technique for confidence interval construction, and by developping a stable and fast fitting procedure for the AATH-model. From engineering point of view, the question may be raised why the signal intensity conversion to CA concentration is not always performed with the most accurate numerical method (see chapter 4). However, as no post-processing software for DCE-MRI and pharmacokinetic modeling exists, the medical research community is mainly interested in a straightforward conversion method that can plainly be implemented. In post-processing software, our first-order method has the ability to speed up the concentration calculation, as it does not require numerical minimization, or it can be used in simulation studies. As mentioned in chapter 7, the MLM estimator and the corresponding confidence interval construction should be embedded in post-processing software. For population-averaged AIF, we have shown their superiority above the currently used LSQ-methods, especially for pharmacokinetic modeling applications in which the knowledge of the kinetic parameter precision is indispensable. For individually measured AIF, the accuracy of the MLM confidence intervals should be investigated further. As mentioned in a footnote in chapter 7, preliminary results shows that when the concentration noise is minimized by flip angle optimization for arterial concentrations, the coverage of the MLM constructed confidence intervals remains close to 95% for the individually measured AIF strategy. This is a very interesting subject for future research and shows again the power of flip angle optimization. For the other AIF strategies, in particular the joint estimation of the AIF and the pharmacokinetic parameters, the

MLM constructed confidence intervals may be an underestimation of the true uncertainty, as additional AIF parameters have to be estimated. Again, this should be subject of further investigation. Nevertheless, the MLM-methods are a very important step in the development of a statistical framework to evaluate the precision and the measurement variability of pharmacokinetic parameterers between and within centers.

## 9.5 Limitations

Apart from several already mentioned shortcomings, the main limitations of our work is the relative absence of in vivo validation. Only for flip angle optimization and for the first-order corrected conversion method an in vivo proof-of-concept was proposed. For post-processing or protocol design however, such validation is a very difficult task. First of all, there is no golden standard to test the accuracy of the pharmacokinetic estimates, which makes use dependent on simulations. The precision of the pharmacokinetic parameters on the other hand, could be experimentally assessed by performing paired examinations in a population of test subjects, as performed by Galbraith et al [66]. This method is prone to other measurement variations, such as improper patient placement between scans, patient motion, injection protocol or physiological changes, that cannot be explained from our CRLB-framework constructed confidence intervals. In addition, to test a number of different DCE-MRI protocols, the scale of the population study should be infeasibly high. Nevertheless, the clinical acceptance of this work will benefit greatly if we would succeed in demonstrating the realisations and innovations of our results in clinical studies.

# List of Figures

# List of Tables

# Bibliography


[1] MLW Ah-See and AR Padhani. Dynamic magnetic resonance imaging in breast cancer. In A. Jackson, D.L. Buckley, and G.J.M. Parker, editors, *Dynamic Contrast-Enhanced Magnetic Resonance Imaging in Oncology*, pages 145–174. Springer, Manchester, 1 edition, 2003.

[2] AR Padhani and MO Leach. Antivascular cancer treatments: functional assessments by dynamic contrast-enhanced magnetic resonance imaging. *Abdominal Imaging*, 30(3):324–341, 2005.

[3] P Carmeliet and RK Jain. Angiogenesis in cancer and other diseases. *Nature*, 407(6801):249–257, 2000.

[4] IS Gribbestad, KI Gjesdal, G Nilsen, S Lundgren, MHB Hjelstuen, and A Jackson. An introduction to dynamic contrast-enhanced MRI in oncology. In A. Jackson, D.L. Buckley, and G.J.M. Parker, editors, *Dynamic Contrast-Enhanced Magnetic Resonance Imaging in Oncology*, pages 4–22. Springer, Manchester, 1 edition, 2003.

[5] JW Rak, BD StCroix, and RS Kerbel. Consequences of angiogenesis for tumor progression, metastasis and cancer-therapy. *Anti-Cancer Drugs*, 6(1):3–18, 1995.

[6] RK Jain. Normalization of tumor vasculature: An emerging concept in antiangiogenic therapy. *Science*, 307(5706):58–62, 2005.

[7] M Moon, D Cornfeld, and J Weinreb. Dynamic Contrast-Enhanced Breast MR Imaging. *Magnetic Resonance Imaging Clinics of North America*, 17(2):351+, 2009.

[8] I Debergh, N Van Damme, P Pattyn, M Peeters, and WP Ceelen. The low-molecular-weight heparin, nadroparin, inhibits tumour angiogenesis in a rodent dorsal skinfold chamber model. *British Journal of Cancer*, 102(5):837–843, 2010.

[9] RA Gatenby, HB Kessler, JS Rosenblum, LR Coia, Moldofsky PJ, WH Hartz, and GJ Broder. Oxygen distribution in squamous-cell carcinoma metastases and its relationship to outcome of radiation-therapy.

*International Journal of Radiation Oncology Biology Physics*, 14(5):831–838, 1988.

[10] TE Yankeelov and JC Gore. Dynamic contrast enhanced magnetic resonance imaging in oncology: Theory, data acquisition, analysis, and examples. *Current Medical Imaging Reviews*, 3(2):91–107, 2007.

[11] LW Dobrucki and AJ Sinusas. Imaging angiogenesis. *Current Opinion in Biotechnology*, 18(1):90–96, 2007.

[12] V Goh, AR Padhani, and S Rasheed. Functional imaging of colorectal cancer angiogenesis. *Lancet Oncology*, 8(3):245–255, 2007.

[13] P Carmeliet. Angiogenesis in life, disease and medicine. *Nature*, 438(7070):932–936, 2005.

[14] MA Cobleigh, VK Langmuir, GW Sledge, KD Miller, L Haney, WF Novotny, JD Reimann, and A Vassel. A phase I/II dose-escalation trial of bevacizumab in previously treated metastatic breast cancer. *Seminars in Oncology*, 30(5, 16):117–124, 2003.

[15] RJ Mayer. Two steps forward in the treatment of colorectal cancer. *New England journal of Oncology*, 350(23):2406–2408, 2004.

[16] PS Tofts. Modeling tracer kinetics in dynamic Gd-DTPA MR imaging. *Journal of Magnetic Resonance Imaging*, 7(1):91–101, 1997.

[17] PS Tofts, G Brix, DL Buckley, JL Evelhoch, E Henderson, M Knopp, HBW Larsson, TY Lee, NA Mayr, GJM Parker, RE Port, J Taylor, and RM Weisskoff. Estimating kinetic parameters from dynamic contrast-enhanced T-1-weighted MRI of a diffusable tracer: Standardized quantities and symbols. *Journal of Magnetic Resonance Imaging*, 10(3):223–232, 1999.

[18] DL Buckley. Uncertainty in the analysis of tracer kinetics using dynamic contrast-enhanced T-1-weighted MRI. *Magnetic Resonance in Medicine*, 47(3):601–606, 2002.

[19] AR Padhani. Dynamic contrast-enhanced MRI in clinical oncology: Current status and future directions. *Journal of Magnetic Resonance Imaging*, 16(4):407–422, 2002.

[20] AR Padhani and MO Leach. Antivascular cancer treatments: functional assessments by dynamic contrast-enhanced magnetic resonance imaging. *Abdominal Imaging*, 30(3):324–341, 2005.

[21] DJ Collins and AR Padhani. Dynamic magnetic resonance imaging of tumor perfusion. *IEEE Engineering in Medicine and Biology*, 23(5):65–83, 2004.

[22] S Sourbron. Technical aspects of MR perfusion. *European Journal of Radiology*, 76(3):304–313, 2010.

[23] R G P Lopata, W H Backes, P P J van den Bosch, and N A W van Riel. On the identifiability of pharmacokinetic parameters in dynamic contrast-enhanced imaging. *Magnetic Resonance in Medicine*, 58(2):425–429, 2007.

[24] LE Kershaw and HLM Cheng. Temporal resolution and SNR requirements for accurate DCE-MRI data analysis using the AATH model. *Magnetic Resonance in Medicine*, 64(6):1772–1780, 2010.

[25] D De Naeyer, Y De Deene, WP Ceelen, P Segers, and P Verdonck. Precision analysis of kinetic modelling estimates in dynamic contrast enhanced MRI. *Magnetic Resonance Materials in Physics Biology and Medicine*, 24(2):51–66, 2011.

[26] E Henderson, J Sykes, D Drost, HJ Weinmann, BK Rutt, and TY Lee. Simultaneous MRI measurement of blood flow, blood volume, and capillary permeability in mammary tumors using two different contrast agents. *Journal of Magnetic Resonance Imaging*, 12(6):991–1003, 2000.

[27] HLM Cheng. Investigation and optimization of parameter accuracy in dynamic contrast-enhanced MRI. *Journal of Magnetic Resonance Imaging*, 28(3):736–743, 2008.

[28] M Heisen, X Fan, J Buurman, NAW van Riel, GS Karczmar, and BMH Romeny. The Influence of Temporal Resolution in Determining Pharmacokinetic Parameters From DCE-MRI Data. *Magnetic Resonance in Medicine*, 63(3):811–816, 2010.

[29] E Henderson, BK Rutt, and TY Lee. Temporal sampling requirements for the tracer kinetics modeling of breast disease. *Magnetic Resonance Imaging*, 16(9):1057–1073, 1998.

[30] MC Schabel and DL Parker. Uncertainty and bias in contrast concentration measurements using spoiled gradient echo pulse sequences. *Physics in Medicine and Biology*, 53(9):2345–2373, 2008.

[31] J L Evelhoch. Key factors in the acquisition of contrast kinetic data for oncology. *Journal of Magnetic Resonance Imaging*, 10(3):254–259, 1999.

[32] X Yang and MV Knopp. Quantifying Tumor Vascular Heterogeneity with Dynamic Contrast-Enhanced Magnetic Resonance Imaging: A Review. *Journal of Biomedicine and Biotechnology*, 2011.

[33] M Heilmann, F Kiessling, M Enderlin, and LR Schad. Determination of pharmacokinetic parameters in DCE MRI - consequence of nonlinearity between contrast agent concentration and signal intensity. *Investigative Radiology*, 41(6):536–543, 2006.

[34] D De Naeyer, I Debergh, WP De Deene, Yand Ceelen, P Segers, and P Verdonck. First order correction for T2*-relaxation in determining contrast agent concentration from spoiled gradient echo pulse sequence signal intensity. *Journal of Magnetic Resonance Imaging* , Published online before print(?):?, 2011.

[35] MR Orton, DJ Collins, S Walker-Samuel, JA d'Arcy, DJ Hawkes, D Atkinson, and MO Leach. Bayesion estimation of pharmacokinetic parameters for DCE-MRI with a robust treatment of enhancement onset time. *Physics in Medicine and Biology*, 52(9):2393–2408, 2007.

[36] P Di Giovanni, CA Azlan, TS Ahearn, SI Semple, FJ Gilbert, and TW Redpath. The accuracy of pharmacokinetic parameter measurement in DCE-MRI of the breast at 3T. *Physics in Medicine and Biology*, 55(1):121–32, 2010.

[37] T E et al. Yankeelov. Integration of quantitative DCE-MRI and ADC mapping to monitor treatment response in human breast cancer: initial results. *Magnetic Resonance Imaging*, 25(1):1–13, 2007.

[38] DL Buckley, PJ Drew, S Mussurakis, JRT Monson, and A Horsman. Microvessel density in invasive breast cancer assessed by dynamic Gd-DTPA enhanced MRI. *Journal of Magnetic Resonance Imaging*, 7(3):461–464, 1997.

[39] F Kiessling, M Krix, M Heilmann, S Vosseler, M Lichy, C Fink, N Farhan, K Kleinschmidt, L Schad, NE Fusenig, and S Delorme. Comparing dynamic parameters of tumor vascularization in nude mice revealed by magnetic resonance imaging and contrast-enhanced intermittent power Doppler sonography. *Investigative Radiology*, 38(8):516–524, 2003.

[40] RGJ Kierkels and et al. Comparison between perfusion computer tomography and dynamic contrast-enhanced magnetic resonance imaging in rectal cancer. *International Journal of Radiation Oncology Biology Physics*, 77(2):400–408, 2010.

[41] JP Parkka, P Niemi, A Saraste, JW Koskenvuo, M Komu, V Oikonen, JO Toikka, TO Kiviniemi, J Knuuti, H Sakuma, and JJ Hartiala. Comparison of MRI and positron emission tomography for measuring myocardial perfusion reserve in healthy humans. *Magnetic Resonance in Medicine*, 55(4):772–779, 2006.

[42] MA Bernstein, KF King, and Xiaohong JZ. Basic pulse sequences. In *Handbook of MRI pulse sequences*, volume 1, page 1017. Elsevier Academic Press, 2004.

[43] Y De Deene. Magnetic resonance imaging: from basic principles to advanced techniques. 2008.

[44] M Rohrer, H Bauer, J Mintorovitch, M Requardt, and HJ Weinmann. Comparison of magnetic properties of MRI contrast media solutions at different magnetic field strengths. *Investigative Radiology*, 40(11):715–724, 2005.

[45] D Vincensini, V Dedieu, PA Eliat, C Vincent, C Bailly, J de Certaines, and F Joffre. Magnetic resonance imaging measurements of vascular permeability and extracellular volume fraction of breast tumors by dynamic Gd-DTPA-enhanced relaxometry. *Magnetic Resonance Imaging*, 25(3):293–302, 2007.

[46] JM Bonny, L Foucat, W Laurent, and JP Renou. Optimization of signal intensity and t-1-dependent contrast with nonstandard flip angles in spin-echo and inversion-recovery MR imaging. *Journal of Magnetic Resonance*, 130(1):51–57, 1998.

[47] DL Buckley and GJM Parker. Measuring contrast agents concentration in T1-weighted dynamic contrast-enhanced MRI. In A. Jackson, D.L. Buckley, and G.J.M. Parker, editors, *Dynamic Contrast-Enhanced Magnetic Resonance Imaging in Oncology*, pages 69–80. Springer, Manchester, 1 edition, 2003.

[48] P Wedeking, CH Sotak, J Telser, K Kumar, CA Chang, and MF Tweedle. Quantitative dependence of mr signal intensity on tissue concentration of gd(hp-do3a) in the nephrectomized rat. *Magnetic Resonance Imaging*, 10(1):97–108, 1992.

[49] MC Schabel and GR Morrell. Uncertainty in t-1 mapping using the variable flip angle method with two flip angles. *Physics in Medicine and Biology*, 54(1):N1–N8, 2009.

[50] HLM Cheng and GA Wright. Rapid high-resolution T-1 mapping by variable flip angles: accurate and precise measurements in the presence of radiofrequency field inhomogeinity. *Magnetic Resonance in Medicine*, 55(3):566–574, 2006.

[51] JA Brookes, TW Redpath, FJ Gilbert, AD Murray, and RT Staff. Accuracy of T1 measurement in dynamic contrast-enhanced breast MRI using two- and three-dimensional variable flip angle fast low-angle shot. *Journal Magnetic Resonance Imaging*, 9(2):163–171, 1999.

[52] Y De Deene, C De Wagter, W De Neve, and E Achten. Artefacts in multi-echo T-2 imaging for high-precision gel dosimetry: II. Analysis of B-1-field inhomogeneity. *Physics in Medicine and Biology*, 45(7):1825–1839, 2000.

[53] S Chung, D Kim, E Breton, and L Axel. Rapid B(1)(+) Mapping Using a Preconditioning RF Pulse with TurboFLASH Readout. *Magnetic Resonance in Medicine*, 64(2):439–446, 2010.

[54] CA Azlan, P Di Giovanni, TS Ahearn, SIK Semple, FJ Gilbert, and TW Redpath. B(1) Transmission-Field Inhomogeneity and Enhancement Ratio Errors in Dynamic Contrast-Enhanced MRI (DCE-MRI) of the Breast at 3T. *Journal of Magnetic Resonance Imaging*, 31(1):234–239, 2010.

[55] CK Kuhl, H Kooijman, J Gieseke, and HH Schild. Effect of B-1 inhomogeneity on breast imaging at 3.0 T. *Radiology*, 244(3):929–930, 2007.

[56] GJM Parker, GJ Barker, and PS Tofts. Accurate multislice gradient echo T-1 measurement in the presence of non-ideal RF pulse shape and RF field nonuniformity. *Magnetic Resonance in Medicine*, 45(5):838–845, 2001. 7th Annual ISMRM Meeting, PHILADELPHIA, PA, MAY, 1999.

[57] JA Brookes, TW Redpath, FJ Gilbert, G Needham, and AD Murray. Measurement of spin-lattice relaxation times with FLASH for dynamic MRI of the breast. *British Journal of Radiology*, 69(819):206–214, 1996.

[58] WH Perman, MA Bernstein, and JC Sandstrom. A method for correctly setting the rf flip angle. *Magnetic Resonance in Medicine*, 9(1):16–24, 1989.

[59] C Preibisch and R Deichmann. Influence of RF Spoiling on the Stability and Accuracy of T(1) Mapping Based on Spoiled FLASH With Varying Flip Angles. *Magnetic Resonance in Medicine*, 61(1):125–135, 2009.

[60] A Garpebring, R Wirestam, N Ostlund, and M Karlsson. Effects of Inflow and Radiofrequency Spoiling on the Arterial Input Function in Dynamic Contrast-Enhanced MRI: A Combined Phantom and Simulation Study. *Magnetic Resonance in Medicine*, 65(6):1670–1679, 2011.

[61] VL Yarnykh. Optimal Radiofrequency and Gradient Spoiling for Improved Accuracy of T(1) and B(1) Measurements Using Fast Steady-State Techniques. *Magnetic Resonance in Medicine*, 63(6):1610–1626, 2010.

[62] F Peeters, L Annet, L Hermoye, and BE Van Beers. Inflow correction of hepatic perfusion measurements using T-1-weighted, fast gradient-echo, contrast-enhanced MRI. *Magnetic Resonance in Medicine*, 51(4):710–717, 2004.

[63] BL Daniel, YF Yen, GH Glover, RL Ikeda, DM Birdwell, AM Sawyer-Glover, JW Black, SK Plevritis, SS Jeffrey, and RJ Herfkens. Breast disease: dynamic spiral MR imaging. *Radiology*, 209(2):499–509, 1998.

[64] XP Zhu, KL Li, and A Jackson. Dynamic contrast-enhanced MRI in cerebral tumours. In A. Jackson, D.L. Buckley, and G.J.M. Parker, editors, *Dynamic Contrast-Enhanced Magnetic Resonance Imaging in Oncology*, pages 117–144. Springer, Manchester, 1 edition, 2003.

[65] N F Schwenzer, I Kotter, J C Henes, C Schraml, J Fritz, C D Claussen, and M Horger. The role of dynamic contrast-enhanced MRI in the differential diagnosis of psoriatic and rheumatoid arthritis. *American Journal of Roentgenology*, 194(3):715–720, 2010.

[66] SM Galbraith, MA Lodge, NJ Taylor, GJS Rustin, S Bentzen, JJ Stirling, and AR Padhani. Reproducibility of dynamic contrast-enhanced MRI in human muscle and tumours: comparison of quantitative and semi-quantitative analysis. *NMR in Biomedicine*, 15(2):132–142, 2002.

[67] PS Tofts and AG Kermode. Measurement of the blood-brain-barrier permeability and leakage space using dynamic mr imaging .1. fundamental-concepts. *Magnetic Resonance in Medicine*, 17(2):357–367, 1991.

[68] G Brix, W Semmler, R Port, LR Schad, G Layer, and WJ Lorenz. Pharmacokinetic parameters in cns gd-dtpa enhanced mr imaging. *Journal of Computer Assisted Tomography*, 15(4):621–628, 1991.

[69] HBW Larsson, M Stubgaard, JL Frederiksen, M Jensen, O Henriksen, and OB Paulson. Quantitation of blood-brain-barrier defect by magnetic-resonance-imaging and gadolinium-dtpa in patients with multiple-sclerosis and brain-tumors. *Magnetic Resonance in Medicine*, 16(1):117–131, 1990.

[70] B Tofts, P S an Berkowitz and M D Schnall. Quantitative-analysis of dynamic gd-dtpa enhancement in breast-tumors using a permeability model. *Magnetic Resonance in Medicine*, 33(4):564–568, 1995.

[71] U Hoffmann, G Brix, M V Knopp, T Hess, and W J Lorenz. Pharmacokinetic mapping of the breast - a new method for dynamic mr mammography. *Magnetic Resonance in Medicine*, 33(4):506–514, 1995.

[72] TS Koh, CH Thng, PS Lee, S Hartono, H Rumpel, BC Goh, and S Bisdas. Hepatic metastases: In vivo assessment of perfusion parameters at dynamic contrast-enhanced MR imaging with dual-input two-compartment tracer kinetics model. *Radiology*, 249(1):307–320, 2008.

[73] S S Kety. The theory and application of the exchange of inert gas at the lungs and tissues. *Pharmacological Reviews*, 3(1):1–41, 1951.

[74] K Ohno, KD Pettigrew, and SI Rapoport. Lower limits of cerebrovascular permeability to non-electrolytes in conscious rat. *American Journal of Physiology*, 235(3):H299–H307, 1978.

[75] TPL Roberts and MD Noseworthy. Contrast agents for magnetic resonance imaging. In A. Jackson, D.L. Buckley, and G.J.M. Parker, editors, *Dynamic Contrast-Enhanced Magnetic Resonance Imaging in Oncology*, pages 23–37. Springer, Manchester, 1 edition, 2003.

[76] EM Renkin. Transport of potassium-42 from blood to tissue in isolated mammalian skeletal muscles. *American Journal of Physiology*, 197(6):1205–1210, 1959.

[77] C Crone. Permeability of capillaries in various organs as determined by use of indicator diffusion method. *Acta Physiologica Scandinavica*, 58(4):292–305, 1963.

[78] JA Johnson and TA Wilson. A model for capillary exchange. *American Journal of Physiology*, 210(6):1299–1303, 1966.

[79] KS St Lawrence and TY Lee. An adiabatic approximation to the tissue homogeneity model for water exchange in the brain: I. theoretical derivation. *Journal of Cerebral Blood Flow and Metabolism*, 18(12):1365–1377, 1998.

[80] KS St Lawrence and TY Lee. An adiabatic approximation to the tissue homogeneity model for water exchange in the brain: Ii. experimental validation. *Journal of Cerebral Blood Flow and Metabolism*, 18(12):1378–1385, 1998.

[81] A Garpebring, N Ostlund, and M Karlsson. A novel estimation method for physiological parameters in dynamic contrast-enhanced mri: Application of a distributed parameter model using fourier-domain calculations. *IEEE Transactions on Medical Imaging*, 28(9):1375–1383, 2009.

[82] IO Jelescu, IR Leppert, S Narayanan, D Araujo, DL Arnold, and GB Pike. Dual-Temporal Resolution Dynamic Contrast-Enhanced MRI Protocol for Blood-Brain Barrier Permeability Measurement in Enhancing Multiple Sclerosis Lesions. *Journal of Magnetic Resonance Imaging*, 33(6):1291–1300, 2011.

[83] A Kassner, DM Mandell, and DJ Mikulis. Measuring Permeability in Acute Ischemic Stroke. *Neuroimaging Clinics of North America*, 21(2):315+, 2011.

[84] NG Harris, V Gauden, PA Fraser, SR Williams, and GJM Parker. MRI measurement of blood-brain barrier permeability following spontaneous reperfusion in the starch microsphere model of ischemia. *Magnetic Resonance Imaging*, 20(3):221–230, 2002.

[85] M Haris, N Husain, A Singh, R Awasthi, RKS Rathore, M Husain, and RK Gupta. Dynamic contrast-enhanced (DCE) derived transfer coefficient (k(trans)) is a surrogate marker of matrix metalloproteinase 9 (MMP-9) expression in brain tuberculomas. *Journal of Magnetic Resonance Imaging*, 28(3):588–597, 2008.

[86] M. Haris and et al. Assessment of therapeutic response in brain tuberculomas using serial dynamic contrast-enhanced MRI. *Clinical Radiology*, 63(5):562–574, 2008.

[87] RJ Hodgson, P O'Connor, and R Moots. MRI of rheumatoid arthritis-image quantitation for the assessment of disease activity, progression and response to therapy. *Rheumatology*, 47(1):13–21, 2008.

[88] DW Workie, BJ Dardzinski, TB Graham, T Laor, WA Bommer, and KJ O'Brien. Quantification of dynamic contrast-enhanced MR imaging of the knee in children with juvenile rheumatoid arthritis based on pharmacokinetic modeling. *Magnetic Resonance Imaging*, 22(9):1201–1210, 2004.

[89] TB Workie, DW Graham, T Laor, A Rajagopal, KJ O'Brien, WA Bommer, JM Racadio, NJ Shire, and BJ Dardzinski. Quantitative MR characterization of disease activity in the knee in children with juvenile idiopathic arthritis: a longitudinal pilot study. *Pediatric Radiology*, 37(6):535–543, 2007.

[90] RJ Hodgson, S Connolly, T Barnes, B Eyes, RSD Campbell, and R Moots. Pharmacokinetic Modeling of dynamic contrast-enhanced MRI of the hand and wrist in rheumatoid arthritis and the response to anti-tumor necrosis factor-alpha therapy. *Magnetic Resonance in Medicine*, 58(3):482–489, 2007.

[91] JC Gardener, ML Alerhut, and GC Gardner. Vascularity in the RA wrist at 1-2 months following initiation of anti-TNFalpha and methotrexate therapy. *Rheumatoloy*, 47(1):S131, 2003.

[92] E Kirkhus, A Bjornerud, J Thoen, V Johnston, K Dale, and HJ Smith. Contrast-enhanced dynamic magnetic resonance imaging of finger joints in osteoarthritis and rheumatoid arthritis: an analysis based on pharmacokinetic modeling. *Acta Radiologica*, 47(8):845–851, 2006.

[93] C Calcagno, V Mani, S Ramachandran, and ZA Fayad. Dynamic contrast enhanced (DCE) magnetic resonance imaging (MRI) of atherosclerotic plaque angiogenesis. *Angiogenesis*, 13(2):87–99, 2010.

[94] WS Kerwin, M Oikawa, C Yuan, GP Jarvik, and TS Hatsukami. MR imaging of adventitial vasa vasorum in carotid atherosclerosis. *Magnetic Resonance in Medicine*, 59(3):507–514, 2008.

[95] C Calcagno, JC Cornily, F Hyafil, JHF Rudd, KC Briley-Saebo, V Mani, G Goldschlager, J Machac, V Fuster, and ZA Fayad. Detection of neovessels in atherosclerotic plaques of rabbits using dynamic contrast enhanced MRI and 18F-FDG PET. *Arteriosclerosis, Thrombosis and Vascular Biology*, 28(7):1311–1317, 2008.

[96] WS Kerwin, A Hooker, M Spilker, P Vicini, M Ferguson, T Hatsukami, and C Yuan. Quantitative magnetic resonance imaging analysis of neovasculature volume in carotid atherosclerotic plaque. *Circulation*, 107(6):851–856, 2003.

[97] A Oto, X Fan, D Mustafi, SA Jansen, GS Karczmar, DT Rubin, and A Kayhan. Quantitative Analysis of Dynamic Contrast Enhanced MRI for Assessment of Bowel Inflammation in Crohn's Disease: Pilot Study. *Academic Radiology*, 16(10):1223–1230, 2009.

[98] T Franiel, B Hamm, and H Hricak. Dynamic contrast-enhanced magnetic resonance imaging and pharmacokinetic models in prostate cancer. *European Radiology*, 21(3):616–626, 2011.

[99] KM Pondman and et al. MR-guided biopsy of the prostate: An overview of techniques and a systematic review. *European Urology*, 54(3):517–527, 2008.

[100] I Ocak, M Bernardo, G Metzger, T Barrett, P Pinto, PS Albert, and PL Choyke. Dynamic contrast-enhanced MRI of prostate cancer at 3 T: A study of pharmacokinetic parameters. *American Journal of Roentgenology*, 189(4):W192–W201, 2007.

[101] F Kiessling, M Lichy, R Grobholz, N Farhan, M Heilmann, MS Michel, L Trojan, A Werner, J Rabe, S Delorme, HU Kauczor, and HP Schlemmer. Detection of prostate carcinomas with T1-weighted dynamic contrast-enhance MRI. Value of two-compartment model. *Radiologe*, 43(6):474–480, 2003.

[102] FA van Dorsten, M van der Graaf, MRW Engelbrecht, GJLH van Leenders, A Verhofstad, M Rijpkema, JJMCH de la Rosette, JO Barentsz, and A Heerschap. Combined quantitative dynamic contrast-enhanced MR imaging and H-1 MR spectroscopic imaging of human prostate cancer. *Journal of Magnetic Resonance Imaging*, 20(2):279–287, 2004.

[103] DL Langer, TH van der Kwast, AJ Evans, J Trachtenberg, BC Wilson, and MA Haider. Prostate Cancer Detection With Multi-parametric MRI: Logistic Regression Analysis of Quantitative T2, Diffusion-Weighted Imaging, and Dynamic Contrast-Enhanced MRI. *Journal of Magnetic Resonance Imaging*, 30(2):327–334, 2009.

[104] A Sciarra, J Barentsz, A Bjartell, J Eastham, H Hricak, V Panebianco, and JA Witjes. Advances in Magnetic Resonance Imaging: How They Are Changing the Management of Prostate Cancer. *European Urology*, 59(6):962–977, 2011.

[105] T Hambrock and et al. Magnetic Resonance Imaging Guided Prostate Biopsy in Men With Repeat Negative Biopsies and Increased Prostate Specific Antigen. *Journal of Urology*, 183(2):520–527, 2010.

[106] S Xu and et al. Real-time MRI-TRUS fusion for guidance of targeted prostate biopsies. *Computer Aided Surgery*, 13(5, SI):255–264, 2008. 10th International Conference on Medical Image Computing and Computer-Assisted Intervention (MICCAI 2007), Brisbane, AUSTRALIA, OCT 29-NOV 02, 2007.

[107] ASN Jackson and et al. Dynamic contrast-enhanced MRI for prostate cancer localization. *British Journal of Radiology*, 82(974):148–156, 2009.

[108] JJ Fuetterer and et al. Prostate cancer localization with dynamic contrast-enhanced MR imaging and proton MR spectroscopic imaging. *Radiology*, 241(2):449–458, 2006.

[109] D Yakar and et al. Feasibility of 3T Dynamic Contrast-Enhanced Magnetic Resonance-Guided Biopsy in Localizing Local Recurrence of Prostate Cancer After External Beam Radiation Therapy. *Investigative Radiology*, 45(3):121–125, 2010.

[110] MR Moman and et al. Focal salvage guided by t(2)-weighted and dynamic contrast-enhanced magnetic resonance imaging for prostate cancer recurrences. *International Journal of Radiation Oncoloy Biology Physics*, 76(3):741–746, 2010.

[111] LE Kershaw, CE Hutchinson, and DL Buckley. Benign prostatic hyperplasia: evaluation of T1, T2 and microvascular characteristics with T1-weighted dynamic contrast-enhanced MRI. *Journal of Magnetic Resonance Imaging*, 29(3):641–648, 2009.

[112] DL Buckley, C Roberts, GJM Parker, JP Logue, and CE Hutchinson. Prostate cancer: Evaluation of vascular characteristics with dynamic contrast-enhanced T1-weighted MR imaging - Initial experience. *Radiology*, 233(3):709–715, 2004.

[113] LE Kershaw and DL Buckley. Precision in measurements of perfusion and microvascular permeability with T-1-weighted dynamic contrast-enhanced MRI. *Magnetic Resonance in Medicine*, 56(5):986–992, 2006.

[114] CRLPN Jeukens, CAT van den Berg, R Donker, M van Vulpen, CJG Bakker, MS. Van Leeuwen, and UA van der Heide. Feasibility and measurement precision of 3D quantitative blood flow mapping of the prostate using dynamic contrast-enhanced multi-slice CT. *Physics in Medicine and Biology*, 51(17):4329–4343, 2006.

[115] C Andersen and FT Jensen. Differences in blood-tumour-barrier leakage of human intracranial tumours: Quantitative monitoring of vasogenic oedema and its response to glucocorticoid treatment. *Acta Neurochirurgica*, 140(9):919–924, 1998.

[116] XP Zhu, KL Li, ID Kamaly-Asl, DR Checkley, JJL Tessier, JC Waterton, and A Jackson. Quantification of endothelial permeability, leakage space, and blood volume in brain tumors using combined T1 and T2*contrast-enhanced dynamic MR imaging. *Journal of Magnetic Resonance Imaging*, 11(6):575–585, 2000.

[117] M Haris and et al. Differentiation of infective from neoplastic brain lesions by dynamic contrast-enhanced MRI. *Neuroradiology*, 50(6):531–540, 2008.

[118] S Bisdas, T Naegele, R Ritz, A Dimostheni, C Pfannenberg, M Reimold, TS Koh, and U Ernemann. Distinguishing Recurrent High-grade Gliomas from Radiation Injury: A Pilot Study Using Dynamic Contrast-enhanced MR Imaging. *Academic Radiology*, 18(5):575–583, 2011.

[119] LW Turnbull. Dynamic contrast-enhanced mri in the diagnosis and management of breast cancer. *NMR in Biomedicine*, 22(1):28–39, 2009.

[120] D Saslow and et al. American Cancer Society guidelines for breast screening with MRI as an adjunct to mammography. *CA-A Cancer Journal for Clinicians*, 57(2):75–89, 2007.

[121] CK Kuhl, HH Schild, and N Morakkabati. Dynamic bilateral contrast-enhanced MR imaging of the breast: Trade-off between spatial and temporal resolution. *Radiology*, 236(3):789–800, 2005.

[122] E Furman-Haran, E Schechtman, F Kelcz, K Kirshenbaum, and H Degani. Magnetic resonance imaging reveals functional diversity of the vasculature in benign and malignant breast lesions. *Cancer-American Cancer Society*, 104(4):708–718, 2005.

[123] MC Schabel, GR Morrell, KY Oh, CA Walczak, RB Barlow, and LA Neumayer. Pharmacokinetic Mapping for Lesion Classification in Dynamic Breast MRI. *Journal of Magnetic Resonance Imaging*, 31(6):1371–1378, 2010.

[124] S Mussurakis, DL Buckley, PJ Drew, JN Fox, PJ Carleton, LW Turnbull, and A Horsman. Dynamic MR imaging of the breast combined with analysis of contrast agent kinetics in the differentiation of primary breast tumours. *Clinical Radiology*, 52(7):516–526, 1997.

[125] A Radjenovic, BJ Dall, JP Ridgway, and MA Smith. Measurement of pharmacokinetic parameters in histologically graded invasive breast tumours using dynamic contrast-enhanced MRI. *British Journal of Radiology*, 81(962):120–128, 2008.

[126] MLW Ah-See and et al. Early Changes in Functional Dynamic Magnetic Resonance Imaging Predict for Pathologic Response to Neoadjuvant Chemotherapy in Primary Breast Cancer. *Clinical Cancer Research*, 14(20):6580–6589, 2008.

[127] MF Akisik, K Sandrasegaran, G Bu, C Lin, GD Hutchins, and EG Chiorean. Pancreatic Cancer: Utility of Dynamic Contrast-enhanced MR Imaging in Assessment of Antiangiogenic Therapy. *Radiology*, 256(2):441–449, 2010.

[128] S Kim, LA Loevner, H Quon, A Kilger, E Sherman, G Weinstein, A Chalian, and H Poptani. Prediction of Response to Chemoradiation Therapy in Squamous Cell Carcinomas of the Head and Neck Using Dynamic Contrast-Enhanced MR Imaging. *American Journal of NeuroRadiology*, 31(2):262–268, 2010.

[129] WR Jarnagin and et al. Regional chemotherapy for unresectable primary liver cancer: results of a phase II clinical trial and assessment of DCE-MRI as a biomarker of survival. *Annals of Oncology*, 20(9):1589–1595, 2009. 43rd Annual Meeting of the American-Society-of-Clinical-Oncology, Chicago, IL, JUN 01-05, 2007.

[130] SM Zahra, KG Hollingsworth, E Sala, DJ Lomas, and LT Tan. Dynamic contrast-enhanced mri as a predictor of tumour response to radiotherapy. *Lancet oncology*, 8(1):63–74, 2007.

[131] W Ceelen, P Smeets, W Backes, N Van Damme, T Boterberg, P Demetter, I Bouckenooghe, M De Visschere, M Peeters, and P Pattyn. Noninvasive monitoring of radiotherapy-induced microvascular changes using dynamic contrast enhanced magnetic resonance imaging (DCE-MRI) in a colorectal tumor model. *International Journal of Radiation Oncology Biology Physics*, 64(4):1188–1196, 2006.

[132] MA Zahra and et al. Semiquantitative and quantitative dynamic contrast-enhanced magnetic resonance imaging measurements predict radiation response in cervix cancer. *International Journal of Radiation Oncology Biology Physics*, 74(3):766–773, 2009.

[133] K Gulliksrud, KM Ovrebo, B Mathiesen, and EK Rofstad. Differentiation between hypoxic and non-hypoxic experimental tumors by dynamic contrast-enhanced magnetic resonance imaging. *Radiotherapy and Oncology*, 98(3):360–364, 2011.

[134] C Ellingsen, TAM Egeland, K Gulliksrud, JV Gaustad, B Mathiesen, and EK Rofstad. Assessment of hypoxia in human cervical carcinoma xenografts by dynamic contrast-enhanced magnetic resonance imaging. *International Journal of Radiation Oncology Biology Physics*, 73(3):838–845, 2009.

[135] TT et al Batchelor. AZD2171, a pan-VEGF receptor tyrosine kinase inhibitor, normalizes tumor vasculature and alleviates edema in glioblastoma patients. *Cancer Cell*, 11(1):83–95, 2007.

[136] S Kummar, ME Gutierrez, A Chen, IB Turkbey, D Allen, YR Horneffer, L Juwara, L Cao, Y Yu, YS Kim, J Trepel, H Chen, P Choyke, G Melillo, AJ Murgo, J Collins, and JH Doroshow. Phase I trial of vandetanib and bevacizumab evaluating the VEGF and EGF signal transduction pathways in adults with solid tumours and lymphomas. *European Journal of Cancer*, 47(7):997–1005, 2011.

[137] J. D. Lickliter and et al. Phase I trial of CYT997, a novel cytotoxic and vascular-disrupting agent. *British Journal of Cancer*, 103(5):597–606, 2010.

[138] B Morgan and et al. Dynamic contrast-enhanced magnetic resonance imaging as a biomarker for the pharmacological response of PTK787/ZK 222584, an inhibitor of the vascular endothelial growth factor receptor tyrosine kinases, in patients with advanced colorectal cancer and liver metastases: Results from two phase I studies. *Journal of Clinical Oncology*, 21(21):3955–3964, 2003.

[139] GJM Parker, C Roberts, A Macdonald, GA Buonaccorsi, S Cheung, DL Buckley, A Jackson, Y Watson, K Davies, and GC Jayson. Experimentally-derived functional form for a population-averaged high-temporal-resolution arterial input function for dynamic contrast-enhanced MRI. *Magnetic Resonance in Medicine*, 56(5):993–1000, 2006.

[140] AR Padhani, C Hayes, S Landau, and MO Leach. Reproducibility of quantitative dynamic MRI of normal human tissues. *NMR in Biomedicine*, 15(2):143–153, 2002.

[141] C Yang, GS Karczmar, M Medved, A Oto, M Zamora, and WM Stadler. Reproducibility assessment of a multiple reference tissue method for quantitative dynamic contrast enhanced-MRI analysis. *Magnetic Resonance in Medicine*, 61(4):851–859, 2009.

[142] GO Cron, C Foottit, TE Yankeelov, LI Avruch, ME Schweitzer, and I Cameroni. Arterial Input Functions Determined From MR Signal Magnitude and Phase for Quantitative Dynamic Contrast-Enhanced MRI in the Human Pelvis. *Magnetic Resonance in Medicine*, 66(2):498–504, 2011.

[143] R Meng, SD Chang, EC Jones, SL Goldenberg, and P Kozlowski. Comparison between Population Average and Experimentally Measured Arterial Input Function in Predicting Biopsy Results in Prostate Cancer. *Academic Radiology*, 17(4):520–525, 2010.

[144] DA Kovar, M Lewis, and GS Karczmar. A new method for imaging perfusion and contrast extraction fraction: Input functions derived from reference tissues. *Journal of Magnetic Resonance Imaging*, 8(5):1126–1134, 1998.

[145] T E Yankeelov, J J Luci, M Lepage, R Li, L Debusk, P C Lin, R R Price, and J C Gore. Quantitative pharmacokinetic analysis of DCE-MRI data without an arterial input function: a reference region model. *Magnetic Resonance Imaging*, 23(4):519–529, 2005.

[146] S Walker-Samuel, CC Parker, MO Leach, and DJ Collins. Reproducibility of reference tissue quantification of dynamic contrast-enhanced data: comparison with a fixed vascular input function. *Physics in Medicine and Biology*, 52(1):75–89, 2007.

[147] T E Yankeelov, G O Cron, C L Addison, J C Wallace, R C Wilkins, B A Pappas, G E Santyr, and J C Gore. Comparison of a reference region model with direct measurement of an AIF in the analysis of DCE-MRI data. *Magnetic Resonance in Medicine*, 57(2):353–361, 2007.

[148] C Yang, GS Karczmar, M Medved, and WM Stadler. Estimating the arterial input function using two reference tissues in dynamic contrast-enhanced MRI studies: Fundamental concepts and simulations. *Magnetic Resonance in Medicine*, 52(5):1110–1117, 2004.

[149] C Yang, GS Karczmar, M Medved, and WM Stadler. Multiple reference tissue method for contrast agent arterial input function estimation. *Magnetic Resonance in Medicine*, 58(6):1266–1275, 2007.

[150] JU Fluckiger, MC Schabel, and EVR DiBella. Model-based blind estimation of kinetic parameters in dynamic contrast enhanced (DCE)-MRI. *Magnetic Resonance in Medicine*, 62(6):1447–1486, 2009.

[151] MC Schabel, JU Fluckiger, and EVR DiBella. A model-constrained Monte Carlo method for blind arterial input function estimation in dynamic contrast-enhanced MRI: I. Simulations. *Physics in Medicine and Biology*, 55(16):4783–4806, 2010.

[152] MC Schabel, EVR DiBella, RL Jensen, and KL Salzman. A model-constrained Monte Carlo method for blind arterial input function estimation in dynamic contrast-enhanced MRI: II. In vivo results. *Physics in Medicine and Biology*, 55(16):4807–4823, 2010.

[153] MY Su, YC Cheung, JP Fruehauf, H Yu, O Nalcioglu, E Mechetner, A Kyshtoobayeva, SC Chen, S Hsueh, CE McLaren, and YL Wan. Correlation of dynamic contrast enhancement MRI parameters with microvessel density and VEGF for assessment of angiogenesis in breast cancer. *Journal of Magnetic Resonance Imaging*, 18(4):467–477, 2003. 9th Annual Meeting of the International-Society-for-Magnetic-Resonance-in-Medicine (ISMRM), GLASGOW, SCOTLAND, APR 21-27, 2001.

[154] JH Naish, DM McGrath, LJ Bains, K Passera, C Roberts, Y Watson, S Cheung, MB Taylor, JP Logue, DL Buckley, J Tessier, H Young,

JC Waterton, and GJM Parker. Comparison of Dynamic Contrast-Enhanced MRI and Dynamic Contrast-Enhanced CT Biomarkers in Bladder Cancer. *Magnetic Resonance Imaging*, 66(1):219–226, 2011.

[155] JH Naish, LE Kershaw, DL Buckley, A Jackson, JC Waterton, and GJM Parker. Modeling of contrast agent kinetics in the lung using T1-weighted dynamic contrast-enhanced MRI. *Magnetic Resonance in Medicine*, 61(6):1507–1514, 2009.

[156] DL Parker and GT Gullberg. Signal-to-noise efficiency in magnetic-resonance-imaging. *Medical Physics*, 17(2):250–257, 1990.

[157] A Macovski. Noise in mri. *Magnetic Resonance in Medicine*, 36(3):494–497, 1996.

[158] BM Dale, JA Jesberger, JS Lewin, CM Hillenbrand, and JL Duerk. Determining and optimizing the precision of quantitative measurements of perfusion from dynamic contrast enhanced MRI. *Journal of Magnetic Resonance Imaging*, 18(5):575–584, 2003.

[159] H. Gudbjartsson and S. Patz. The rician distribution of noisy MRI data. *Magnetic Resonance in Medicine*, 34(2):910–914, 1995.

[160] MA Stephens. Tests of fit for the logistic distribution based on the empirical distribution function. *Biometrika*, 66(3):591–595, 1979.

[161] NJ Pelc. Optimization of flip angle for T1 dependent contrast in MRI. *Magnetic Resonance in Medicine*, 29(5):695–699, 1993.

[162] D De Naeyer, J Verhulst, WP Ceelen, P Segers, Y De Deene, and P Verdonck. Flip Angle Optimization for Dynamic Contrast-enhanced Mri-studies with Spoiled Gradient echo Pulse Sequences. *Physics in Medicine and Biology*, pages 5373–95.

[163] M D Pickles, D J Manton, M Lowry, and L W Turnbull. Prognostic value of pre-treatment DCE-MRI parameters in predicting disease free and overall survival for breast cancer patients undergoing neoadjuvant chemotherapy. *European Journal of Radiology*, 71(3):498–505, 2009.

[164] M Heisen, X Fan, J Buurman, N A W van Riel, G S Karczmar, and B M T Romeny. The use of a reference tissue arterial input function with low-temporal-resolution DCE-MRI data. *Physics in Medicine and Biology*, 55(16):4871–4883, 2010.

[165] D P Bradley, J L Tessier, D Checkley, H Kuribayashi, J C Waterton, J Kendrew, and S R Wedge. Effects of AZD2171 and vandetanib (ZD6474, zactima) on haemodynamic variables in an sw620 human colon tumour model: an investigation using dynamic contrast-enhanced MRI and the rapid clearance blood pool contrast agent, P792 (gadomelitol). *NMR Biomed.*, 21(1):42–52, 2008.

[166] TE Yankeelov and et al. Integration of quantitative DCE-MRI and ADC mapping to monitor treatment response in human breast cancer: initial results. *Magnetic Resonance Imaging*, 25(1):1–13, 2007.

[167] RB Buxton, RR Edelman, BR Rosen, GL Wismer, and TJ Brady. Contrast in rapid mr imaging - T1-weighted and T2-weighted imaging. *Journal of Computed Assisted Tomography*, 11(1):7–16, 1987.

[168] EH Haselhoff. Optimization of flip angle for T-1 dependent contrast: A closed form solution. *Magnetic Resonance in Medicine*, 38(3):518–518, 1997.

[169] J Vautier, M Heilmann, C Walczak, J Mispelter, M Zamora, and A Volk. 2d and 3d radial multi-gradient-echo dce mri in murine tumor models with dynamic r2*-corrected r1 mapping. *Magnetic Resonance in Medicine*, 64(1):313–318, 2010.

[170] Y De Deene, R Van de Walle, E Achten, and C De Wagter. Mathematical analysis and experimental investigation of noise in quantitative magnetic resonance imaging applied in polymer gel dosimetry. *Signal Processing*, 70(2):85–101, 1998.

[171] A Singh, RKS Rathore, M Haris, SK Verma, N Husain, and RK Gupta. Improved bolus arrival time and arterial input function estimation for tracer kinetic analysis in DCE-MRI. *Journal of Magnetic Resonance Imaging*, 29(1):166–176, 2009.

[172] C Radhakrishna Rao. Information and the accuracy attainable in the estimation of statistical parameters. *Bulletin of the Calcutta Mathematical Society*, 37:81–91, 1945.

[173] GJ Stanisz and RM Henkelman. Gd-dtpa relaxivity depends on macromolecular content. *Magnetic Resonance in Medicine*, 44(5):665–667, 2000.

[174] C Lavini and JJC Verhoeff. Reproducibility of the gadolinium concentration measurements and of the fitting parameter of the vascular input function in the superior sagittal sinus in a patient population. *Magnetic Resonance Imaging*, 28(10):1420–1430, 2010.

[175] HJWL Aerts, NAW van Riel, and WH Backes. System identification theory in pharmacokinetic modeling of dynamic contrast-enhanced MRI: Influence of contrast injection. *Magnetic Resonance in Medicine*, 59(5):1111–1119, 2008.